

Rowan University

Rowan Digital Works

---

Theses and Dissertations

---

11-15-2022

## AN IN SILICO STUDY OF THE DELTA OPIOID RECEPTOR USING SMALL MOLECULES

Emily Dean  
*Rowan University*

Follow this and additional works at: <https://rdw.rowan.edu/etd>



Part of the [Medicinal Chemistry and Pharmaceutics Commons](#)

---

### Recommended Citation

Dean, Emily, "AN IN SILICO STUDY OF THE DELTA OPIOID RECEPTOR USING SMALL MOLECULES" (2022).  
*Theses and Dissertations*. 3070.  
<https://rdw.rowan.edu/etd/3070>

This Thesis is brought to you for free and open access by Rowan Digital Works. It has been accepted for inclusion in Theses and Dissertations by an authorized administrator of Rowan Digital Works. For more information, please contact [graduateresearch@rowan.edu](mailto:graduateresearch@rowan.edu).

**AN *IN SILICO* STUDY OF THE DELTA OPIOID RECEPTOR USING SMALL  
MOLECULES**

by

Emily Dean

A Thesis

Submitted to the  
Department of Chemistry and Biochemistry  
College of Science and Mathematics  
In partial fulfillment of the requirement  
For the degree of  
Master of Science in Pharmaceutical Sciences  
at  
Rowan University

Thesis Chair: Chun Wu, Ph.D., Associate Professor, Chemistry & Biochemistry

Committee Members:

Gregory A. Caputo, Ph.D., Associate Dean CSM, Chemistry & Biochemistry  
Thomas M. Keck, Ph.D., Associate Professor, Chemistry & Biochemistry

© 2022 Emily Dean

## **Dedications**

I dedicate my work to my parents, Christopher and Lisa Dean. Their love and support is forever endless. Without it, I would not be where I am today. They have not only taught me to work hard, but also that everything will always work out in the end. To consider myself lucky to have them by my side would be an understatement. I cannot thank them enough for everything.



## **Acknowledgments**

I would like to thank Dr. Chun Wu for helping me grow in this field and always pushing me to better myself. Your guidance and teachings have brought me to where I am today. I thank you for not only this, but for allowing me to join your lab when I had no experience and all the help and support you have given me through everything. I would also like to thank Dr. Gregory Caputo for his support through my journey, as well as always being there to answer any of my questions even though I was never a student of his. You have always been someone I knew I could come to if I needed anything.

## Abstract

Emily Dean

AN *IN SILICO* STUDY OF THE DELTA OPIOID RECEPTOR USING SMALL  
MOLECULES

2020-2021

Chun Wu, Ph.D.

Master of Science in Pharmaceutical Sciences

The DOR is the least studied out of the three opioid receptors ( $\mu$ ,  $\kappa$  and  $\delta$ ). The most is known of the Mu Opioid receptor (MOR) and the drugs that target it have led to the global opioid epidemic due to their adverse effects of tolerance and addiction. The DOR is not known for the same adverse effects and therefore, is a promising pharmacological target for the development of new opioid ligands. In this thesis, molecular modeling, simulations and other computational methods are introduced in Chapter 1 where these methods are used to study the activation mechanism of DOR (Chapter 2) and are used to identify novel DOR agonists (Chapter 3). Recently, both the inactive and active conformations of the DOR have been solved. However, the activation mechanism remains to be elusive. In Chapter 2, molecular dynamics (MD) simulations will offer a deeper insight into the dynamics and interactions beginning with the inactive conformation of the receptor when bound to an agonist undergoing a conformational change. Chapter 3 will involve the use of high-throughput screening of new molecules for potential agonist candidates using multiple conformations of the active conformation of the DOR. The top lead compounds subjected further computational analysis on their drug properties to ensure that they do not cause any unwanted side effects. Final lead compounds are available for experimental testing.

## Table of Contents

Abstract .....	v
List of Figures .....	x
List of Tables .....	xii
Chapter 1: Introduction to Molecular Dynamic Simulations.....	1
1.1 Background.....	1
1.2 Methodology .....	3
1.2.1 Homology Modeling.....	3
1.2.2 Molecular Docking and Structure Based Virtual Screening.....	4
1.2.3 Molecular Dynamics Simulations.....	6
1.2.4 MM-GBSA/MM-PBSA Binding Free Energy Calculations .....	7
1.3 Thesis Outline .....	8
Chapter 2: To Probe the Activation Mechanism of the Delta Opioid Receptor by an Agonist ADL5859 Started From Inactive Conformation Using Molecular Dynamics Simulations .....	11
2.1 Introduction.....	11
2.1.1 Problems With Opioid Receptors .....	11
2.1.2 History of DOR Agonists.....	12
2.1.3 Crystal Structures and Previous MD Simulation Studies of the DOR.....	12
2.1.4 Experimental Overview .....	14
2.2 Methods.....	15
2.2.1 Multiple Sequence Alignment and Analysis.....	15
2.2.2 The Homology Modeling of the DOR.....	16
2.2.3 Molecular Docking of ADL5859.....	16

## Table of Contents (Continued)

2.2.4 Molecular Dynamics Simulation System Setup .....	17
2.2.5 Trajectory Clustering Analysis .....	19
2.2.6 RMSD of Protein Structure Analysis.....	20
2.2.7 Analysis of Microswitches and Pairwise Residue Distance .....	20
2.2.8 Normal Mode Analysis .....	21
2.3 Results.....	21
2.3.1 Sequence-Based Comparison of Human DOR With Other Class A GPCRs.....	21
2.3.2 Homology Model of Human DOR Without Fusion Protein.....	21
2.3.3 Docked Conformation of ADL5859 Shows Similarity With the Co-Crystallized Conformation of DPI-287 and Subtle Difference With Naltrindole .....	22
2.3.4 MD Simulations of Human DOR With ADL5859 and Naltrindole Assume Steady State.....	24
2.3.5 ADL5859-DOR System Shows Adopting Toward the Crystal Active Conformation While Naltrindole-DOR System Maintains Inactive Conformation .....	26
2.3.6 ADL5859-DOR System Has Multiple Clusters Folding Toward the Active State.....	31
2.3.7 Secondary Structure Analysis Shows Maintained Helices but With Subtle Differences Between the Two Complexes.....	35
2.3.8 Key Interactions of ADL5859 and Naltrindole With Human DOR .....	36
2.3.9 DOR Shows Flexibility When Bound to ADL5859 Than Naltrindole.....	37
2.3.10 Distance of ADL5859 With Side Chain of D95 Decreases While Naltrindole Shows No Change.....	40
2.3.11 Role of Molecular Switches in the Activation of DOR by ADL5859.....	41

## Table of Contents (Continued)

2.3.12 Center of Mass Distances Identify Activation Related Changes .....	43
2.3.13 Normal Mode Analysis Shows the Overall Motion of the Receptor .....	47
2.4 Discussion .....	47
Chapter 3: To Probe Activation Mechanism of Agonist DPI-287 to Delta Opioid Receptor and Novel Agonists to Using Ensemble-Based Virtual Screening With Molecular Dynamics Simulations .....	56
3.1 Introduction .....	56
3.1.1 The Opioid Epidemic .....	56
3.1.2 DOR Target Potential .....	57
3.1.3 Previous Studies on the DOR .....	58
3.1.4 High-Throughput Virtual Screening Reasoning .....	58
3.1.5 Ensemble-Based Approaches .....	59
3.1.6 Experimental Overview .....	60
3.2 Methods .....	61
3.2.1 Virtual Screening Workflow Overview .....	61
3.2.2 Normal Mode Analysis .....	69
3.2.3 Dynamical Network Model .....	69
3.3 Results .....	70
3.3.1 Crystal Conformation Maintained Stability During MD Simulation .....	70
3.3.2 Crystal Complex Produces Other Conformations to Use for HTVS .....	73
3.3.3 Top 8 Compounds Assume Steady State .....	80
3.3.4 MD Simulations Improved the Binding Pose of the Top Eight Ligands .....	82
3.3.5 Protein-Ligand Interactions of Top Compounds to the DOR .....	83

## Table of Contents (Continued)

3.3.6 Secondary Structure Shows Maintained Helices .....	87
3.3.7 RMSF Shows Fluctuation in Regions of the Protein With Respect to the Ligand .....	87
3.3.8 Network Analysis Helped to Understand Communications Among Different Regions of the DOR.....	88
3.4 Discussion .....	91
References.....	94
Appendix A: To Probe the Activation Mechanism of the Delta Opioid Receptor by an Agonist ADL5859 Started From Inactive Conformation Using Molecular Dynamic Simulations .....	104
Appendix B: To Probe Activation Mechanism of Agonist DPI-287 to Delta Opioid Receptor and Novel Agonists to Using Ensemble-Based Virtual Screening With Molecular Dynamics Simulations.....	149

## List of Figures

Figure	Page
Figure 1. Chemical Structures of Agonist ADL5859, Agonist DPI-287, and Antagonist Naltrindole to DOR.....	13
Figure 2. Comparison Between the Docked Pose With the Crystal Pose of Ligands ....	23
Figure 3. Protein (Blue) and Ligand (Red) RMSD.....	25
Figure 4. Receptor RMSDs of Varied Parts From Agonist and Antagonist Simulation Systems Against the Two Solved Crystal Receptor Structures .....	29
Figure 5. Most Abundant Agonist Cluster of the First Trajectory Compared to Solved Crystal Structures and Structural RMSD Calculations.....	34
Figure 6. Protein-Ligand 2D Interaction Diagram.....	37
Figure 7. RMSF Comparison.....	39
Figure 8. Average Distance Timeline Between Positively Charged Nitrogen Atom of Ligand and Side Chain of D95.....	40
Figure 9. Molecular Switches .....	42
Figure 10. DOR Activation Pathway .....	55
Figure 11. Structural Organization of the Active Conformation of the DOR and Ligand .....	60
Figure 12. Virtual Screening Workflow .....	62
Figure 13. Simulation Interaction Diagrams After MD Simulation of the Crystal Structure.....	72
Figure 14. Superimposition of the Active Crystal DOR Structure With the Most Abundant Conformations From the MD Simulations With Agonist DPI-287 .....	74
Figure 15. Predicted Binding Pocket of the Different DOR Conformations.....	75
Figure 16. Top 2 Low Frequency Vibrational Modes From the Normal Mode Analysis.....	76
Figure 17. Network Analysis .....	77

## List of Figures (Continued)

Figure	Page
Figure 18. RMSD of the Top 8 Zinc Compounds .....	81
Figure 19. Comparison of Glide XP Docking Pose (Blue) and MD Simulation Pose (Red) for the Top 8 Compounds .....	83
Figure 20. Protein-Ligand 2D Interaction Diagrams From the MD Simulation for the Top 8 Compounds .....	86
Figure 21. Optimal Signal Transduction Pathway of the Transmission Switch and the Toggle Switch .....	90



## List of Tables

Table	Page
Table 1. The Combined Mean RMSF Values of the Ligand Bound Complex From N-Terminal to C-Terminal .....	38
Table 2. Residue Pairs for Center of Mass Distance Measurement.....	44
Table 3. Average Atomic and Center of Mass Distances .....	46
Table 4. Comparison Between MOR and DOR.....	57
Table 5. Various Properties of the Top 8 Compounds Identified From Our Virtual Screening Work Flow .....	80
Table 6. The Predicted Pharmacokinetics ADME Properties.....	80
Table 7. Protein-Ligand Interactions During MD Simulations for the Top 8 Compounds From the MD Simulations .....	84

## Chapter 1

### Introduction to Molecular Dynamic Simulations

#### 1.1 Background

The detailed molecular information on the drug targets are not used in traditional developmental methods of new drugs. Consequently, when a new drug is brought into the market using the traditional developmental methods, the money, amount of time needed, and risk of failure can be very costly, taking anywhere from 10-15 years from the initial identification until the drug is developed and on the market, in addition to costing between 800 million to 1.8 billion US dollars<sup>1</sup>. The increase in databases and the genomic and protein information plus an advancement in computational methods, with higher performance and better algorithms to process these valuable information greatly advances the drug discovery process<sup>2,3</sup>.

Computational tools used for the discovery and development of a new drug to aid in human health range from a number of applications and methods. Computer aided drug design (CADD) is a powerful application that has been developed that uses the rational drug design approach that provides more knowledge and information about binding affinity and any interactions in the protein-ligand complex<sup>1</sup>. The use of this tool has enhanced the preliminary stage of the drug discovery process by reducing the failures of potential molecules at the drug development level to be brought onto market, as well as minimizing the cost. CADD consists of two general approaches: structure-based and ligand-based. Both of these methods have made their own advancements without the other.

Structure-based drug design (SBDD) begins with identifying and processing the desired three-dimensional (3D) target with all of its structural information<sup>4</sup>. By using a 3D structure of the protein target, this allows for the use of computation to delve into experimental results at the atomic level and to gain more understanding of disease at the molecular level. This target structure can be taken from a variety of different methods such as experimental methods like NMR and X-ray crystallography downloaded to a database, or purely computational methods like homology modeling and molecular dynamics (MD) simulations. SBDD can be divided into two subcategories within itself: the de novo approach and the virtual screening approach. The de novo approach produces some lead compounds, but mainly offers new scaffolds of ligands that can be further developed due to their attractive properties by using fragments of molecules that correspond with the binding site<sup>1,5</sup>. The idea is based on the primary constraints of ligands and receptors that are already known to produce novel compounds. The virtual screening (VS) approach uses commercially available small molecule libraries to identify compounds predicted to have attractive binding affinities for the target protein of a known structure. Once these compounds are identified, it is with the thought that they will then be experimentally tested on. This method does not produce novel ligands.

Ligand-based drug design (LBDD) is the method of CADD that is useful when the desired protein target is missing important structural information or when its entire 3D structure itself is absent<sup>6</sup>. If this is the case, the approach is to use the information from the known ligands that bind to the target of interest to determine the lacking structural and/or physiochemical information causing the observed biological response<sup>1</sup>.

LBDD utilizes two approaches: quantitative structure-activity relationships (QSARs) and pharmacophore-based techniques.

Molecular dynamics (MD) simulations is a computational technique that further enhances the drug design process. It is used to simulate a molecular system in a period of time to study the interactions and stability based on the physical laws.<sup>7</sup> This technique can help rule out ligands that will not remain stable in complex with the target. This only adds more insight into the interacting behavior of a ligand with its target in higher spatial and temporal resolution than traditional experimental methods.

Because of the advancement in computational methods with higher performance and better algorithms, the preliminary stage of the drug discovery process has become much more reliable with higher accuracy and less costly procedures<sup>3</sup>. This is largely in part due to the vast availability of both genomic and protein information, as well as the access to computational tools and applications such as ligand design, modeling, pharmacophore mapping, protein-ligand molecular dynamic simulations, and toxicity predictions.

## **1.2 Methodology**

### ***1.2.1 Homology Modeling***

To study a protein, whether it be the protein's dynamics or finding ligand candidates, the three-dimensional (3D) structure of the protein is typically required.<sup>8,9</sup> The 3D structure is determined from the protein sequence. Experimental methods such as NMR spectroscopy and X-ray crystallography are how protein structures are determined but both methods are time consuming and cannot necessarily be used for each protein. In

the case of NMR spectroscopy, the protein molecules generally need to be smaller and with X-ray crystallography, the molecules need to be crystallized. There are difficulties when it comes to protein purification and crystallization, most notably in membrane proteins that make up a majority of therapeutic targets, which causes a deficiency in high resolution 3D protein structures.

Homology modeling is considered to be a powerful computational prediction tool with two main observations: the 3D protein structure is determined precisely by its amino acid sequence, and protein structure is very conserved with change happening at a slow rate.<sup>8</sup> It is also fast with low cost and simple steps. There are seven standard steps with this modeling method: (1) The identification and the selection of templates using sequence similarity as well as environmental and phylogenetic factors, (2) Sequence alignment with careful inspection and alignment correction, (3) Model building, (4) Loop modeling with accuracy determining the significance of the model for future use, (5) Side chain modeling using the backbone, (6) Model Optimization to improve the model quality, (7) Model Validation where the functionality is determined by the quality of the model.

### ***1.2.2 Molecular Docking and Structure Based Virtual Screening***

Molecular docking is a key tool used in the drug discovery process due to its fast and cost-efficient methodologies that predict the binding pose of ligands to the active site of their respective targets. Docking has been a great help with screening large libraries of molecules, meaning it has the ability to work in combination with structure-based virtual screening (SBVS). This works by docking large libraries of small molecules to a target in

a short time frame. The docking software generates a molecular surface of the target structure on the basis of high-resolution structure that achieves the docking poses. Spheres are generated in a known ligand binding site of the target and determine all the possible orientations of new ligands. A scoring function is then used that ranks the different poses by most favorable to least favorable binding. Docking has three main scoring functions. The force-field based approach is the first that is based on experimental data that estimates binding affinity. Empirical scoring has a simplified version of the parameters in the force-field based approach that gives slightly less accurate results. The knowledge-based scoring function is the third approach that is taken from known binding interactions and is more common than using random distribution. After filtering by docking score functions, ADMET(absorption, distribution, metabolism, excretion and toxicity) property prediction is utilized for SBVS by providing insight into different relevant properties that tell if a molecule is druggable. About half of the potential drugs tested fail in clinical trials due to poor ADMET properties, making early prediction cut out a lot of time and cost that would be wasted on testing unnecessary ligands. Schrodinger's Glide extra precision (XP) docking uses extensive algorithms that uses not only water desolvation energy terms, but also QikProp ADME prediction.

$$\text{XP Glide Score} = \Delta E_{\text{coul}} + \Delta E_{\text{vdW}} + E_{\text{bind}} + E_{\text{penalty}}$$

$$E_{\text{bind}} = E_{\text{hyd\_enclosure}}^4 + E_{\text{hb\_nn\_motif}}^5 + E_{\text{hb\_cc\_motif}}^6 + E_{\text{pl}}^7 + E_{\text{hb\_pair}} + E_{\text{phobic\_pair}}$$

$$E_{\text{penalty}} = E_{\text{desolv}} + E_{\text{ligand\_strain}}$$

### *1.2.3 Molecular Dynamics Simulations*

Molecular dynamics simulations are a technique that uses the integration of Newton's equations of motion.<sup>7</sup> The purpose is to simulate behaviors of a dynamic molecular system throughout a period of time. Using the Newton's laws of motion, MD simulations predict the motions of the atoms when acted upon by forces. The forces that are calculated in these simulations are based on force fields, which are the equations used to set up parameters that determine the potential energy interactions of the system. These interactions and features include bond rotations, bond length, and Coulomb's law, comprising of van der Waals and electrostatic interactions.<sup>10</sup> There are two different solvent models to simulations that have different levels of atomic detail. Explicit solvent models are effective by imitating the most realistic solvent effects but are high in cost. This type of model is better for comparing drastically different systems. Implicit models use a dielectric constant and treat the solvent as a continuous medium, making it cheaper to use and a better option for comparing systems that are more similar to each other. After the system is prepared, the simulation is ran and reaches equilibrium, snap shots are taken throughout the simulation time, creating the simulation trajectory. The position of all the atoms in the system have coordinates that are contained in each of the snap shots. Using this, different post simulation analyses can be performed to help determine the questions asked beforehand. Trajectory clustering is one of the analyses performed post-simulation to identify the populated conformation by first aligning each snapshot of the trajectory. After the initial alignment, the different populated clusters are based on the root mean squared deviation (RMSD) of the backbone of the target protein to determine structural similarity and represent the different structural families. The populated

conformations generated can then be used as the most ideal binding positions of the target.

#### ***1.2.4 MM-GBSA/MM-PBSA Binding Free Energy Calculations***

To determine if a bound ligand is stable in its target's binding pocket, the binding free energy during the simulation can be calculated. There are different prediction methods of binding free energy, however, the end point methods have been particularly useful by calculating the bound and unbound states of solvated molecules.<sup>11</sup> The two known end point methods are the molecular mechanics generalized Born surface area (MM-GBSA) and molecular mechanics Poisson-Boltzmann surface area (MM-PBSA). These binding free energy methods are fast and widely exploited.<sup>12</sup> The calculations are done through minimization on the receptor alone, the ligand alone, and then the receptor-ligand complex. There are three components involved in the energy decomposition of these calculations which are van der Waals, electrostatic, and hydrophobic interactions using surface area. Each component contributes to the final result of the total binding energy. This gives further insight into the most optimal binding conformation of the ligand in the binding pocket. The calculations of binding free energy do not include a solute entropic term; therefore, the true binding free energy could be much lower. This is compensated for when different binding poses have comparable solute entropies to each other, allowing the relative binding free energy to be relative to MM-GBSA binding energies. In the equations, the internal energy change ( $\Delta E_{int}$ ) is canceled due to the receptor and ligand being extracted from the same trajectory. This makes the electrostatic ( $\Delta E_{ELE}$ ) plus the van der Waals ( $\Delta E_{VDW}$ ) energies equal to the gas phase interaction energy ( $\Delta E_{gas}$ ) from the receptor and ligand. In the fourth equation, polar and nonpolar



energy terms together make up the solvation free energy ( $\Delta G_{sol}$ ). While the polar contribution ( $\Delta G_{(GB)}$ ) is calculated using the GB model, the nonpolar energy term ( $\Delta G_{(Surf)}$ ) is calculated using solvent-accessible surface area. Because the entropy term is neglected, the binding free energy ( $\Delta G_{bind}$ ) is the sum of the gas-phase and solvation free energy.

$$\Delta G_{bind} = (G_{complex}) - (G_{receptor}) - (G_{ligand}) \quad (1)$$

$$\Delta G_{bind} = \Delta H - T\Delta S \approx \Delta E_{gas} + \Delta G_{sol} - T\Delta S \quad (2)$$

$$\Delta E_{gas} = \Delta E_{int} + \Delta E_{ELE} + \Delta E_{VDW} \quad (3)$$

$$\Delta G_{sol} = \Delta G_{(GB)} + \Delta G_{(Surf)} \quad (4)$$

### ***1.3 Thesis Outline***

In Chapter 2, the activation mechanism of the Delta Opioid receptor (DOR) was probed using novel agonist ADL5859 in multiple microsecond molecular dynamics simulations. Out of the three opioid receptors, (Mu, Kappa, Delta) the Delta receptor is the least studied with the potential for reduced adverse side effects. Recently, crystal structures of both the inactive and active conformation of the DOR were solved. However, the activation mechanism for this specific receptor remains elusive. To give deeper insight into what the activation mechanism may be, we started with a homology model of the inactive conformation of the DOR and docked the agonist ADL5859 into the binding pocket before starting the 1 microsecond MD simulations. Because all crystal structures contained fusion proteins at the N terminus, they were removed to rule out any probability that they may have played a role in the conformational change. The crystal

antagonist Naltrindole was also used and underwent 1 microsecond MD simulations to serve as an inactive control to compare our active complex. The most notable difference between the active and inactive state of class A GPCRs is the outward movement of transmembrane 6 (TM6) that opens up the intracellular portion of the receptor to allow G protein signaling and ultimately activation. After performing the MD simulations on both ligand complexes, the outward movement of TM6 was observed in the agonist bound complex. Additional analyses were performed including the molecular switch analysis and measuring the center of mass distances of known residue contacts for class A GPCRs and other unique distances to this study. Through our findings, key residues were identified that played a role in the activation of the DOR using an agonist starting with the inactive state of the receptor. In Chapter 3, HTVS coupled with MD simulations were used to find potential agonist candidates targeting the DOR. The world still struggles with opioid addiction. Addiction is a side effect found in agonists that target the MOR. The DOR has shown to not have addictive properties, indicating that finding ligands that target this receptor while eliciting the biological response of antinociception is of high importance. The HTVS and MD simulations were not just run on the active conformation, but on two other active conformations found while simulating the active crystal DOR with the crystal agonist ligand, making this an ensemble-based approach. The reasoning for this is due to the flexibility of receptors creating challenges within the binding site with amino acid side-chains that have dozens of rotatable conformations. The ensemble-based approach samples the degrees of freedom of the side chains instead of using just one conformation. The HTVS was ran on the multiple conformations and the top molecules were simulated to assess their stability. Through this and additional

analyses, 8 compounds were identified that should be considered for experimental testing.

## Chapter 2

### To Probe the Activation Mechanism of the Delta Opioid Receptor by an Agonist ADL5859 Starting from the Inactive Conformation Using Molecular Dynamics Simulations

#### 2.1 Introduction

##### *2.1.1 Problems With Opioid Receptors*

Ligands that bind to receptors are typically classified as an agonist or antagonist, meaning they either elicit a biological response or they block the response, respectively. Opioid receptors, members of G-protein-coupled receptors (GPCR), bind an agonist such as opioids outside the cell and adopt the active conformation to activate G protein-dependent signal transduction pathways, ultimately, inducing the biological response of antinociception.<sup>13, 14</sup> There are three types ( $\mu$ ,  $\delta$  and  $\kappa$ ) of opioid receptors (MOR, DOR and KOR)<sup>15</sup>, all exhibiting antinociceptive properties. There is a fourth opioid receptor, nociception/orphanin (NOR) that little is known about. However, it is thought that due to its location in the brain and spinal cord that its activation can be similar to MOR effects or sometimes oppose them.<sup>16</sup> Among them, MOR is the major pharmacological target of current opioid drugs such as morphine. However, these drugs targeting MOR are known for their high propensity for abuse and tolerance, leading to the current opioid epidemic in the United States and the rest of the world. Thus, there is pressing need to develop non-MOR-based opioid drugs. While drugs acting at the KOR produce dysphoria and anhedonia<sup>17, 18 19, 20</sup>, these same adverse effects are not observed when testing drugs that

act at the DOR. This makes the DOR a promising pharmacological target for developing new opioid drugs for pain medication.<sup>21</sup>

### ***2.1.2 History of DOR Agonists***

Over the years, researchers have been able to produce agonists that can target the DOR and cause antinociception and/or antidepressant-like effects without adverse weight-based effects.<sup>22-24</sup> However, these molecules caused convulsant activities in vivo, making the search for an optimal agonist for the DOR continue. Through trial and error, ADL5859, a small molecule agonist targeting the DOR has been discovered with promising properties, including no adverse effects on convulsant activities. This ligand completed phase I in clinical trials, showing it was well absorbed after oral administration and was generally well tolerated, ready to move on to phase II.<sup>25</sup> While this drug has shown promising activities in vivo, there is no crystal structure of ADL5859 with the DOR. Because of this, the detailed interaction of this ligand with the receptor is unknown, as well as the activation mechanism.

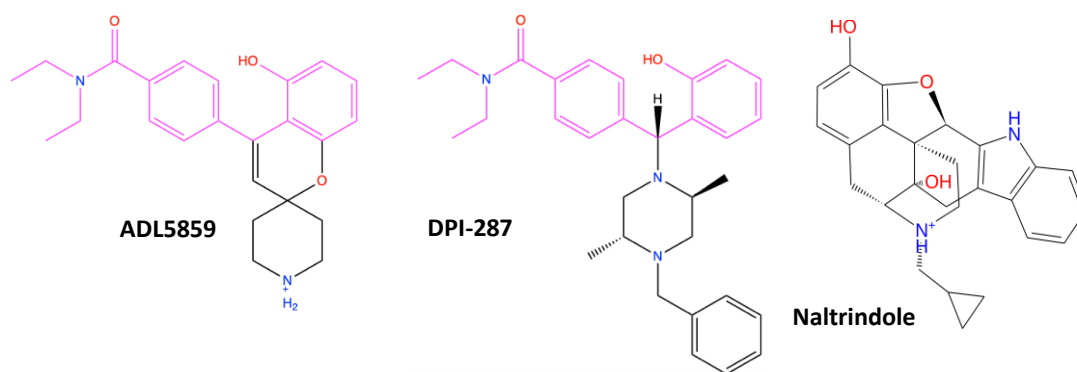
### ***2.1.3 Crystal Structures and Previous MD Simulation Studies of the DOR***

Recently, three crystal structures of the DOR have been solved; one is of the inactive state receptor with an amino terminal *b*<sub>562</sub>RIL fusion protein in complex with the antagonist, naltrindole (PDB ID: 4N6H), and two structures are of the active state DOR with the peptide agonist KGCHM07 (PDB ID: 6PT2) and with the small molecule agonist DPI-287 (PDB ID: 6PT3), both with a *b*<sub>562</sub>RIL fusion protein that contained three point mutations. When aligning the crystal structures (Figure A1), the two agonist bound complexes (6PT2 & 6PT3) show significant overlap, but in contrast, the antagonist

complex (4N6H) shows great differences mainly in the fusion protein, as well as TM5, intracellular loop (ICL) 3, and TM6. The difference in transmembrane (TM) 6 between the crystal structures appears to be one of the molecular switches in GPCR activation known as the Transmission Switch, and is a hallmark of GPCR activation, indicating the agonist bound complexes as the active crystal structures and the antagonist bound receptor as the inactive crystal structure. However, because the fusion protein also adopts very different conformations in the two complexes, the probability of the fusion protein causing the conformational change of TM6 cannot be completely ruled out. Because both DPI-287 and ADL5859 share the same pharmacophore and biological activity, their action on the DOR should be similar (*Figure 1*).

### Figure 1

*Chemical Structures of Agonist ADL5859, Agonist DPI-287, and Antagonist Naltrindole to DOR*



*Note.* Pharmacophore of agonists highlighted in pink to show similarity.

The DOR has not been as well studied as the MOR and KOR. With computational research on the rise, studies were conducted that modeled the DOR even before a crystal structure was available using templates such as bovine rhodopsin. Through this and a 20 ns molecular dynamic (MD) simulation, it was suggested that between residues D128 and R192, an internal salt bridge exists. Another study delved into the possible interfaces of DOR homodimeric complexes<sup>26, 27</sup>. After solved crystal structures of the DOR became available, a study that solved two DOR crystal structures themselves modeled the active state DOR and docked small molecules and peptides into their crystal structure to evaluate water-mediated interactions in the binding pocket.<sup>28</sup> Although the motion of TM6 is a known hallmark of activation for GPCRs, the key change at the residue level is not known for the DOR. Recently, a study<sup>29</sup> has suggested an activation pathway for  $\beta_2$ -adrenergic receptor, M2 muscarinic receptor,  $\mu$ -opioid receptor,  $\kappa$ -opioid receptor, and adenosine A<sub>2A</sub> receptor. However, the DOR has not been confirmed to have this pathway, leaving its activation pathway unknown.<sup>29</sup>

#### ***2.1.4 Experimental Overview***

To give a better insight and understanding of the activation mechanism and detailed interaction of an agonist with the DOR, we ran multiple 1 $\mu$ s molecular dynamic simulations of the novel ADL5859 and of naltrindole starting with a homology model of the inactive DOR (4N6H). Starting with the inactive conformation and an agonist allows us to probe the conformational change of the receptor toward the active conformation through MD simulations, giving insight into a potential activation mechanism for the DOR. To rule out the probability of the fusion protein causing the conformational change, it was removed. The ADL5859 was first docked to the inactive receptor

homology model and this initial structure was used for the simulations. Our most abundant structure from our MD simulation was then compared to the active state crystal complex to find the similarities and differences in the protein-ligand binding interactions and dynamics between the two systems. We observed TM6 move outward with a favorable overlap of our complex with the agonist bound crystal complex, supporting the evidence of the molecular switches for this receptor, specifically the Transmission Switch. Center of mass distances were measured as well using known residue contacts for some class A GPCRs as well as unique distances to our study to determine the conformation change occurring after beginning with the inactive state. The motion of TM6, as well as our additional distance analyses, offers insight into the activation mechanism of the DOR bound with agonist ADL5859. Given the hallmark movements and known residues, we believe our simulation has reached the active-like conformation. Our findings allows for an experimental mutagenesis study using our key residue pathway. The detailed interaction of ADL5859 with the DOR will also help to develop the opioid class of drugs.

## **2.2 Methods**

### ***2.2.1 Multiple Sequence Alignment and Analysis***

Conservation of residues among 62 members of class A GPCR was investigated using Jalview program<sup>30</sup>. Protein sequences of 61 class A GPCRs listed in the GPCR-EXP database (<https://zhanglab.org/GPCR-EXP/>) and 5 class A GPCRs listed in the subfamily A4 of rhodopsin family in the Pfam database (<http://pfam.xfam.org/family/PF00001>) were retrieved from the UniProt database and



MUSCLE tool<sup>31</sup> with default settings was used for the multiple sequence alignment. Positional occupancy of each residues was analyzed at both family and subfamily levels.

### ***2.2.2 The Homology Modeling of the DOR***

The FASTA files of human DOR-1(P41143) were obtained from the UniProt website to fix any nonnative mutations.<sup>32</sup> The sequence is shown in Figure A2.<sup>33,34</sup> The Prime feature in Maestro<sup>35,36</sup> was used to build the homology model based on pre-aligned crystal structure of human  $\delta$ -opioid 7TM receptor bound with antagonist naltrindole (PDB ID: 4N6H) oriented in the membrane from the OPM web server site.<sup>37</sup> The crystal structure of human  $\delta$ -opioid 7TM receptor bound with with agonist DPI-287 (PDB ID: 6PT3) was used for comparison. Alignment is based on the backbone residues of TM1-5&7 (4N6H: 39-77, 82-111, 117-152, 161-187, 206-243, 293-321; 6PT3: 45-77, 82-111, 117-152, 161-187, 206-243, 293-321).

### ***2.2.3 Molecular Docking of ADL5859***

Protein structures were prepared using Maestro's Protein Preparation Wizard.<sup>38</sup> The charge state of the preprocessed protein was optimized at pH 7. A restrained minimization was then performed to relax the protein structure using OPLS3 force field.<sup>39</sup> The 3D structures of naltrindole and ADL5859 were prepared using Maestro Elements. Figure 1 shows the chemical structures of the ligands. The 2D structure of ADL5859 was drawn using Maestro's 2D sketcher, converting into 3D structure. 3D structure of naltrindole was extracted from the crystal structure (PDB ID: 4N6H). Both ligands had their bond orders fixed and underwent the pKa calculation. The ionization/tautomeric states were generated at pH 7 using Maestro's Epik tool based on

the more accurate Hammett and Taft methodologies.<sup>38</sup> The lowest ionization/tautomeric state (+1) was selected and the geometry was then minimized to the most energetically favorable structure to relax the structure of the ligand.

The receptor grid files were generated from the prepared receptors, in which the centroid of the crystal ligand, naltrindole, was used to specify the active site. The prepared ligands (naltrindole and ADL5859) were docked into their corresponding generated grids using Glide XP scoring with default procedures and parameters.<sup>40, 41</sup> In detail, the receptor grid required for the docking process was generated using van der Waals scaling factor of 1 and partial charge cutoff 0.25. Docking was performed using a ligand-centered grid using OPLS3 force field.<sup>39</sup> Glide XP Dock performed a comprehensive systematic search for the best receptor conformations and orientations to fit the ligand. The docked poses were compared to the inactive crystal complex (PDB ID: 4N6H) with an antagonist to verify if the docked ligand poses were reasonable. Both ligands were bound within the binding pocket with naltrindole binding similar to the crystal ligand with subtle differences, providing a reasonable starting pose for later molecular dynamic simulations. The binding pose can then be refined given the full conformation flexibility in the simulations.

#### ***2.2.4 Molecular Dynamics Simulation System Setup***

Two MD simulation systems were constructed using the prepared and refined receptor-ligand complex from the Glide XP docking and crystal structure (4N6H) as input files. Each system was built using SPC as water solvent model<sup>42</sup> using orthorhombic solvent box with 10Å water buffer. System was neutralized using Na<sup>+</sup> and

Cl<sup>-</sup> ions and were added to maintain the salt concentration of 0.15 M NaCl. After the system was successfully solvated, OPLS3 force field<sup>39</sup> was used to represent the receptor-ligand.

Using Desmond module, the system was first relaxed using the default relaxation protocol for membrane proteins.<sup>43</sup> This relaxation protocol consists of eight stages: 1). Minimization with restraints on solute heavy atoms; 2). Minimization without any restraints; 3). Simulation with heating from 0 K to 300 K, H<sub>2</sub>O barrier and gradual restraining; 4). Simulation under the NPT ensemble (constant number of particles, constant pressure of 1 bar and constant temperature of 300 K) with H<sub>2</sub>O barrier and with heavy atoms restrained; 5). Simulation under the NPT ensemble with equilibration of solvent and lipids; 6). Simulation under the NPT ensemble with protein heavy atoms annealing from 10.0 kcal/mol to 2.0 kcal/mol; 7). Simulation under the NPT ensemble with C $\alpha$  atoms restrained at 2kcal/mol; and 8). Simulation for 1.5 ns under the NPT ensemble with no restraints. After the relaxation, three trajectories (1000.0 ns of each) were conducted under the NPT ensemble for each of the systems using the default protocol. In details, temperature was controlled by using the Nosé-Hoover chain coupling scheme<sup>44</sup> with a coupling constant of 1.0 ps. Pressure was controlled using the Martyna-Tuckerman-Klein chain coupling scheme<sup>44</sup> with coupling constant of 2.0 ps. M-SHAKE<sup>45</sup> was applied to constrain all bonds connecting hydrogen atoms, enabling a 2.0 fs time step in the simulation. The k-space Gaussian split Ewald method<sup>46</sup> was used to treat long-range electrostatic interactions under periodic boundary conditions (charge grid spacing of  $\sim 1.0$  Å, and direct sum tolerance of  $10^{-9}$ ). The cutoff distance for short-range non-bonded interactions was 9 Å, with the long-range Van der Waals interactions based

on a uniform density approximation. To reduce the computation, non-bonded forces were calculated using an r-RESPA integrator<sup>47</sup> where the short-range forces were updated every step and the long-range forces updated every three steps. The trajectories were saved at 40.0 ps intervals for analysis.

To check the convergence of MD simulations, the protein C $\alpha$  and ligand RMSD plots were investigated for each trajectory. The relatively flat plots within last 200 ns indicates that the complex systems have reached a steady state.

Desmond SID tool was used to analyze the behavior and interaction of proteins and ligands during the course of simulation including RMSD; protein-ligand contacts including H-bonds, hydrophobic, ionic, and water-bridge contacts; secondary structure changes and Root Mean Square Fluctuation (RMSF) measures.

### ***2.2.5 Trajectory Clustering Analysis***

Desmond trajectory clustering tool<sup>48</sup> was used to group complex structures from the last 100 ns simulation of each complex system. Backbone RMSD matrix was used as structural similarity metric, the hierarchical clustering with average linkage<sup>48</sup> was selected as the clustering method. The merging distance cutoff was set to be 2Å. The centroid structure (i.e. the structure having the largest number of neighbors in the structural family) was used to represent the structural family. The centroid structures of populated structural families (>2% of total structure population) are shown in Figures A5-A6 of the supporting material.

### ***2.2.6 RMSD of Protein Structure Analysis***

We analyzed the RMSD of the whole protein, transmembrane domain (TMD), and TM6 for each trajectory in reference to both the solved inactive crystal structure of the DOR (PDB ID: 4N6H) and the solved active crystal structure of the DOR (PDB ID: 6PT3) to aid in differentiating the protein in the active or inactive state. Alignment of the whole protein is based on the backbone residues of the protein excluding backbone residues of TM6 (4N6H: 36-248, 288-321, 6PT3: 45-248, 288-321), and alignment of the 7TMs is based on backbone residues of TM1-5&7 (4N6H: 39-77, 82-111, 117-152, 161-187, 206-243, 293-321; 6PT3: 45-77, 82-111, 117-152, 161-187, 206-243, 293-321), both of which exclude oxygen. RMSD calculations are of the backbone residues of the whole protein (4N6H: 36-321, 6PT3: 45-321), 7TMs (4N6H: 39-77, 82-111, 117-152, 161-187, 206-243, 250-286, 293-321; 6PT3: 45-77, 82-111, 117-152, 161-187, 206-243, 250-286, 293-321), and TM6 (250-286). Maestro's Simulation Event Analysis was used to calculate the RMSD of the MD simulation. VMD RMSD Calculator<sup>49</sup> was used to calculate the RMSD of the portions of each representative structure of abundant clusters from each trajectory.

### ***2.2.7 Analysis of Microswitches and Pairwise Residue Distance***

We analyzed three important microswitches<sup>50</sup>, i.e., transmission (CWXP), tyrosine toggle (NPXXY) and ionic lock (DRY) which are used to differentiate between active and inactive states of class A GPCR. Another lock known as 3-7 lock<sup>50</sup> was also investigated.

Frame-wise center of mass distances were calculated for 23 pairs of residues. Out of 23 pairs of residues, 20 were previously used by Zhou et al.,<sup>29</sup> to define the activation mechanism of class A GPCRs. For calculation of atomic and center of mass distances, VMD<sup>49</sup> was used.

### ***2.2.8 Normal Mode Analysis***

The individual trajectories from both systems were used in the Normal Mode Wizard in VMD<sup>51</sup> to generate a principal component analysis of the top 10 normal modes.

## **2.3 Results**

### ***2.3.1 Sequence-Based Comparison of Human DOR With Other Class A GPCRs***

Comparison of primary sequence of human DOR with 61 class A GPCRs revealed that DOR sequence was more conserved at subfamily level than the family level. Residues belonging to molecular switches such as CPXY, NPXXY and D/ERY motifs showed high level of conservation at both family and subfamily levels. DOR showed more than 50% identity with kappa ( $\kappa$ ) and mu ( $\mu$ ) opioid receptors.

### ***2.3.2 Homology Model of Human DOR Without Fusion Protein***

Homology models of the DOR for the generation of ADL5859 and naltrindole bound complexes were obtained based on experimentally resolved crystal structure of the human DOR with naltrindole (PDB ID: 4N6H) as described in the methods section. In the homology model of the DOR, mutation P37S present in the crystal structure of DOR was corrected. A cartoon representation is shown in Figure A2 from top and side

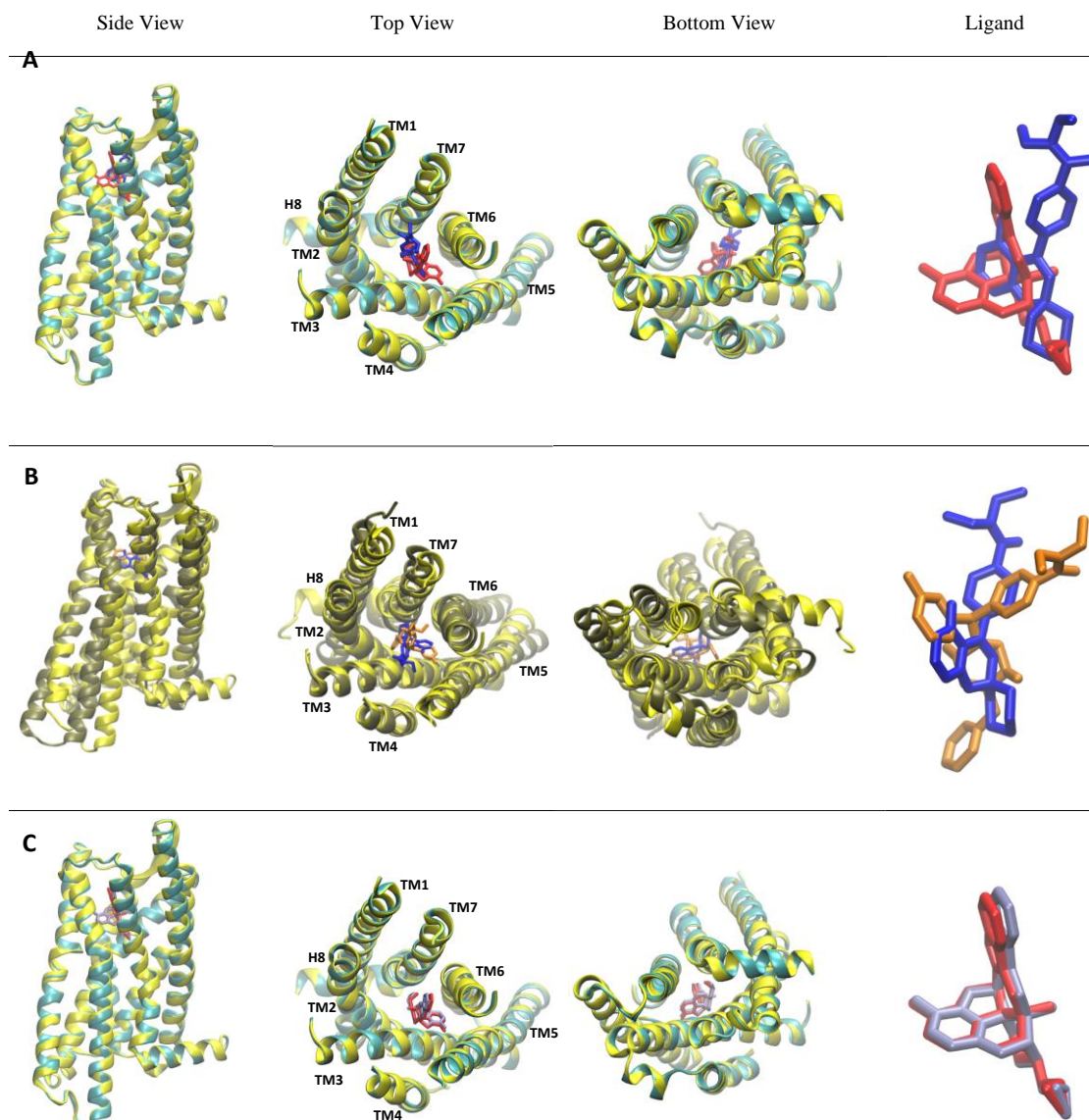
viewpoints. This homology model is a valid starting structure for molecular docking and simulations to inspect the activation mechanism.

### ***2.3.3 Docked Conformation of ADL5859 Shows Similarity With the Co-Crystallized Conformation of DPI-287 and Subtle Difference With Naltrindole***

The docking protocol was validated by docking the co-crystallized naltrindole back into the crystal structure of DOR (Figure 2). The result had an almost identical overlap which suggests a satisfactory docking method. ADL5859 was docked into the inactive receptor, resulting in a similar binding pose as the crystal agonist. Docked conformation of ADL5859 showed interaction with salt bridge with D128 and non-polar interactions with M132, W274, V281, L300 and Y308.

## Figure 2

### Comparison Between the Docked Pose With the Crystal Pose of Ligands



*Note.* A: Comparison between final docked pose of ADL5859 (dark blue) with the crystal pose of Naltrindole (red) in the inactive crystal complex structure (cyan) (PDB ID: 4N6H) B: Comparison of final docked pose of agonist ADL5859 with the crystal pose of DPI-287 (orange) in the active crystal complex structure (tan) (PDB ID: 6PT3). C: Comparison of antagonist Naltrindole (light blue) with the crystal pose of Naltrindole (red) in the inactive crystal complex structure (cyan) (PDB ID: 4N6H) (C). Intracellular and extracellular loops were removed in the top view for clarity.

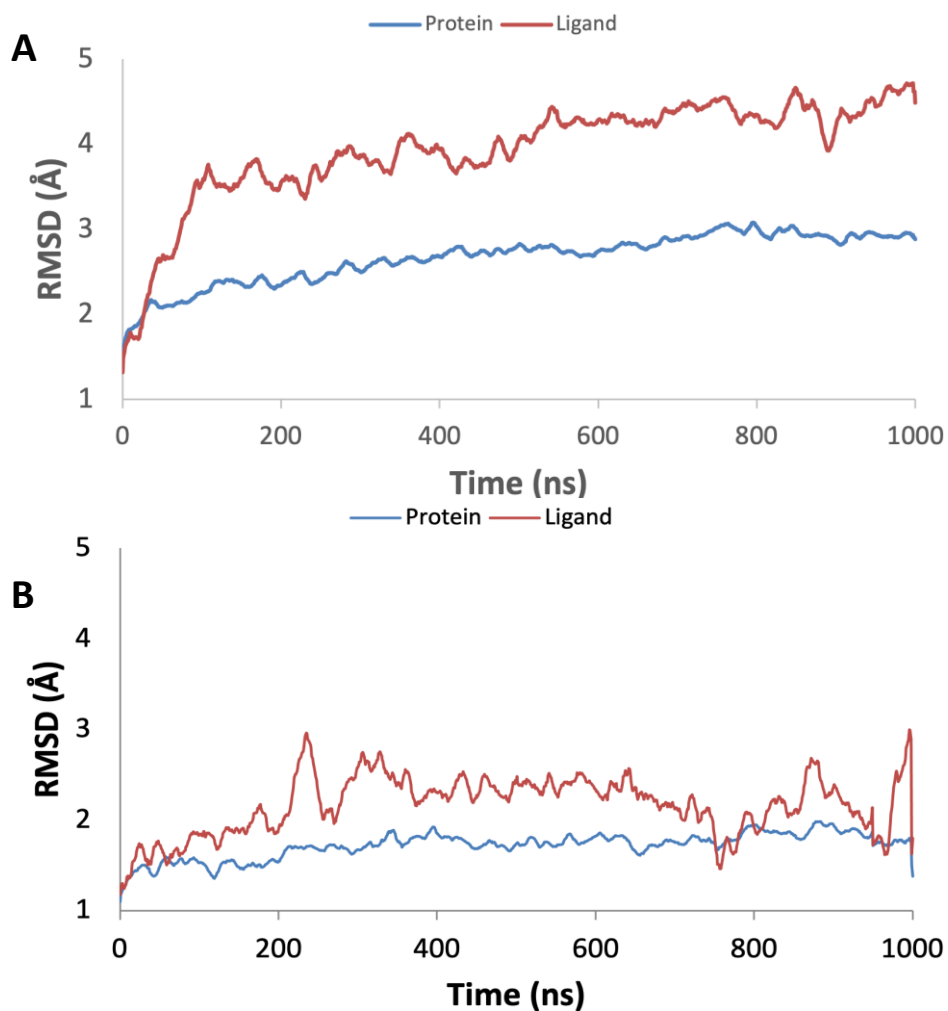


#### ***2.3.4 MD Simulations of Human DOR With ADL5859 and Naltrindole Assume Steady State***

The complexes from Glide XP docking were used as the input structures to perform six independent 1  $\mu$ s molecular dynamic simulation for ADL5859-DOR complex and three 1  $\mu$ s molecular dynamic simulation for naltrindole-DOR complex. The RMSD values of ADL5859 and naltrindole shows the flexibility of the ligand interaction with the DOR. The movement of the ligand and the receptor during the simulation was analyzed using the RMSD (Figure 3 and Figure A3 and A4). In the RMSD plots for systems, the protein and ligand RMSD are approaching stable values within the last 200 ns, indicating that the two complexes had been sufficiently equilibrated and allowed for rigorous analysis. The protein RMSD for ADL5859 changes  $\sim 3\text{\AA}$  which indicates that the protein is undergoing a large conformational change during the simulation (Figure 3). The protein RMSD for naltrindole has a lower RMSD value and remains more stable. The ligand RMSD for ADL5859 shows multiple fluctuations around 200-400 ns during the simulation (Figure 3). Naltrindole RMSD has a large fluctuation around 200 ns and again between 800-950 ns.

**Figure 3**

*Protein (Blue) and Ligand (Red) RMSD*



*Note:* Averaged over the six independent trajectories for agonist ADL5859-DOR system (A) and three independent trajectories for antagonist Naltrindole-DOR system (B). Alignment is based on the C $\alpha$  atoms of the protein and the RMSD calculation with reference to the first frame. Ligand RMSD calculated the ligand heavy atoms after the complex is first aligned on the protein backbone of the reference.

### ***2.3.5 ADL5859-DOR System Shows Adopting Toward the Crystal Active Conformation While Naltrindole-DOR System Maintains Inactive Conformation***

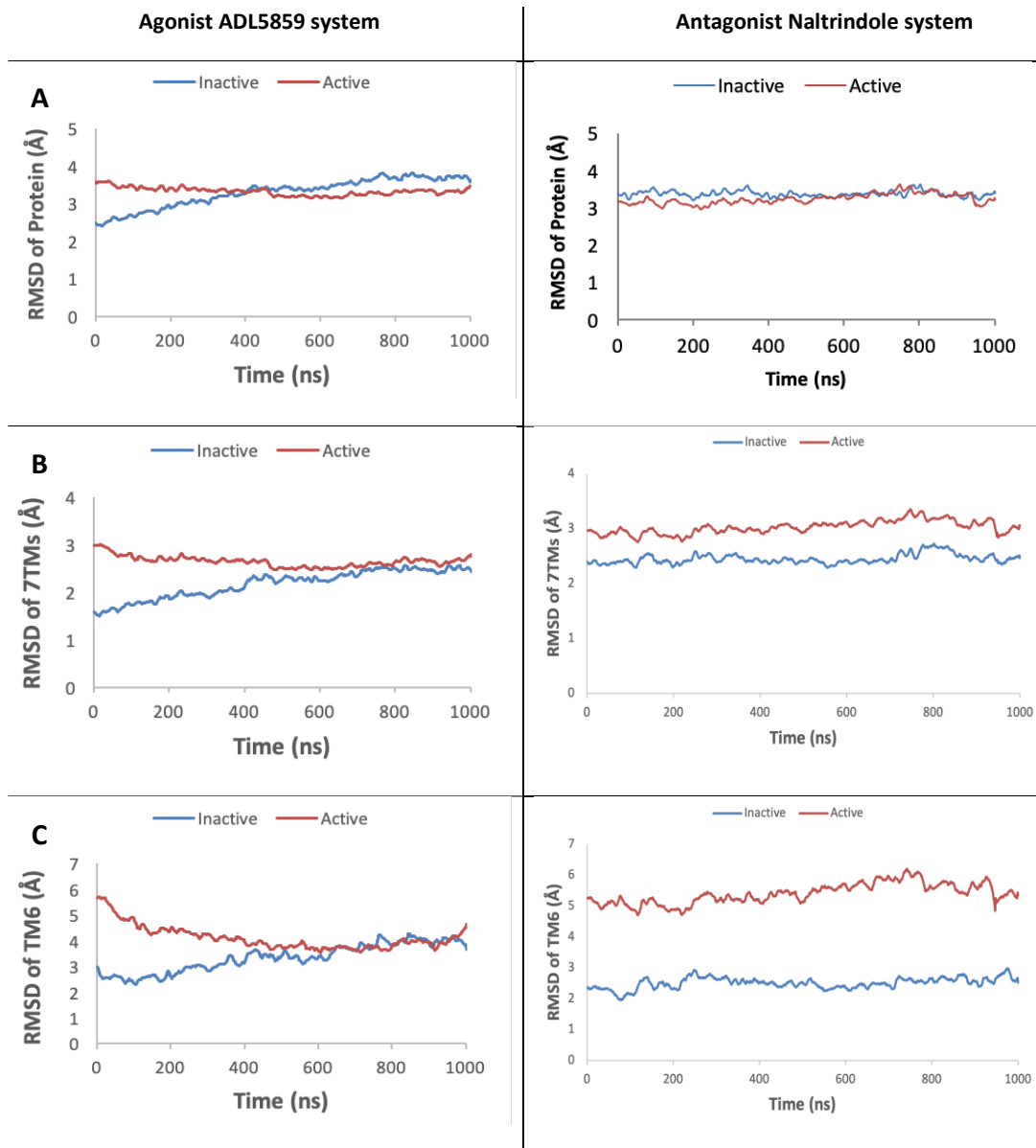
To determine whether our agonist MD complex can adopt toward the active conformation and move away from the inactive conformation, the RMSD of the receptor against the active and inactive crystal structures was calculated throughout the whole trajectory. The RMSD of the whole protein, TMD, and TM6 of the receptor was calculated to home in on which portion of the protein has the most conformational change, presumably leading to activation. The RMSD of the same regions for the antagonist naltrindole system was calculated as well to determine if the MD complex will maintain the inactive conformation to serve as a control. For this to be clear, our complexes were aligned against the inactive and active crystal structures (4N6H & 6PT3) using the backbone residues of the TMD excluding TM6. The reason for this exclusion is because TM6 appears to have the most dynamics while the other transmembranes are more rigid. Aligning the rigid parts of the receptor will better show the change in conformation of the flexible part. Examining the whole protein of the individual agonist RMSD plots (Figure A5) revealed that trajectories 1, 3, 5, and 6 behave similarly as they clearly show a general trend where they increase in RMSD when against the inactive crystal structure and decrease in RMSD when against the active crystal structure. This trend becomes more pronounced when looking at the RMSD of the TMD for these trajectories and even more so for the RMSD of TM6. Using trajectory 1 as an example, the RMSD value of the TMD at the beginning of the trajectory against the inactive crystal structure is 1.9Å and ends at 2.4Å; and when against the active crystal structure, the RMSD value begins at 3.0Å and ends at 2.4Å. With this same process for TM6 in trajectory 1, the RMSD values when it first begins against the inactive crystal structure is

3.3Å and ends with an RMSD value of 4.2Å; and when against the active crystal structure, it begins with an RMSD value of 5.7Å and ends with an RMSD value of 4.0Å. This indicates the major part contributing to the protein folding is the movement in TM6. Trajectory 4 of the agonist system shows the same trend within the first 800 ns as trajectories 1, 3, 5, and 6 but after 800 ns, it reverses the process with an increasing trend against the active crystal structure and decreasing trend against the inactive crystal structure. Trajectory 2 of the agonist system differs from the others in which it only maintains the same RMSD trend as the other trajectories during the first 200 ns but still not as clear. After 200 ns, especially for the RMSD of TM6, it loses the general trend and levels out. To clarify what this means, using the RMSD of TM6 in trajectory 2, when against the inactive conformation at 200 ns has an RMSD value of 2.3Å and ends with an RMSD value of 2.4Å; and when it is against the active conformation at 200 ns has an RMSD value of 4.3Å and ends with an RMSD value of 4.5Å. In the case of the RMSD for the antagonist naltrindole system (Figure A6), all three trajectories displayed the same pattern for each protein region in which there was no change in RMSD when against either crystal structures. From these results we can speculate that if the system adopts toward the active conformation, it should decrease in RMSD against the active crystal, favoring smaller RMSD values, and increase in RMSD against the inactive crystal, favoring larger RMSD values. If there is no protein folding within the system, then the RMSD should not change which would be validated by flat RMSD plots. Because the majority of the agonist trajectories shared a general trend in RMSD and all antagonist trajectories shared a general trend in RMSD, the individual trajectories were averaged to simplify the results (Figure 4). After averaging the trajectories for both systems, a

noticeable feature in the RMSD became more apparent. For both simulation systems (agonist & antagonist), there is a gap between the starting values of the RMSD when against the reference structures, with the inactive reference structure at much lower values than when against the active crystal structure. Our simulation systems began using the inactive conformation which correlates with this feature that our systems are more similar to the inactive crystal structure at the beginning of the trajectory, depicted by lower RMSD values. This gap gets larger as the protein regions get more specific (whole protein → TMD → TM6), indicating the difference between the conformation of the reference structures increases as the RMSD gets more specific. The averaged agonist trajectories show to have maintained the same clear trend in RMSD as its individual trajectories throughout the protein regions, with the gap diminishing between the reference structures throughout the trajectory, and the most prominent trend occurring in TM6.

**Figure 4**

*Receptor RMSDs of Varied Parts From Agonist and Antagonist Simulation Systems Against the Two Solved Crystal Receptor Structures*



*Note:* A: RMSD of protein = backbone residues 36-321 (4N6H), 45-321 (6PT3). B: RMSD of 7TMs = backbone residues of TM1-7. C: RMSD of TM6 = backbone residues 250-286. (PDB ID: 6PT3 Active state DOR in complex w/ agonist DPI-287) (PDB ID: 4N6H Inactive state DOR in complex w/ antagonist Naltrindole).

The RMSD of the averaged agonist system of the whole protein against the active crystal begins with an RMSD of 3.5Å and ends with a decreasing RMSD of 3.4Å showing a difference of .1Å. When against the inactive crystal, the whole protein begins with an RMSD of 2.4Å and ends with an increasing RMSD of 3.4Å, showing a difference of 1Å. The TMD displays the trend in RMSD more clearly with the average agonist trajectories against the active crystal beginning at an RMSD of 2.9Å and ending with an RMSD of 2.7Å, showing a decreasing difference of 0.2Å. When against the inactive crystal, the TMD begins with an RMSD of 1.6Å and ends with an RMSD of 2.6Å, showing an increasing difference of 1Å. The greatest difference in RMSD lies in TM6 beginning with an RMSD of 5.6Å against the active crystal and ending with a decreasing RMSD of 4.4Å, indicating a 1.2Å difference. When against the inactive crystal structure, TM6 of the averaged agonist trajectories begins with an RMSD of 2.6Å and ends with an increasing RMSD of 3.6Å, showing a 1Å difference. The trend in RMSD of the whole protein and the TMD of the agonist system was not as drastic, indicating TM6 shows the most change in conformation. When viewing the RMSD of the averaged antagonist trajectories, they have still maintained the trend of no change in RMSD with relatively flat plots. The gap between the reference structures is maintained throughout the whole trajectory for each protein region, indicating the antagonist system is more similar to the inactive crystal structure and less similar to the conformation of the active crystal structure. When against the active crystal structure, the averaged antagonist system of the whole protein begins with an RMSD of 3.1Å and ends with an RMSD of 3.2Å, showing a .1Å difference. When against the inactive crystal structure, the RMSD of the whole protein begins at 3.3Å and ends with an RMSD of 3.3Å, indicating no change from the inactive reference

structure. The RMSD of the TMD when against the active crystal structure begins at 2.9Å and ends with an RMSD of 3.0Å, showing an increase of .1Å. When against the inactive crystal structure, the TMD starts with an RMSD of 2.4Å and ends with an RMSD of 2.4Å, again showing the antagonist system has not folded away from the inactive conformation. The RMSD of TM6 of the averaged antagonist system when against the active crystal structure begins at 5.2Å and ends at an RMSD of 5.3Å, showing a 0.1Å increase. When against the inactive crystal structure, TM6 begins with an RMSD of 2.4Å and ends with an RMSD of 2.5Å, showing another 0.1Å increase. This data alludes to our agonist system folding towards the active conformation as the gap between the reference structures dies out with a decreasing trend against the active crystal structure and an increasing trend against the inactive crystal structure. Lower RMSD values against the active crystal structure indicate greater similarity with the active conformation and in this same respect, higher values against the inactive crystal structure indicate the difference from the inactive conformation. This trend was the most prominent for the RMSD of TM6 of the agonist system, which movement of is associated with activation in GPCRs. In the case of the antagonist system, the RMSD of the different protein regions showed either a change of 0.1Å or no change at all while also maintaining the gap between reference structures, which would imply that the system has not folded away from the inactive conformation. From the backbone RMSD plots, it is clear the activation related conformational changes are unique to the agonist-ADL5859 bound DOR.

### ***2.3.6 ADL5859-DOR System Has Multiple Clusters Folding Toward the Active State***

The clustering analysis was done after the MD simulation to identify the populated conformation for each trajectory. Based on the clustering algorithm, each



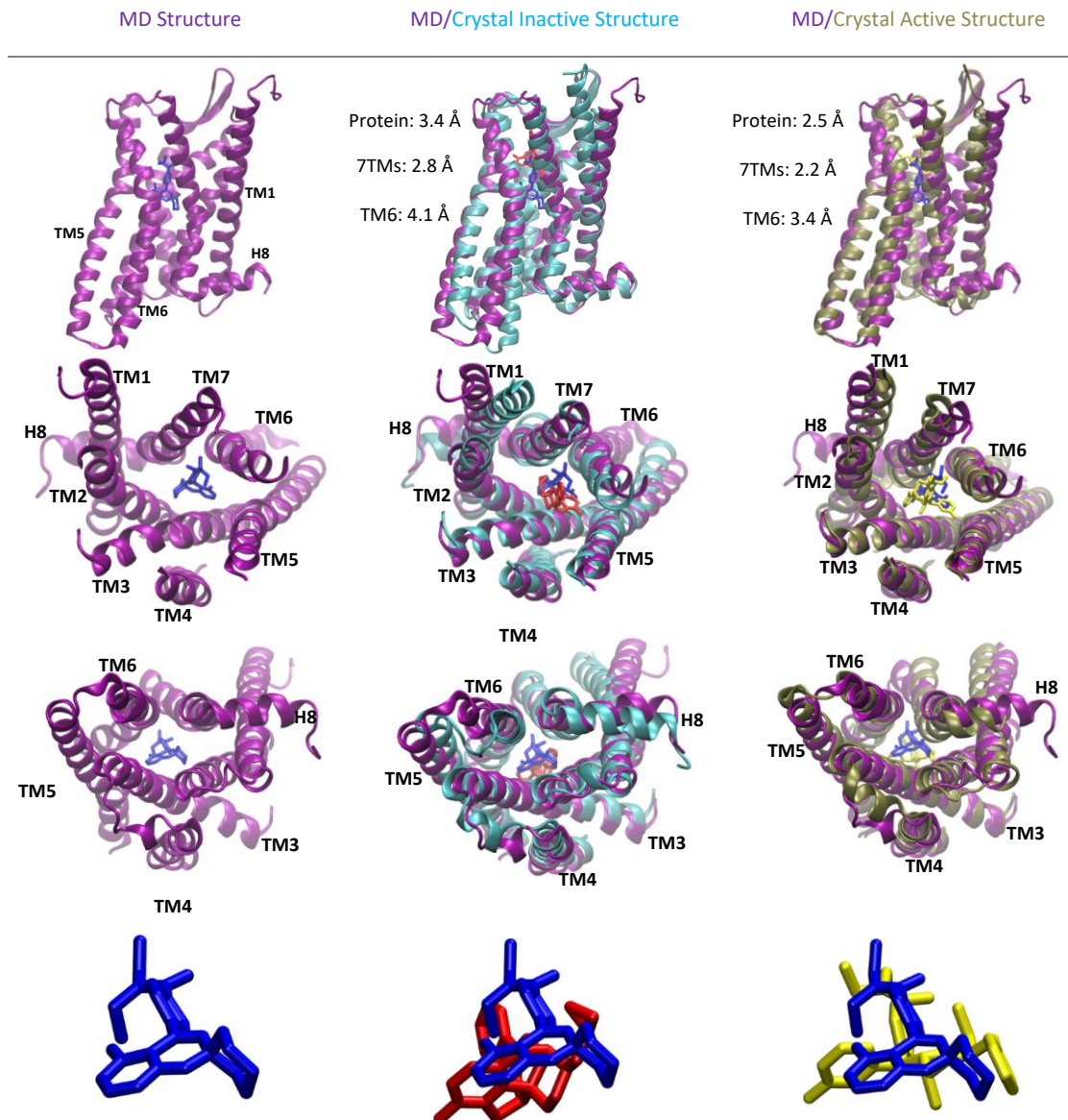
cluster conformation contains a percentage of abundance in which a cutoff of 1% was used. The clustering results are clearly tabulated in Table A1. There was a total of 15 abundant clusters from the six agonist trajectories with each trajectory containing at least two abundant conformations, with the exception of trajectory 2. For the three antagonist trajectories, there were three abundant clusters, one for each independent trajectory. The clustering result for both systems corresponds with the thought that the agonist system is believed to be folding towards the active state which would produce more than one conformation; and in this same regard, the antagonist system should not have any folding, which would result in one conformation.

To acquire a deeper insight into the conformation of the MD structures, the RMSD of the whole protein, TMD, and TM6 of each abundant cluster against the inactive and active crystal structures was calculated as described in the Methods (Table A1 and Figure A7-A8). To consider an abundant cluster as folded toward the active state, when comparing the RMSD values of the protein regions against the different crystal structures, especially in the case of TM6, they should differ roughly by at least 1 Å, with lower values when against the active crystal structure, indicating greater similarity. The RMSD values of the abundant clusters from the antagonist system against both crystal structures were also taken into consideration when determining the criteria for folding toward the active state as this system should remain in the inactive state. Each cluster of the antagonist system had an RMSD ranging from 3.1-3.4Å for the whole protein when against the active crystal structure and 3.1-3.3Å when against the inactive crystal structure. When looking at the TMD, the antagonist abundant clusters had an RMSD ranging from 2.8-3.0Å when against the active crystal structure and 2.7-2.8Å when

against the inactive crystal structure. The last protein region calculated for the RMSD of the naltrindole complexes, TM6, had RMSD values ranging from 4.9-5.5Å against the active crystal structure and 1.8-2.9Å against the inactive crystal structure. After calculating the RMSD of each of the agonist clusters against the crystal structures, there were three trajectories (trj1, trj4, trj6) and four clusters (trj1 cluster 1&3, trj4 cluster 5, trj6 cluster 1) that can be considered in the active state. The most abundant cluster (cluster 1) from trajectory 1 in the agonist system is the most favorable from this system and is used as the representative structure (Figure 5). The interactions of agonist ADL5859 with the DOR from the first trajectory were examined, along with the crystal antagonist naltrindole in the crystal inactive state DOR, and the crystal agonist DPI-287 in the crystal active state DOR. With this, ADL5859 directly interacted with polar histidine 278 of the DOR during the simulation, which is consistent with the interactions of crystal agonist DPI-287 and the DOR. Both agonists also have exposure to solvent on the same CH3 of their structures. The clusters from the naltrindole system show good agreement with the inactive crystal structure and were validated by the RMSD values with the abundant cluster from the first trajectory used as the representative structure (Table A1, Figure A7 and Figure A8). Naltrindole directly interacted with negatively charged aspartic acid 128 of the DOR during the simulation which is consistent with the interactions of crystal antagonist naltrindole and the DOR. This indicates the conformational changes occurring to the receptor are unique to the agonist ADL5859-DOR system.

**Figure 5**

*Most Abundant Agonist Cluster of the First Trajectory Compared to Solved Crystal Structures and Structural RMSD Calculations*



*Note.* MD DOR-agonist-ADL5859 structure (purple&blue) of the most abundant cluster (52%) of the first trajectory, its comparison to the solved crystal structures (Inactive PDB ID: 4N6H, cyan&red) (Active PDB ID: 6PT3, tan&yellow) in the side, top, and bottom views respectively. RMSD of the protein, 7TMs, and TM6 of the MD structure against crystal structures is listed. Alignment is using backbone residues of TM1-5&7, excluding oxygen. Ligand view of MD-DOR-ADL5859, crystal antagonist Naltrindole in inactive DOR, and crystal agonist DPI-287 in active DOR.

While the RMSD of the superimposed agonist structures indicated four clusters folding toward the active state, there were other abundant clusters from the agonist-ADL5859 system that are thought to contain intermediate conformations of the protein folding toward the active state (Figure A7). These other noteworthy structures are cluster 1 and cluster 2 from trajectory 3 with a percentage of abundance of 90 and 11 respectively; trajectory 4 cluster 1, cluster 3, and cluster 4 with percentages of abundance of 43, 20, and 5 respectively; and cluster 1 from trajectory 5 with a percentage of abundance of 56. Even though these structures did not have as favorable of RMSD values as the others that were identified, they are speculated to be intermediate conformations in the activation-related folding process, as they also still display agreement with the active crystal structure and contain great differences from the inactive crystal structure. The differences from the inactive crystal structure mentioned mainly lie in TM5, ICL3, and TM6 while similarities to the active crystal structure mainly lie in TM1, TM5, and TM6. These clusters, along with the ones identified from the RMSD as folding toward the active state, are consistent with the results from the backbone RMSD plots (Figure A5-A6), in which the trajectories these cluster conformations were generated from (trj1, trj3, trj4, trj5, trj6) displayed the general trend implying protein folding toward the active conformation throughout the simulation. This adds further support of the agonist-ADL5859 system folding toward the active state.

### ***2.3.7 Secondary Structure Analysis Shows Maintained Helices but With Subtle Differences Between the Two Complexes***

Secondary structure elements (SSE) plots illustrate where the major differences occur in the transmembrane sections for comparisons to be made between the agonist and

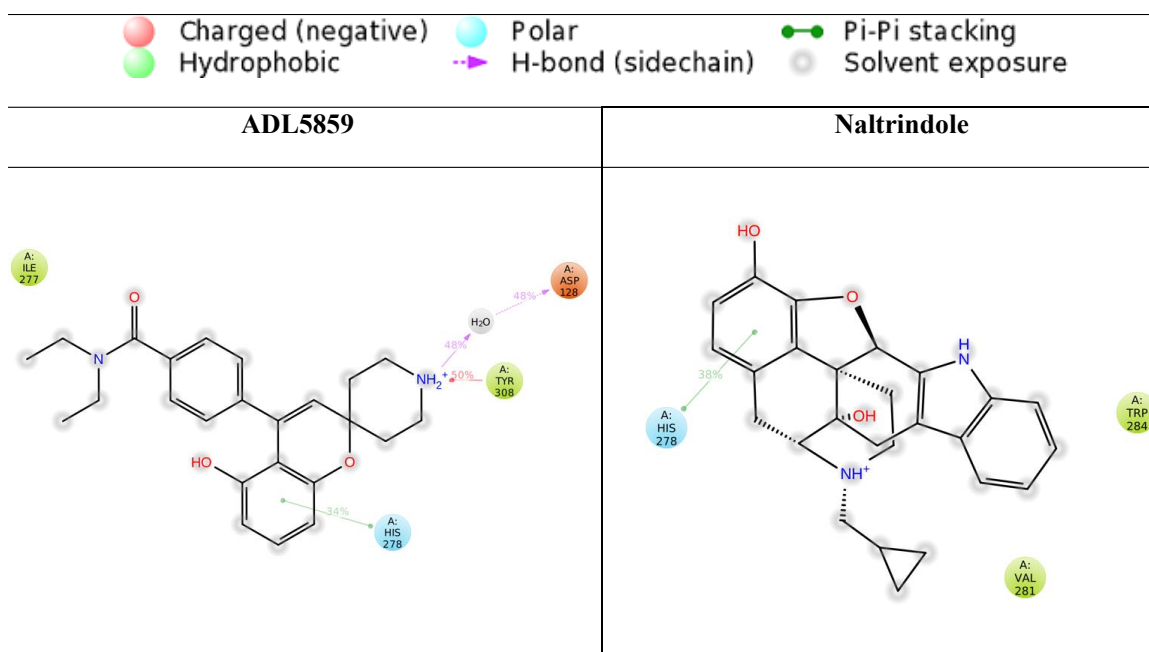
antagonist (Figure A9). Some of the noteworthy features include: A) Additional kink in ADL5859 in TM6. B) Additional kinks in naltrindole in TM2 and TM7.

### ***2.3.8 Key Interactions of ADL5859 and Naltrindole With Human DOR***

The Desmond Simulation Interaction Diagram was used, as described in the methods section, to analyze and compare the residues involved in both naltrindole and ADL5859 binding to the receptor (Figure 6). The key interacting residues that interacted with each ligand of the combined trajectories for more than 5% of the simulation are tabulated for clarity in Table S4. Key interacting residues of the individual trajectories for the agonist and antagonist systems that lasted more than 20% of the MD simulation can be found in Figure A10 and Figure A11, respectively. Interacting residues during the simulation in histogram format of the individual agonist and antagonist trajectories can be found in Figure A12 and Figure A13, respectively. Using Figure 6 it can be understood that ADL5859 interacted with a greater number of residues from the receptor with a total of 47 interacting residues that mainly occur in TM2, TM3, TM5, TM6, and TM7. Naltrindole had a total of 30 interacting residues in which 26 of them were conserved in ADL5859. In TM6, there were 6 conserved interacting residues between the two systems. Naltrindole, however, interacted with residue I282 which differed from ADL5859 that interacted with residues F270 and W285. The major differences lie in TM7 where ADL5859 had 10 interacting residues: V297; L300; H301; C303; I304; G307; Y308; N310; S311; N314 whereas naltrindole had only 6: L300; I304; G307; Y308; N310; and S311. The 2D interaction diagram indicates that  $\pi$ - $\pi$  stacking is crucial for the binding of both ligands (Figure 6).

**Figure 6**

*Protein-Ligand 2D Interaction Diagram*



*Note:* Interactions lasting more than 20% of the molecular dynamics simulation from the combined agonist (left) and antagonist (right) trajectories are shown in the 2D interaction diagrams.

**2.3.9 DOR Shows Flexibility When Bound to ADL5859 Than Naltrindole**

The receptor RMSF (Table 1, Figure 7 and Figure A14-A15) shows higher RMSF values in areas of high flexibility such as the intra- and extracellular loops, as well as the N- and C- terminals. In contrast, the helices, or rigid areas of the receptor, show lower RMSF values. When the DOR was bound to ADL5859, the receptor RMSF values were higher than when bound to naltrindole. ADL5859 has higher ligand RMSF values in comparison to naltrindole (Figure 7). In Figure 7, naltrindole has lower RMSF values at almost every atom. This is consistent with what was expected from the structures of the

two ligands – for naltrindole contains one more six membered ring than ADL5859, as well as two five membered rings and one three membered ring, making naltrindole a more rigid ligand compared to ADL5859. These differences indicate that the DOR exhibited greater flexibility when interacting with an agonist (ADL5859) than with an antagonist (naltrindole). This is likely because the receptor was undergoing activation when in complex with ADL5859. Receptor RMSF data of the individual trajectories can be found in Figure A14-A15 of the appendix and individual ligand RMSF data can be found in Figure A16-A17 of the appendix.

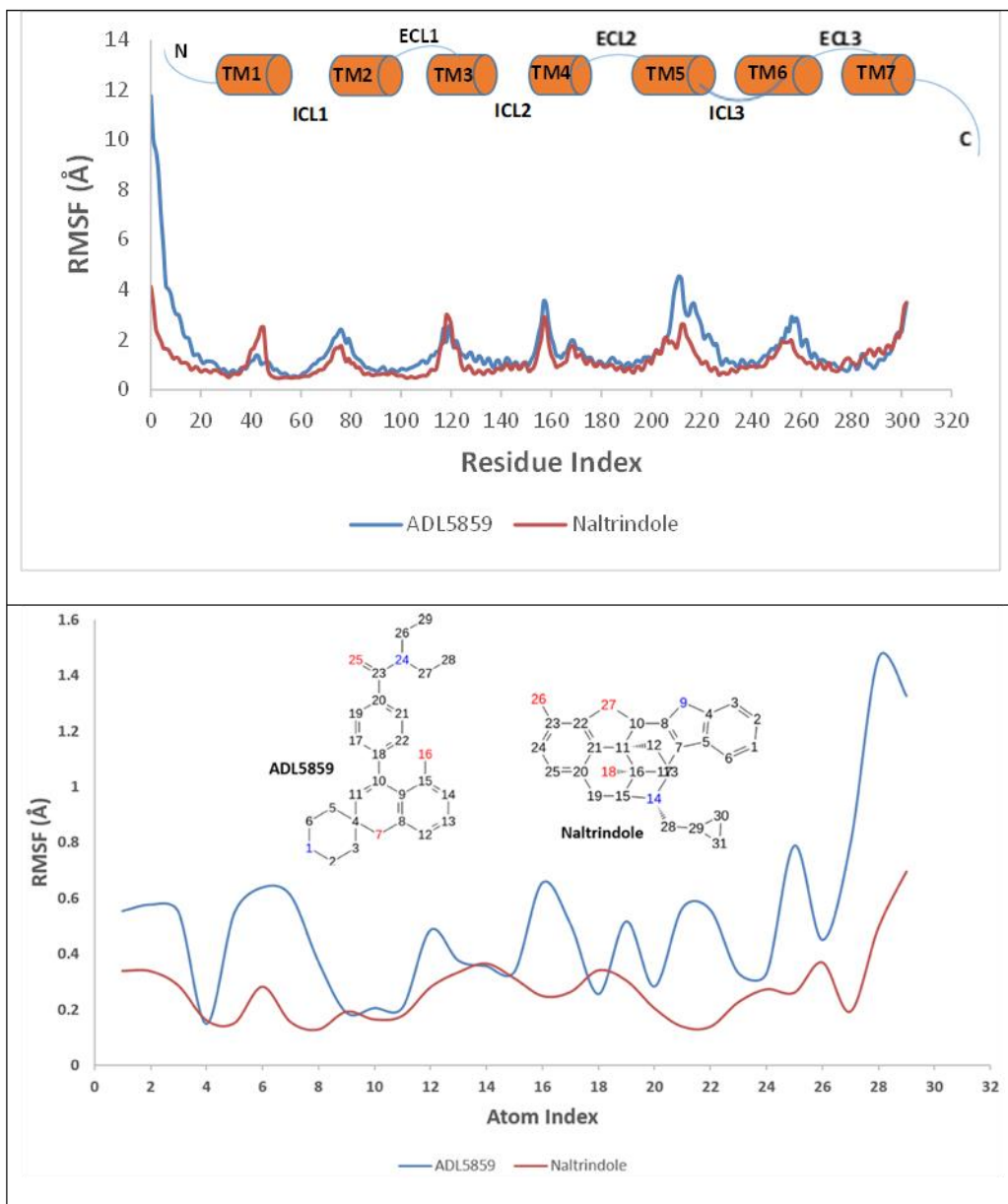
**Table 1**

*The Combined Mean RMSF Values of the Ligand Bound Complex From N-Terminal to C-Terminal*

<b>RMSF (Å)</b>	<b>N-term</b>	<b>ICL</b>	<b>ECL</b>	<b>Helices</b>	<b>Ligand</b>
ADL5859	8.1	2.2	2.0	1.27	0.5
Naltrindole	2.5	1.9	1.5	0.9	0.3

**Figure 7**

*RMSF Comparison*



*Note.* The root mean square fluctuation of the C $\alpha$  atom for residues in the delta opioid receptor in complex with agonist ADL5859 (trj1) (blue) and antagonist Naltrindole (trj1) (red) is shown with the DOR architecture above for reference (top). Ligand RMSF values for ADL5859 (blue) and Naltrindole (red) (bottom). The root mean square fluctuation of the atoms in both ligands as indicated in their numbering.

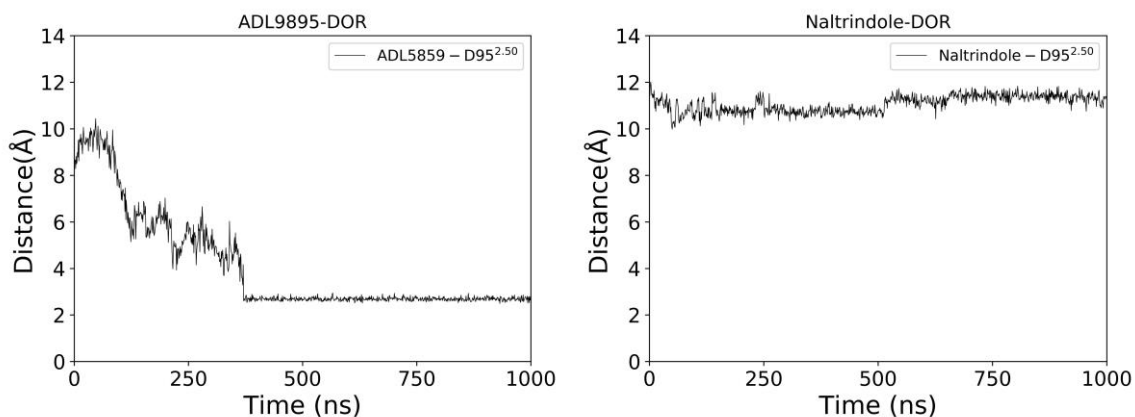


### 2.3.10 Distance of ADL5859 With Side Chain of D95 Decreases While Naltrindole Shows No Change

Residue D95<sup>2.50</sup> plays an important role in DOR activation signaling. Mutagenesis studies have shown that G protein signaling is affected in GPCRs when D<sup>2.50</sup> is replaced with a neutral amino acid.<sup>52</sup> Measuring the distance of the positively charged nitrogen atom of agonist ADL5859 and antagonist naltrindole with D95 of the protein shows a clear difference between the two systems (Figure 8). In the agonist ADL5859 system, the distance decreases about 4Å inferring a salt bridge formed with the ligand. The antagonist system shows no change in distance, further supporting the DOR in complex with the antagonist naltrindole maintained the inactive conformation.

**Figure 8**

*Average Distance Timeline Between Positively Charged Nitrogen Atom of Ligand and Side Chain of D95*



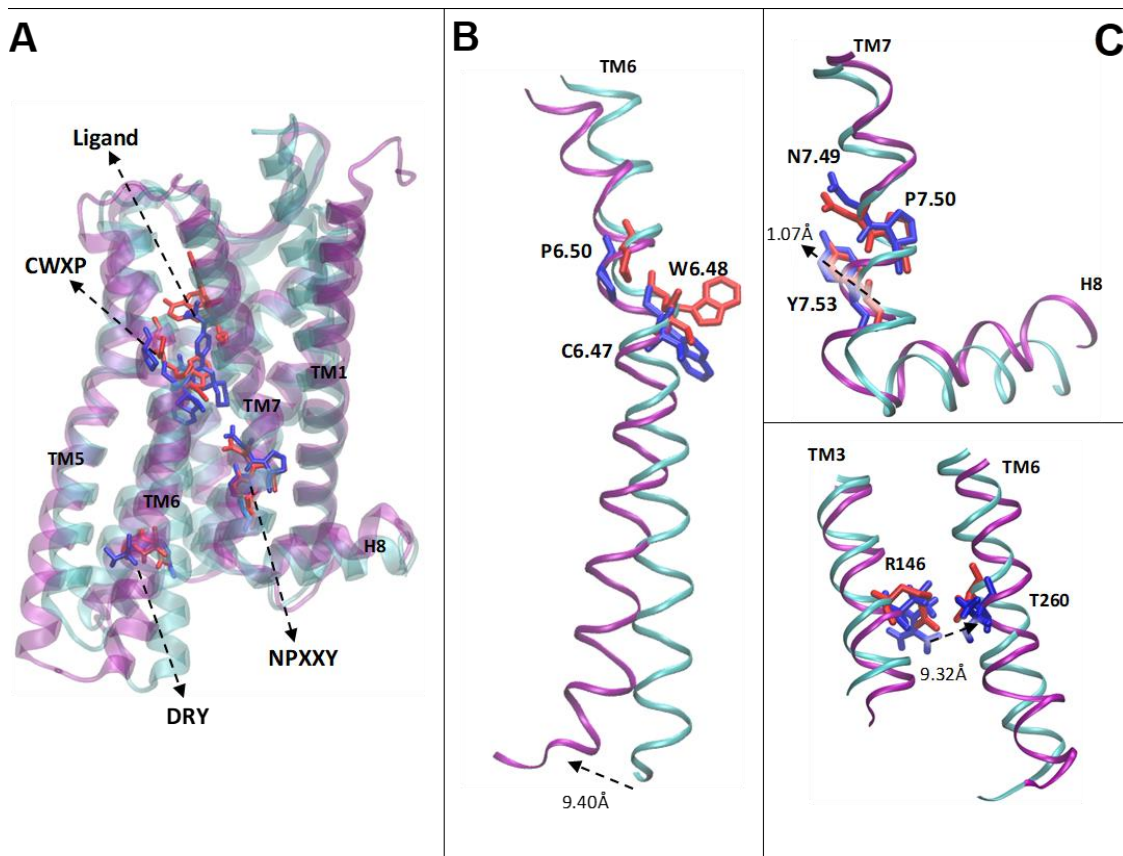
*Note:* For ADL5959-DOR system, average values of traj1 and traj6 and for naltrindole-DOR system average values of all three trajectories over 1µs are shown.

### ***2.3.11 Role of Molecular Switches in the Activation of DOR by ADL5859***

Class A GPCRs share a set of conserved motifs which are known as molecular switches. Activation of the class A GPCR can be characterized by the conformational changes in one or more molecular switches. Molecular switches were evaluated throughout the entire trajectories of ADL5859-DOR and naltrindole-DOR systems. For the DOR, three such motifs are considered to be critical in regulating its activity: Transmission Switch (CWXP) in TM6, Ionic Lock Switch (DRY) in TM3 and TM6, and Tyrosine-Toggle Switch (NPXXY, X represents any amino acid) in TM7. Each abundant cluster from the individual trajectories of both simulation systems was compared to the solved crystal structure of the inactive DOR in complex with antagonist naltrindole (PDB ID: 4N6H) to measure the switch distances. We have determined five abundant clusters in the agonist system (trj1 cluster 1&3, trj3 cluster 2, trj4 cluster 5, trj6 cluster 1) to have broken molecular switches, inferring activation, based on the transmission switch and ionic lock switch as there was no significant change in the tyrosine toggle switch for any of the clusters (Figure 9, Figure A18-A25). Trajectory 1 cluster 1 is the most favorable from the agonist system as is used as the representative structure (Figure 9). The key distances characterizing the switches for all trajectories of ADL5859 and naltrindole are summarized in Table A2.

**Figure 9**

*Molecular Switches*



*Note:* The crystal structure of Naltrindole and MD ADL5859 (trj 1 cluster 1) ligands in complex with DOR (crystal Naltrindole/DOR: red/cyan; ADL5859/DOR: blue/purple). B. Transmission Switch (CWXP) C. Tyrosine Toggle Switch (NPXXY) D. Ionic Lock Switch (DRY). B-D: crystal Naltrindole/DOR: red/cyan; ADL5859/DOR: blue/purple.

The transmission switch is the most observable switch out of the three that when in the active state, a large outward “swing” occurs in TM6. Our molecular switch analysis shows this same “swing” in our agonist ADL5859 system ranging from 9.2Å-13.9Å. The naltrindole system displays a motion of 3.8Å and 3.0Å in TM6 indicating it lacks any significant outward motion of TM6. One of the aromatic rings of ADL5859 showed

interaction with the side chain of W274, a highly conserved residue in the transmission switch. This is consistent with the active crystal structures of the DOR exhibiting slight rotameric change at the level of W274. Naltrindole also interacts with W274 but interaction is weak compared to ADL5859. The salt bridge between D<sup>3.49</sup> and R<sup>3.50</sup> residues in the DRY motif is already disrupted in the inactive DOR with distances of  $>3.5\text{\AA}$  and is missing an acidic residue in position 6.30, which is only conserved in about 30% of GPCRs. To compensate for this, we measured the hydrogen bonding between residues R146<sup>3.50</sup> and T260<sup>6.34</sup>, for this interaction is thought to stabilize receptors in the inactive state and may be important for regulating receptor signaling.<sup>53</sup> When measuring the distance of the agonist-ADL5859 system, the hydrogen bonding between residues R146<sup>3.50</sup> and T260<sup>6.34</sup> was disrupted in trj1 cluster 1, trj3 cluster 2, trj4 cluster 5, and trj6 cluster 1 with distances ranging from  $4.2\text{\AA}$ - $9.3\text{\AA}$ , implying the inactive state of the receptor was destabilized. The distances for the ionic lock switch in the antagonist-naltrindole system ranged from  $3.7\text{\AA}$ - $4.4\text{\AA}$ , indicating it was only broken in one trajectory (trj 2).

### ***2.3.12 Center of Mass Distances Identify Activation Related Changes***

The conserved motifs in molecular switches of Class A GPCRs were used as the motivation to search for other potential motifs in examining the conformational changes throughout the simulation systems (Table 2).

**Table 2***Residue Pairs for Center of Mass Distance Measurement*

ID	Residue pair	Location	Nature of interaction	Reference
1	S249-S249	TM6	Self CA-CA distance	Present study
2	W274-W274	TM6	Self CA-CA distance	Present study
3	Y318-Y318	TM7	Self CA-CA distance	Present study
4	R146-T260	TM3-TM6	H-bond	1
5	I226 <sup>5.51</sup> -F270 <sup>6.44</sup>	TM5-TM6	Hydrophobic/ <i>van der Waals</i> contact	2
6	I136 <sup>3.40</sup> -W274 <sup>6.48</sup>	TM3-TM6	Hydrophobic/ <i>van der Waals</i> contact	
7	T230 <sup>5.55</sup> -V267 <sup>6.41</sup>	TM5-TM6	Van der Waals contact	
8	L139 <sup>3.47</sup> -N314 <sup>7.49</sup>	TM3-TM7	Van der Waals contact	
9	Y233 <sup>5.58</sup> -V266 <sup>6.40</sup>	TM5-TM6	Hydrophobic/ <i>van der Waals</i> contact	
10	L139 <sup>3.43</sup> -Y318 <sup>7.53</sup>	TM3-TM7	Hydrophobic/ <i>van der Waals</i> contact	
11	M142 <sup>3.46</sup> -Y318 <sup>7.53</sup>	TM3-TM7	Hydrophobic/ <i>van der Waals</i> contact	
12	M142 <sup>3.46</sup> -R146 <sup>3.50</sup>	TM3-TM3	Van der Waals contact	
13	R146 <sup>3.50</sup> -Y318 <sup>7.53</sup>	TM3-TM7	H-bond/Cation pi	
14	V70 <sup>1.53</sup> -A319 <sup>7.54</sup>	TM1-TM7	Hydrophobic/ <i>van der Waals</i> contact	
15	L237 <sup>5.62</sup> -V263 <sup>6.36</sup>	TM5-TM6	Hydrophobic/ <i>van der Waals</i> contact	
16	L139 <sup>3.43</sup> -V267 <sup>6.41</sup>	TM3-TM6	Hydrophobic/ <i>van der Waals</i> contact	
17	V266 <sup>6.40</sup> -N314 <sup>7.49</sup>	TM6-TM7	Hydrophobic/ <i>van der Waals</i> contact	
18	M142 <sup>3.46</sup> -V263 <sup>6.37</sup>	TM3-TM6	Hydrophobic/Van der Waals contact	
19	R146 <sup>3.50</sup> -V263 <sup>6.37</sup>	TM3-TM6	Hydrophobic/ <i>van der Waals</i> contact	
20	D145 <sup>3.49</sup> -R146 <sup>3.50</sup>	TM3-TM3	Van der Waals contact/Salt bridge	
21	V70 <sup>1.53</sup> -Y318 <sup>7.53</sup>	TM1-TM7	Hydrophobic/ <i>van der Waals</i> contact	
22	M236 <sup>5.61</sup> -A319 <sup>7.54</sup>	TM5-TM7	Hydrophobic/ <i>van der Waals</i> contact	
23	R146 <sup>3.50</sup> -A149 <sup>3.53</sup>	TM3-TM3	Van der Waals contact	
24	V265 <sup>6.39</sup> -L321 <sup>7.56</sup>	TM6-TM3	Van der Waals contact	
25	R258 <sup>6.32</sup> -E323 <sup>8.48</sup>	TM6-TM8	Salt bridge	Present study
26	L139 <sup>3.43</sup> -V266 <sup>6.40</sup>	TM3-TM6	Van der Waals contact	Present study
27	I88 <sup>2.43</sup> -M262 <sup>6.36</sup>	TM2-TM6	Hydrophobic/ <i>van der Waals</i> contact	Present study

1. Claff, T.; Yu, J.; Blais, V.; Patel, N.; Martin, C.; Wu, L.; Han, G. W.; Holleran, B. J.; Van der Poorten, O.; White, K. L.; Hanson, M. A.; Sarret, P.; Gendron, L.; Cherezov, V.; Katritch, V.; Ballet, S.; Liu, Z.-J.; Müller, C. E.; Stevens, R. C., Elucidating the active  $\delta$ -opioid receptor crystal structure with peptide and small-molecule agonists. *Sci Adv* 2019, 5, eaax9115-eaax9115.

2. Zhou, Q.; Yang, D.; Wu, M.; Guo, Y.; Guo, W.; Zhong, L.; Cai, X.; Dai, A.; Jang, W.; Shakhnovich, E. I.; Liu, Z.-J.; Stevens, R. C.; Lambert, N. A.; Babu, M. M.; Wang, M.-W.; Zhao, S., Common activation mechanism of class A GPCRs. *eLife* 2019, 8, e50279.

From the literature, 18 pair-wise residues were identified that were analyzed in this study, including several hydrophobic and van der Waals contacts, as well as hydrogen bonding and salt bridges.<sup>29</sup> In addition, four atomic mass distances were measured from the molecular switch motifs: S249-S249 in TM6, W274-W274 in TM6, Y318-Y318 in TM7, R146-T260 hydrogen bonding between TM3-TM6.<sup>28</sup> When a residue is a part of TM6, the distance between that and the other transmembrane helices, particularly TM3 and TM7, should increase, breaking any interactions. Based on this, four pair-wise residues involving TM6 that are also conserved in the subfamily (opioid receptors) level were additionally measured: V265-L321 Van der Waals contact, R258-E323 salt bridge, L139-V266 Van der Waals contact, I88-M262 hydrophobic and Van der Waals contact. In total, we analyzed 27 distances, measuring the center of mass between residues, to investigate the conformational changes over the whole trajectory for the average of both simulation systems (Table 3). Through this, seven distance profiles were identified that are associated with activation. A significant increase in the distance of the center of mass is observed in the agonist system when one of the residues in a pair is a part of TM6. The timelines for the distances involving residues in TM6 for both systems are shown in Figure A26. In the agonist-ADL5859 system, trajectory 1 and 6 displayed similar distance profiles with a general increasing trend, and because of this, were averaged together to simplify the distance timeline. The three antagonist-naltrindole trajectories displayed similar distance profiles as well with a general slightly decreasing trend, and therefore, were averaged together to simplify the distance timeline. The greatest difference between the two simulation systems can be observed between residues I88<sup>2.43</sup> and M262<sup>6.36</sup> located at the intracellular portions of TM2 and TM6. Over the

course of the simulation for the agonist system, this residue shows a large increase throughout the ADL5859 timeline with a change of 4.1Å. The timeline of the naltrindole system shows this residue to be gradually decreasing throughout the simulation with a change of 0.2Å. This is consistent with the previously mentioned thought that the distance between TM6 and other transmembrane helices should increase.

**Table 3**

*Average Atomic and Center of Mass Distances*

ID	Residue Pair	Agonist (Average of 6 trajectories)				Antagonist (Average of 3 trajectories)			
		1000ns	First 100 ns	Last 100 ns	Change	1000 ns	First 100 ns	Last 100 ns	Change
1	S249 <sup>6,23</sup> -S249 <sup>6,23</sup>	5.6±2.4	5.3±1.5	5.3±2.0	0.0	3.2±1.7	2.3±0.1	4.3±1.6	2.0
2	W274 <sup>6,48</sup> -W274 <sup>6,48</sup>	2.0±0.9	1.6±0.7	2.2±0.9	0.6	0.9±0.3	0.8±0.0	1.1±0.2	0.2
3	Y318 <sup>7,53</sup> -Y318 <sup>7,53</sup>	1.9±0.5	1.7±0.4	1.9±0.3	0.2	1.0±0.4	0.9±0.1	1.0±0.4	0.1
4	R146 <sup>3,50</sup> -T260 <sup>6,34</sup>	5.2±1.6	4.6±0.1	6.5±2.6	1.9	4.6±0.4	4.6±0.0	4.6±0.1	0.0
5	I226 <sup>3,51</sup> -F270 <sup>6,44</sup>	11.4±0.7	11.7±0.4	11.1±0.6	-0.6	11.4±0.5	11.5±0.0	11.2±0.1	-0.3
6	I136 <sup>3,40</sup> -W274 <sup>6,48</sup>	7.5±0.6	7.4±0.7	7.7±0.3	0.3	7.4±0.4	7.3±0.2	7.6±0.1	0.3
7	T230 <sup>5,55</sup> -V267 <sup>6,41</sup>	10.4±0.6	10.1±0.4	10.5±0.2	0.4	9.5±0.6	9.6±0.0	9.4±0.5	-0.2
8	L139 <sup>3,47</sup> -N314 <sup>7,49</sup>	11.2±0.5	11.1±0.4	11.1±0.3	0.0	11.6±0.6	11.8±0.4	11.3±0.3	-0.5
9	Y233 <sup>5,58</sup> -V266 <sup>6,40</sup>	12.0±1.2	11.7±1.2	11.6±0.9	-0.1	10.1±0.6	9.8±0.0	10.5±0.4	0.5
10	L139 <sup>3,43</sup> -Y318 <sup>7,53</sup>	11.5±0.6	11.7±0.2	11.3±0.3	-0.4	11.9±0.5	12.4±0.0	11.7±0.2	-0.7
11	M142 <sup>3,46</sup> -Y318 <sup>7,53</sup>	11.1±0.7	11.2±0.4	10.8±0.4	-0.4	11.4±0.5	11.4±0.4	11.3±0.3	-0.1
12	M142 <sup>3,46</sup> -R146 <sup>3,50</sup>	7.0±0.5	7.2±0.2	6.7±0.2	-0.5	7.2±0.4	7.4±0.1	7.2±0.1	-0.2
13	R146 <sup>3,50</sup> -Y318 <sup>7,53</sup>	15.0±1.1	15.1±0.8	14.3±0.7	-0.8	15.4±0.7	15.1±0.7	15.5±0.7	0.4
14	V70 <sup>1,53</sup> -A319 <sup>7,54</sup>	9.7±0.5	9.5±0.1	9.7±0.2	0.2	9.6±0.4	9.7±0.4	9.6±0.3	-0.1
15	L237 <sup>5,62</sup> -V263 <sup>6,36</sup>	12.5±1.2	12.0±0.8	12.3±1.4	0.3	11.0±0.6	10.8±0.0	11.3±0.1	0.5
16	L139 <sup>3,43</sup> -V267 <sup>6,41</sup>	5.6±0.7	5.3±0.4	6.3±0.9	1.0	5.7±0.4	5.5±0.0	6.0±0.1	0.6
17	V266 <sup>6,40</sup> -N314 <sup>7,49</sup>	8.2±1.0	7.8±0.5	8.4±1.0	0.6	8.7±0.5	8.8±0.2	8.7±0.4	-0.1
18	M142 <sup>3,46</sup> -V263 <sup>6,37</sup>	6.5±1.0	5.5±0.1	7.4±1.3	1.9	6.2±0.7	6.1±0.3	6.1±0.7	0.0
19	R146 <sup>3,50</sup> -V263 <sup>6,37</sup>	7.1±1.0	6.9±0.5	7.0±0.5	0.1	6.6±0.2	6.5±0.0	6.6±0.2	0.1
20	D145 <sup>3,49</sup> -R146 <sup>3,50</sup>	4.7±0.5	4.6±0.2	4.8±0.6	0.2	4.8±0.2	4.7±0.0	4.8±0.0	0.1
21	V70 <sup>1,53</sup> -Y318 <sup>7,53</sup>	7.0±0.4	7.2±0.1	7.0±0.2	-0.2	7.0±0.4	7.2±0.5	7.0±0.2	-0.2
22	M236 <sup>5,61</sup> -A319 <sup>7,54</sup>	22.2±1.2	22.3±0.6	21.8±1.3	-0.5	21.6±0.8	21.8±0.0	21.6±0.3	-0.2
23	R146 <sup>3,50</sup> -A149 <sup>3,53</sup>	5.1±0.4	4.8±0.2	5.4±0.5	0.6	4.8±0.3	4.8±0.0	4.8±0.2	0.0
24	V265 <sup>6,39</sup> -L321 <sup>7,56</sup>	8.1±0.8	7.3±0.3	8.5±0.7	1.2	7.4±0.8	7.2±0.2	7.3±1.3	0.1
25	R258 <sup>6,32</sup> -E323 <sup>8,48</sup>	11.0±1.9	9.4±0.8	11.5±1.4	2.1	10.3±1.4	10.6±0.1	9.6±1.3	-1.0
26	L139 <sup>3,43</sup> -V266 <sup>6,40</sup>	7.7±1.0	7.0±0.2	8.7±1.3	1.7	7.8±0.7	7.7±0.2	7.9±0.7	0.2
27	I88 <sup>2,43</sup> -M262 <sup>6,36</sup>	11.4±2.5	8.9±1.1	13.0±2.1	4.1	10.4±2.0	10.0±0.6	10.2±2.6	0.2

### ***2.3.13 Normal Mode Analysis Shows the Overall Motion of the Receptor***

The normal mode analysis (Figure S27-S28) shows the top 10 low vibrational modes identified from the principal component analysis, however modes 1-3 show the most difference in motion. The overall motion of the receptor is significant, however, the motion of TM6 is presumed to be a hallmark in determining the state of the receptor (i.e. active, inactive) and therefore can be focused in on for clarity. Using our representative structures from our two systems, our analysis identified the ADL5859 system having a higher degree of fluctuation and a more distinct motion when compared to naltrindole. In the top mode of the ADL5859 system, the ends of TM5, TM6, and ICL3 appear to be moving outward, deeming the bottom of the receptor to be open, or otherwise, in the active state. The motion in the naltrindole system of the same region can be observed as moving back towards TM3 and TM4, still in a closed position. This analysis was also performed on trajectory six of the ADL5859 system and the remaining two trajectories of the naltrindole system. Trajectory six of the ADL5859 system had maintained similar modes of motion from the first agonist trajectory-. The two trajectories from the naltrindole system also maintained similar modes of motion from the first antagonist trajectory.

## **2.4 Discussion**

Computational studies have been utilized in studying the DOR even before crystal structures became available, however, to our best knowledge, no known studies have applied the use of MD simulations to study its activation mechanism started from an inactive conformation. Molecular dynamic simulations is extremely powerful tool to



probe deeper into the interactions and dynamics occurring in a protein system. Starting from the inactive state of the DOR and sampling its active conformation in the presence of a small molecule agonist offers an opportunity to explore the structural basis of DOR activation. Using agonist ADL5859 adds to the novelty due to its lack of a crystal structure and unknown interactions with the DOR. ADL5859 shares a pharmacophore with the crystal agonist DPI-287 (Figure 1), implying their interactions with the DOR will be similar, validating the use of this small molecule ligand for this study. The crystal antagonist naltrindole was used as our second simulation system in order to determine if the inactive conformation of the DOR when bound to an antagonist can be maintained in MD simulations to serve as a negative control. Here we present the first study probing the active conformation of the DOR started from an inactive conformation using MD simulations.

After docking the ligands into the homology model, both agonist ADL5859 and antagonist naltrindole resulted in docking conformations consistent with the crystal ligand poses (Figure 2).<sup>28, 54</sup> This validated our initial poses for the MD simulation of both ligands. Following the simulation of both systems, the calculation of RMSD throughout the simulation of different protein regions against both crystal structures (4N6H, 6PT3) offered a deeper insight into the structural change response of the DOR when bound to an agonist or antagonist (Figure 4). The gap between the crystal reference structures in the RMSD plots indicated both simulation systems were more similar to the inactive conformation at the start of the simulation, which is consistent with our starting structures that were generated based on the inactive crystal structure (4N6H). Decreasing in RMSD against the active crystal structure while increasing in RMSD against the

inactive crystal structure would suggest that the system is adopting toward the active conformation. Encouragingly, the agonist-ADL5859 system followed this RMSD trend with the most apparent in TM6. This correlates with what is known about GPCRs, that TM6 outward opening is a hallmark of the activation in class A GPCRs.<sup>50</sup> The RMSDs in the antagonist system only showed no change. This analysis supports our agonist system folding toward the active conformation and our antagonist system maintaining the inactive conformation.

The trajectory clustering analysis identified the populated conformations of the individual trajectories throughout the simulation that helped to gain further insight into the DOR complexes (Table A1, Figure 5, Figure A7-A8). Expecting the agonist bound DOR to undergo conformation change, it can be understood that the majority of the individual agonist trajectories contained more than one populated cluster conformation. In contrast, the individual antagonist trajectories each generated only one populated cluster conformation, as they were not expected to have changed from their initial inactive conformation.

After calculating the RMSD of different portions of the receptor when superimposed with the crystal structures, we were able to identify three independent activating events of the ADL5859 system that supports the DOR folding toward the active conformation, with the most notable hallmark as the RMSD of TM6. The first event occurred in the first trajectory where cluster 1 (52%) and cluster 3 (17%) were structurally similar to the active crystal complex with favorable RMSD values (Cluster 1 RMSD TM6 Inactive: 4.1Å Active: 3.4Å · Cluster 3 RMSD TM6 Inactive: 3.3Å Active: 2.9Å). The second event happened in the fourth trajectory where cluster 5 (1%) showed

agreement with the active crystal complex with favorable RMSD values (Cluster 5 RMSD TM6 Inactive: 5.8Å Active: 2.8Å). The third event was in the sixth trajectory's most abundant cluster (76%) that was structurally similar to the active crystal structure with favorable RMSD values (Cluster 1 RMSD TM6 Inactive: 3.9Å Active: 3.2Å). The percentage of abundance of each event indicates >70% folding into the active state with the 1% of abundance from trajectory 4 cluster 5 as a partial folding event. The agonist bound clusters shared similar interacting protein-ligand residues as the active crystal structure as well. In the three individual naltrindole trajectories, each abundant cluster showed structural agreement with the inactive crystal structure (4N6H) with lower RMSD values against 4N6H and higher values against 6PT3, further inferring its similarity to the inactive conformation. This is further validating that the activation related changes are unique to our agonist bound complex.

Superimposing the abundant structures to the crystal structures and calculating the RMSD of different protein regions also opened speculation to other populated clusters from the individual agonist trajectories as intermediate conformations in the protein folding toward the active state. Trajectory 3 clusters 1 (90%) and 2 (11%); trajectory 4 clusters 1 (43%), 3 (20%), and 4 (5%); and trajectory 5 cluster 1 (56%) show some to great agreement to the active crystal structure, especially in regions TM5-6, while showing disagreement to the inactive crystal structure in these same regions. These speculated intermediate active state folding structures add further support that our agonist-ADL5859 system has undergone protein folding toward the active state as the trajectories from which the structures came (trj3, trj4, trj5), in addition to the respective trajectories of the identified active folding structures from the clustering RMSD

calculation (trj1, trj4, trj6), are consistent with the individual agonist trajectories determined as adopting toward the active conformation from the RMSD time series of the whole simulation (trj1, trj3, trj4, trj5, trj6) (Figure A5-A6). This analysis has not only offered support to the previous RMSD analysis, but has also added more insight into the speculated activation process towards the activated DOR.

Comparing the two representative structures from the MD complexes revealed a clear conformational difference in the receptors in the transmembranes as well as the intra- and extracellular loops and the ligand binding pose. These differences in the protein structures are consistent with the differences between the active and inactive crystal structures. The binding pose of ADL5859 is lower than that of naltrindole, which may be a result of the great conformational change occurring that could be pulling the ligand deeper into the binding pocket. The MD simulations were successful in producing different conformations in the DOR when bound to an agonist and antagonist. Our simulation data supports the conformation selection mechanism for DOR activation.

The RMSF of the receptor (Figure 7 and Figure A14-A15) when bound to agonist-ADL5859 indicated the complex had greater flexibility in the loops and terminals when compared to the antagonist-naltrindole system which is consistent with not only the pharmacological actions of the two ligands (agonist/antagonist), but also our hypothesis that our agonist system adopted toward the active conformation. The ligand RMSF also supports our hypothesis due to ADL5859 itself showing greater flexibility than naltrindole. This is consistent with what is known, that an antagonist (naltrindole) typically binds tighter to the receptor than an agonist (ADL5859). Naltrindole is also a more rigid ligand compared to ADL5859, with more aromatic rings and less rotatable

bonds, which tells enough in itself about the predicted flexibility of the ligands that was produced in the ligand RMSF. The RMSF analysis is another indication supporting that our agonist system underwent a conformational change.

Residue D95<sup>2,50</sup> is believed to be an important residue in the agonist-induced cyclic adenosine monophosphate (cAMP) response that occurs in activated GPCRs.<sup>52</sup> In timeline plots, we see that in traj1 and traj6 decrease in the distance between ADL5859 and D95 correlates with DOR activation (Figure 8). In contrast, the distance between D95 and naltrindole has no change throughout the simulation, inferring that the helices have not shifted, remaining in the inactive state.

Molecular switches are hallmarks in the classification of the activation state of class A GPCRs.<sup>50</sup> Previous studies have identified the lack of a salt bridge in inactive opioid receptors which have a hydrophobic Leu<sup>6,30</sup> in place of the usual acidic Glu<sup>6,30</sup>.<sup>54</sup> It was later realized hydrogen bonding between R146<sup>3,50</sup> and T260<sup>6,34</sup> residues may stabilize the receptor in the inactive state similar to the salt bridge in the Ionic Lock Switch.<sup>53</sup> This interaction was analyzed as the Ionic Lock Switch along with the usual Transmission and Tyrosine Toggle Switches. This hydrogen bonding was broken in multiple trajectories with a distances of 4.2-9.3Å. A very recent study by Claff and coworkers reported on the distance of the transmission switch on a mutant active state DOR with a large outward movement on helix 6 with a distance of approximately 9.4 to 11.2Å<sup>28</sup>, which is consistent with our data that showed distances of 9.2-13.9Å. The sidechain of W274 of the transmission switch also showed slight rotameric change, indicating the receptor is in the active state. Any slight change in the orientation of side chain of W274 can have direct effect on the residues of TM6 and other regions of DOR.

This same study as previously mentioned also reported an inward shift of helix 7 at a distance of 3.9Å, however, they speculate this greater shift may be attributed to the three mutations they made in the sodium-binding pocket (N90<sup>2.45</sup>S, D95<sup>2.50</sup>G, N131<sup>3.35</sup>S).<sup>28</sup> In contrast, this shift was not observed in the trajectories of the agonist-ADL5859 bound DOR. Tyrosine-toggle switch did not show significant change in ADL5859-DOR complex. As for the Naltrindole complex, the three molecular switches remain intact, which obstruct the outward movement of TM6 thus, blocking G protein signaling.

In addition, we have used multiple atomic and center of mass distances to characterize the conformation differences between the active and inactive states of the DOR. These differences could contribute the activation. Indeed, the seven residue pairs were identified that are associated with activation.

The normal mode analysis (Figure A27-A28) shows the top 10 low vibrational modes identified from the principal component analysis. Previous knowledge tells us that the motion and conformation of transmembrane six is relative to the state of the receptor (i.e. active, inactive). While the overall motion is significant, this area can be focused in on for clarity. We conducted this analysis on trajectory 1 and 6 from our agonist system and all three antagonist trajectories. Our analysis identified the ADL5859 system having a higher degree of fluctuation and a more distinct motion when compared to naltrindole. Altogether, the two agonist trajectories had seven conserved vibrational modes in which they had similar motion (mode 1, 2, 3, 4, 7, 8, 9). The conserved vibrational modes where motion was favored between the two trajectories were modes 1, 2, 4, and 8 where the ends of TM5 and TM6 swing outward, opening the intracellular portion of the receptor for G protein signaling that is crucial in GPCR activation. The motion of the naltrindole

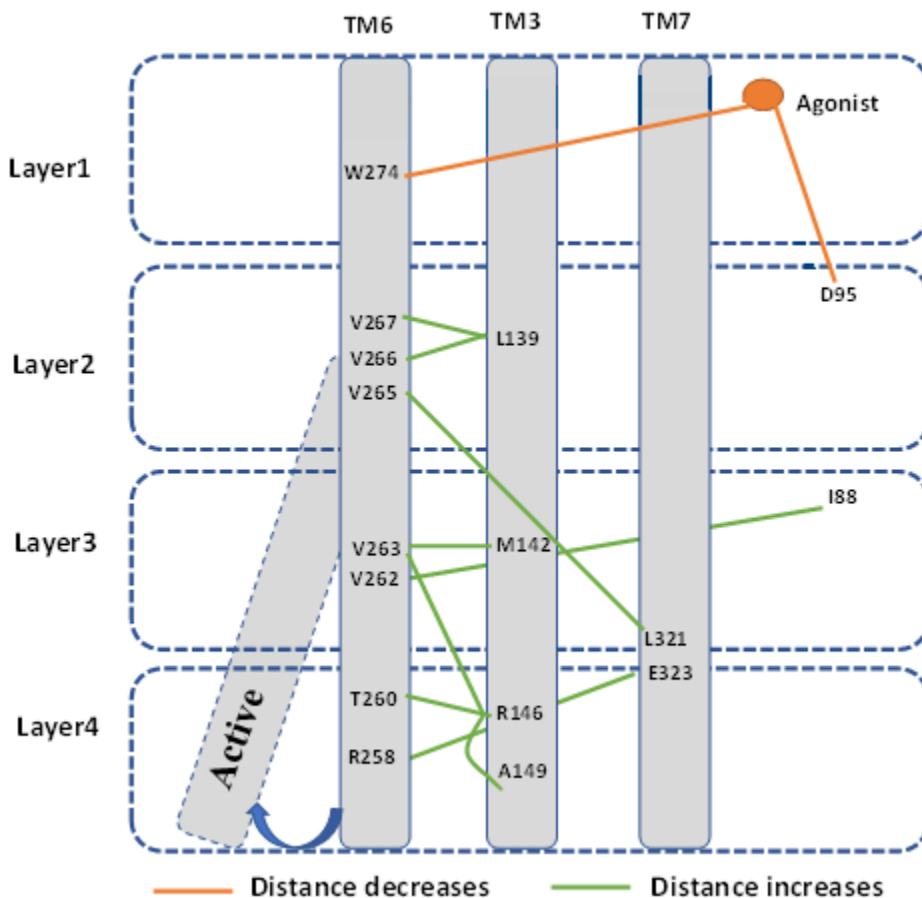
system in the majority of the modes for all three trajectories of the same region can be observed as moving back towards TM3 and TM4 or downward, still in a closed inactive position. This further provided another level of insight into the essential dynamics of these complexes in the lowest vibrational states. We can conclude from the normal mode analysis that the overall dynamics of the two complexes are distinct from one another, which further supports that the motion differences of these complexes are due to their dynamic interactions as well as their pharmacological actions. Our analyses including RMSD, RMSF, molecular switches, measuring the center of mass, and normal mode analysis help to explain the activity differences on the receptor that cannot be explained from the crystal antagonist alone.

The proposed activation pathway of the receptor started from the allosteric signal from the agonist ligand to the intracellular domain that interact with the effector G-protein has been summarized in Figure 10. When the agonist is bound to the DOR, it forms strong interactions with W274 and D95 in layer 1-2, further leads to break important interaction pairs from layer2 by layer4 such as V267-L139, V263-M142 and others, and finally causing an outward shift of the intracellular domain of TM6. This is consistent with what is known about class A GPCRs that the intracellular portion of this helices should move outward when activating to allow for G-protein signaling.<sup>50</sup> In this same respect, TM3 shifts away from TM6, breaking any hydrogen bonding that stabilizes the inactive conformation. While this occurs, TM7 also moves away from both TM3 and TM6. During all of this movement, the extracellular portion of TM1 folds away from the ligand and the binding pocket while TM2 shifts closer to the ligand. The key residues in

the activation pathway identified from this study provides a short list for future experimental mutagenesis study.

**Figure 10**

*DOR Activation Pathway*



*Note.* Binding of agonist to DOR led to flow of allosteric signal from layer 1 (containing agonist binding residues) to different layers of human DOR.



## Chapter 3

# To Probe Activation Mechanism of Agonist DPI-287 to Delta Opioid Receptor and Novel Agonists to Using Ensemble-Based Virtual Screening With Molecular Dynamics Simulations

### 3.1 Introduction

#### 3.1.1 *The Opioid Epidemic*

While pharmaceuticals have made great strides over the years in many areas, the field of pain management is still lacking. There are great medications that target pain and are effective, however, there has been a rise in the use of opioids over the years that has led to the opioid epidemic that Northern America and other parts of the world are in. The use of opioids (legally and illegally) has risen between 10-14 times in the last 20 years, with more than 42,000 deaths in 2016 in the USA occurring from opioid overdoses alone.<sup>55, 56</sup> Most prescribed opioids target the Mu Opioid receptor (MOR) which are located in the reward areas of the brain.<sup>55, 57, 58</sup> When opioid agonists bind to and activate these receptors, it causes euphoria which can lead to addiction after repeated use. When people have long-term use of opioids, they can build up a tolerance, meaning they need higher doses to feel the same effect, and/or physical dependence, inferring the need for opioid use to continue normalcy. If the user is leading down this track, it can cause decreased gastrointestinal motility, anorexia, urinary retention, and finally, respiratory depression leading to an opioid overdose. When a user stops taking opioids after addiction and physical dependence has taken place, it leads to withdrawal symptoms such as bone pain with muscle aches, changes in body temperature, hyperalgesia, insomnia,

stomach cramps, nausea, and many dysphoric effects.<sup>56</sup> Physical dependency along with the known unattractive symptoms of withdrawal are major reasons people do not stop taking opioids. The need for better pain management without addictive properties is pressing.

### 3.1.2 DOR Target Potential

The DOR has shown to have potential in not only pain management, but also in psychiatric and neurological disorders without the potential for dependence or respiratory depression (Table 4).<sup>59-66</sup> This makes the DOR an attractive target to further study to potentially help alleviate the opioid epidemic in the world.

**Table 4**

*Comparison Between MOR and DOR*

<b>Receptor Type</b>	<b>Therapeutic Function &amp; Side Effects</b>	<b>Model Type</b>	<b>Reference</b>
Mu	Pain relief Euphoric effect – Addiction, physical dependence, respiratory depression	Humans	(Shipton, et al. 2018), (Pergolizzi Jr, et al. 2020), (Volkow, et al. 2017), (Centers for Disease, et al. 2016)
Delta	Chronic pain relief	Spinal administration rat, Gene knockout mice	(Holdridge, et al. 2007) (Nadal, et al. 2006) (Gavériaux-Ruff, et al. 2008)
	anti-depression	Gene knockout mice, Forced swim assay rats	(Filliol, et al. 2000) (Broom, et al. 2002)
	ischemic preconditioning	Ischemia reperfusion injury rats, post-ischemic mice	(Tian, et al. 2013) (Min, et al. 2018)
	Convulsions	Systemic administration mice, rats, electroencephalographic rhesus monkeys	(Comer, et al. 1993) (Jutkiewicz, et al. 2005) (Danielsson, et al. 2006)

### ***3.1.3 Previous Studies On the DOR***

However, multiple studies have reported on convulsions in various animal models with the use of DOR agonists. After systemic administration of a DOR agonist, mice displayed convulsive effects.<sup>67</sup> Using rats, tolerance rapidly developed to convulsive and locomotor-stimulating effects of a selective DOR agonist but did not display tolerance to the antidepressant-like effects.<sup>68</sup> When using rhesus monkeys, only one out of the four monkeys had convulsions, however, this same monkey did not display convulsive activity when given a smaller dose weeks later or even the same dose one year later.<sup>69</sup> The difference in convulsions in species could indicate that these are species-dependent effects. As mentioned previously, the DOR is distributed in different areas of the spinal cord in rodents versus primates. In rodents, the delta receptor is found dispersed in the spinal cord, whereas it is limited to the superficial laminae of the spinal dorsal horn in humans and non-human primates.

### ***3.1.4 High-Throughput Virtual Screening Reasoning***

High-throughput virtual screening (HTVS) is a useful computational process that can screen for thousands of molecules that bind to a molecular target and can also identify toxic or unfavorable pharmacodynamics and pharmacokinetic properties of these compounds.<sup>70</sup> Structure-based virtual screening (SBVS) is a HTVS approach that predicts the interactions between ligands and proteins as a complex, ranking them by their affinity to the receptor. The top hit compounds are then selected based on the desired parameters and are then optimized to undergo preclinical and clinical trials. Computational methods such as molecular modeling are used in the HTVS approach to speed up the drug

discovery process by analyzing the interactions of multiple molecules in a shorter period of time, which can look into interactions before the drug is even synthesized. SBVS is a good technique due to its low cost, faster result time, and good results achieved.

### ***3.1.5 Ensemble-Based Approaches***

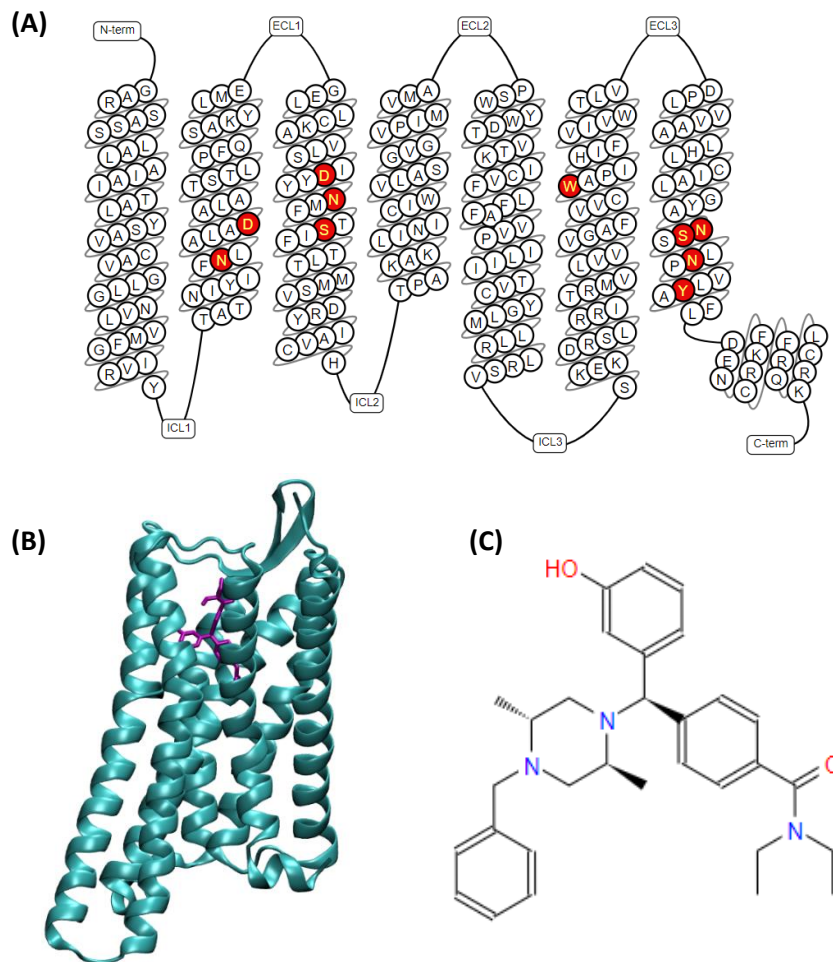
The flexibility of receptors is a challenge researchers face as binding sites usually consist of 10-20 amino acid side-chains that have dozens of rotatable conformations, which is larger than the rotatable torsions of a ligand.<sup>71</sup> The movements of the backbone can make this even worse by affecting multiple side chains. Using an ensemble-based receptor technique combats this issue in HTVS and MD simulations by sampling the degrees of freedom instead of traditional techniques using one receptor conformation with a flexible ligand. It has been found in cases to also improve docking scores. With previous studies it has been suggested that ensembles generated from simulations have been closely similar in replicating the dynamics of proteins in NMR experiments.<sup>72, 73</sup> It is better to use a few specifically selected conformations as using too many could give false results. In the case of virtual screening, using the top 10% of a library subset is more efficient with this approach.<sup>71</sup> Previous studies using ensemble-based virtual screening have been successful in screening ligands against various drug targets.<sup>74, 75</sup> The integration of this ensemble-based technique helps to have a better understanding of the structural dynamics of a receptor, have a better understanding of ligand-receptor interactions which aids in discovering novel ligand binding modes, and helps to develop better therapeutic molecules.<sup>76</sup>

### 3.1.6 Experimental Overview

In the present study, we used MD simulations to probe the active conformation of the DOR starting with the active crystal conformation (PDB ID: 6PT3) with the crystal agonist DPI-287 (Figure 11). This agonist is highly selective towards the DOR and has shown antidepressant effects with less convulsive properties than the other drugs in this drug family in the rat forced swim test.<sup>77</sup>

**Figure 11**

*Structural Organization of the Active Conformation of the DOR and Ligand*



Using the ensemble-based method, two representative conformations were identified from the clustering and principal component analysis based on the MD simulation. These two conformations and the crystal conformation were used to screen 17 million compounds from the zinc database. As a result, 69 drugs were identified on the basis of docking scores. These 69 complexes underwent MD simulations to assess their stability. From this, 8 were identified that showed significantly improved MM-GBSA binding free energy scores with high blood brain barrier (BBB) permeability and high gastrointestinal (GI) absorption. This study helps to identify potential compounds to be further tested that will aid in antinociception without addictive or convulsive properties for the DOR.

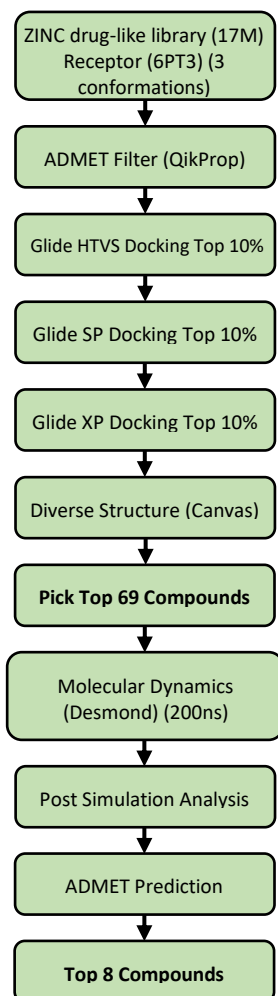
## **3.2 Methods**

### ***3.2.1 Virtual Screening Workflow Overview***

Using the Zinc 15 drug-like library that contains 17 million entries, a virtual screening workflow (VSW) was developed to identify lead agonists to the DOR. The VSW is made up of ten steps that includes drug property prediction, molecular docking, and molecular dynamics simulations (Figure 12).

**Figure 12**

*Virtual Screening Workflow*



Inputting the prepared protein structure and ligand library is the first step of the VSW. In steps 2-5, the compounds were then filtered by drug property with docking and multiple Glide docking score functions that have increasing accuracy (Glide HTVS, SP, and XP). In the next step, a ligand similarity analysis was performed to identify different molecular scaffolds. In step 7, the ligands that were removed were based on if they had a worse

Glide XP score than the reference compound (PDB ID: 6PT3 ligand DPI-287) and/or if they had more than one red flag in drug property (number of stars, from QikProp). The top compounds were manually selected from the remaining compounds by maximizing the number of molecular scaffolds (i.e. different ligand cluster IDs). The 200ns MD simulations were carried out in step 8 which was then followed by the post simulation analyses in step 9, including MMGBSA binding free energy calculation, simulation interaction diagram analysis, and protein conformation clustering analysis. In the last step, the ADMET (Absorption, Distribution, Metabolism, Excretion, and Toxicity) prediction was used to examine the human oral bioavailability of potential drug candidates. From this, the compounds with better MM-GBSA binding free energy than the reference compound were selected and presented in the main text. The ten steps are presented in detail in the following six modules.

### 1. Preparation of Protein and Ligand Library

The crystal structure (6PT3) of the active conformation of the DOR was prepared and preprocessed using Maestro's Protein Preparation Wizard.<sup>78</sup> The charge state of the preprocessed protein was optimized at pH 7. A restrained minimization was then performed to relax the protein structure using OPLS3 force field.<sup>79</sup> The 3D structures of DPI-287 and the Zinc compounds were prepared using Maestro Elements. The 3D structure of DPI-287 was extracted from the crystal structure (PDB ID: 6PT3) and the Zinc compounds were downloaded from the Zinc15 database (<https://zinc15.docking.org/>). The ionization/tautomeric states for the ligands were generated at pH 7 using Maestro's Epik tool based on the more accurate Hammett and Taft methodologies.<sup>78</sup> The lowest ionization/tautomeric state was selected and the



geometry was then minimized to the most energetically favorable structure to relax the structure of the ligand. A geometry optimization was utilized using quantum mechanics in Jaguar as the final step.

## 2. Filtering and Docking

The prepared protein and ligand were merged into a complex to then be ran through the Schrodinger Virtual Screening Interface using prefilters through Lipinski's Rule and filtered with ADMET risk parameter assessments through QikProp. The receptor grid files were generated from the prepared receptors, in which the centroid of the crystal ligand, DPI-287, was used to specify the active site. The prepared ligands were docked into their corresponding generated grids using Glide XP scoring with default procedures and parameters.<sup>79</sup> In detail, the receptor grid required for the docking process was generated using van der Waals scaling factor of 1 and partial charge cutoff 0.25. Docking was performed using a ligand-centered grid using OPLS3 force field. Glide XP Dock performed a comprehensive systematic search for the best receptor conformations and orientations to fit the ligand. The docked poses were compared to the active crystal complex (PDB ID: 6PT3) with an agonist to verify if the docked ligand poses were reasonable. All ligands were bound within the binding pocket with DPI-287 binding similar to the crystal ligand, providing a reasonable starting pose for later molecular dynamic simulations. The binding pose can then be refined given the full conformation flexibility in the simulations. The docking results comprised of 69 top compounds with higher docking scores than the reference ligand (6PT3), indicating they all had high affinity for the receptor.

### 3. Ligand Similarity Clustering

The canvas program was used for the ligand similarity clustering. This program uses pharmacophore fingerprinting and hierarchical clustering to further filter out top compounds. Pharmacophore fingerprinting identified similar groups of compounds to match the crystal structure.<sup>80</sup> Hierarchical clustering was then utilized to form cluster groups of similar compounds based on their docking score, binding affinity, drug properties, and ligand similarities.<sup>81, 82</sup> The poses were manually generated and evaluated based on their binding score and similarity to known FDA-approved drugs. The top 69 compounds were then used for the MD simulations.

### 4. MD Simulation

#### *4.1. MD Simulation System Setup*

The 69 prepared receptor-ligand complexes were used to construct MD simulation systems using the prepared and refined receptor-ligand complex from the Glide XP docking, crystal structure (6PT3), and generated conformations as input files. Each system was built using SPC as water solvent model<sup>83</sup> using orthorhombic solvent box with 6Å water buffer. The system was neutralized using Na<sup>+</sup> and Cl<sup>-</sup> ions and were added to maintain the salt concentration of 0.15 M NaCl. After the system was successfully solvated, OPLS3 force field using Desmond System Builder<sup>79</sup> was used to represent the receptor-ligand.

#### *4.2. Relaxation and Production Runs*

Using Desmond module, the system was first relaxed using the default relaxation protocol for membrane proteins.<sup>84</sup> This relaxation protocol consists of eight stages: 1). Minimization with restraints on solute heavy atoms; 2). Minimization without any restraints; 3). Simulation with heating from 0 K to 300 K, H<sub>2</sub>O barrier and gradual restraining; 4). Simulation under the NPT ensemble (constant number of particles, constant pressure of 1 bar and constant temperature of 300 K) with H<sub>2</sub>O barrier and with heavy atoms restrained; 5). Simulation under the NPT ensemble with equilibration of solvent and lipids; 6). Simulation under the NPT ensemble with protein heavy atoms annealing from 10.0 kcal/mol to 2.0 kcal/mol; 7). Simulation under the NPT ensemble with C $\alpha$  atoms restrained at 2kcal/mol; and 8). Simulation for 1.5 ns under the NPT ensemble with no restraints.

After the relaxation, each system was submitted to a 200 ns production run conducted under the NPT ensemble for each of the systems using the default protocol. In details, temperature was controlled by using the Nosé-Hoover chain coupling scheme<sup>85</sup> with a coupling constant of 1.0 ps. Pressure was controlled using the Martyna-Tuckerman-Klein chain coupling scheme<sup>85</sup> with coupling constant of 2.0 ps. M-SHAKE<sup>86</sup> was applied to constrain all bonds connecting hydrogen atoms, enabling a 2.0 fs time step in the simulation. The k-space Gaussian split Ewald method<sup>87</sup> was used to treat long-range electrostatic interactions under periodic boundary conditions (charge grid spacing of  $\sim 1.0$  Å, and direct sum tolerance of  $10^{-9}$ ). The cutoff distance for short-range non-bonded interactions was 9 Å, with the long-range Van der Waals interactions based on a uniform density approximation. To reduce the computation, non-bonded forces were calculated using an r-RESPA integrator<sup>88</sup> where the short-range forces were updated

every step and the long-range forces updated every three steps. The trajectories were saved at 40.0 ps intervals for analysis.

## 5. Post Simulation Analysis

### *5.1. Simulation Interaction Diagram (SID) Analysis*

Desmond SID tool was used to analyze the behavior and interaction of proteins and ligands during the course of simulation including RMSD; protein-ligand contacts including H-bonds, hydrophobic, ionic, and water-bridge contacts; secondary structure changes and Root Mean Square Fluctuation (RMSF) measures. To check the convergence of MD simulations, the protein C $\alpha$  and ligand RMSD plots were investigated for each trajectory. Relatively flat plots indicate that the complex systems have reached a steady state.

### *5.2. Trajectory Clustering Analysis*

Desmond trajectory clustering tool<sup>89</sup> was used to group complex structures from the last 100 ns simulation of each complex system. Backbone RMSD matrix was used as structural similarity metric, the hierarchical clustering with average linkage was selected as the clustering method. The merging distance cutoff was set to be 2Å. The centroid structure (i.e. the structure having the largest number of neighbors in the structural family) was used to represent the structural family.

### *5.3. Binding Energy Calculations and Decompositions*

The surface-area-based Generalized Born model<sup>90,91</sup> was used to calculate the ligand-binding affinities on the frames in the last 50 ns of each MD simulation with an

implicit membrane solvation model (VSGB 2.0).<sup>92</sup> Slab-shaped regions with a low dielectric constant between 1 and 4 were excluded from the implicit membrane and were assigned with the solvent (water) dielectric constant of 80. The MM-GBSA calculation used an OPLS3 force field and the default Prime procedure.<sup>79</sup> The OPLS3 force field employs a CM1A-BCC-based charge model based on a combination of Cramer-Truhlar CM1A charges<sup>93</sup> with an extensive parameterization of bond charge correction terms (BCC). This process begins with minimizing the receptor only, then the ligand only, and then the receptor-ligand complex. Using equation 1, the MM-GBSA binding free energy for each system was calculated from three separate simulations: ligand-only, receptor-only, and the receptor-ligand complex. Equation 2 contains 4 components: Van der Waals interaction energy (VDW), hydrophobic interaction energy (SUR), electrostatic interaction (GBELE), and the change of the conformation energy for the receptor and ligand that were calculated based on equations 3 and 4.

$$\Delta E = E_{complex} - E_{rec\_free} - E_{lig\_free} \quad (1)$$

$$\Delta E = \Delta E_{vdw} + \Delta E_{SUR} + \Delta E_{GBELE} + \Delta E_{conformation} \quad (2)$$

$$\Delta E_x = E_{x\_complex} - E_{x\_rec\_complex} - E_{x\_lig\_complex}, \quad x = vdw, sur \text{ and } gbele \quad (3)$$

$$\Delta E_{conformation} = E_{rec\_complex} + E_{lig\_complex} - E_{rec\_free} - E_{lig\_free} \quad (4)$$

The MM-GBSA scoring function lacks the solute conformational entropy contribution, which causes higher negative values when compared to actual values. It is essential being able to rank a drug's ability to target a receptor when it is used to rank different drugs targeting receptors with comparable entropy values.<sup>94</sup> MM-GBSA has shown to be a powerful tool in ranking ligands supported by multiple studies.<sup>95-98</sup>

## 6. ADMET Prediction

ADMET properties were predicted for the best ZINC compounds were performed on the SwissADME web server (<http://www.swissadme.ch/>). The SwissADME server was developed by the Swiss Institute of Bioinformatics and is used to provide physiochemical descriptors, ADMET parameters, pharmacokinetic properties, and drug-like small molecules to support drug discovery.<sup>99</sup> In order to receive each compounds ADMET properties, their respective SMILE codes were inserted into the webserver.

### *3.2.2 Normal Mode Analysis*

The trajectory for the crystal complex (PDB ID: 6PT3) was used in the Normal Mode Wizard in VMD<sup>100</sup> to generate a principal component analysis of the top 10 normal modes.

### *3.2.3 Dynamical Network Model*

A dynamic network model, defined as a set of nodes connected by edges,<sup>97, 101-104</sup> was generated using the individual trajectories of each system using the NetworkView plugin<sup>41</sup> in VMD.<sup>49</sup> We first generated a contact map for each system of the top compounds and the crystal complex that added an edge between nodes whose heavy atoms interacted within a cutoff of 4.5 Å for at least 75% of the MD simulation time. The edge distance was derived from pairwise correlations<sup>103</sup> in the contact map using the program Carma<sup>105</sup>, which defines the probability of information transfer across a given edge using the following equation:

$$C_{ij} = \frac{\langle \Delta \vec{r}_i(t) \cdot \Delta \vec{r}_j(t) \rangle}{(\langle \Delta \vec{r}_i(t)^2 \rangle \langle \Delta \vec{r}_j(t)^2 \rangle)^{1/2}}$$

The edges in the dynamic network model are weighted ( $w_{ij}$ ) between two nodes  $i$  and  $j$  which uses the following calculation:  $w_{ij} = -\log(|C_{ij}|)$ . The weight of the edge is correlated with the probability for information to transfer across the edge between two nodes. Because of this, a thicker edge is characterized as a higher probability of information transfer. The network for each system was further grouped into communities, or subnetworks based on groups of nodes with more frequent and stronger connection to each other, by applying the Girvan-Newman algorithm to the original network.<sup>106</sup> The critical nodes that connect communities to each other were identified as well. Optimal communication paths were generated between the ligand node and the molecular switch residue number using the data from the molecular switches.

### 3.3 Results

#### 3.3.1 *Crystal Conformation Maintained Stability During MD Simulation*

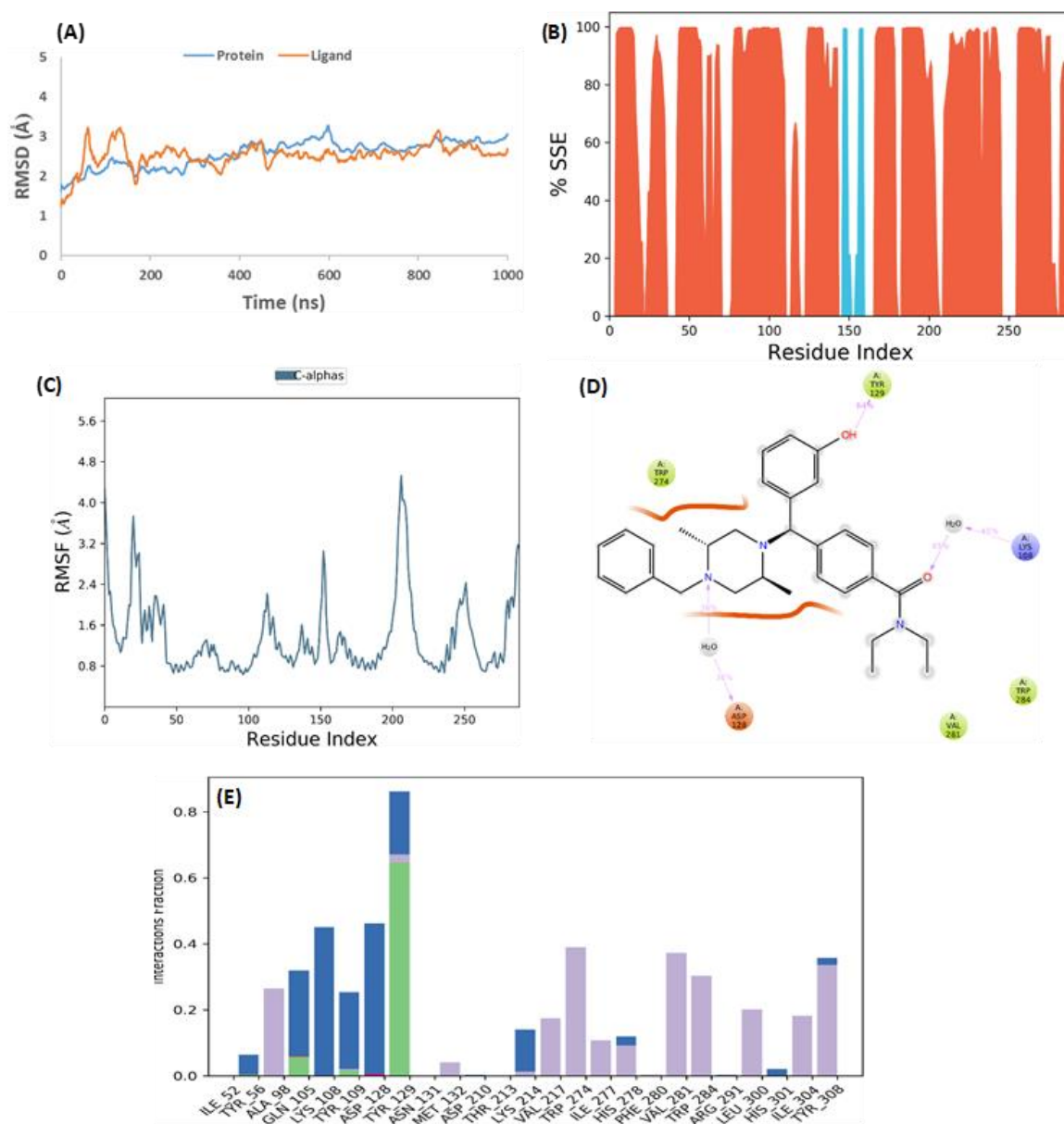
The crystal complex of the active conformation of the human DOR (PDB ID: 6PT3) with crystal agonist DPI-287 was used in the experiment to set the standard serve as the control. DPI-287 was first docked back into the crystal conformation and resulted in a similar binding pose with the crystal pose with a docking score of -8.6 kcal/mol, validating the docking protocol. The docked complex was used as the input structure to perform 1000 ns MD simulations to be further analyzed (Figure 13). First, the RMSD checked for convergence, in which the last 200 ns show the system to have converged with relatively flat plots. The secondary structure elements (SSE) shows the helices were maintained during the simulation. The RMSF shows fluctuation in the intra- and

extracellular loops, as well as the terminals, which are the most flexible parts of the receptor. The 2D ligand-protein interactions shows the residues that interacted with the ligand for at least 30% of the simulation, which shows mostly hydrophobic contacts and some hydrogen bonding. Looking at the protein-ligand histogram shows the interacting residues for the whole simulation. This corresponds with the 2D interactions where most interactions with residues are hydrophobic or hydrogen bonding. Overall, the system was shown to be stable and mimic the crystal structure with a stable binding pose.



**Figure 13**

*Simulation Interaction Diagrams After MD Simulation of the Crystal Structure*



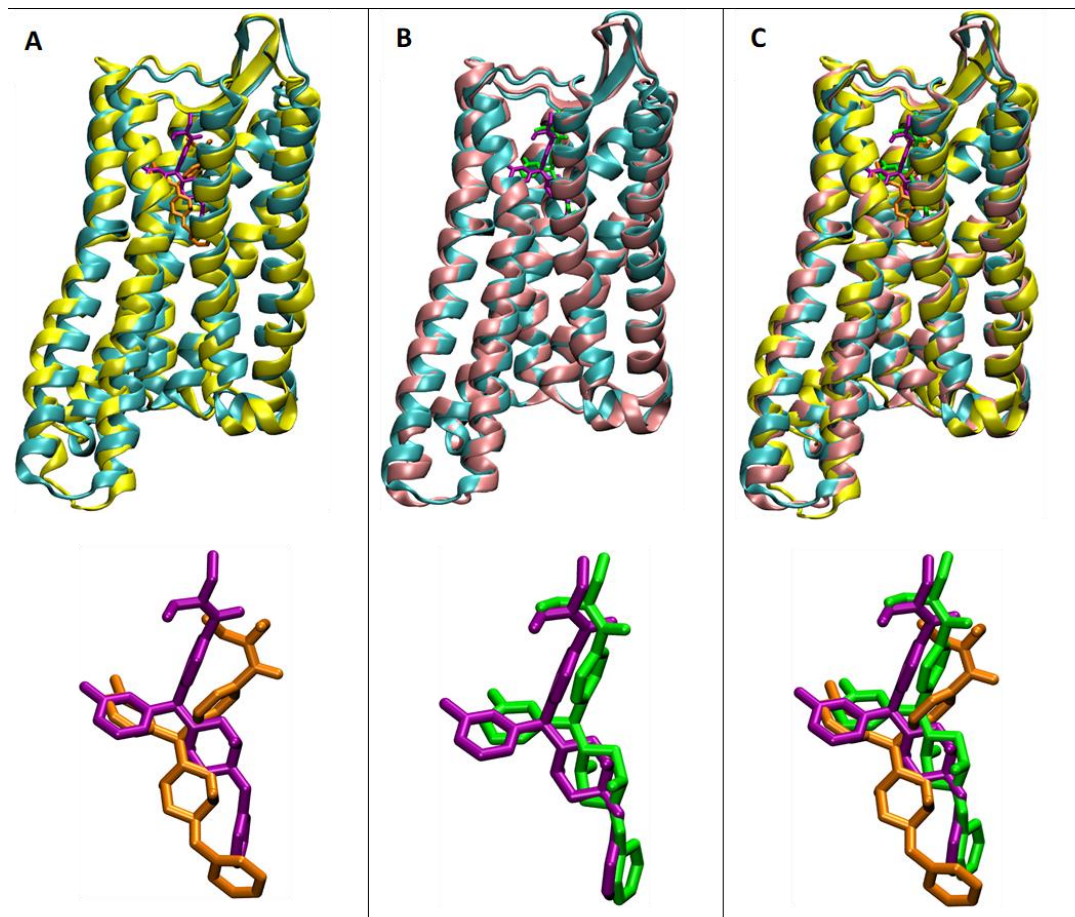
*Note:* (A) RMSD plot from MD simulation of 200ns. (B) Protein Secondary Structure elements (SSE). Orange represents alpha helices, blue represents beta strands. (C) RMSF graph of protein of the crystal complex structure. (D) 2D ligand-protein interaction diagram from the MD trajectory. The residue displayed interacted with ligand for at least 30% of the simulation time. (E) Protein-ligand contacts during MD simulations. Interaction fraction greater than 1 is because of multiple contacts on one residue.

### ***3.3.2 Crystal Complex Produces Other Conformations to Use For HTVS***

The clustering analysis was done after the MD simulation to identify the populated conformation for the trajectory. Each cluster conformation contains a percentage of abundance based on the clustering algorithm in which a cutoff of 2% was used. From this, there were two abundant clusters (75% and 24% respectively) produced from the crystal conformation simulation and were compared to the crystal complex (Figure 14).

**Figure 14**

*Superimposition of the Active Crystal DOR Structure With the Most Abundant Conformations From the MD Simulations With Agonist DPI-287*

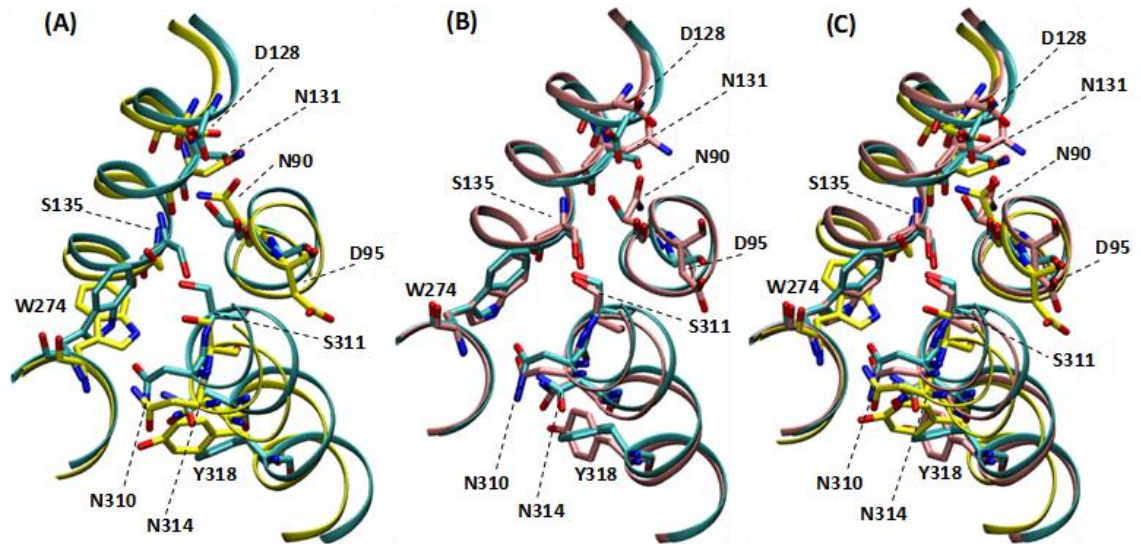


*Note.* (A) DOR crystal conformation superimposed with the first abundant conformation (yellow, 75%) in complex with agonist DPI-287 (orange) including ligand only view; (B) DOR crystal conformation superimposed with the second abundant conformation (pink, 24%) in complex with agonist DPI-287 (green) including ligand only view; (C) DOR crystal conformation superimposed with both abundant clusters and all ligand poses.

The two clusters slightly differ in conformation and the ligand binding pose from the crystal conformation. In a more precise view, the binding pocket of each structure was compared to the crystal pose (Figure 15).

## Figure 15

### *Predicted Binding Pocket of the Different DOR Conformations*



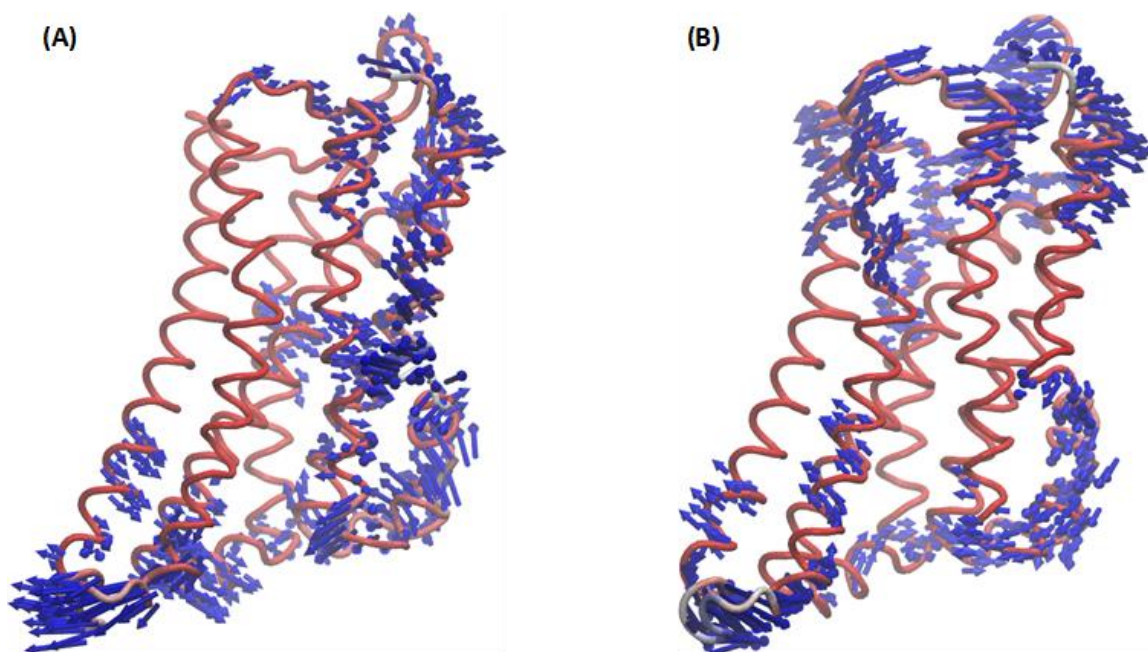
*Note.* Structural alignment of crystal conformation (cyan) with (A) representative conformation 1, (B) representative conformation 2, (C) both conformations.

In this view, differences can be seen in the receptor itself and also the side chains that have adopted different rotamer states. Specific residues where the side chains differ the most from the crystal in both clusters are N90, D95, D128, N131, N310, and Y318.

Using the normal mode analysis on the crystal MD simulation revealed the top two low frequency vibrational modes differ from each other (Figure 16).

## Figure 16

### *Top 2 Low Frequency Vibrational Modes From the Normal Mode Analysis*



*Note* Based on the MD simulation of the crystal conformation of the active DOR in complex with agonist DPI-287. **(A)** Mode 1; **(B)** Mode 2.

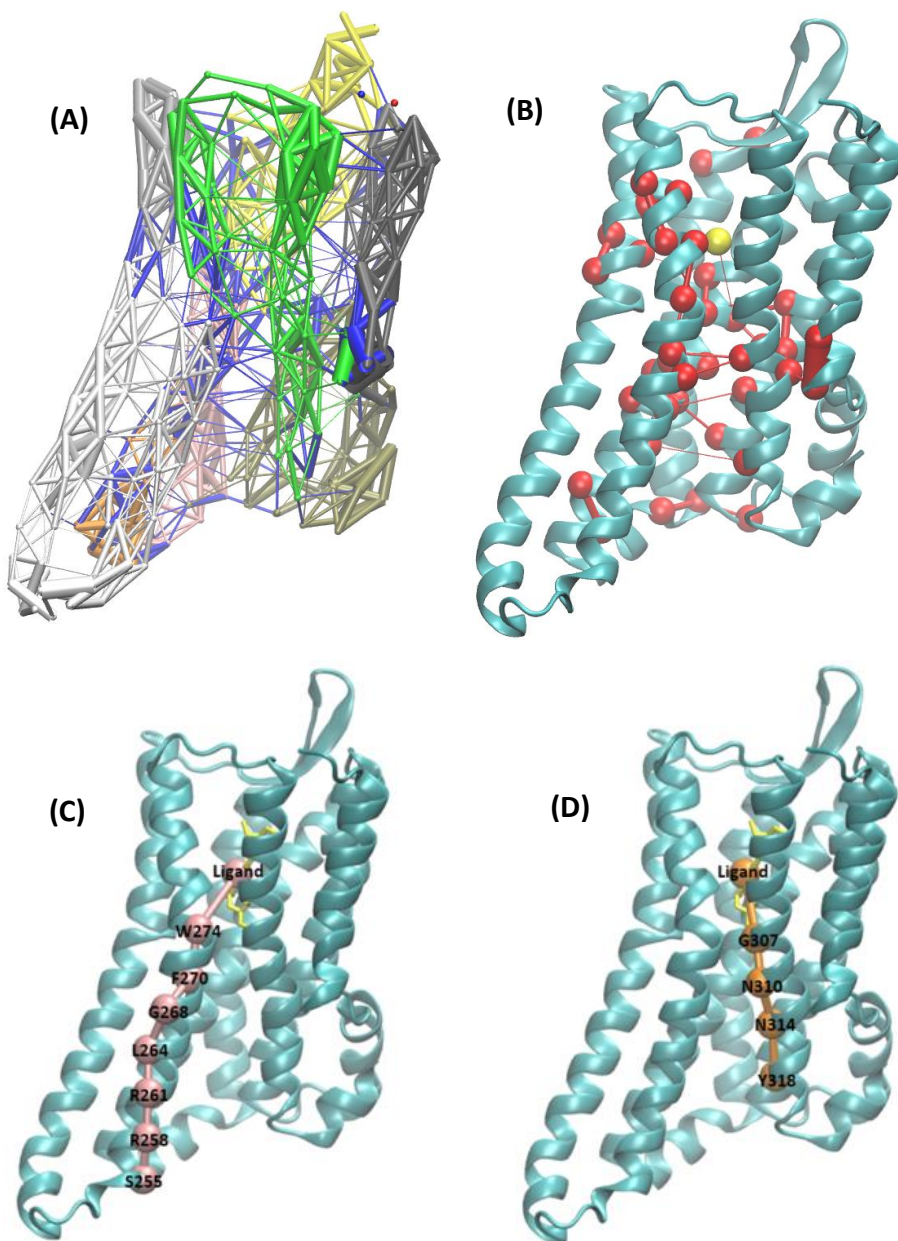
This further validates the result of two cluster conformations that differ from the crystal conformation and therefore can be used as additional conformations to use for HTVS. Unweighted and weighted dynamic network models of the DPI-287/DOR system were calculated as described in the methods section to decipher the allosteric signal transmission pathway. The unweighted network model shows that their connections are in good agreement. Quantifying the correlation between the nodes in the weighted network model reveals the areas of the receptor that are in higher correlation to each other. The system appears to have higher correlations between edges TM5 and TM6. A community network model was generated using the weighted network model which



grouped residues together that interact more frequently and stronger than to residues in other communities (Figure 17).

**Figure 17**

*Network Analysis*



There were 38 critical nodes identified for the crystal system from the community analysis. These critical nodes were involved in signal transduction between different parts of the receptor throughout the simulation and therefore, the critical residue information was then cross referenced with experimentally reported mutagenesis data available on the G-protein coupled receptor databank (GPCRdb) to see if the residues were involved in the physical signal transduction. The DPI-287 system had 9 critical residues that were also naturally occurring mutations (D95, Y129, M132, M142, R160, M186, A269, I282, N310). It also had 3 critical residues that were mutations invitro (D95, W274, S312). Optimal paths generated for the DPI-287/DOR system give insight into the molecular signal transduction pathways involving the ligand. From the weighted network models, the shortest pathways able to pass a signal from the ligand to the site of the molecular switch (Tyrosine Toggle Switch: Y318) and the intracellular end of TM6 (Transmission Switch: S255) were calculated as the optimal paths. DPI-287 has a direct optimal path for the Transmission Switch (CWXP) through TM6 and another direct path for the Tyrosine Toggle Switch (NPXXY) through TM7. The HTVS was then ran on all three conformations (crystal conformation, cluster 1, cluster 2) of the active DOR for FDA approved drugs and compounds from the zinc15 database of 17 million compounds. Comparing the zinc compounds to the FDA approved drugs revealed that the zinc compounds had significantly better docking scores, therefore, ruling out the use of the FDA drugs. Each compound was docked back into the DOR binding pocket and had similar poses to the crystal ligand. Using the docking score of the crystal ligand DPI-287 as a cutoff (-8.6 kcal/mol), the number of stars which tells how drug-like a compound is, and the cluster ID which tells how similar molecule scaffolds are to each other, a total of

69 zinc compounds were chosen. These docked compounds also showed good binding pose agreement with the crystal ligand. Out of the 69 compounds chosen, 32 were targeted to the crystal conformation, 11 were targeted to the first abundant cluster, and 26 were targeted to the second abundant cluster. Each of the 69 compounds underwent 200 ns MD simulations. The MM-GBSA was calculated for each of the molecules to their respective receptor conformation, including the crystal ligand DPI-287, to determine the binding affinity for the receptor with more negative values indicating better binding (Table B1). DPI-287 had an MM-GBSA of -90.2 kcal/mol which was used as the cutoff. With the MM-GBSA as a determinate, another method was used to pick out the top molecules, the SwissADME properties (Table B2). This tells the drugs predicted properties in which high gastrointestinal (GI) absorption and blood brain barrier (BBB) permeability were the major determinates. Also similar to the crystal ligand, having no alerts was attractive as well due to having a low chance of false positives from occurring. Considering all of this, 8 ligands were chosen as the top compounds (Table 5, Table 6). Two of the molecules were targeting the crystal conformation, four were targeting the first abundant cluster, and two were targeting the second abundant cluster. These 8 compounds were further analyzed.



**Table 5**

*Various Properties of the Top 8 Compounds Identified From Our Virtual Screening Workflow*

Receptor Structure	#	ZINC ID	Docking Score (kcal/mol)	VDW (kcal/mol)	ELE (kcal/mol)	Hydrophobic (kcal/mol)	MM-GBSA (kcal/mol)	Receptor RMSD <sup>1</sup> (Å)	Ligand RMSD <sup>1</sup> (Å)
	Ref.	<i>Crystal ligand (6PT3): DPI-287</i>	-8.6	-57.0±2.8	18.5±3.7	-51.7±3.5	-90.2±6.3	2.9±0.1	2.5±0.1
CC	1	ZINC000020559278	-9.9	-44.7±2.8	-31.3±3.7	-40.8±2.3	-116.9±5.0	2.2±0.1	2.5±0.3
CC	17	ZINC000078515864	-8.9	-36.2±3.8	-25.9±5.3	-50.9±2.9	-113.1±6.1	2.6±0.1	2.7±0.2
C1	1	ZINC000025329384	-10.2	-57.2±3.6	-19.9±9.4	-57.7±4.1	-134.9±11.3	2.4±0.1	2.9±0.4
C1	2	ZINC000037556415	-9.4	-58.5±2.4	-9.6±2.3	-43.8±2.6	-111.9±5.1	3.4±0.2	6.0±0.1
C1	6	ZINC000827360794	-9.1	-43.7±3.5	-18.8±8.4	-41.6±2.8	-104.2±11.1	2.4±0.1	2.9±0.1
C1	9	ZINC000078648574	-9.0	-50.4±5.2	-4.1±3.5	-54.1±6.5	-108.7±13.1	2.8±0.1	6.3±0.5
C2	1	ZINC000057999653	-10.1	-47.1±4.1	-8.6±13.5	-38.9±2.4	-94.6±10.9	2.3±0.1	2.7±0.2
C2	5	ZINC000006664413	-9.8	-46.4±2.8	-20.1±7.0	-43.4±3.2	-109.9±8.9	2.6±0.1	3.6±0.3

**Table 6**

*The Predicted Pharmacokinetics ADME Properties*

Compound	GI absorption	BBB permeant	CYP1A2	CYP2C19	CYP2C9	CYP2D6	CYP3A4	Lipinski rule	PAINS	Brenk
Crystal Structure (PDB ID:6PT3)	High	Yes	No	No	No	Yes	Yes	Yes; 0 violation	0 alert	0 alert
ZINC000020559278	High	Yes	Yes	No	No	Yes	Yes	Yes; 0 violation	0 alert	0 alert
ZINC000078515864	High	Yes	No	No	No	Yes	No	Yes; 0 violation	0 alert	0 alert
ZINC000025329384	High	Yes	No	No	No	Yes	Yes	Yes; 0 violation	0 alert	0 alert
ZINC000037556415	High	Yes	No	Yes	Yes	Yes	Yes	Yes; 0 violation	0 alert	0 alert
ZINC000827360794	High	Yes	No	No	No	Yes	Yes	Yes; 0 violation	0 alert	0 alert
ZINC000078648574	High	Yes	No	Yes	Yes	Yes	No	Yes; 0 violation	0 alert	0 alert
ZINC000057999653	High	Yes	Yes	Yes	Yes	Yes	Yes	Yes; 0 violation	0 alert	0 alert
ZINC000006664413	High	Yes	Yes	Yes	Yes	Yes	Yes	Yes; 0 violation	0 alert	0 alert

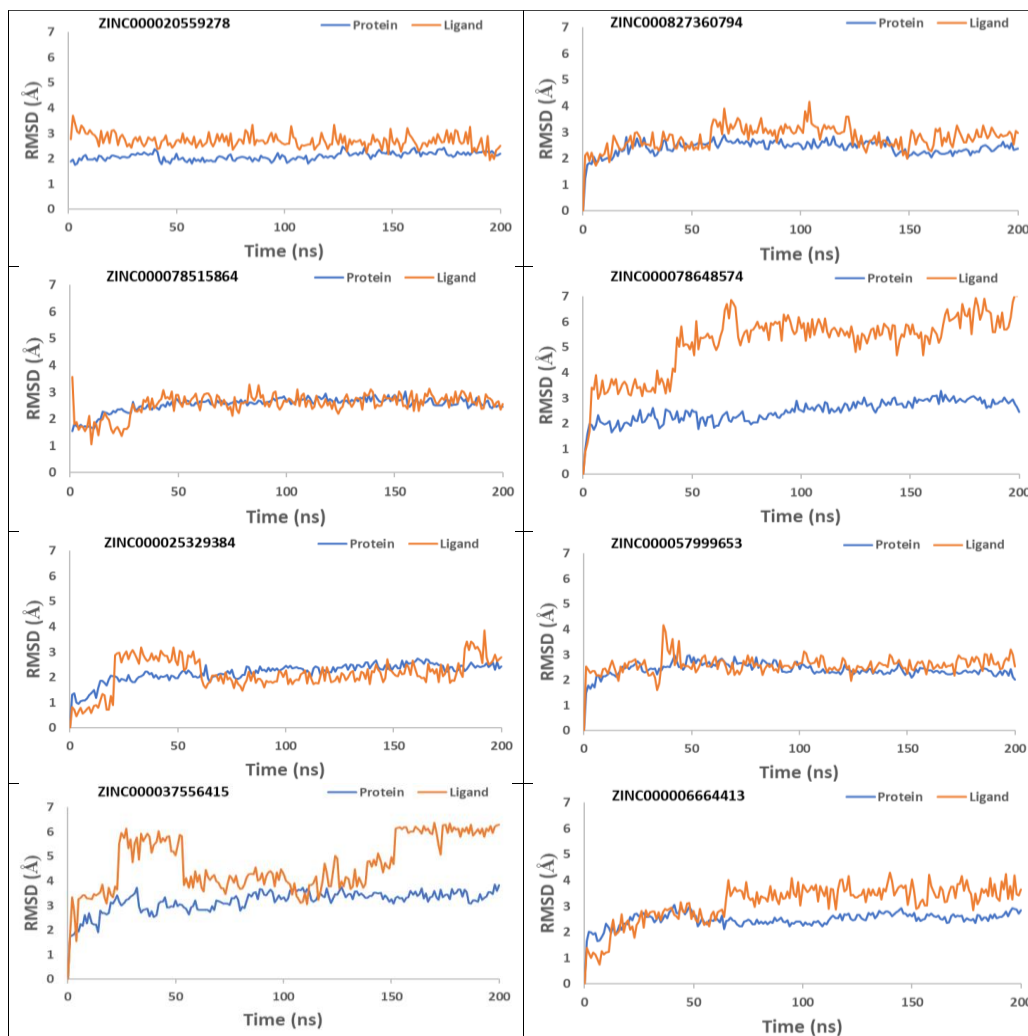
### 3.3.3 Top 8 Compounds Assume Steady State

Each zinc compound was calculated for the RMSD of their respective simulations to check the convergence and if it has reached a steady state (Figure 18). The RMSD analyzes the movement of the ligand the receptor during the simulation. In the case of all 8 compounds, it can be observed by the last 50 ns that they have converged by approaching steady values. The protein RMSD has lower RMSD values and have

remained more stable in each of the complexes. The ligand RMSD indicated compounds in which there are multiple fluctuations such as ZINC000025329384, ZINC000037556415, and ZINC000078648574. The others remained more stable throughout the simulation.

**Figure 18**

*RMSD of the Top 8 Zinc Compounds*



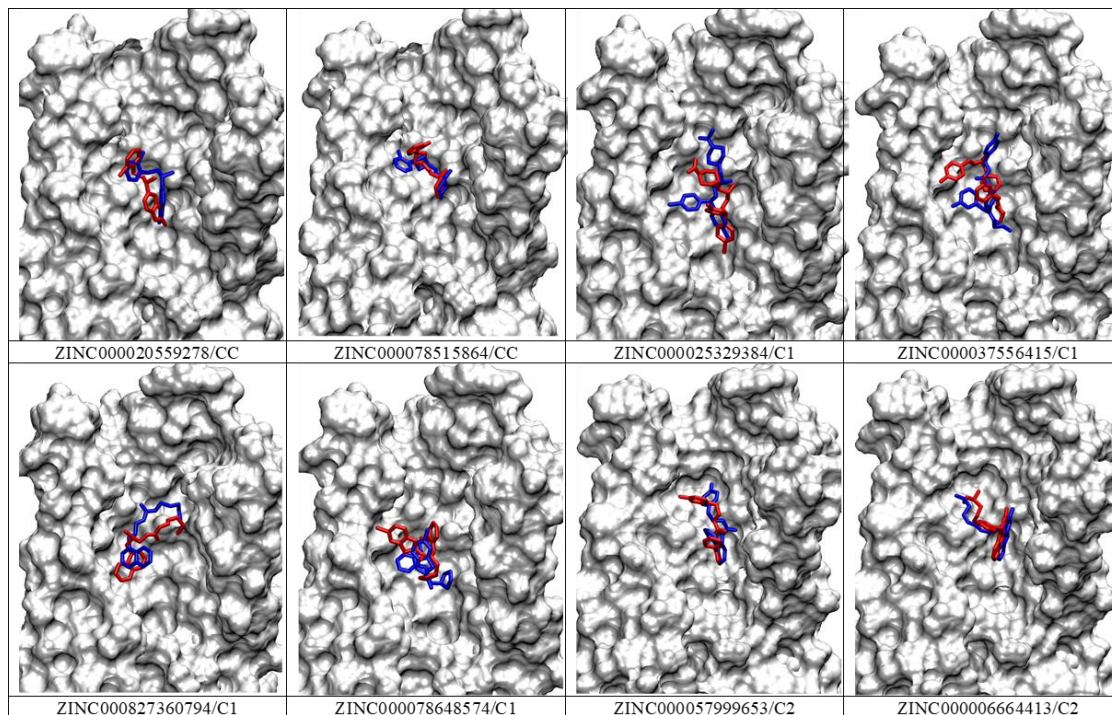
*Note:* C $\alpha$  RMSD during 200 ns MD simulation in reference to the crystal active DOR conformation (PDB ID: 6PT3).

### ***3.3.4 MD Simulations Improved the Binding Pose of the Top Eight Ligands***

The Glide XP docking pose of each of the ligands were superimposed and compared to the pose from the MD simulation (Figure 19). The simulation can significantly alter the ligands original bound conformation to optimize the interactions with the receptor. The simulation improved the binding pose of each of the top compounds. This corresponds with the MM-GBSA results (Table 5) that was used to estimate the binding free energy of the compounds where the binding interaction between the protein-ligand complexes is specified by the free energy binding. The crystal ligand was used as a control where its score was -90.2 kcal/mol. The top compounds picked had significantly higher binding energy to the DOR with the lowest of the scores being -94.6 kcal/mol.

**Figure 19**

*Comparison of Glide XP Docking Pose (Blue) and MD Simulation Pose (Red) for the Top 8 Compounds*



### ***3.3.5 Protein-Ligand Interactions of Top Compounds to the DOR***

The residues involved in the compounds binding to the receptor were analyzed as described in the methods section with the Desmond Simulation Interaction Diagram. All interacting residues to the top 8 compounds and crystal ligand are clearly tabulated in Table 7.

**Table 7**

*Protein-Ligand Interactions During MD Simulations for the Top 8 Compounds From the MD Simulations*

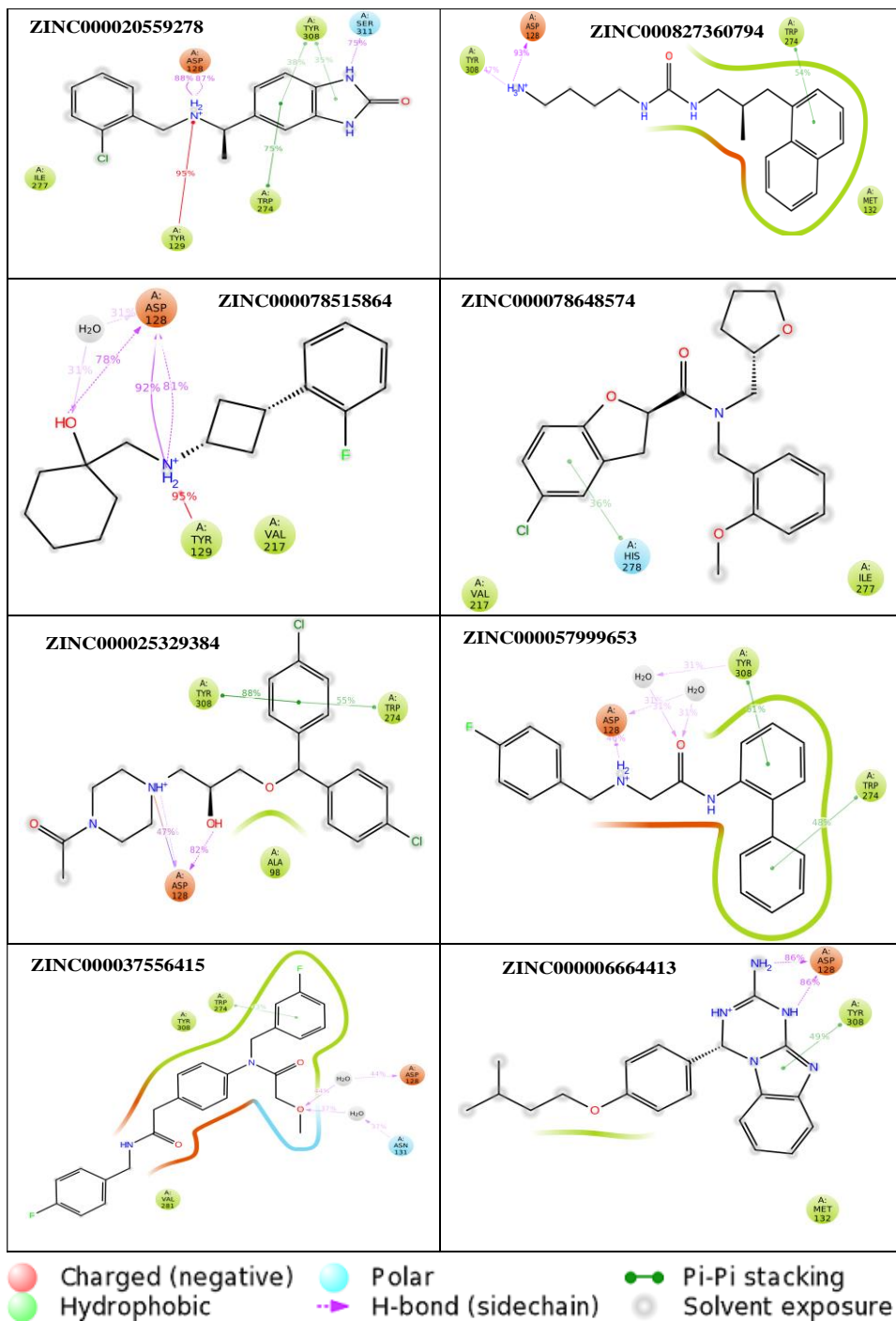
Ref Comp	ZINC20559278	ZINC78515864	ZINC25329384	ZINC37556415	ZINC827360794	ZINC78648574	ZINC57999653	ZINC6664413
ILE 52								
TYR 56							TYR 56	TYR 56
				ALA 94				
ALA 98	ASP 95 ALA 98		ALA 98	ALA 98			ALA 98	ALA 98
					THR 101 LEU 102			THR 101
GLN 105		GLN 105	GLN 105	GLN 105	GLN 105		GLN 105	GLN 105
LYS 108				LYS 108	LYS 108		LYS 108	LYS 108
TYR 109								
					VAL124 LEU 125		VAL124	VAL124 LEU 125
ASP 128	ILE 127 ASP 128	ASP 128	ASP 128	ASP 128	ASP 128		ASP 128	ASP 128
TYR 129	TYR 129	TYR 129	TYR 129	TYR 129	TYR 129	TYR 129	TYR 129	
ASN 131	ASN 131		ASN 131	ASN 131	ASN 131			
MET 132	MET 132 SER 135	MET 132	MET 132	MET 132	MET 132	MET 132	MET 132	MET 132
						ILE 136	SER 135 ILE 136	
ASP 210								
THR 213				THR 213				
LYS 214	LYS 214	LYS 214		LYS 214	LYS 214	LYS 214		
VAL 217	VAL 217	VAL 217 PHE 218	VAL 217	VAL 217	VAL 217	VAL 217	VAL 217	VAL 217
					ALA 221 PHE 270	ALA 221		
TRP 274	TRP 274	TRP 274	TRP 274	TRP 274	TRP 274	TRP 274	TRP 274	TRP 274
ILE 277	ILE 277	ILE 277	ILE 277	ILE 277	ILE 277	ILE 277	ILE 277	ILE 277
HIS 278	HIS 278	HIS 278		HIS 278	HIS 278	HIS 278	HIS 278	
PHE 280		PHE 280						PHE 280
VAL 281	VAL 281	VAL 281		VAL 281			VAL 281	VAL 281
				ILE 282 TRP 284				
TRP 284		TRP 284						TRP 284
ARG 291								
LEU 300		LEU 300		LEU 300		LEU 300		LEU 300
HIS 301				HIS 301			HIS 301	
ILE 304	ILE 304	ILE 304	ILE 304	ILE 304	ILE 304	ILE 304	ILE 304	ILE 304
	GLY 307			GLY 307				CYS 303 ILE 304
TYR 308	TYR 308 SER 311	TYR 308	TYR 308	TYR 308	TYR 308	TYR 308	TYR 308	TYR 308
				SER 311		SER 311		

The highest amount of hydrogen bonding was in compounds ZINC000078515864, ZINC000006664413, and ZINC000020559278. ASP128 is the main residue involved in hydrogen bonding in seven of the eight compounds and is also maintained in the crystal ligand (Figure 20). ZINC000037556415, ZINC000827360794, ZINC000078648574, ZINC000057999653, and ZINC000006664413 have the highest number of hydrophobic contacts which the interaction of such generally involves hydrophobic amino acids and an

aromatic or aliphatic group on the ligand. Ionic interactions were mainly observed in ZINC000025329384 and ZINC000057999653. Water bridges occurred in all top 8 compounds with the exception of ZINC000078648574 which is the same compound that did not show hydrogen bonding to residue ASP128. The majority of the compounds showed higher hydrophobic interactions and hydrogen bonding in comparison to the crystal structure, leading to higher GI absorption.

**Figure 20**

*Protein-Ligand 2D Interaction Diagrams From the MD Simulation for the Top 8 Compounds*



### ***3.3.6 Secondary Structure Shows Maintained Helices***

The protein SSE was monitored throughout the MD simulation where the plots summarize the structure elements distribution by residue position throughout the protein. The three categories are Alpha-helices, Beta-strands, and random coils. Alpha-helices are mainly made up of hydrophobic residues that are located in the core of the protein and are depicted by the orange sections. Beta-strands, however, contain both hydrophobic and polar amino acids which are depicted by blue sections. The random coil is not one specific shape of a polymer conformation, but a distribution of statistics of all chains depicted by the white spaces in the plots. The secondary structure is more rigid than the loop regions, inferring that they have less fluctuation.

### ***3.3.7 RMSF Shows Fluctuation in Regions of the Protein With Respect to the Ligand***

The RMSF calculated the fluctuation of the protein in complex with each compound using the C $\alpha$  atom. Specifically, the changes in the protein backbone were observed during the simulation (Figure B9). Higher values depicted by peaks are areas of the protein that fluctuate the most, such as the N- and C-terminals as well as the intra- and extracellular loops. ZINC000037556415 showed the greatest fluctuation at nearly 5Å around residue 200 which is located in extracellular loop 2. All compounds showed similar fluctuation at the same residue positions between 1-3Å. A small fluctuation from ZINC000078648574 and ZINC000020559278 was observed around residue 250. Using the crystal structure as a positive control, each complex showed the same or higher residual fluctuation throughout the simulations.



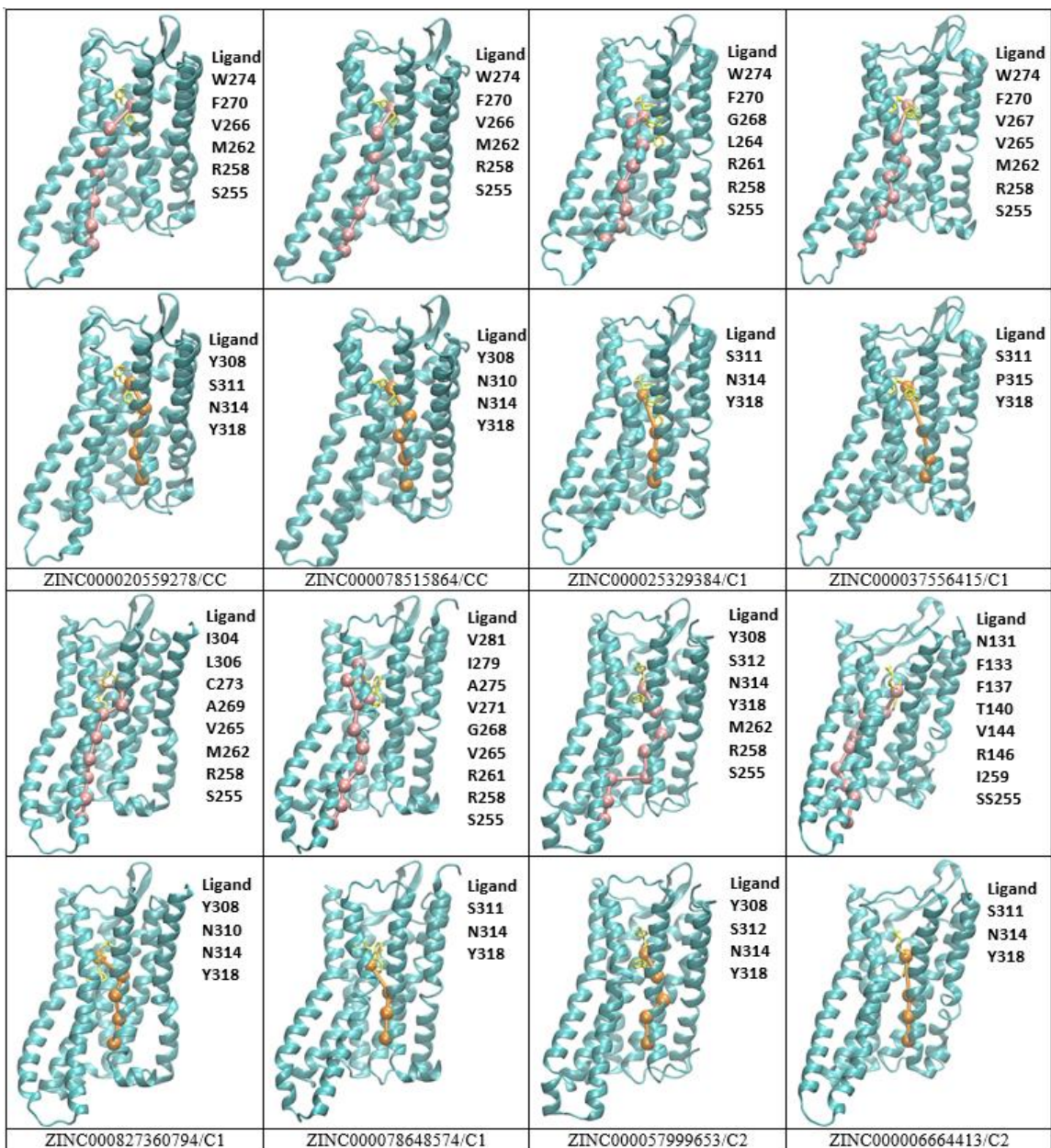
### ***3.3.8 Network Analysis Helped to Understand Communications Among Different Regions of the DOR***

Unweighted and weighted network models of the DPI-287/DOR system and the top compound systems were calculated as described in the methods section to decipher the allosteric signal transmission pathway. The comparison of the unweighted network models between the systems show that their connections are in good agreement. Quantifying the correlation between the nodes in the weighted network model reveals similarities observed between the systems. All systems appear to have higher correlations between edges TM5 and TM6. Community network models were generated using the weighted network model which grouped residues together that interact more frequently and stronger than to residues in other communities. The systems that seem to communicate more similarly to the crystal complex are ZINC000020559278, ZINC000078515864, ZINC000827360794, ZINC000078648574, ZINC000057999653, and ZINC000006664413. The basis for the similarity is that the intracellular portion of TM5 and TM6 are in the same community represented by one single color. Another thing that was observed in most of the similar systems is that the extracellular portion of TM6 and TM7 belong to the same community while the same region in TM5 belongs to a different community. This trend occurred in ZINC000078515864, ZINC000827360794, and ZINC000078648574. The systems that had the most similarities in critical nodes with the crystal system are ZINC000020559278 with 11 of the same critical nodes, ZINC000078515864 with 13, and ZINC000078648574 with 11 (Table B3). When calculating the optimal paths of the Transmission and Toggle Switch for each of the top compounds, multiple systems showed great similarities to the crystal complex (Figure 21 & Table B4). ZINC000025329384 shared every residue as the crystal with the

Transmission Switch pathway and two out of the four residues of the Toggle Switch pathway. ZINC000020559278, ZINC000078515864, and ZINC000037556415 also had many similar residues to the crystal complex with the Transmission Switch and Toggle Switch. ZINC000827360794 had the most residues similar to the crystal with the Toggle Switch.

**Figure 21**

*Optimal Signal Transduction Pathway of the Transmission Switch and the Toggle Switch*



*Note:* Transmission switch (pink nodes) and the Toggle switch (orange nodes) starting from the ligand of each of the top 8 compounds.

### 3.4 Discussion

The opioid epidemic has brought to light of the need for better opioid alternatives in public health all around the world. The continued rise of opioid addiction and overdose will not stop until there are better therapeutic agents available. Researchers and scientists have discovered that the DOR shows potential in not only pain management, but also in neurological and psychiatric disorders. Agonists targeting the DOR are strongly believed to not display addictive or dependence properties, such as MOR agonists, having the potential to help combat the addictive opioid crisis today.

Though previous studies have been done on the DOR, none to our best knowledge have ever utilized multiple conformations from MD simulations for HTVS. MD simulations are able to probe deeper into interactions and dynamics that happen in a system that cannot be obtained from a crystal structure alone. Sampling the conformations from the active state DOR and using them for HTVS offers an opportunity to find better potential agonists to be of therapeutic use. Running long MD simulations on each of the top compounds takes it a step further by predicting if the compounds bound to the DOR will remain stable and looking into any protein-ligand interactions that may occur. Here we present the first study using ensemble-based HTVS to discover potential agonists to target the DOR.

Based on our findings using the bioinformatics tools and drug similarity search, we analyzed compounds from Zinc15 and targeted novel agonists of the DOR using the virtual screening workflow which gave us a promising top 69 hits (32 from crystal conformation, 11 from cluster conformation 1, and 26 from cluster conformation 2).

These top 69 compounds were then further validated and compressed to eight of the agonists, which were further validated by the MM-GBSA score of binding free energy, MD simulation, and predicted drug ADME properties. The MM-GBSA score helped to investigate the binding interaction between the ligands and protein. The predicted drug ADME properties helped to specify if the compounds were highly (GI) absorbent as well as BBB permeant. These were the properties most valued due to opioids coming in an oral form and the receptors being located in areas of the brain. Without these specific properties, the compounds could be ruled out.

The protein-ligand interaction further confirmed the top potential agonists. The large dataset and extended HTVS method portray the best interactions between ligands to form a complex with a molecular target. The adverse effects and related articles of the selected compounds were checked through CAS Scifinder and PubChem, where the compounds showed no adverse effects. Out of the top eight, ZINC000057999653 is patented to be useful for altering the lifespan of eukaryotic organisms. These results further validate the top hits to be potential agonists.

The use of dynamic network models based on MD simulations data has shown to be efficient in extracting correlated motions, allosteric signals, and signal transduction networks within complex systems. The correlated motions are thought to be linked to their activity which is normally difficult to accurately distinguish through visualization of the MD simulations alone.<sup>107, 108</sup> In addition, the communities that are generated with the dynamic network are highly correlated and provide insight into the overall communication network from ligand binding.<sup>107, 109, 110</sup> In our study, the dynamic network analysis aided in identifying similar communication systems between the crystal DPI-287

and top compound systems. These similarities became more apparent when comparing the weighted networks that base their correlated motion in the simulation trajectories to the connections between nodes in the networks. The community models show that compound systems of ZINC000078515864, ZINC000827360794, and ZINC000078648574 communicate the most similar to the DPI-287 system. This analysis highlights how the structural differences of the ligands can have similar or different dynamics to the DOR due to the grouping of communities based on residues that interact strongly and frequently with one another.

Based on the results, the potential binding and agonistic effects of the top eight compounds are indicated. Ensemble-based structure HTVS is a useful approach to find potential molecules that could target the binding pocket of the DOR. After examining 17 million Zinc15 compounds using structure-based HTVS methods, the most potential hits were validated by MD simulations. This study has the potential to assist in the efforts to aid in the opioid epidemic. Experimental studies can be conducted on these compounds to help in the efforts of opioid addiction.

## References

1. Macalino, S. J. Y.; Gosu, V.; Hong, S.; Choi, S., Role of computer-aided drug design in modern drug discovery. *Archives of Pharmacal Research* **2015**, *38* (9), 1686-1701.
2. Iskar, M.; Zeller, G.; Zhao, X.-M.; van Noort, V.; Bork, P., Drug discovery in the age of systems biology: the rise of computational approaches for data integration. *Current Opinion in Biotechnology* **2012**, *23* (4), 609-616.
3. Singh, D. B., Success, Limitation and Future of Computer Aided Drug Designing. *Translational Medicine* **2014**, *04*.
4. Lionta, E.; Spyrou, G.; Vassilatis, D. K.; Cournia, Z., Structure-based virtual screening for drug discovery: principles, applications and recent advances. *Curr Top Med Chem* **2014**, *14* (16), 1923-1938.
5. Rodrigues, T.; Schneider, G., Flashback Forward: Reaction-Driven De Novo Design of Bioactive Compounds. *Synlett* **2013**, *25*.
6. Aparoy, P.; Reddy, K. K.; Reddanna, P., Structure and ligand based drug design strategies in the development of novel 5- LOX inhibitors. *Curr Med Chem* **2012**, *19* (22), 3763-3778.
7. Salmaso, V.; Moro, S., Bridging Molecular Docking to Molecular Dynamics in Exploring Ligand-Protein Recognition Process: An Overview. *Front Pharmacol* **2018**, *9*, 923-923.
8. Muhammed, M. T.; Aki-Yalcin, E., Homology modeling in drug discovery: Overview, current applications, and future perspectives. *CHEMICAL BIOLOGY & DRUG DESIGN* **2019**, *93* (1), 12-20.
9. Xiang, Z. X., Advances in homology protein structure modeling. *CURRENT PROTEIN & PEPTIDE SCIENCE* **2006**, *7* (3), 217-227.
10. Hospital, A.; Goñi, J. R.; Orozco, M.; Gelpí, J. L., Molecular dynamics simulations: advances and applications. *Adv Appl Bioinform Chem* **2015**, *8*, 37-47.
11. Greenidge, P.; Kramer, C.; Mozziconacci, J.-C.; Wolf, R., MM/GBSA Binding Energy Prediction on the PDBbind Data Set: Successes, Failures, and Directions for Further Improvement. *Journal of chemical information and modeling* **2012**, *53*.
12. Zhang, X.; Perez-Sanchez, H.; Lightstone, F. C., A Comprehensive Docking and MM/GBSA Rescoring Study of Ligand Recognition upon Binding Antithrombin. *Curr Top Med Chem* **2017**, *17* (14), 1631-1639.

13. Shang, Y.; LeRouzic, V.; Schneider, S.; Bisignano, P.; Pasternak, G. W.; Filizola, M., Mechanistic Insights into the Allosteric Modulation of Opioid Receptors by Sodium Ions. *Biochemistry* **2014**, *53* (31), 5140-5149.
14. Ritter, S. L.; Hall, R. A., Fine-tuning of GPCR activity by receptor-interacting proteins. *Nature Reviews Molecular Cell Biology* **2009**, *10* (12), 819-830.
15. Chan, A. S. L.; Law, P. Y.; Loh, H. H.; Ho, P. N. N.; Wu, W. M.; Chan, J. S. C.; Wong, Y. H., The first and third intracellular loops together with the carboxy terminal tail of the delta-opioid receptor contribute toward functional interaction with G alpha(16). *Journal of Neurochemistry* **2003**, *87* (3), 697-708.
16. Toll, L.; Bruchas, M. R.; Calo, G.; Cox, B. M.; Zaveri, N. T., Nociceptin/Orphanin FQ Receptor Structure, Signaling, Ligands, Functions, and Interactions with Opioid Systems. *Pharmacological reviews* **2016**, *68* (2), 419-57.
17. Gallantine, E. L.; Meert, T. F., Antinociceptive and Adverse Effects of mu- and kappa-Opioid Receptor Agonists: A Comparison of Morphine and U50488-H. *Basic & Clinical Pharmacology & Toxicology* **2008**, *103* (5), 419-427.
18. Meert, T. F.; Vermeirsch, H. A., A preclinical comparison between different opioids: antinociceptive versus adverse effects. *Pharmacology Biochemistry and Behavior* **2005**, *80* (2), 309-326.
19. Land, B. B.; Bruchas, M. R.; Lemos, J. C.; Xu, M.; Melief, E. J.; Chavkin, C., The dysphoric component of stress is encoded by activation of the dynorphin kappa-opioid system. *Journal of Neuroscience* **2008**, *28* (2), 407-414.
20. Knoll, A. T.; Carlezon, W. A., Dynorphin, stress, and depression. *Brain Research* **2010**, *1314*, 56-73.
21. Hudzik, T. J.; Maciag, C.; Smith, M. A.; Caccese, R.; Pietras, M. R.; Bui, K. H.; Coupal, M.; Adam, L.; Payza, K.; Griffin, A.; Smagin, G.; Song, D.; Swedberg, M. D. B.; Brown, W., Preclinical Pharmacology of AZD2327: A Highly Selective Agonist of the delta-Opioid Receptor. *Journal of Pharmacology and Experimental Therapeutics* **2011**, *338* (1), 195-204.
22. Saitoh, A.; Sugiyama, A.; Yamada, M.; Inagaki, M.; Oka, J. I.; Nagase, H.; Yamada, M., The novel delta opioid receptor agonist KNT-127 produces distinct anxiolytic-like effects in rats without producing the adverse effects associated with benzodiazepines. *Neuropharmacology* **2013**, *67*, 485-493.
23. Gotoh, L.; Saitoh, A.; Yamada, M.; Fujii, H.; Nagase, H.; Yamada, M., Effects of repeated treatment with a delta opioid receptor agonist KNT-127 on hyperemotionality in olfactory-bulbectomized rats. *Behavioural Brain Research* **2017**, *323*, 11-14.



24. Nozaki, C.; Nagase, H.; Nemoto, T.; Matifas, A.; Kieffer, B. L.; Gaveriaux-Ruff, C., In vivo properties of KNT-127, a novel delta opioid receptor agonist: receptor internalization, antihyperalgesia and antidepressant effects in mice. *British Journal of Pharmacology* **2014**, *171* (23), 5376-5386.
25. Corporation, A., Adolor Corporation Provides Update on R&D Programs. *FierceBiotech* **2008**.
26. Aburi, M.; Smith, P. E., Modeling and simulation of the human delta opioid receptor. *Protein Science* **2004**, *13* (8), 1997-2008.
27. Johnston, J. M.; Aburi, M.; Provasi, D.; Bortolato, A.; Urizar, E.; Lambert, N. A.; Javitch, J. A.; Filizola, M., Making Structural Sense of Dimerization Interfaces of Delta Opioid Receptor Homodimers. *Biochemistry* **2011**, *50* (10), 1682-1690.
28. Claff, T.; Yu, J.; Blais, V.; Patel, N.; Martin, C.; Wu, L.; Han, G. W.; Holleran, B. J.; Van der Poorten, O.; White, K. L.; Hanson, M. A.; Sarret, P.; Gendron, L.; Cherezov, V.; Katritch, V.; Ballet, S.; Liu, Z.-J.; Müller, C. E.; Stevens, R. C., Elucidating the active  $\delta$ -opioid receptor crystal structure with peptide and small-molecule agonists. *Sci Adv* **2019**, *5* (11), eaax9115-eaax9115.
29. Zhou, Q.; Yang, D.; Wu, M.; Guo, Y.; Guo, W.; Zhong, L.; Cai, X.; Dai, A.; Jang, W.; Shakhnovich, E. I.; Liu, Z.-J.; Stevens, R. C.; Lambert, N. A.; Babu, M. M.; Wang, M.-W.; Zhao, S., Common activation mechanism of class A GPCRs. *Elife* **2019**, *8*, e50279.
30. Waterhouse, A. M.; Procter, J. B.; Martin, D. M. A.; Clamp, M.; Barton, G. J., Jalview Version 2—a multiple sequence alignment editor and analysis workbench. *Bioinformatics* **2009**, *25* (9), 1189-1191.
31. Edgar, R. C., MUSCLE: a multiple sequence alignment method with reduced time and space complexity. *BMC Bioinformatics* **2004**, *5*, 113-113.
32. Magrane, M.; Consortium, U., UniProt Knowledgebase: a hub of integrated protein data. *Database (Oxford)* **2011**, *2011*, bar009.
33. Granier, S.; Manglik, A.; Kruse, A. C.; Kobilka, T. S.; Thian, F. S.; Weis, W. I.; Kobilka, B. K., Structure of the delta-opioid receptor bound to naltrindole. *Nature* **2012**, *485* (7398), 400-U171.
34. Huang, W.; Manglik, A.; Venkatakrishnan, A. J.; Laeremans, T.; Feinberg, E. N.; Sanborn, A. L.; Kato, H. E.; Livingston, K. E.; Thorsen, T. S.; Kling, R. C.; Granier, S.; Gmeiner, P.; Husbands, S. M.; Traynor, J. R.; Weis, W. I.; Steyaert, J.; Dror, R. O.; Kobilka, B. K., Structural insights into micro-opioid receptor activation. *Nature* **2015**, *524* (7565), 315-21.

35. Jacobson, M. P.; Pincus, D. L.; Rapp, C. S.; Day, T. J. F.; Honig, B.; Shaw, D. E.; Friesner, R. A., A hierarchical approach to all-atom protein loop prediction. *Proteins-Structure Function and Bioinformatics* **2004**, *55* (2), 351-367.
36. Jacobson, M. P.; Friesner, R. A.; Xiang, Z.; Honig, B., On the Role of the Crystal Environment in Determining Protein Side-chain Conformations. *Journal of Molecular Biology* **2002**, *320* (3), 597-608.
37. Lomize, M. A.; Pogozheva, I. D.; Joo, H.; Mosberg, H. I.; Lomize, A. L., OPM database and PPM web server: resources for positioning of proteins in membranes. *Nucleic Acids Research* **2012**, *40* (D1), D370-D376.
38. Sastry, G. M.; Adzhigirey, M.; Day, T.; Annabhimoju, R.; Sherman, W., Protein and ligand preparation: parameters, protocols, and influence on virtual screening enrichments. *Journal of computer-aided molecular design* **2013**, *27* (3), 221-34.
39. Harder, E.; Damm, W.; Maple, J.; Wu, C.; Reboul, M.; Xiang, J. Y.; Wang, L.; Lupyan, D.; Dahlgren, M. K.; Knight, J. L.; Kaus, J. W.; Cerutti, D. S.; Krilov, G.; Jorgensen, W. L.; Abel, R.; Friesner, R. A., OPLS3: A Force Field Providing Broad Coverage of Drug-like Small Molecules and Proteins. *Journal of Chemical Theory and Computation* **2016**, *12* (1), 281-296.
40. Friesner, R. A.; Banks, J. L.; Murphy, R. B.; Halgren, T. A.; Klicic, J. J.; Mainz, D. T.; Repasky, M. P.; Knoll, E. H.; Shelley, M.; Perry, J. K.; Shaw, D. E.; Francis, P.; Shenkin, P. S., Glide: A new approach for rapid, accurate docking and scoring. 1. Method and assessment of docking accuracy. *Journal of Medicinal Chemistry* **2004**, *47* (7), 1739-1749.
41. Friesner, R. A.; Murphy, R. B.; Repasky, M. P.; Frye, L. L.; Greenwood, J. R.; Halgren, T. A.; Sanschagrin, P. C.; Mainz, D. T., Extra precision glide: Docking and scoring incorporating a model of hydrophobic enclosure for protein-ligand complexes. *Journal of Medicinal Chemistry* **2006**, *49* (21), 6177-6196.
42. Mark, P.; Nilsson, L., Structure and dynamics of the TIP3P, SPC, and SPC/E water models at 298 K. *Journal of Physical Chemistry A* **2001**, *105* (43), 9954-9960.
43. Zhang, J.; Hou, Y.; Wang, Y.; Wang, C.; Zhang, X., The LBFGS quasi-Newtonian method for molecular modeling prion AGAAAAGA amyloid fibrils. *Natural Science* **2012**, *04* (12), 1097-1108.
44. Ikeguchi, M., Partial rigid-body dynamics in NPT, NPAT and NP gamma T ensembles for proteins and membranes. *Journal of Computational Chemistry* **2004**, *25* (4), 529-541.

45. Bailey, A. G.; Lowe, C. P., MILCH SHAKE: An Efficient Method for Constraint Dynamics Applied to Alkanes. *Journal of Computational Chemistry* **2009**, *30* (15), 2485-2493.
46. Shan, Y. B.; Klepeis, J. L.; Eastwood, M. P.; Dror, R. O.; Shaw, D. E., Gaussian split Ewald: A fast Ewald mesh method for molecular simulation. *Journal of Chemical Physics* **2005**, *122* (5).
47. Stuart, S. J.; Zhou, R. H.; Berne, B. J., Molecular dynamics with multiple time scales: The selection of efficient reference system propagators. *Journal of Chemical Physics* **1996**, *105* (4), 1426-1436.
48. Kevin J. Bowers, E. C., Huafeng Xu, Ron O. Dror, Michael P. Eastwood,; Brent A. Gregersen, J. L. K., Istvan Kolossvary, Mark A. Moraes, Federico D. Sacerdoti,; John K. Salmon, Y. S., David E. Shaw, Scalable Algorithms for Molecular Dynamics Simulations on Commodity Clusters. **2006**.
49. Humphrey, W.; Dalke, A.; Schulten, K., VMD: Visual molecular dynamics. *Journal of Molecular Graphics* **1996**, *14* (1), 33-38.
50. Trzaskowski, B.; Latek, D.; Yuan, S.; Ghoshdastider, U.; Debinski, A.; Filipek, S., Action of Molecular Switches in GPCRs - Theoretical and Experimental Studies. *Current Medicinal Chemistry* **2012**, *19* (8), 1090-1109.
51. Bakan, A.; Meireles, L. M.; Bahar, I., ProDy: protein dynamics inferred from theory and experiments. *Bioinformatics (Oxford, England)* **2011**, *27* (11), 1575-7.
52. White, K. L.; Eddy, M. T.; Gao, Z.-G.; Han, G. W.; Lian, T.; Deary, A.; Patel, N.; Jacobson, K. A.; Katritch, V.; Stevens, R. C., Structural Connection between Activation Microswitch and Allosteric Sodium Site in GPCR Signaling. *Structure* **2018**, *26* (2), 259-269.e5.
53. Katritch, V.; Cherezov, V.; Stevens, R. C., Structure-function of the G protein-coupled receptor superfamily. *Annu Rev Pharmacol Toxicol* **2013**, *53*, 531-556.
54. Fenalti, G.; Giguere, P. M.; Katritch, V.; Huang, X. P.; Thompson, A. A.; Cherezov, V.; Roth, B. L.; Stevens, R. C., Molecular control of delta-opioid receptor signalling. *Nature* **2014**, *506* (7487), 191-196.
55. Shipton, E. A.; Shipton, E. E.; Shipton, A. J., A Review of the Opioid Epidemic: What Do We Do About It? *Pain and Therapy* **2018**, *7* (1), 23-36.
56. Pergolizzi Jr, J. V.; Raffa, R. B.; Rosenblatt, M. H., Opioid withdrawal symptoms, a consequence of chronic opioid use and opioid use disorder: Current understanding and approaches to management. *Journal of Clinical Pharmacy and Therapeutics* **2020**, *45* (5), 892-903.

57. Volkow, N. D.; Koroshetz, W., Lack of Evidence for Benefit From Long-term Use of Opioid Analgesics for Patients With Neuropathy. *JAMA Neurology* **2017**, *74* (7), 761-762.
58. Centers for Disease, C.; Prevention, P. H. S. U. S. D. o. H.; Human, S., Guideline for Prescribing Opioids for Chronic Pain. *Journal of Pain & Palliative Care Pharmacotherapy* **2016**, *30* (2), 138-140.
59. Mann, A.; Liebetrau, S.; Klima, M.; Dasgupta, P.; Massotte, D.; Schulz, S., Agonist-induced phosphorylation bar code and differential post-activation signaling of the delta opioid receptor revealed by phosphosite-specific antibodies. *Scientific Reports* **2020**, *10* (1), 8585.
60. Holdridge, S. V.; Cahill, C. M., Spinal administration of a  $\delta$  opioid receptor agonist attenuates hyperalgesia and allodynia in a rat model of neuropathic pain. *European Journal of Pain* **2007**, *11* (6), 685-693.
61. Nadal, X.; Baños, J.-E.; Kieffer, B. L.; Maldonado, R., Neuropathic pain is enhanced in  $\delta$ -opioid receptor knockout mice. *European Journal of Neuroscience* **2006**, *23* (3), 830-834.
62. Gavériaux-Ruff, C.; Karchewski, L. A.; Hever, X.; Matifas, A.; Kieffer, B. L., Inflammatory pain is enhanced in delta opioid receptor-knockout mice. *Eur J Neurosci* **2008**, *27* (10), 2558-2567.
63. Filliol, D.; Ghozland, S.; Chluba, J.; Martin, M.; Matthes, H. W. D.; Simonin, F.; Befort, K.; Gavériaux-Ruff, C.; Dierich, A.; LeMeur, M.; Valverde, O.; Maldonado, R.; Kieffer, B. L., Mice deficient for  $\delta$ - and  $\mu$ -opioid receptors exhibit opposing alterations of emotional responses. *Nature Genetics* **2000**, *25* (2), 195-200.
64. Broom, D. C.; Jutkiewicz, E. M.; Folk, J. E.; Traynor, J. R.; Rice, K. C.; Woods, J. H., Nonpeptidic  $\delta$ -opioid Receptor Agonists Reduce Immobility in the Forced Swim Assay in Rats. *Neuropsychopharmacology* **2002**, *26* (6), 744-755.
65. Tian, X.; Guo, J.; Zhu, M.; Li, M.; Wu, G.; Xia, Y.,  $\delta$ -Opioid receptor activation rescues the functional TrkB receptor and protects the brain from ischemia-reperfusion injury in the rat. *PLoS One* **2013**, *8* (7), e69252-e69252.
66. Min, J.-W.; Liu, Y.; Wang, D.; Qiao, F.; Wang, H., The non-peptidic  $\delta$ -opioid receptor agonist Tan-67 mediates neuroprotection post-ischemically and is associated with altered amyloid precursor protein expression, maturation and processing in mice. *Journal of Neurochemistry* **2018**, *144* (3), 336-347.

67. Comer, S. D.; Hoenicke, E. M.; Sable, A. I.; McNutt, R. W.; Chang, K. J.; De Costa, B. R.; Mosberg, H. I.; Woods, J. H., Convulsive effects of systemic administration of the delta opioid agonist BW373U86 in mice. *J Pharmacol Exp Ther* **1993**, *267* (2), 888-95.
68. Jutkiewicz, E. M.; Kaminsky, S. T.; Rice, K. C.; Traynor, J. R.; Woods, J. H., Differential behavioral tolerance to the delta-opioid agonist SNC80 ([(+)-4-[(alphaR)-alpha-[(2S,5R)-2,5-dimethyl-4-(2-propenyl)-1-piperazinyl]-3-methoxyphenyl)methyl]-N,N-diethylbenzamide) in Sprague-Dawley rats. *J Pharmacol Exp Ther* **2005**, *315* (1), 414-422.
69. Danielsson, I.; Gasiior, M.; Stevenson, G. W.; Folk, J. E.; Rice, K. C.; Negus, S. S., Electroencephalographic and convulsant effects of the delta opioid agonist SNC80 in rhesus monkeys. *Pharmacology Biochemistry and Behavior* **2006**, *85* (2), 428-434.
70. Maia, E. H. B.; Assis, L. C.; de Oliveira, T. A.; da Silva, A. M.; Taranto, A. G., Structure-Based Virtual Screening: From Classical to Artificial Intelligence. *Frontiers in Chemistry* **2020**, *8* (343).
71. Totrov, M.; Abagyan, R., Flexible ligand docking to multiple receptor conformations: a practical alternative. *Curr Opin Struct Biol* **2008**, *18* (2), 178-184.
72. Philippopoulos, M.; Lim, C., Exploring the dynamic information content of a protein NMR structure: Comparison of a molecular dynamics simulation with the NMR and X-ray structures of Escherichia coli ribonuclease HI. *Proteins: Structure, Function, and Bioinformatics* **1999**, *36* (1), 87-110.
73. Salmon, L.; Bouvignies, G.; Markwick, P.; Lakomek, N.; Showalter, S.; Li, D. W.; Walter, K.; Griesinger, C.; Bruschweiler, R.; Blackledge, M., Protein Conformational Flexibility from Structure-Free Analysis of NMR Dipolar Couplings: Quantitative and Absolute Determination of Backbone Motion in Ubiquitin. *ANGEWANDTE CHEMIE-INTERNATIONAL EDITION* **2009**, *48* (23), 4154-4157.
74. Choi, J.; Choi, K.-E.; Park, S. J.; Kim, S. Y.; Jee, J.-G., Ensemble-Based Virtual Screening Led to the Discovery of New Classes of Potent Tyrosinase Inhibitors. *Journal of Chemical Information and Modeling* **2016**, *56* (2), 354-367.
75. Kumar, V.; Liu, H.; Wu, C., Drug repurposing against SARS-CoV-2 receptor binding domain using ensemble-based virtual screening and molecular dynamics simulations. *Computers in Biology and Medicine* **2021**, *135*, 104634.
76. Amaro, R. E.; Li, W. W., Emerging Methods for Ensemble-Based Virtual Screening. *CURRENT TOPICS IN MEDICINAL CHEMISTRY* **2010**, *10* (1), 3-13.

77. Jutkiewicz, E. M.; Chang, K. J.; Rice, K. C.; Woods, J. H., Characterization of a novel nonpeptide delta-opioid agonist analog DPI287 with antidepressant-like activity. *FASEB JOURNAL* **2005**, *19* (5), A1542-A1542.
78. Madhavi Sastry, G.; Adzhigirey, M.; Day, T.; Annabhimoju, R.; Sherman, W., Protein and ligand preparation: parameters, protocols, and influence on virtual screening enrichments. *Journal of Computer-Aided Molecular Design* **2013**, *27* (3), 221-234.
79. Harder, E.; Damm, W.; Maple, J.; Wu, C.; Reboul, M.; Xiang, J. Y.; Wang, L.; Lypyan, D.; Dahlgren, M. K.; Knight, J. L.; Kaus, J. W.; Cerutti, D. S.; Krilov, G.; Jorgensen, W. L.; Abel, R.; Friesner, R. A., OPLS3: A Force Field Providing Broad Coverage of Drug-like Small Molecules and Proteins. *Journal of chemical theory and computation* **2016**, *12* (1), 281-96.
80. Babar, Z.; Khan, M.; Zahra, M.; Anwar, M.; Noor, K.; Hashmi, H. F.; Suleman, M.; Waseem, M.; Shah, A.; Ali, S.; Ali, S. S., Drug similarity and structure-based screening of medicinal compounds to target macrodomain-I from SARS-CoV-2 to rescue the host immune system: a molecular dynamics study. *Journal of Biomolecular Structure and Dynamics* **2020**, 1-15.
81. Debnath, P.; Debnath, B.; Bhaumik, S.; Debnath, S., In Silico Identification of Potential Inhibitors of ADP-Ribose Phosphatase of SARS-CoV-2 nsP3 by Combining E-Pharmacophore- and Receptor-Based Virtual Screening of Database. *ChemistrySelect* **2020**, *5* (30), 9388-9398.
82. Wood, D. J.; Vlieg, J. d.; Wagener, M.; Ritschel, T., Pharmacophore Fingerprint-Based Approach to Binding Site Subpocket Similarity and Its Application to Bioisostere Replacement. *Journal of Chemical Information and Modeling* **2012**, *52* (8), 2031-2043.
83. Mark, P.; Nilsson, L., Structure and Dynamics of the TIP3P, SPC, and SPC/E Water Models at 298 K. *The Journal of Physical Chemistry A* **2001**, *105* (43), 9954-9960.
84. Zhang, J.; Hou, Y.; Wang, Y.; Wang, C.; Zhang, X., The LBFGS quasi-Newtonian method for molecular modelling prion AGAAAAGA amyloid fibrils. *Natural Science* **2012**, *Vol. 4*, 1097-1098.
85. Ikeguchi, M., Partial rigid-body dynamics in NPT, NPAT and NP $\gamma$ T ensembles for proteins and membranes. *Journal of Computational Chemistry* **2004**, *25* (4), 529-541.
86. Bailey, A. G.; Lowe, C. P., MILCH SHAKE: an efficient method for constraint dynamics applied to alkanes. *J Comput Chem* **2009**, *30* (15), 2485-93.
87. Shan, Y.; Klepeis, J. L.; Eastwood, M. P.; Dror, R. O.; Shaw, D. E., Gaussian split Ewald: A fast Ewald mesh method for molecular simulation. *The Journal of chemical physics* **2005**, *122* (5), 54101.

88. Stuart, S. J.; Zhou, R.; Berne, B. J., Molecular dynamics with multiple time scales: The selection of efficient reference system propagators. *The Journal of chemical physics* **1996**, *105* (4), 1426-1436.
89. Bowers, K. J.; Chow, D. E.; Xu, H.; Dror, R. O.; Eastwood, M. P.; Gregersen, B. A.; Klepeis, J. L.; Kolossvary, I.; Moraes, M. A.; Sacerdoti, F. D.; Salmon, J. K.; Shan, Y.; Shaw, D. E. In *Scalable Algorithms for Molecular Dynamics Simulations on Commodity Clusters*, SC '06: Proceedings of the 2006 ACM/IEEE Conference on Supercomputing, 11-17 Nov. 2006; 2006; pp 43-43.
90. Ghosh, A.; Rapp, C. S.; Friesner, R. A., Generalized Born Model Based on a Surface Integral Formulation. *The Journal of Physical Chemistry B* **1998**, *102* (52), 10983-10990.
91. Yu, Z.; Jacobson, M. P.; Friesner, R. A., What role do surfaces play in GB models? A new-generation of surface-generalized born model based on a novel gaussian surface for biomolecules. *Journal of Computational Chemistry* **2006**, *27* (1), 72-89.
92. Li, J.; Abel, R.; Zhu, K.; Cao, Y.; Zhao, S.; Friesner, R. A., The VSGB 2.0 model: a next generation energy model for high resolution protein structure modeling. *Proteins* **2011**, *79* (10), 2794-812.
93. Jorgensen, W. L.; Maxwell, D. S.; Tirado-Rives, J., Development and Testing of the OPLS All-Atom Force Field on Conformational Energetics and Properties of Organic Liquids. *Journal of the American Chemical Society* **1996**, *118* (45), 11225-11236.
94. Kongsted, J.; Söderhjelm, P.; Ryde, U., How accurate are continuum solvation models for drug-like molecules? *J Comput Aided Mol Des* **2009**, *23* (7), 395-409.
95. Hou, T.; Wang, J.; Li, Y.; Wang, W., Assessing the performance of the molecular mechanics/Poisson Boltzmann surface area and molecular mechanics/generalized Born surface area methods. II. The accuracy of ranking poses generated from docking. *J Comput Chem* **2011**, *32* (5), 866-77.
96. Kollman, P. A.; Massova, I.; Reyes, C.; Kuhn, B.; Huo, S.; Chong, L.; Lee, M.; Lee, T.; Duan, Y.; Wang, W.; Donini, O.; Cieplak, P.; Srinivasan, J.; Case, D. A.; Cheatham, T. E., 3rd, Calculating structures and free energies of complex molecules: combining molecular mechanics and continuum models. *Accounts of chemical research* **2000**, *33* (12), 889-97.
97. Sun, H.; Li, Y.; Tian, S.; Xu, L.; Hou, T., Assessing the performance of MM/PBSA and MM/GBSA methods. 4. Accuracies of MM/PBSA and MM/GBSA methodologies evaluated by various simulation protocols using PDBbind data set. *Physical chemistry chemical physics : PCCP* **2014**, *16* (31), 16719-29.

98. Xu, L.; Sun, H.; Li, Y.; Wang, J.; Hou, T., Assessing the performance of MM/PBSA and MM/GBSA methods. 3. The impact of force fields and ligand charge models. *The journal of physical chemistry. B* **2013**, *117* (28), 8408-21.
99. Zoete, V.; Daina, A.; Bovigny, C.; Michielin, O., SwissSimilarity: A Web Tool for Low to Ultra High Throughput Ligand-Based Virtual Screening. *J Chem Inf Model* **2016**, *56* (8), 1399-404.
100. Bakan, A.; Meireles, L. M.; Bahar, I., ProDy: protein dynamics inferred from theory and experiments. *Bioinformatics* **2011**, *27* (11), 1575-1577.
101. del Sol, A.; Fujihashi, H.; Amoros, D.; Nussinov, R., Residues crucial for maintaining short paths in network communication mediate signaling in proteins. *Mol Syst Biol* **2006**, *2*, 2006.0019-2006.0019.
102. Schneider, S.; Provasi, D.; Filizola, M., How Oliceridine (TRV-130) Binds and Stabilizes a  $\mu$ -Opioid Receptor Conformational State That Selectively Triggers G Protein Signaling Pathways. *Biochemistry* **2016**, *55* (46), 6456-6466.
103. Eargle, J.; Luthey-Schulten, Z., NetworkView: 3D display and analysis of protein-RNA interaction networks. *Bioinformatics* **2012**, *28* (22), 3000-3001.
104. Ghosh, A.; Vishveshwara, S., A study of communication pathways in methionyl-tRNA synthetase by molecular dynamics simulations and structure network analysis. *Proceedings of the National Academy of Sciences* **2007**, *104* (40), 15711.
105. Glykos, N. M., Software news and updates carma: A molecular dynamics analysis program. *Journal of Computational Chemistry* **2006**, *27* (14), 1765-1768.
106. Girvan, M.; Newman, M. E. J., Community structure in social and biological networks. *Proc Natl Acad Sci U S A* **2002**, *99* (12), 7821-7826.
107. Bowerman, S.; Wereszczynski, J., Detecting Allosteric Networks Using Molecular Dynamics Simulation. *Methods Enzymol* **2016**, *578*, 429-447.
108. Stolzenberg, S.; Michino, M.; LeVine, M. V.; Weinstein, H.; Shi, L., Computational approaches to detect allosteric pathways in transmembrane molecular machines. *Biochim Biophys Acta* **2016**, *1858* (7 Pt B), 1652-1662.
109. La Sala, G.; Decherchi, S.; De Vivo, M.; Rocchia, W., Allosteric Communication Networks in Proteins Revealed through Pocket Crosstalk Analysis. *ACS Central Science* **2017**, *3* (9), 949-960.
110. Mishra, S. K.; Jernigan, R. L., Protein dynamic communities from elastic network models align closely to the communities defined by molecular dynamics. *PLoS One* **2018**, *13* (6), e0199225.



## Appendix A

### To Probe the Activation Mechanism of the Delta Opioid Receptor by an Agonist

#### ADL5859 Started from Inactive Conformation Using Molecular Dynamic

#### Simulations

**Table A1**

*RMSD Comparison*

Type	Traj #	Cluster ID	Whole Protein (Å)		7TMD (Å)		TM6 (Å)	
			4N6H	6PT3	4N6H	6PT3	4N6H	6PT3
ADL5859	1	<b>1 (52%)</b>	<b>3.4</b>	<b>2.5</b>	<b>2.8</b>	<b>2.2</b>	<b>4.1</b>	<b>3.4</b>
		2 (30%)	2.1	3.0	1.8	2.7	2.0	4.2
		<b>3 (17%)</b>	<b>3.1</b>	<b>2.4</b>	<b>2.5</b>	<b>2.2</b>	<b>3.3</b>	<b>2.9</b>
	2	1 (98%)	2.5	3.1	2.1	2.6	1.7	4.6
	3	1 (90%)	2.3	3.1	1.9	2.6	2.3	3.8
		2 (11%)	2.8	2.9	2.4	2.6	4.5	4.2
	4	1 (43%)	2.4	2.9	2.1	2.4	2.5	3.4
		2 (32%)	2.4	3.3	1.9	2.7	2.2	4.5
		3 (20%)	2.6	2.9	2.0	2.3	2.4	3.5
		4 (5%)	2.7	2.9	1.7	2.3	2.2	3.6
		<b>5 (1%)</b>	<b>3.6</b>	<b>2.7</b>	<b>2.9</b>	<b>2.1</b>	<b>5.8</b>	<b>2.8</b>
	5	1 (56%)	2.8	2.7	2.5	2.4	3.1	3.4
2 (43%)		2.2	3.3	1.7	2.8	2.5	4.9	
6	<b>1 (76%)</b>	<b>3.3</b>	<b>2.8</b>	<b>2.6</b>	<b>2.4</b>	<b>3.9</b>	<b>3.2</b>	
	2 (22%)	2.3	3.0	1.9	2.5	2.0	3.9	
Naltrindole	1	1 (100%)	3.1	3.4	2.7	3.0	1.8	5.5
	2	1 (100%)	3.3	3.1	2.8	2.8	2.9	5.0
	3	1 (100%)	3.2	3.3	2.7	2.9	2.4	4.9

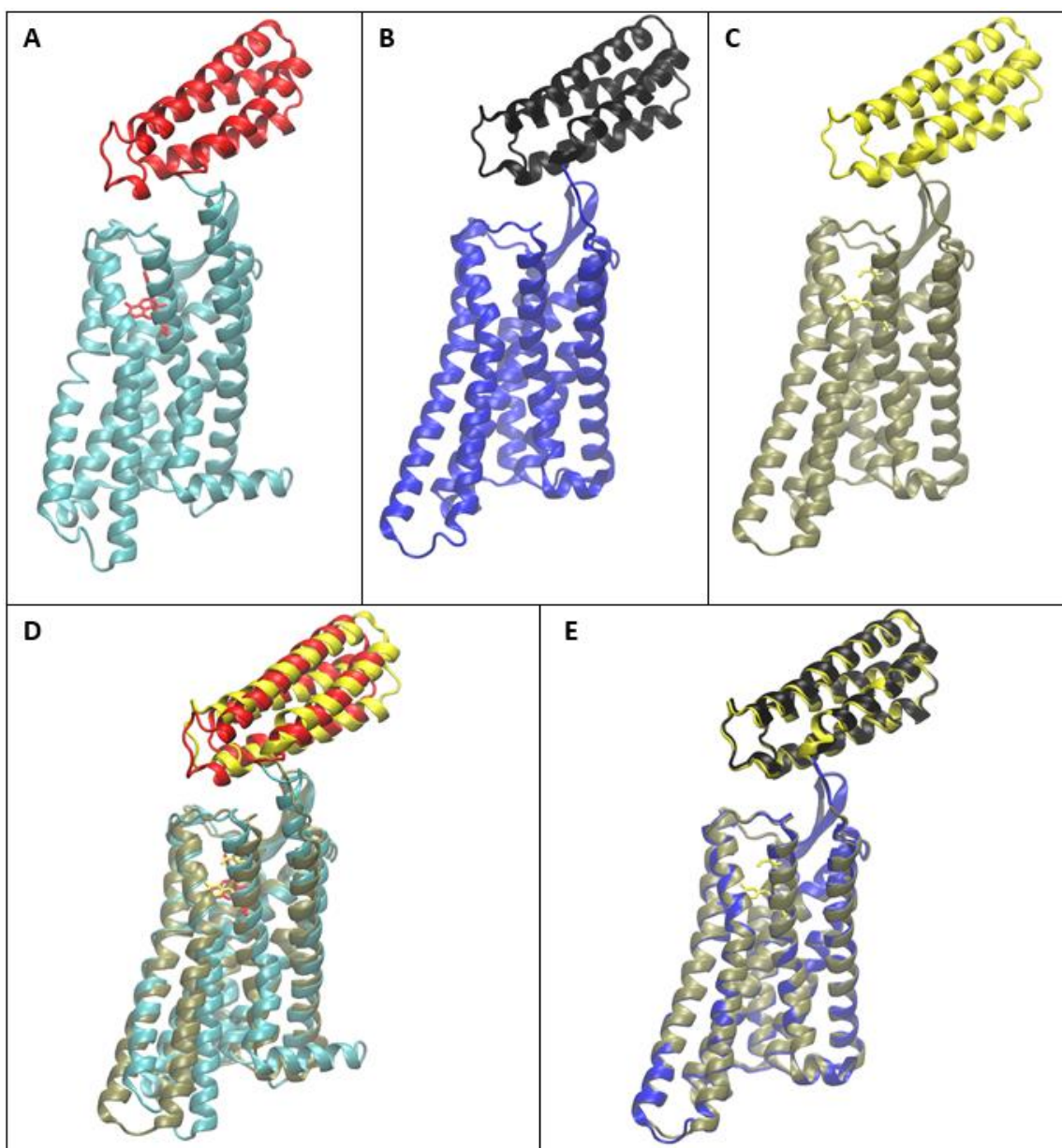
**Table A2**

*Conserved Molecular Switches*

	Traj #	Cluster ID	Distance (Å) Toggle (NPXXY) Y318 <sup>7.53</sup> -Y318 <sup>7.53</sup>	Distance (Å) Transmission (CWXP) S249 <sup>6.23</sup> -S249 <sup>6.23</sup>	Distance (Å) Ionic Lock (DRY) R146 <sup>3.50</sup> -T260 <sup>6.34</sup>
ADL5859	1	<b>1 (52%)</b>	<b>1.1</b>	<b>9.4</b>	<b>9.3</b>
		2 (30%)	1.4	6.9	5.9
		<b>3 (17%)</b>	<b>1.4</b>	<b>10.3</b>	<b>2.3</b>
	2	1 (98%)	1.5	1.3	3.9
		3	1 (90%)	1.7	6.0
	4	<b>2 (11%)</b>	<b>1.1</b>	<b>9.2</b>	<b>6.7</b>
		1 (43%)	2.2	1.7	7.8
		2 (32%)	1.8	2.5	7.2
		3 (20%)	1.5	2.4	7.4
		4 (5%)	0.2	1.3	6.7
5	<b>5 (1%)</b>	<b>1.1</b>	<b>13.9</b>	<b>6.5</b>	
	1 (56%)	0.6	6.2	5.8	
6	2 (43%)	0.4	2.5	6.4	
	<b>1 (76%)</b>	<b>0.5</b>	<b>10.6</b>	<b>4.2</b>	
Naltrindole	1	2 (22%)	1.5	5.9	6.1
		1	1.5	3.0	3.8
	2	1	1.4	3.8	4.4
Naltrindole	3	(100%)			
		1	1.5	3.8	3.7
		(100%)			

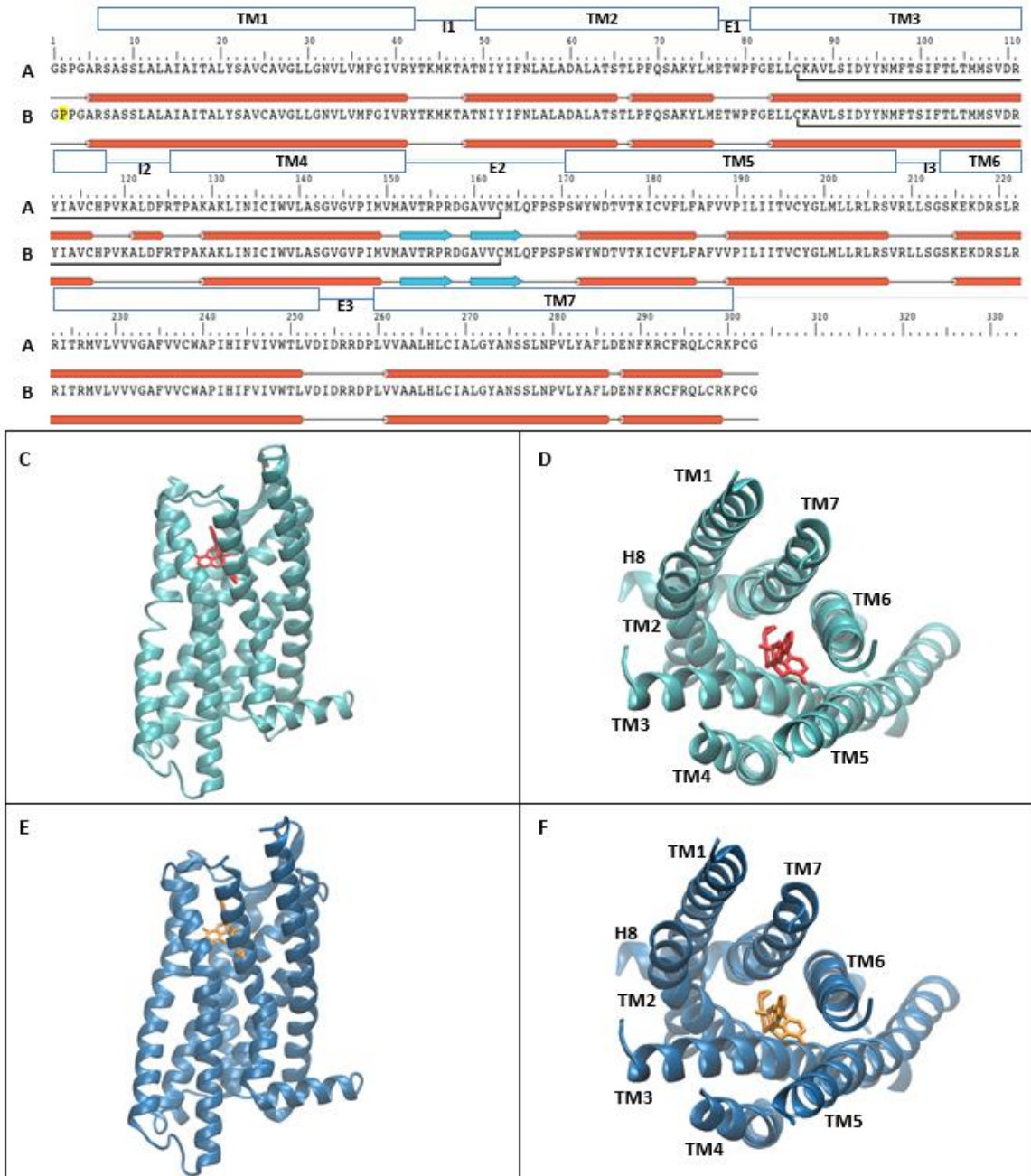
**Figure A1**

*Solved Crystal Structures of the Human DOR With Fusion Proteins*



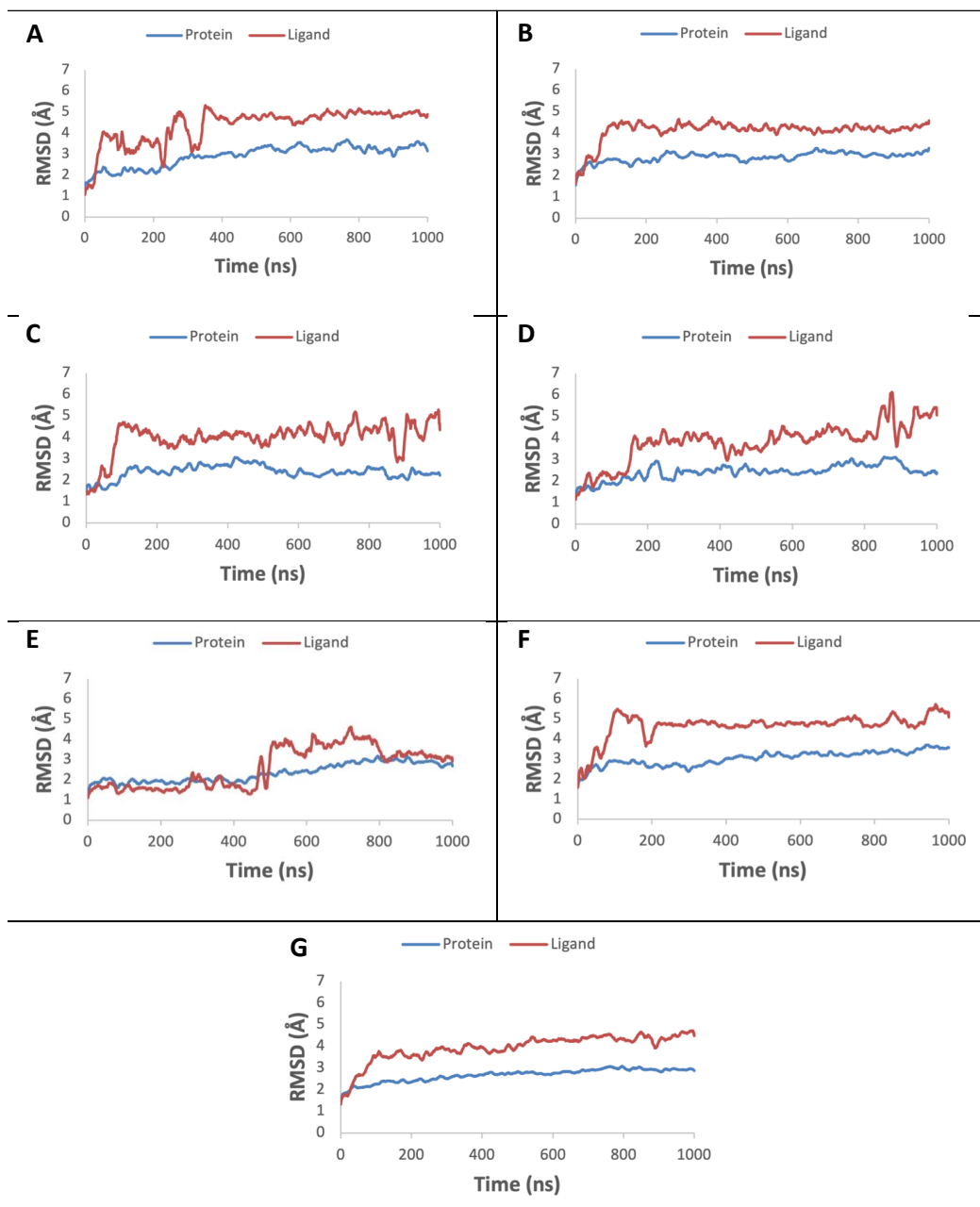
## Figure A2

Sequences of Full-Length Crystal Human Delta Opioid Receptor (PDB ID: 4N6H) (P41143)



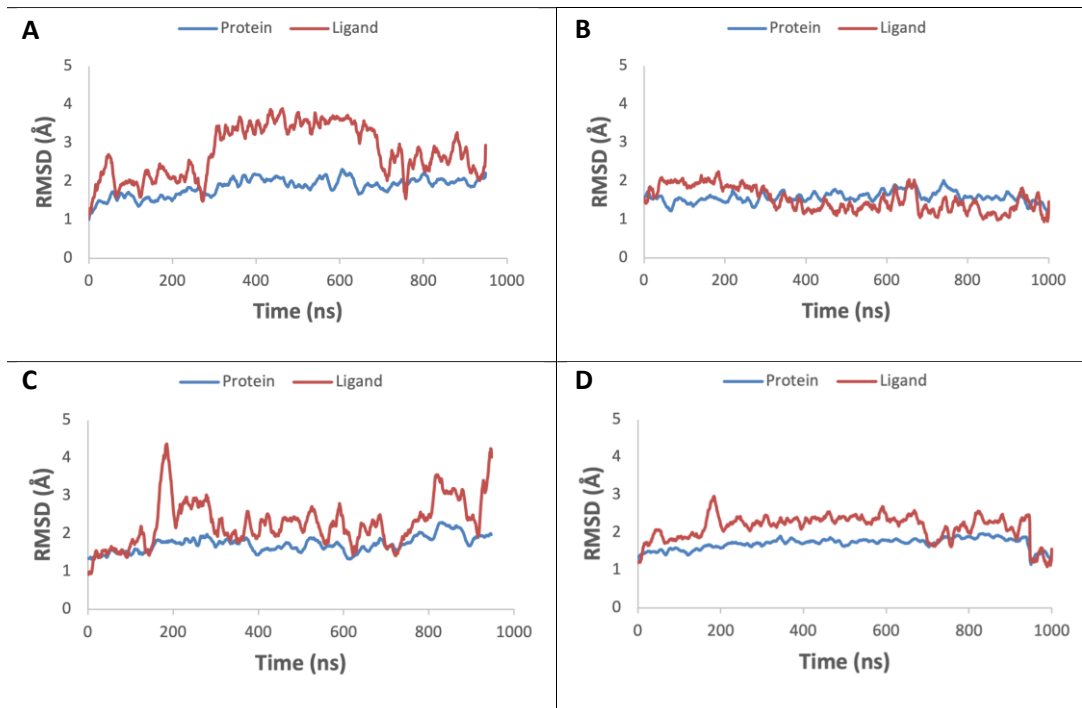
### Figure A3

#### *Protein and Ligand RMSD of the DOR/ADL5859 Agonist System*



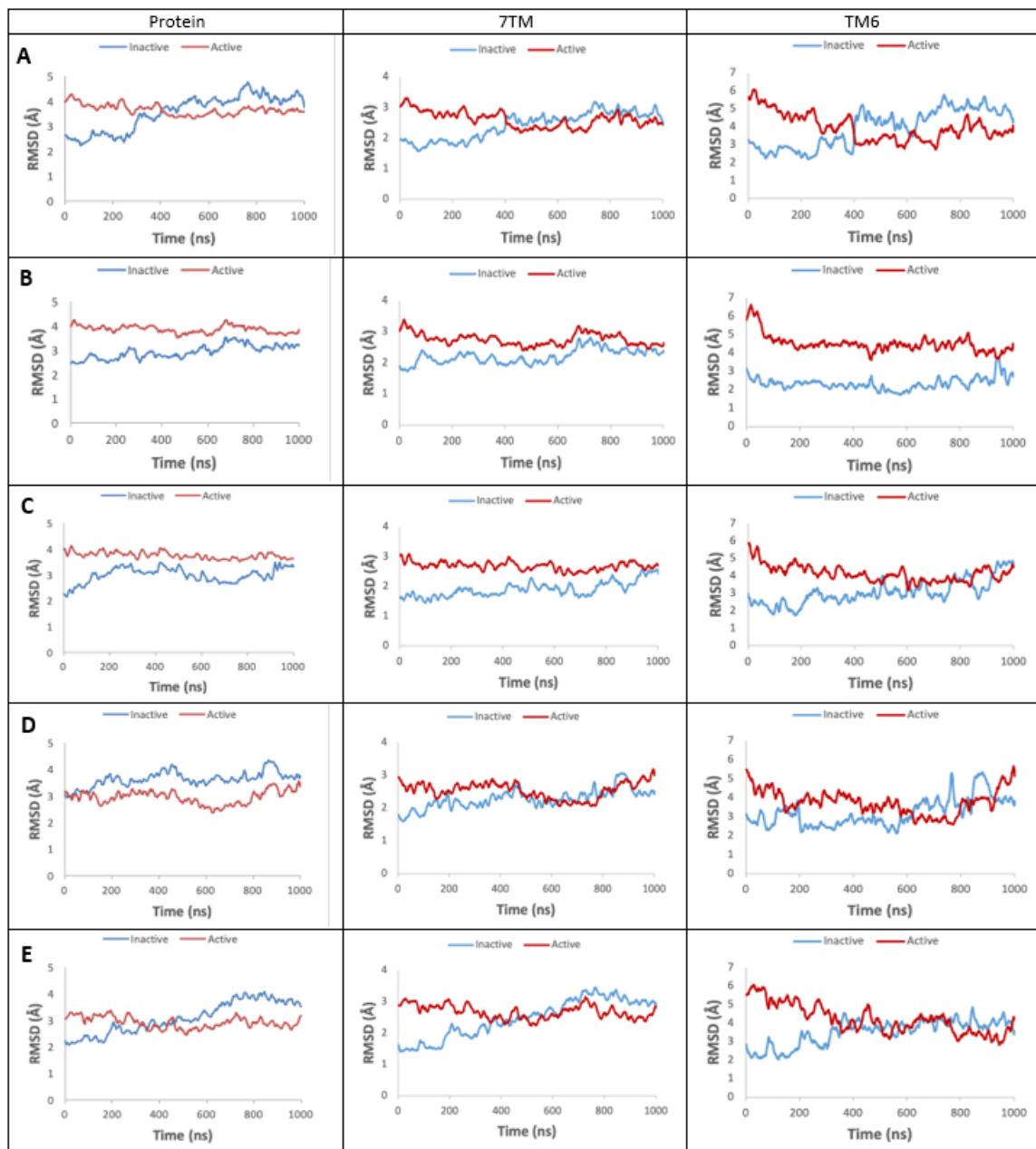
## Figure A4

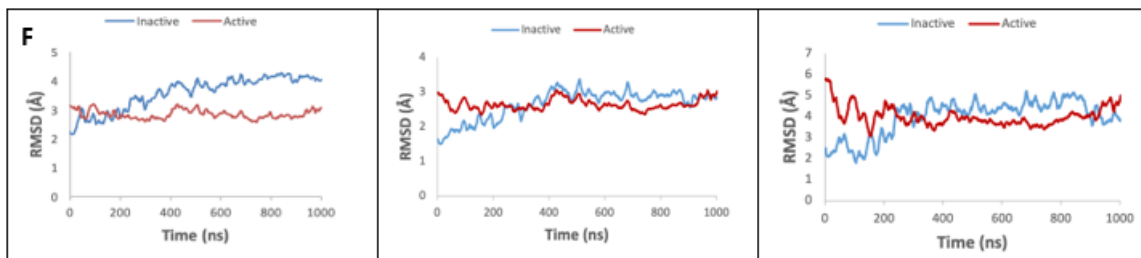
*Protein and Ligand RMSD of the DOR/Naltrindole Antagonist System*



**Figure A5**

*Receptor RMSDs From Individual DOR-Agonist-ADL5859 Simulation Systems Against the Two Solved Crystal Receptor Structures*

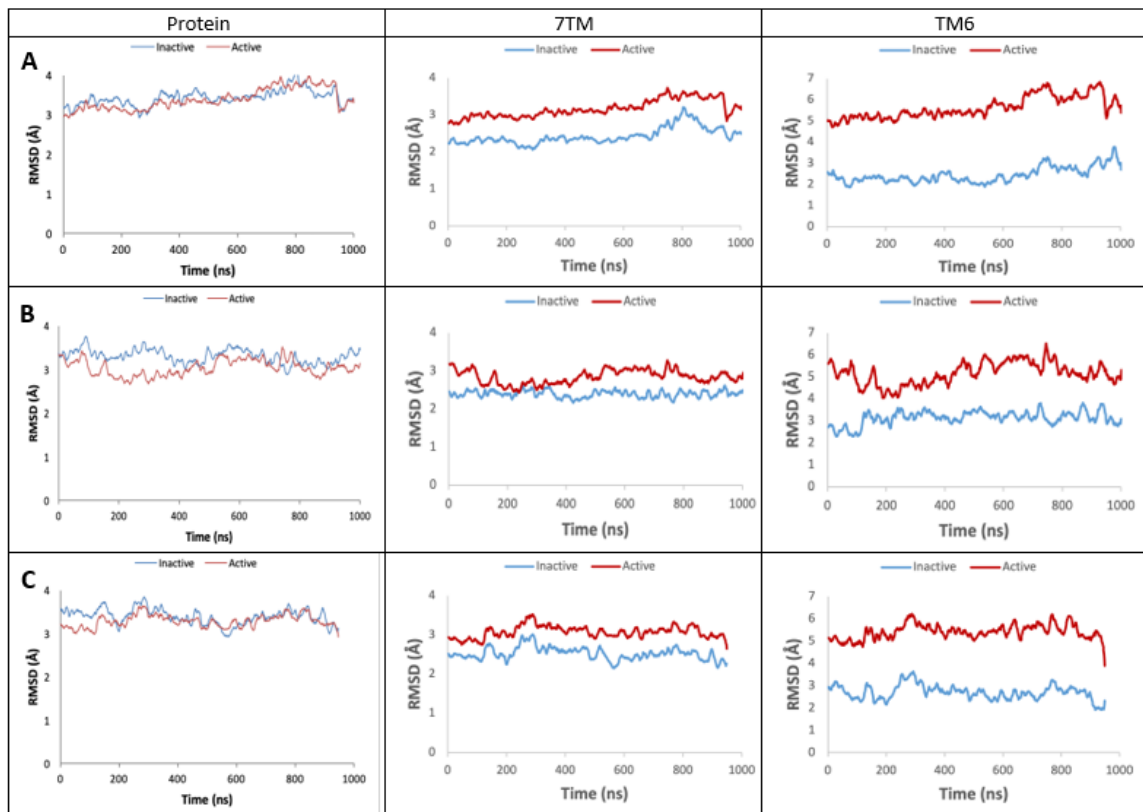






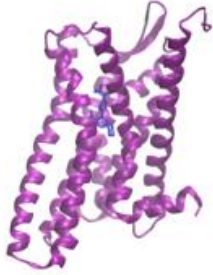

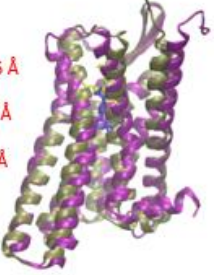

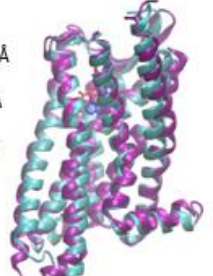
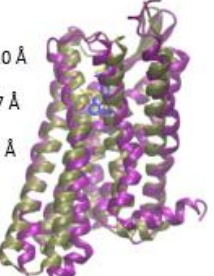

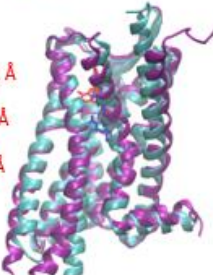
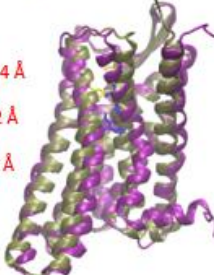
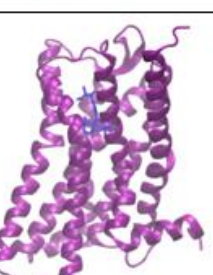
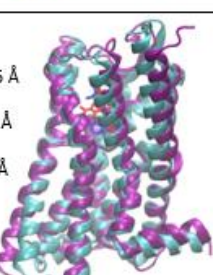
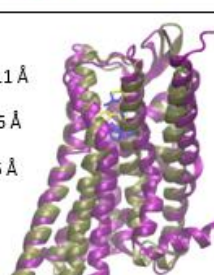
## Figure A6



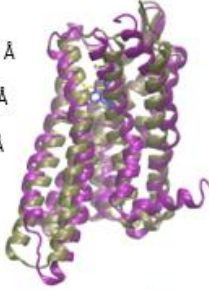
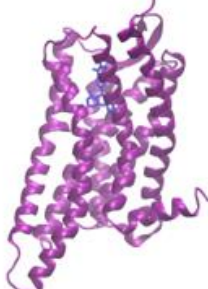
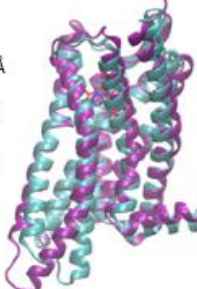
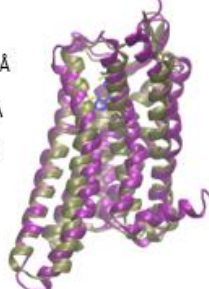

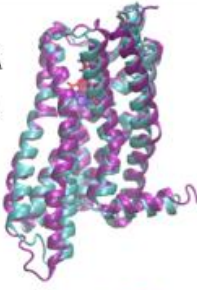
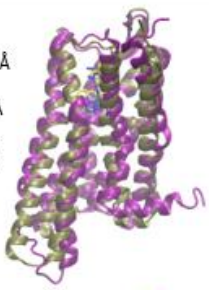
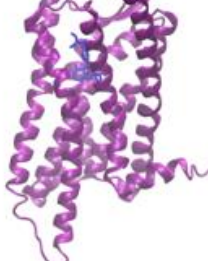

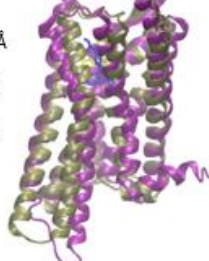
*Receptor RMSDs From Individual DOR-Antagonist-Naltrindole Simulation Systems Against the Two Solved Crystal Receptor Structures*

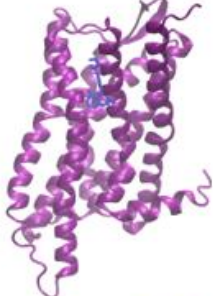
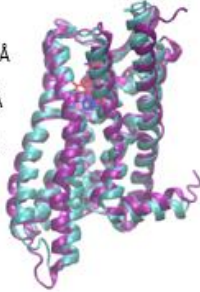
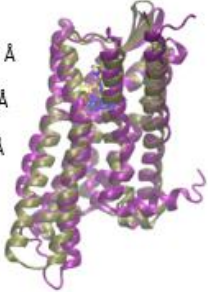

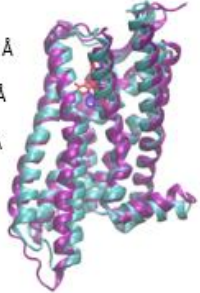
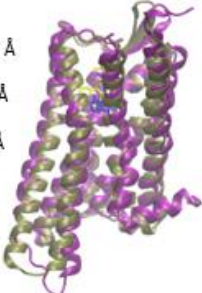


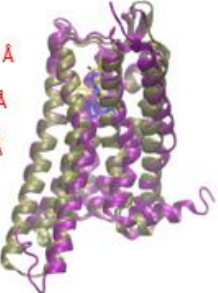

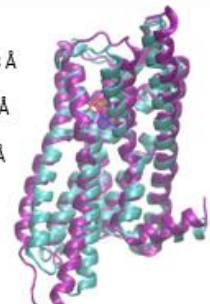
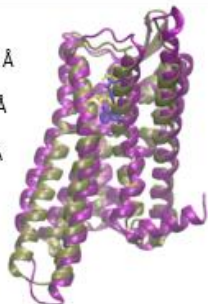


## Figure A7

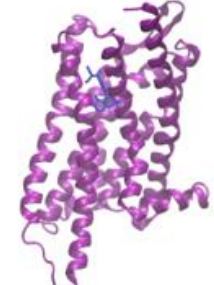
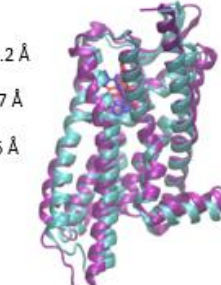
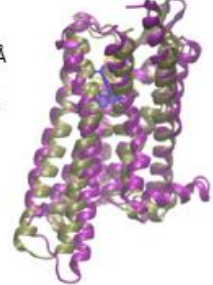

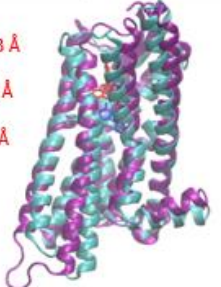
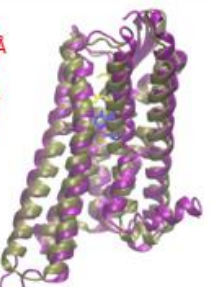

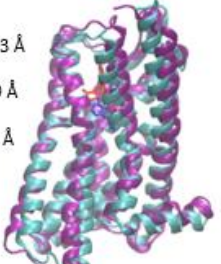
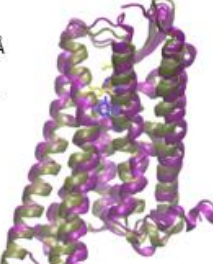
*Representative Structure of Each DOR-Agonist-ADL5859 Cluster and Its Comparison With the Inactive and Active Solved Crystal Structure*

	MD Structure	MD/Crystal Inactive Structure <sup>1</sup>	MD/Crystal Active Structure <sup>2</sup>
Trj 1 Cluster 1 (52%)		Protein: 3.4 Å 7TMs: 2.8 Å TM6: 4.1 Å 	Protein: 2.5 Å 7TMs: 2.2 Å TM6: 3.4 Å 
Trj 1 Cluster 2 (30%)		Protein: 2.1 Å 7TMs: 1.8 Å TM6: 2.0 Å 	Protein: 3.0 Å 7TMs: 2.7 Å TM6: 4.2 Å 
Trj 1 Cluster 3 (17%)		Protein: 3.1 Å 7TMs: 2.5 Å TM6: 3.3 Å 	Protein: 2.4 Å 7TMs: 2.2 Å TM6: 2.9 Å 
Trj 2 Cluster 1 (98%)		Protein: 2.5 Å 7TMs: 2.1 Å TM6: 1.7 Å 	Protein: 3.1 Å 7TMs: 2.6 Å TM6: 4.6 Å 

Tri 3 Cluster 1 (90%)		Protein: 2.3 Å 7TMs: 1.9 Å TM6: 2.3 Å		
Tri 3 Cluster 2 (11%)		Protein: 2.8 Å 7TMs: 2.4 Å TM6: 4.5 Å		
Tri 4 Cluster 1 (43%)		Protein: 2.4 Å 7TMs: 2.1 Å TM6: 2.5 Å		
Tri 4 Cluster 2 (32%)		Protein: 2.4 Å 7TMs: 1.9 Å TM6: 2.2 Å		

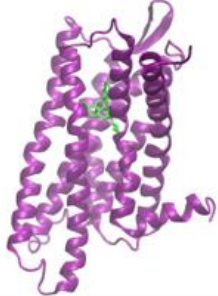
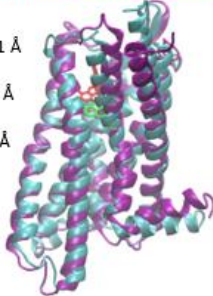
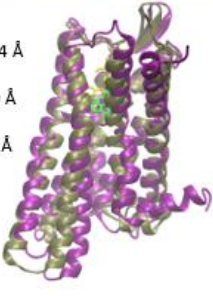
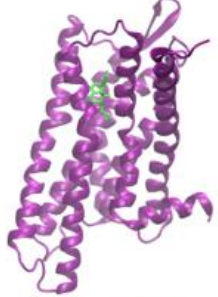
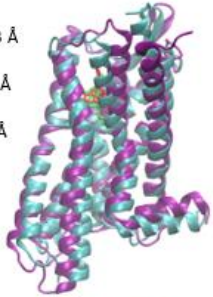
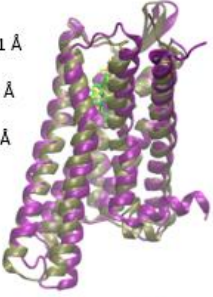

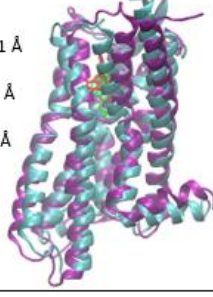
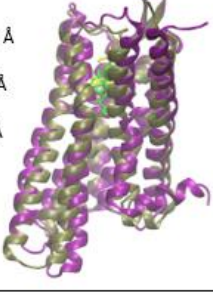
Trij 4 Cluster 3 (20%)		 <p>Protein: 2.6 Å 7TMs: 2.0 Å TM6: 2.4 Å</p>	 <p>Protein: 2.9 Å 7TMs: 2.3 Å TM6: 3.5 Å</p>
Trij 4 Cluster 4 (5%)		 <p>Protein: 2.7 Å 7TMs: 1.7 Å TM6: 2.2 Å</p>	 <p>Protein: 2.9 Å 7TMs: 2.3 Å TM6: 3.6 Å</p>
Trij 4 Cluster 5 (1%)		 <p>Protein: 3.6 Å 7TMs: 2.9 Å TM6: 5.8 Å</p>	 <p>Protein: 2.7 Å 7TMs: 2.1 Å TM6: 2.8 Å</p>
Trij 5 Cluster 1 (56%)		 <p>Protein: 2.8 Å 7TMs: 2.5 Å TM6: 3.1 Å</p>	 <p>Protein: 2.7 Å 7TMs: 2.4 Å TM6: 3.4 Å</p>



Tri 5 Cluster 2 (43%)		 <p>Protein: 2.2 Å 7TMs: 1.7 Å TM6: 2.5 Å</p>	 <p>Protein: 3.3 Å 7TMs: 2.8 Å TM6: 4.9 Å</p>
Tri 6 Cluster 1 (76%)		 <p>Protein: 3.3 Å 7TMs: 2.6 Å TM6: 3.9 Å</p>	 <p>Protein: 2.8 Å 7TMs: 2.4 Å TM6: 3.2 Å</p>
Tri 6 Cluster 2 (22%)		 <p>Protein: 2.3 Å 7TMs: 1.9 Å TM6: 2.0 Å</p>	 <p>Protein: 3.0 Å 7TMs: 2.5 Å TM6: 3.9 Å</p>

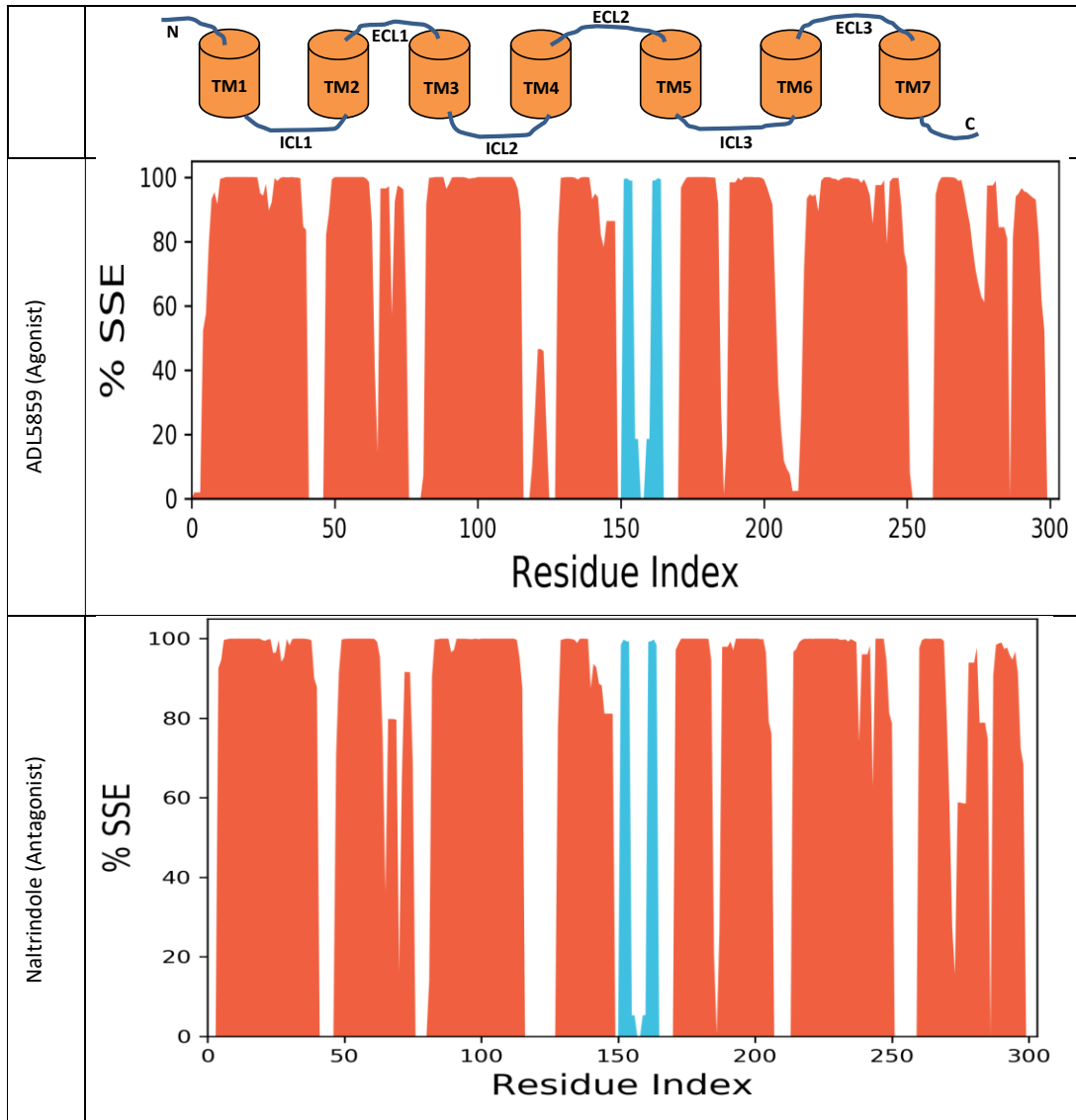
## Figure A8

*Representative Structure of Each DOR-Antagonist-Naltrindole Cluster and Its Comparison With the Inactive and Active Solved Crystal Structure*

	MD Structure	MD/Crystal Inactive Structure <sup>1</sup>	MD/Crystal Active Structure <sup>2</sup>
<b>Tlj 1 (100%)</b>		Protein: 3.1 Å 7TMs: 2.7 Å TM6: 1.8 Å 	Protein: 3.4 Å 7TMs: 3.0 Å TM6: 5.5 Å 
<b>Tlj 2 (100%)</b>		Protein: 3.3 Å 7TMs: 2.8 Å TM6: 2.9 Å 	Protein: 3.1 Å 7TMs: 2.8 Å TM6: 5.0 Å 
<b>Tlj 3 (100%)</b>		Protein: 3.1 Å 7TMs: 2.7 Å TM6: 2.4 Å 	Protein: 3.2 Å 7TMs: 2.9 Å TM6: 4.9 Å 

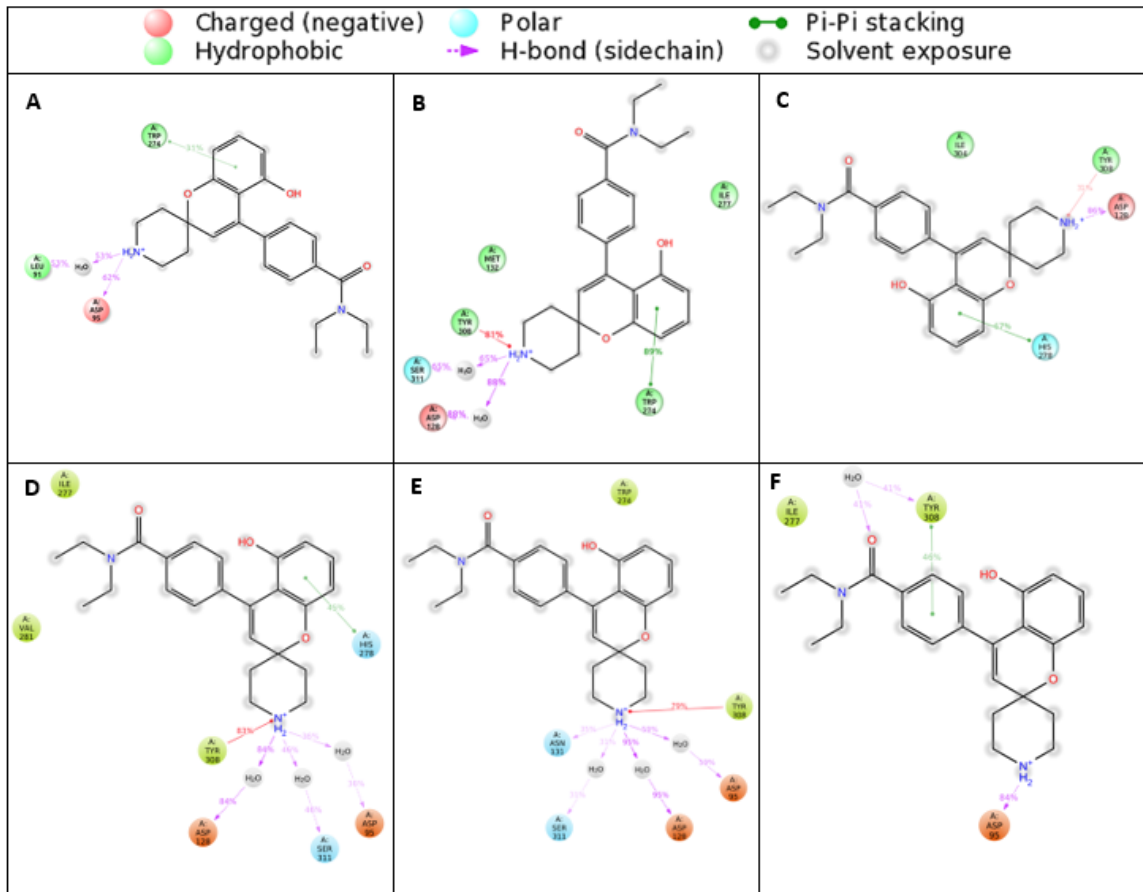
**Figure A9**

*Protein Secondary Structure Comparison*



**Figure A10**

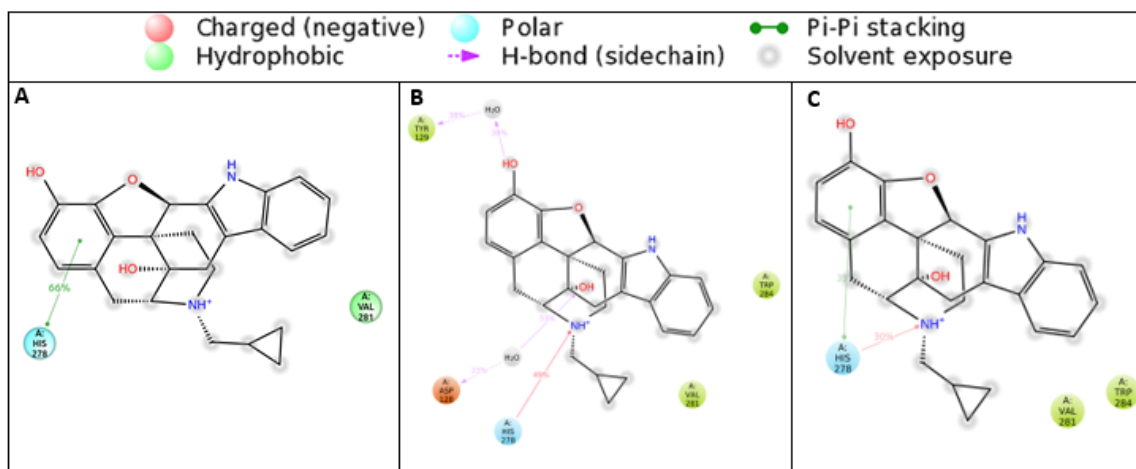
*Protein-Ligand 2D Interaction Diagram*





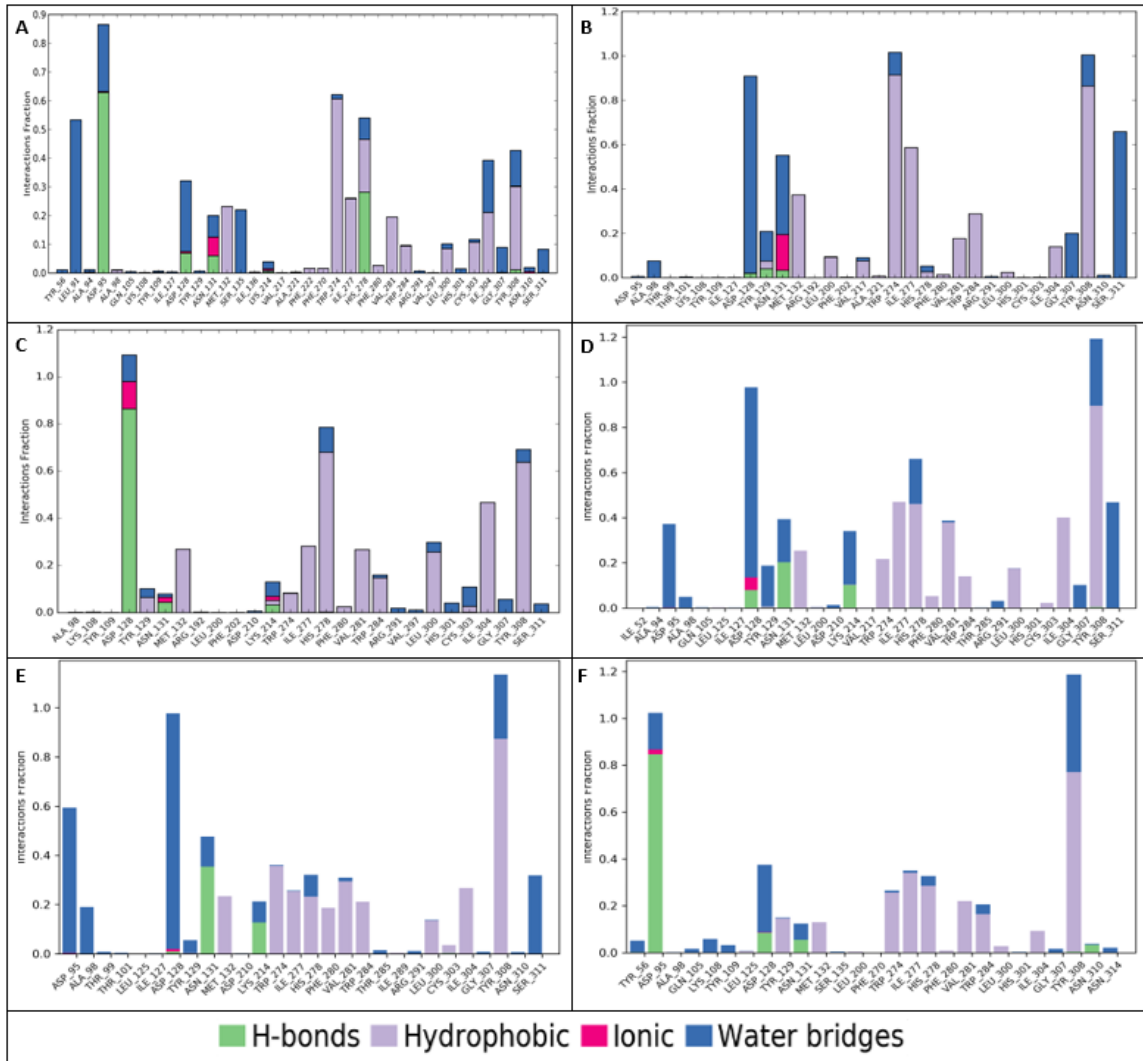
**Figure A11**

*Protein-Ligand 2D Interaction Diagram*



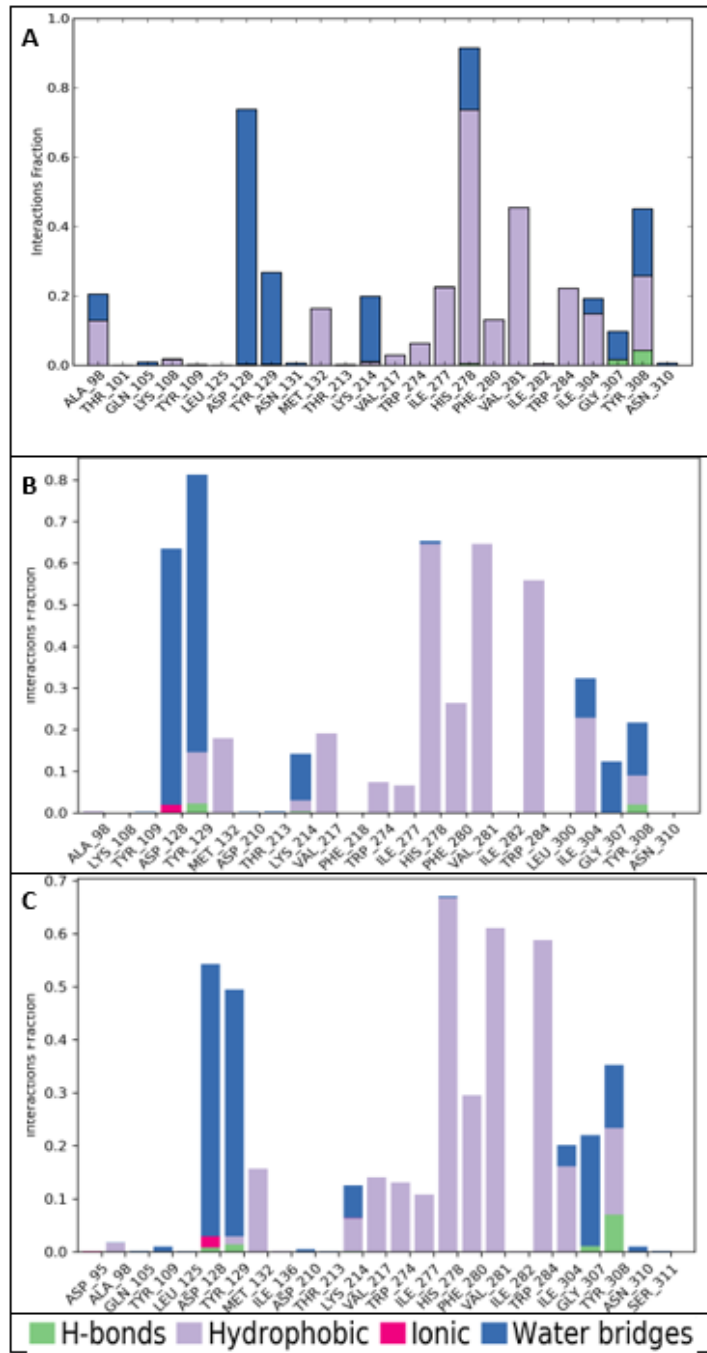
**Figure A12**

*Protein-Ligand Interactions*



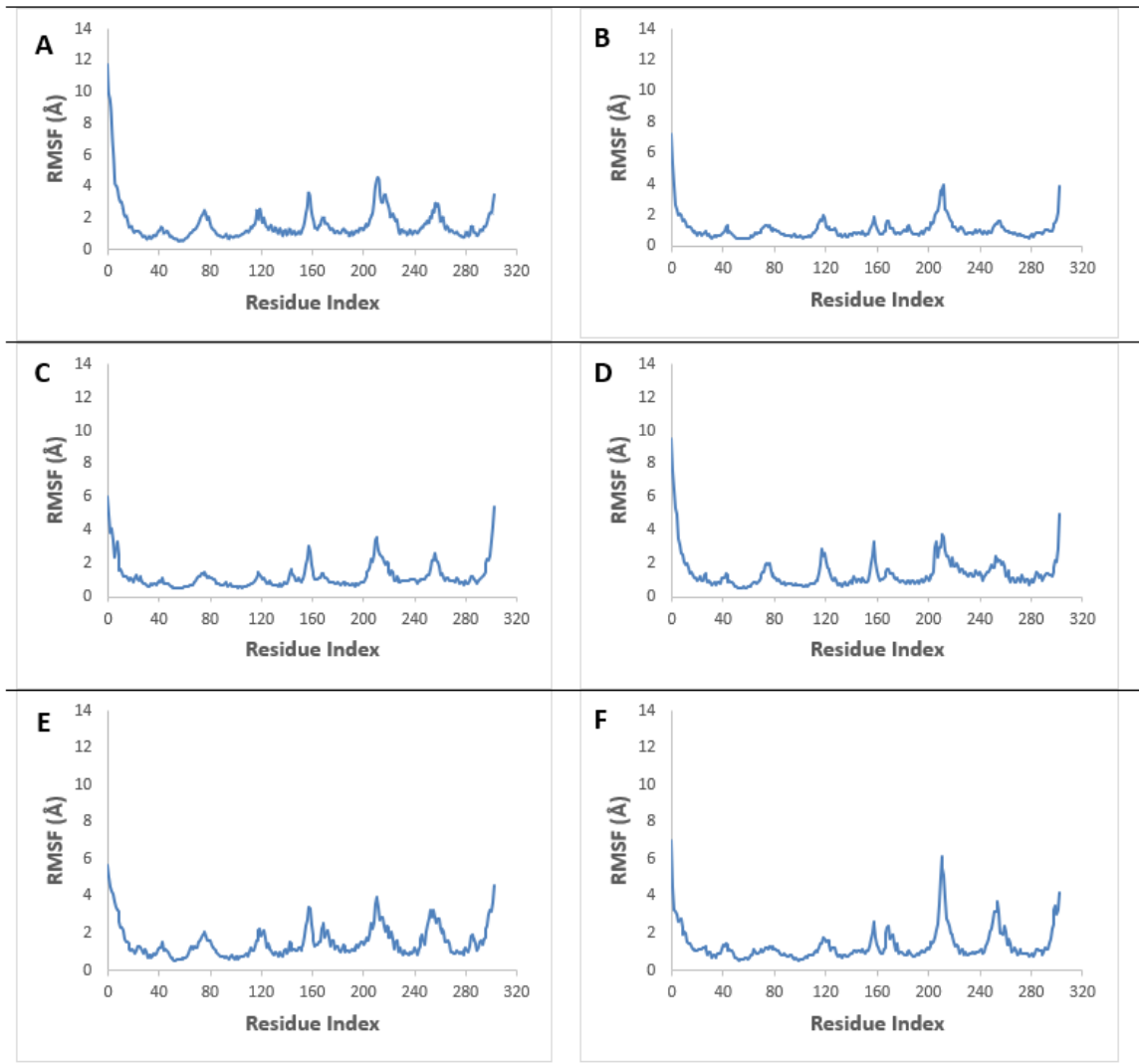
**Figure A13**

*Protein-Ligand Interactions*



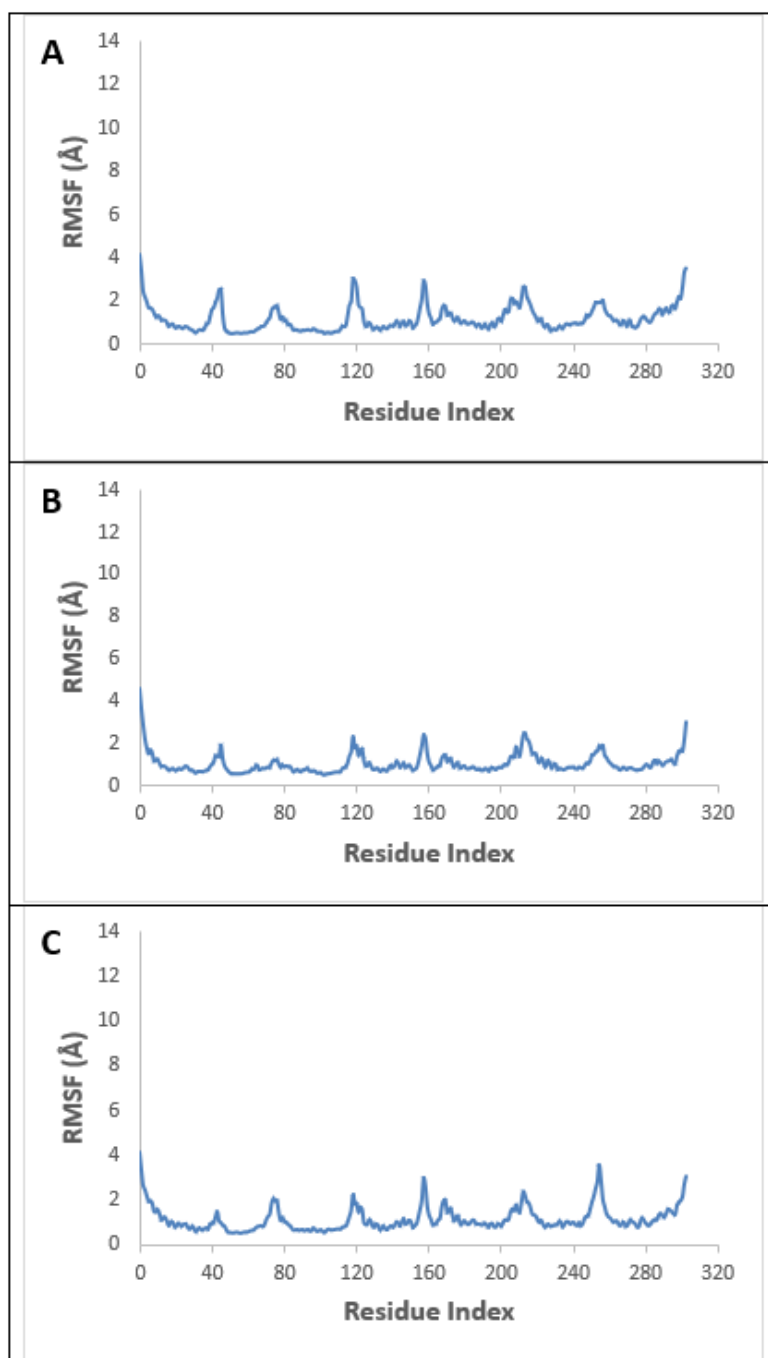
**Figure A14**

*The RMSF of the ADL5859 System*



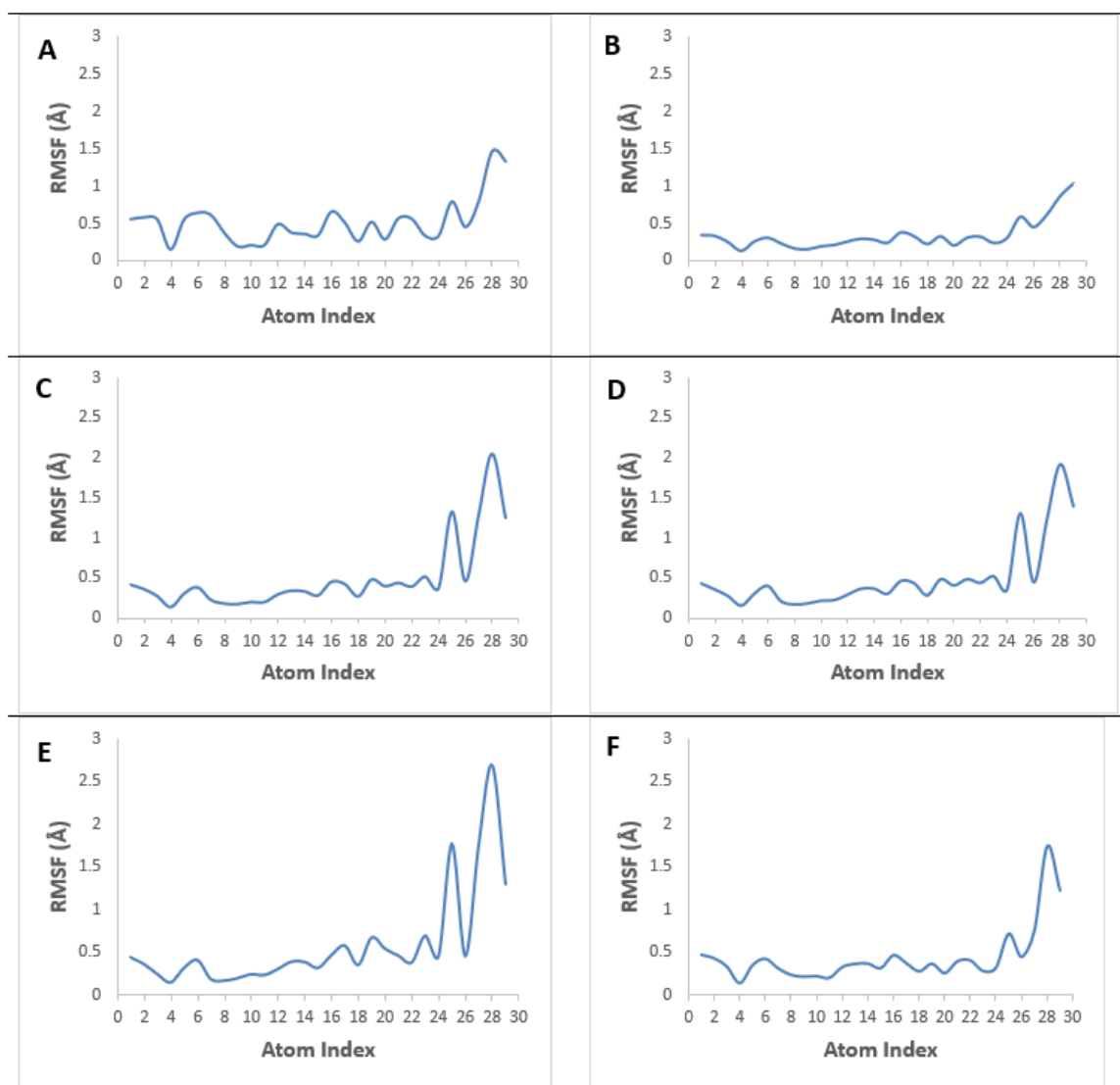
## Figure A15

*The RMSF of the Naltrindole System*



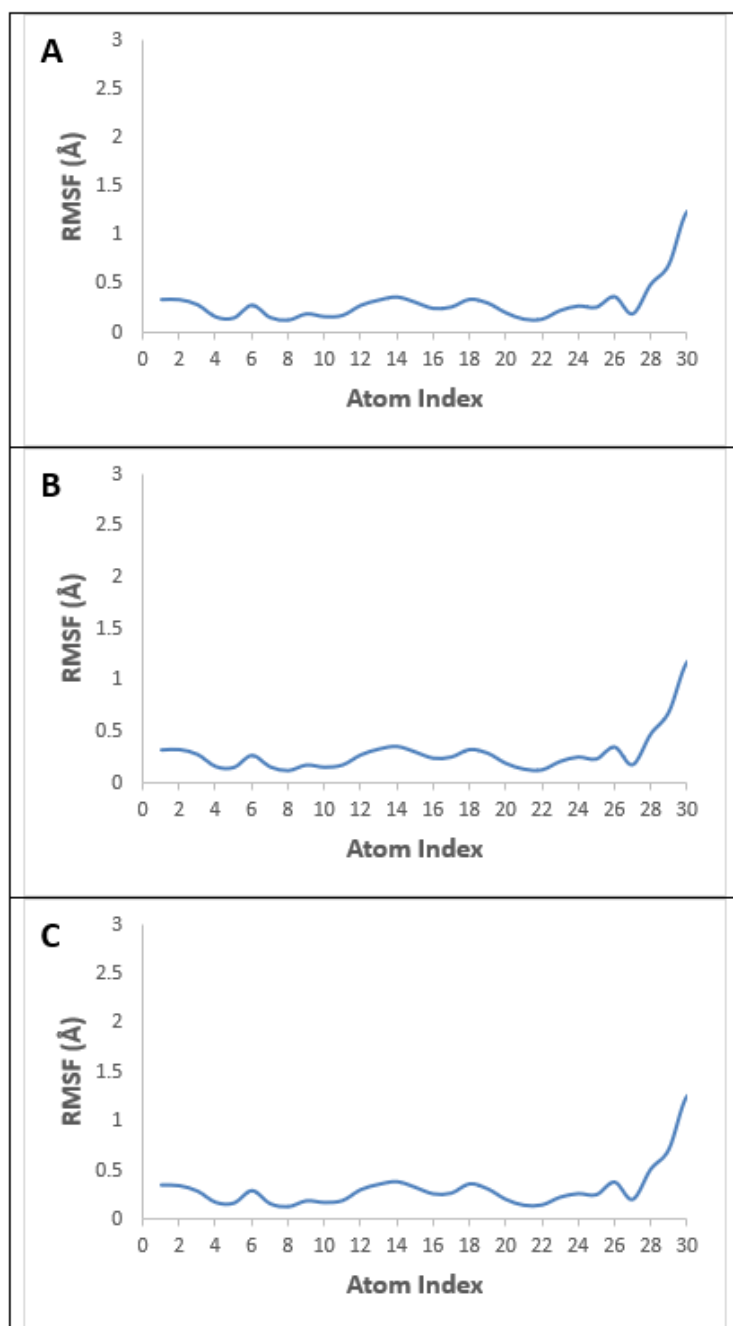
**Figure A16**

*Ligand RMSF Values For ADL5859*



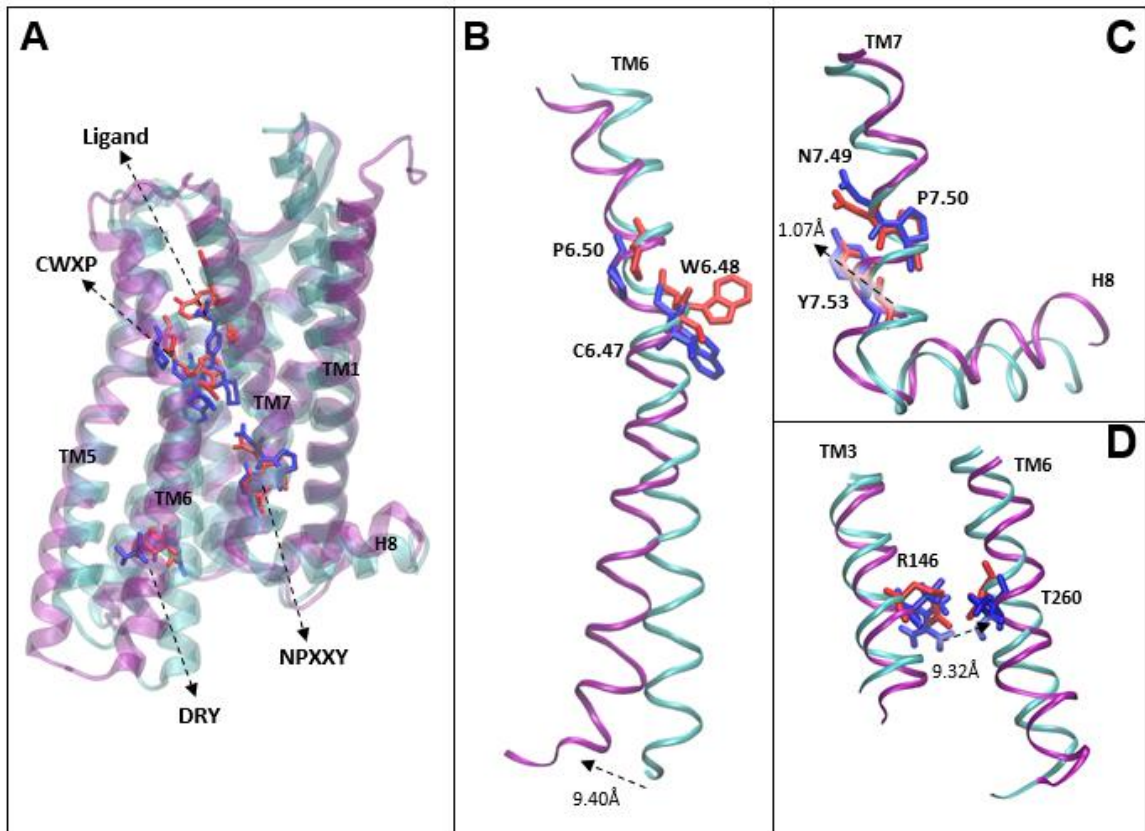
## Figure A17

*Ligand RMSF Values For Naltrindole*



## Figure A18

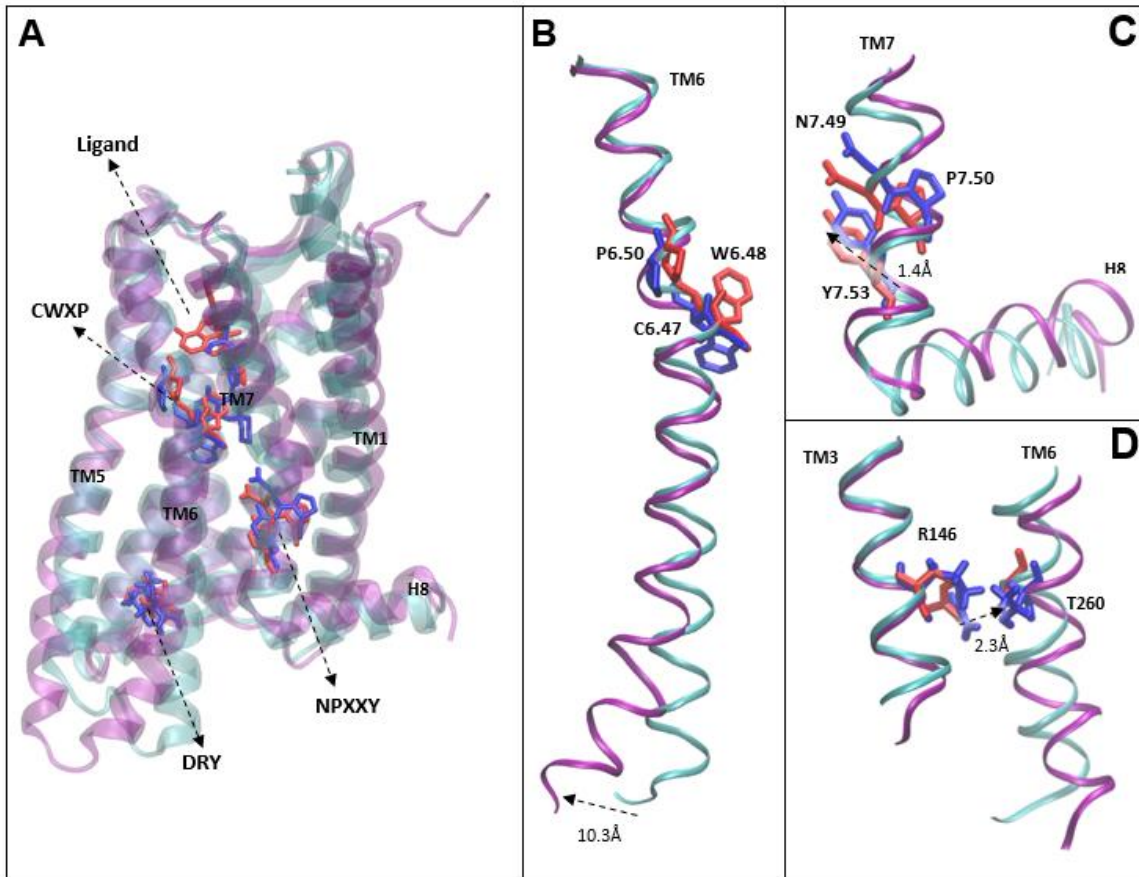
*Molecular Switches of ADL5859 (Trj 1 Cluster 1)*





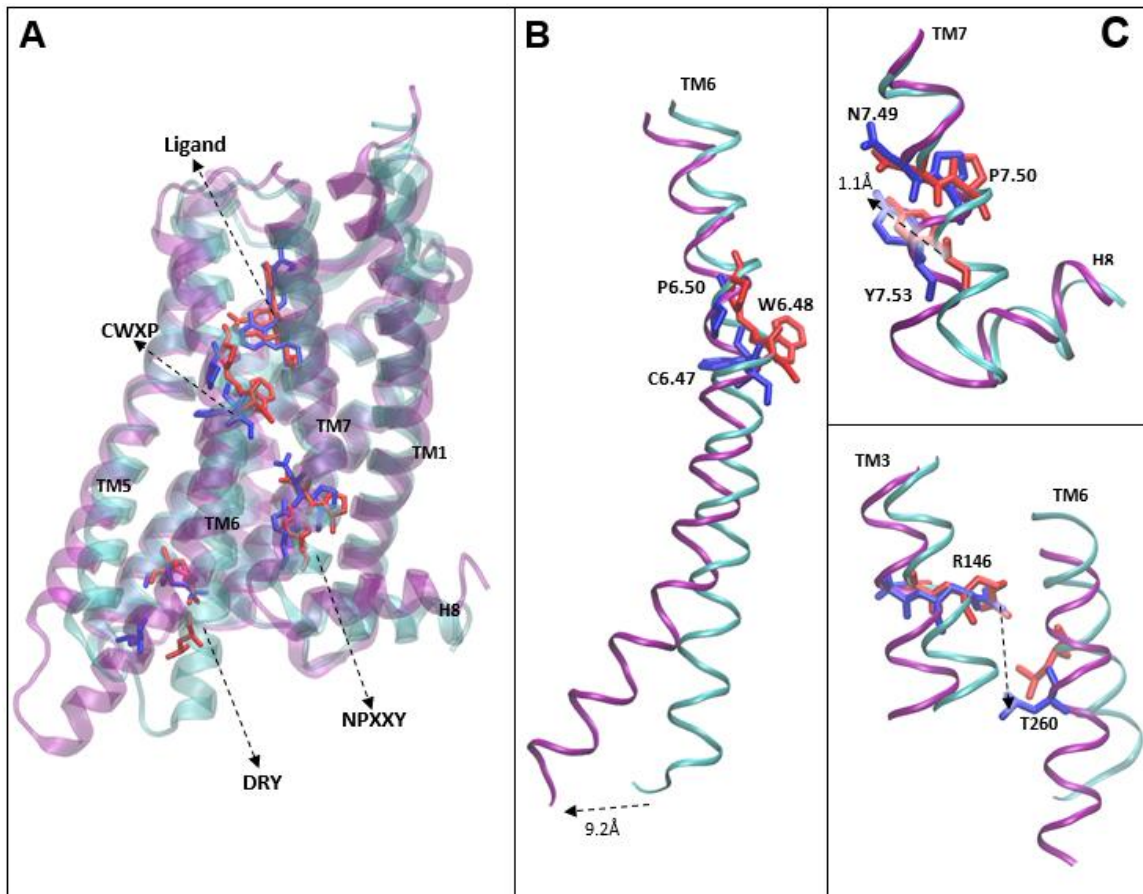
**Figure A19**

*Molecular Switches of ADL5859 (Trj 1 Cluster 3)*



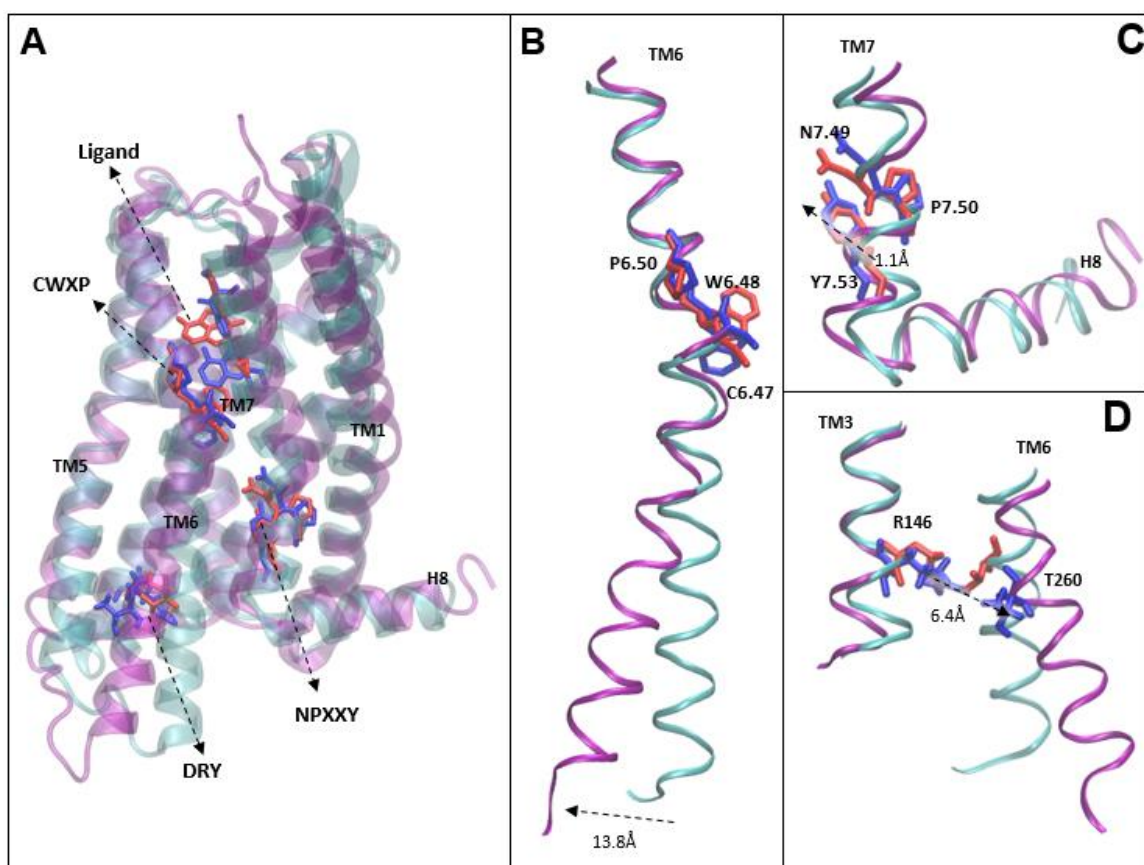
**Figure A20**

*Molecular Switches of ADL5859 (Trj 3 Cluster 2)*



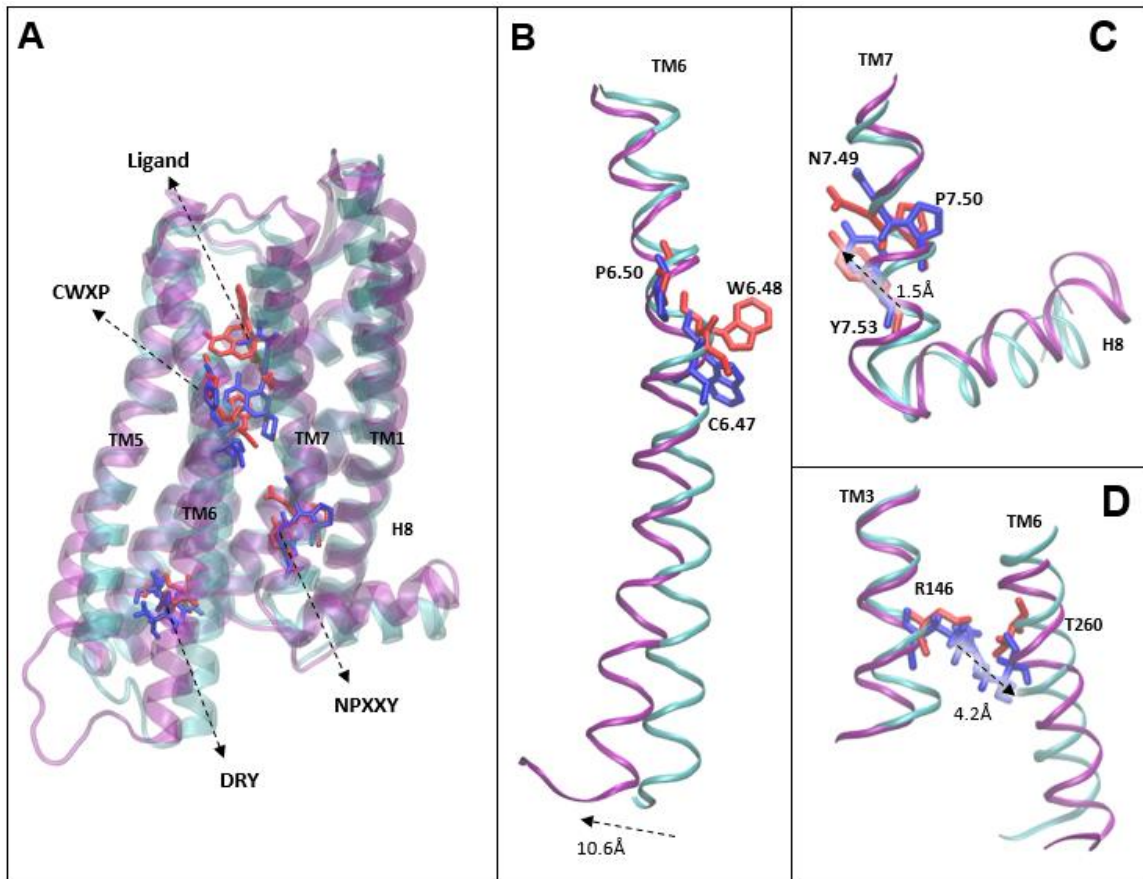
**Figure A21**

*Molecular Switches of ADL5859 (Trj 4 Cluster 5)*



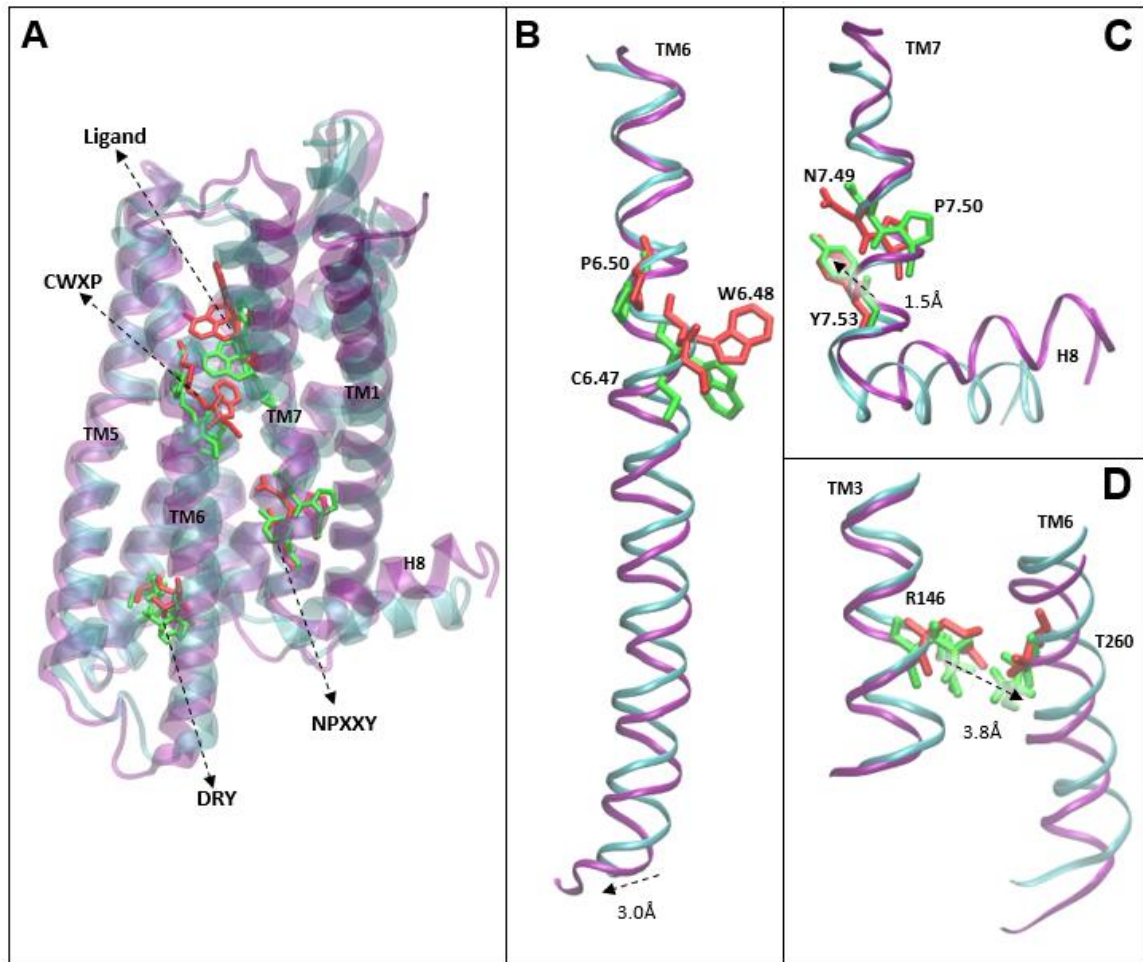
**Figure A22**

*Molecular Switches of ADL5859 (Trj 6 Cluster 1)*



**Figure A23**

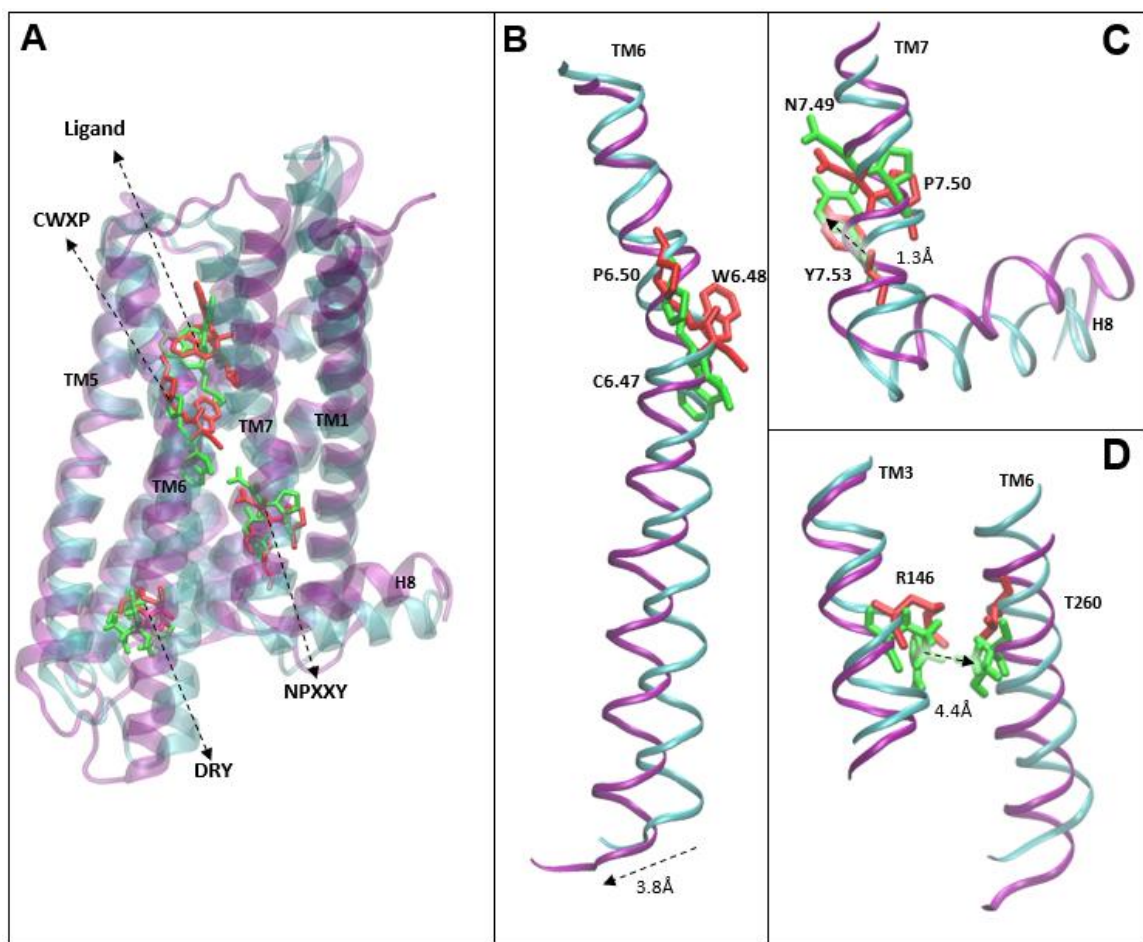
*Molecular Switches of Naltrindole (Trj 1)*





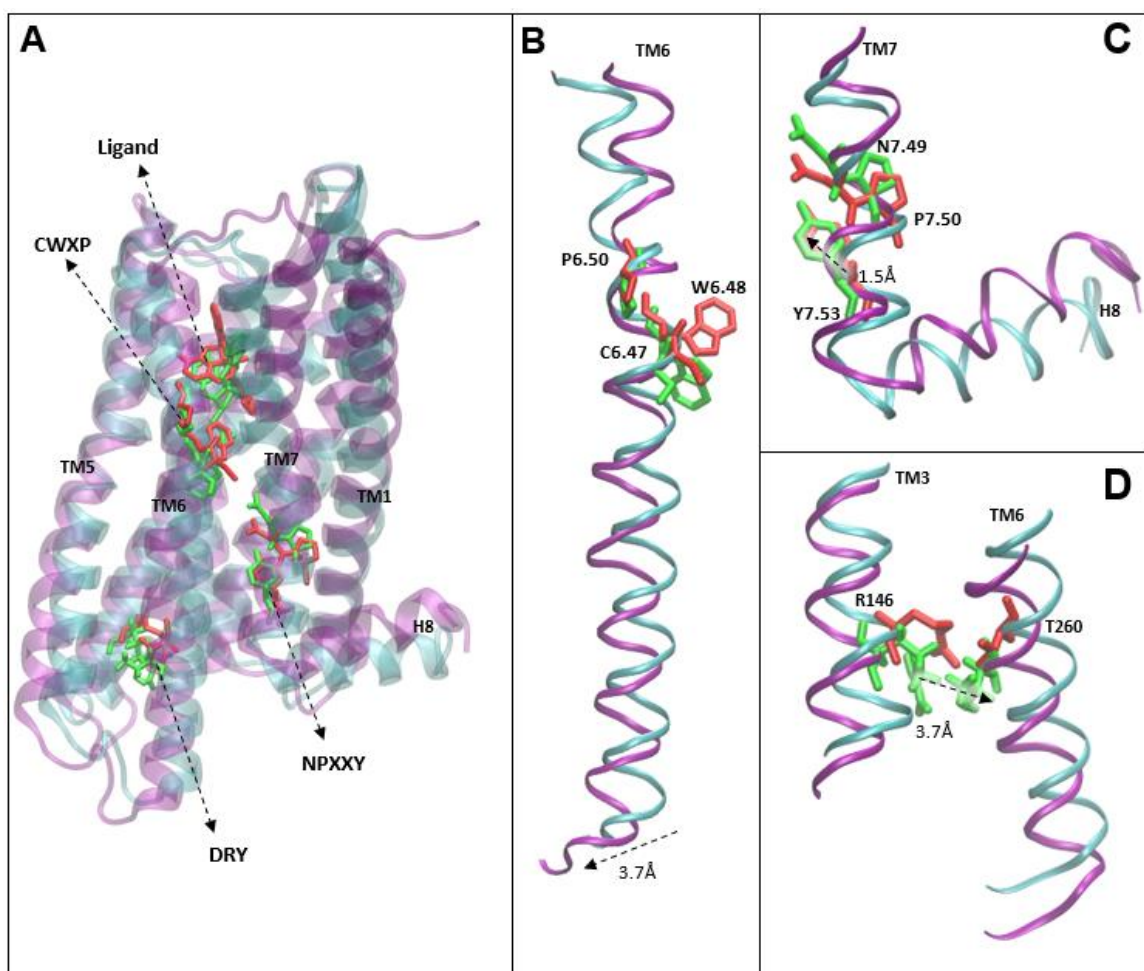
**Figure A24**

*Molecular Switches of Naltrindole (Trj 2)*



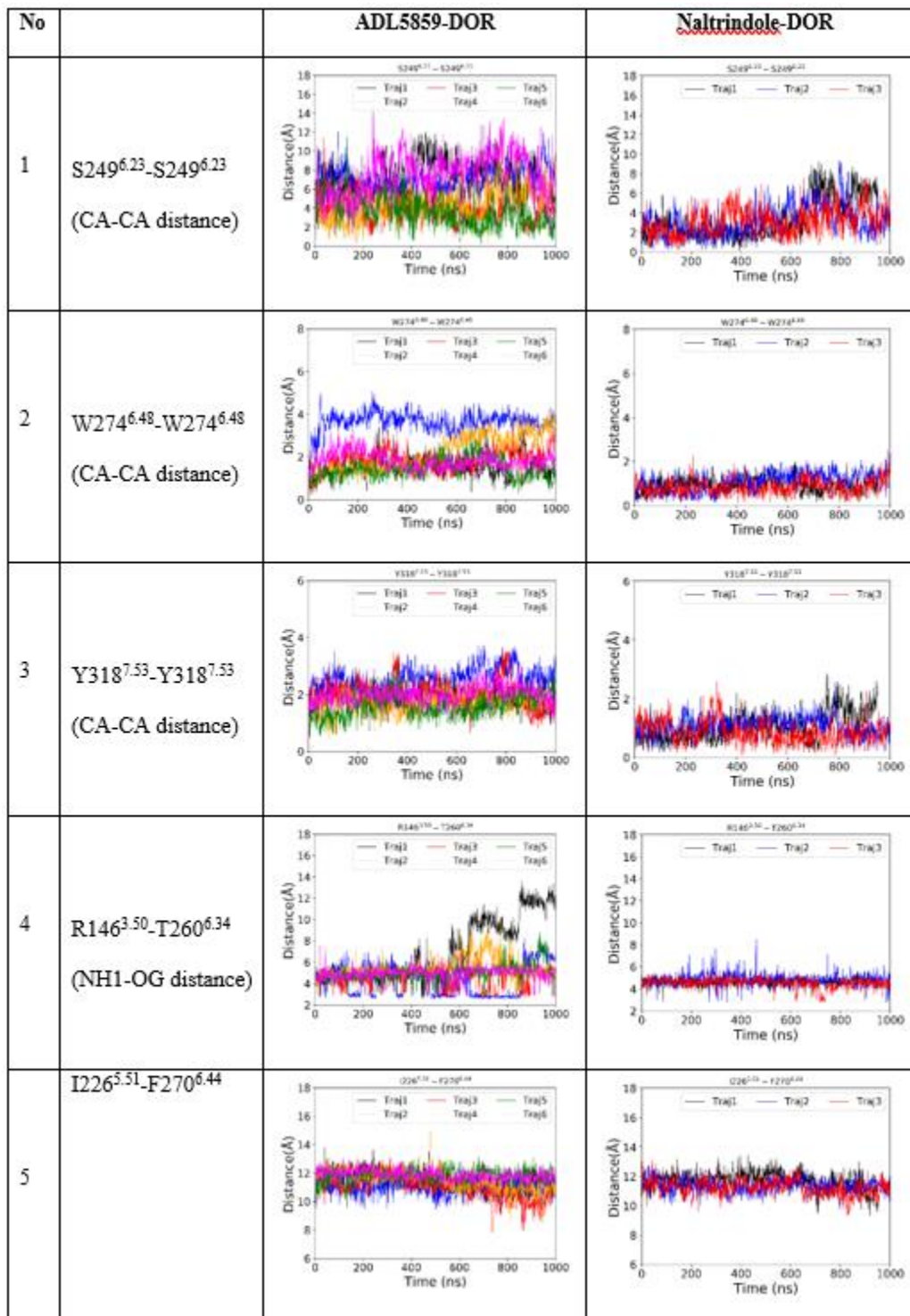
**Figure A25**

*Molecular Switches of Naltrindole (Trj 3)*

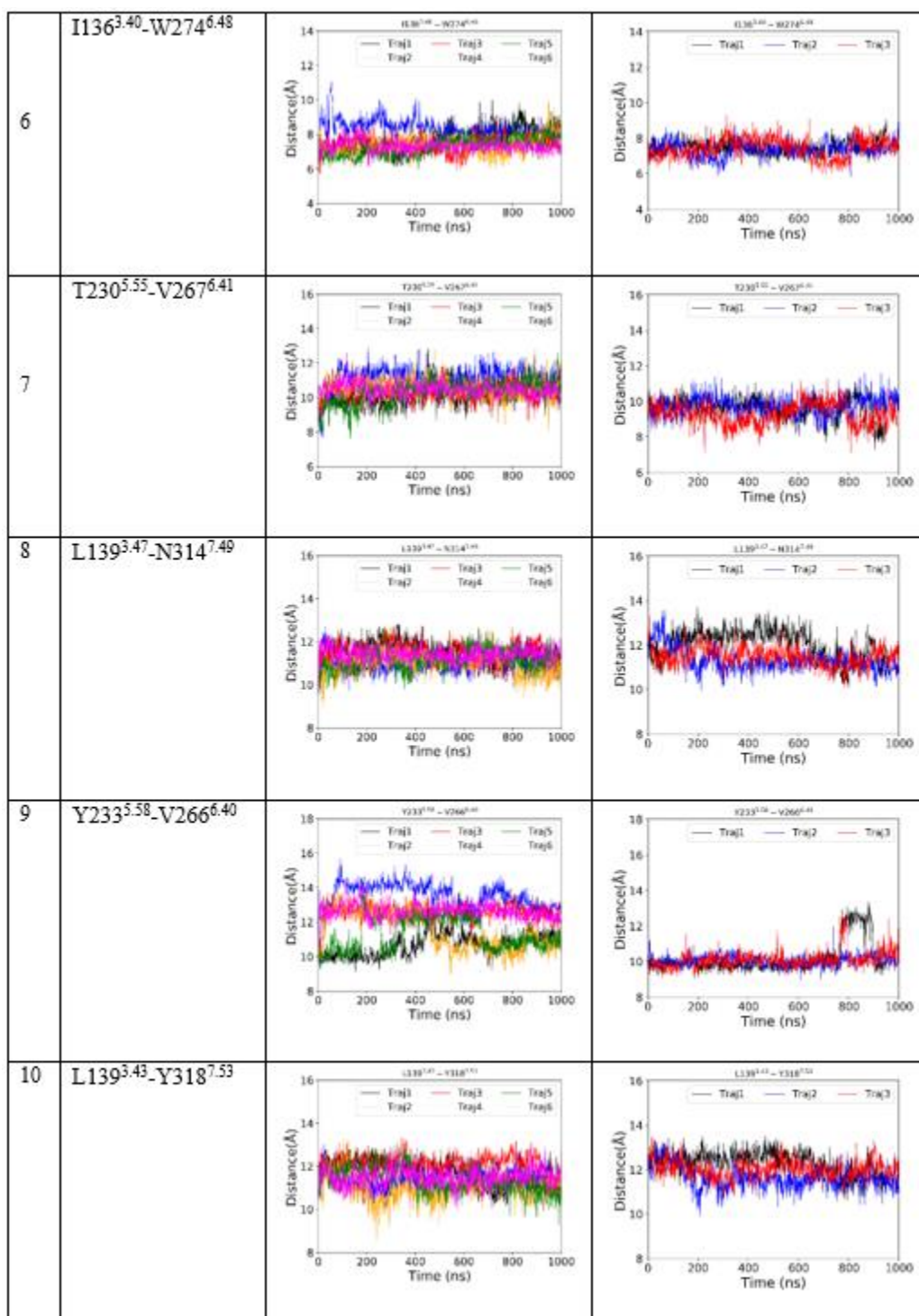


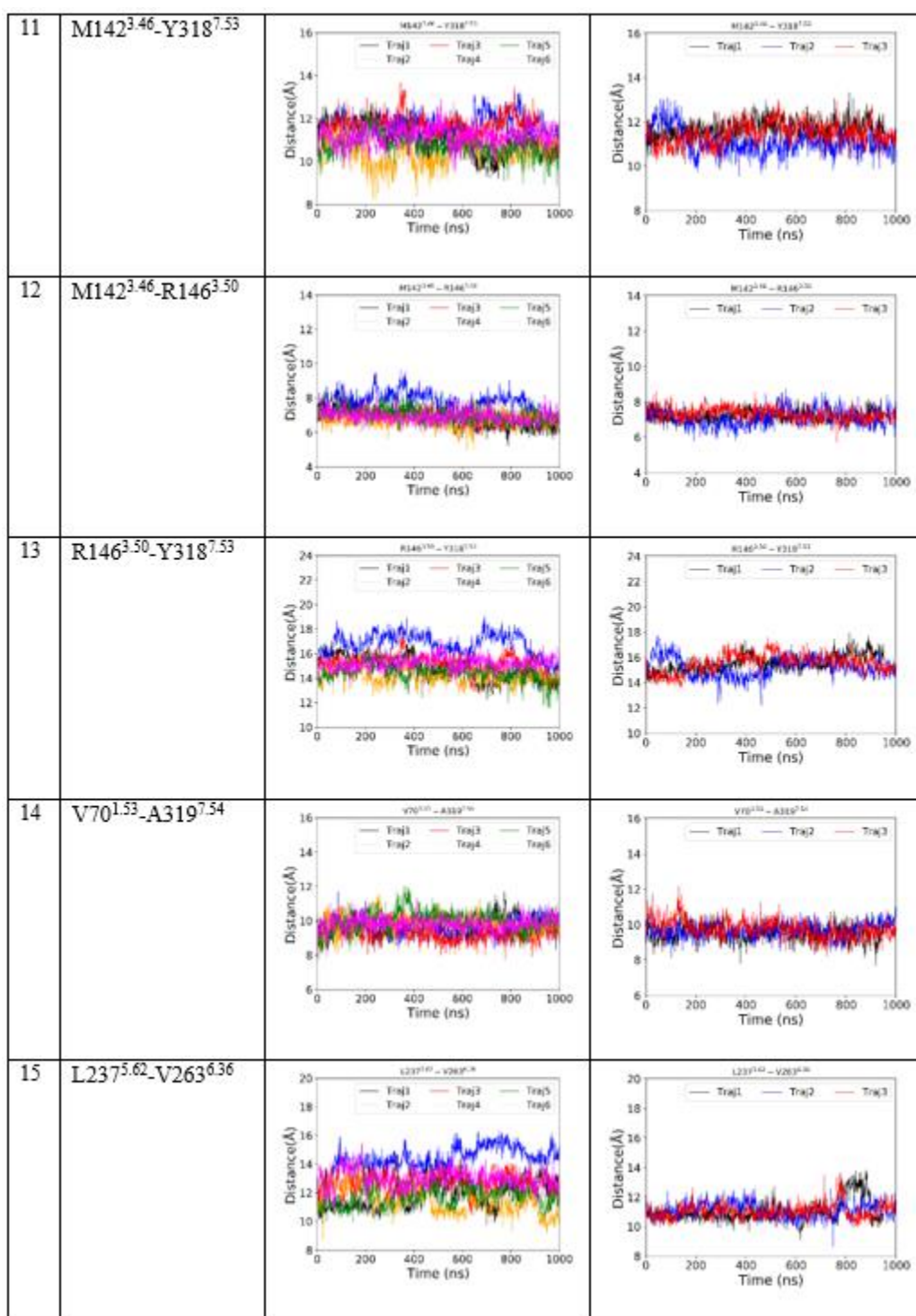
**Figure A26**

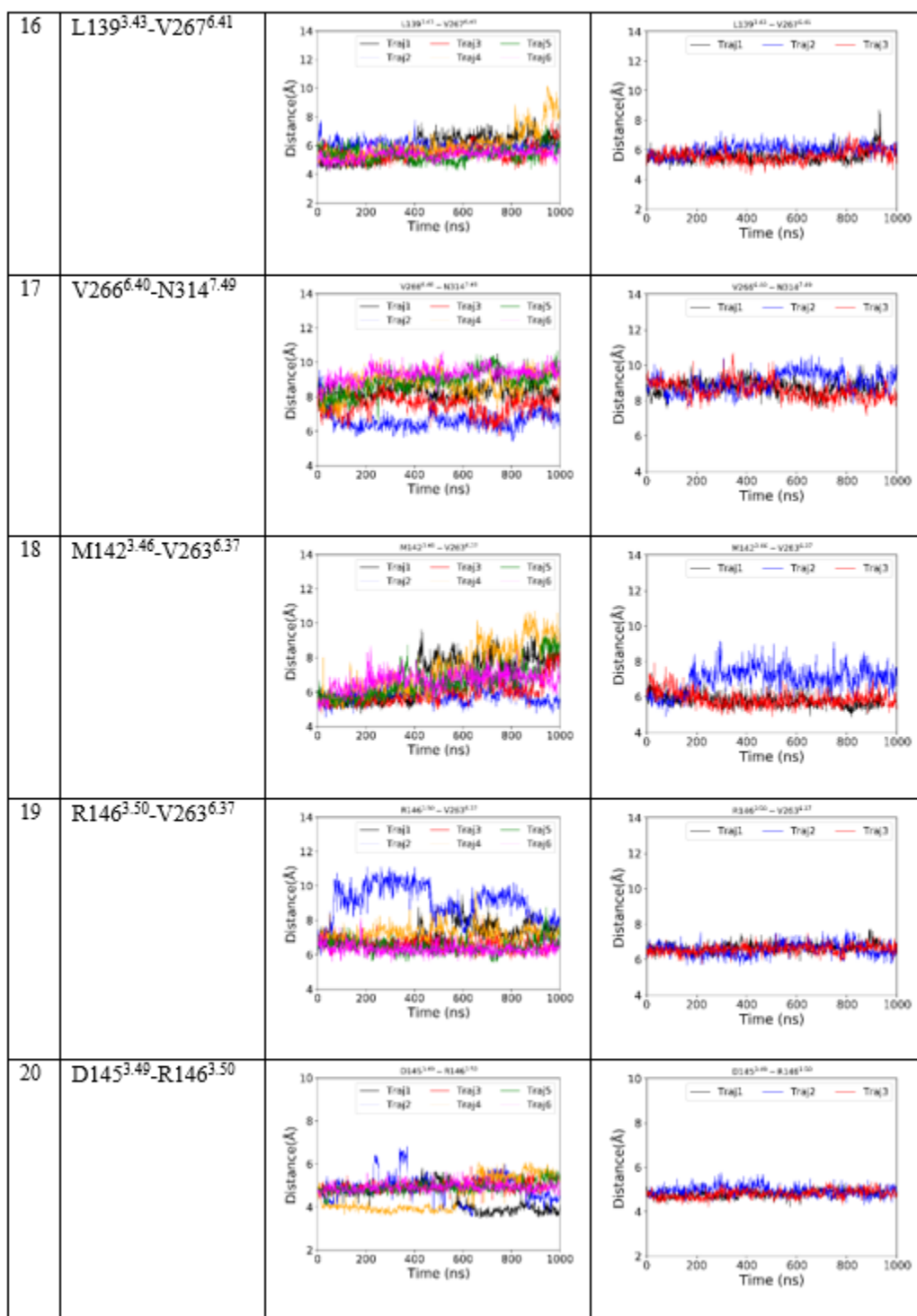
*Plots Showing Atomic (1-4) and Center of Mass (5-27) Distances Between Selected Residues of Human DOR in the Agonist and Antagonist Bound DOR Systems*

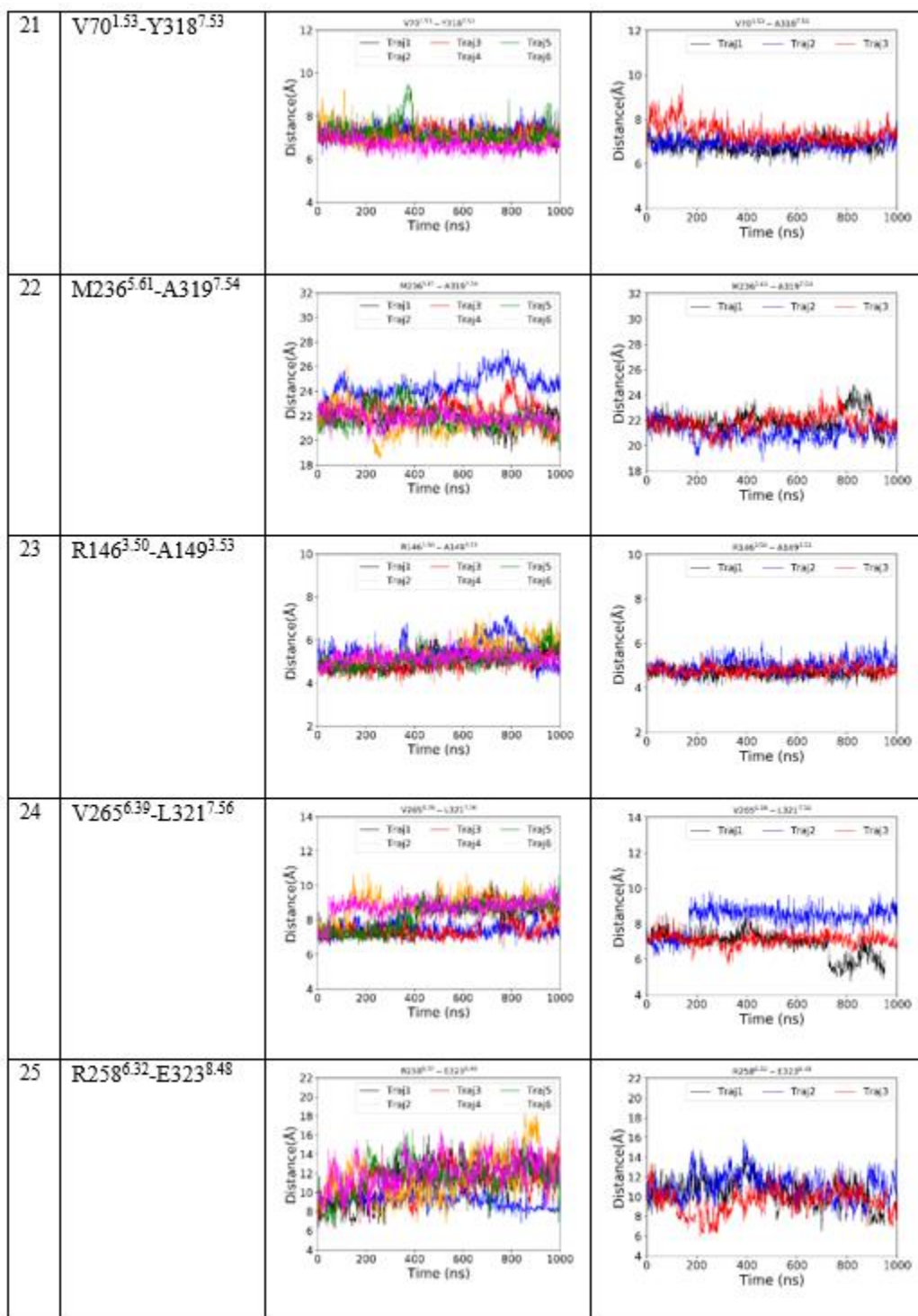


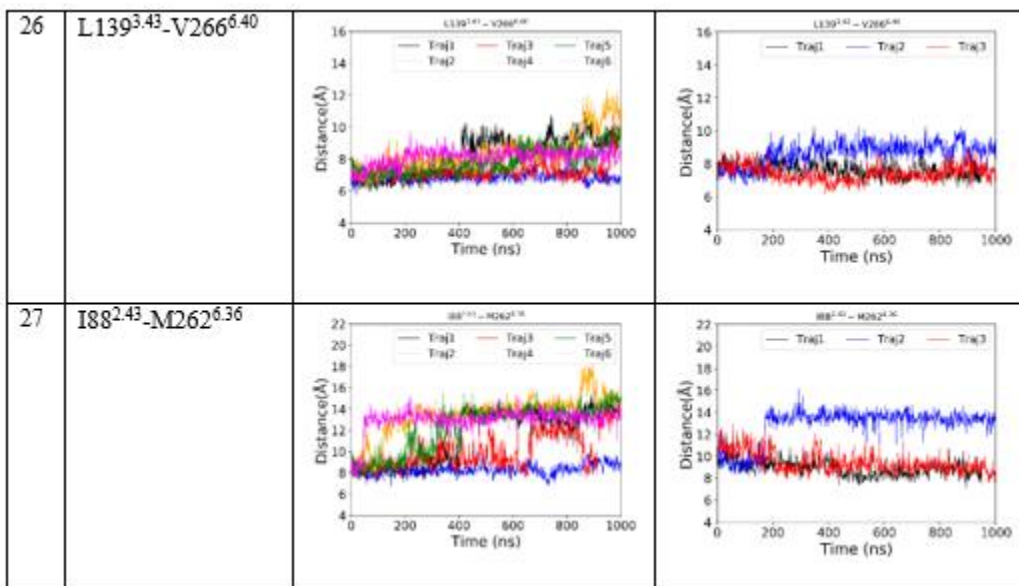








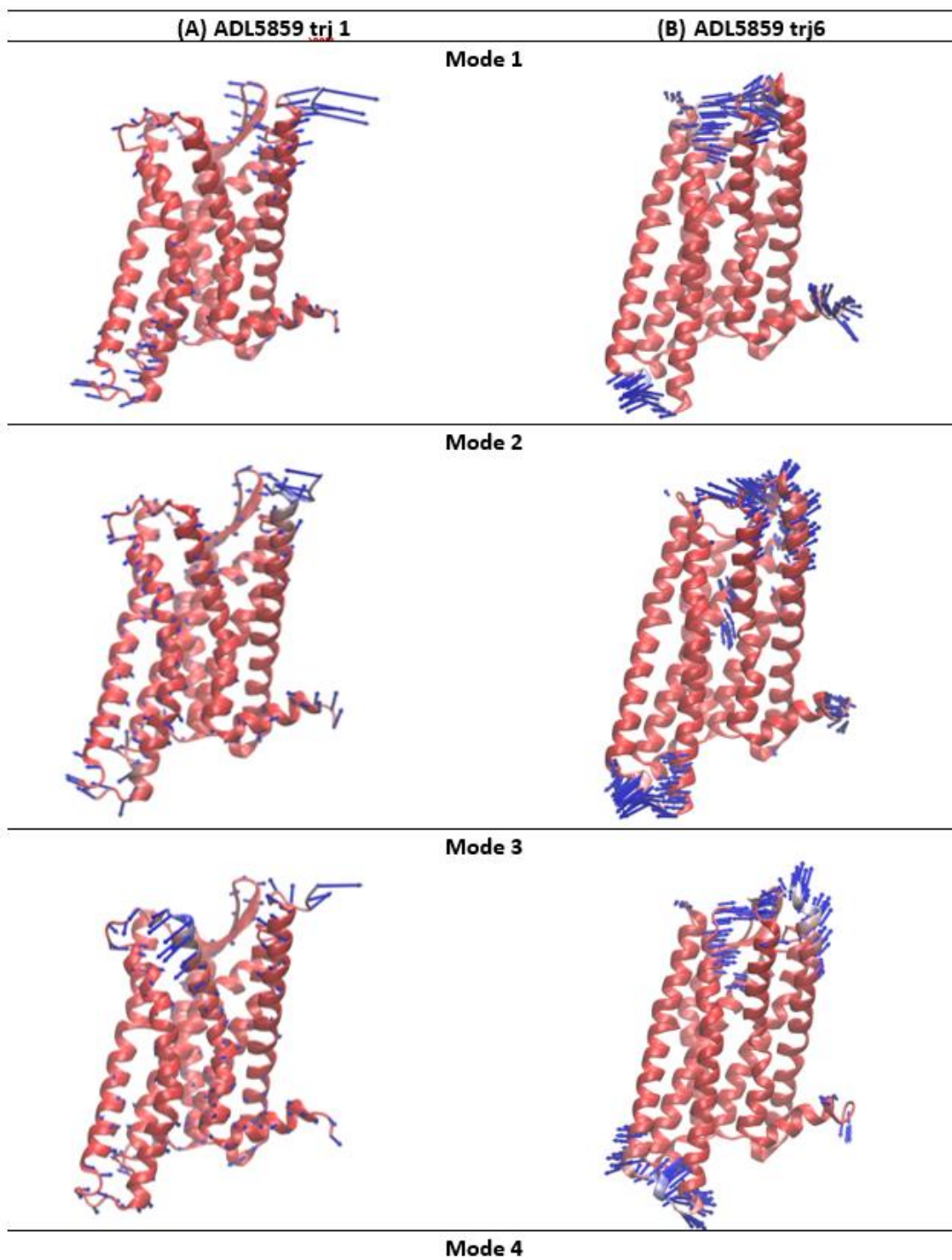


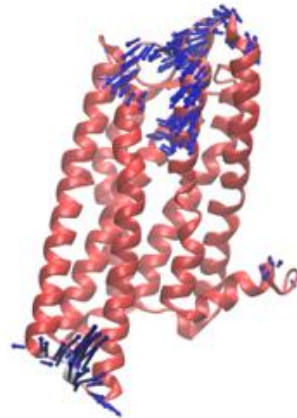
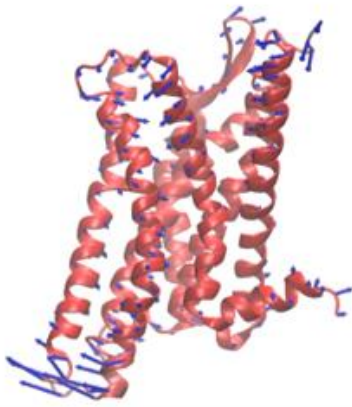




**Figure A27**

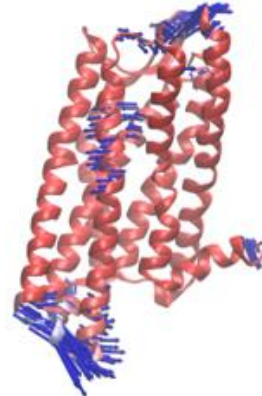
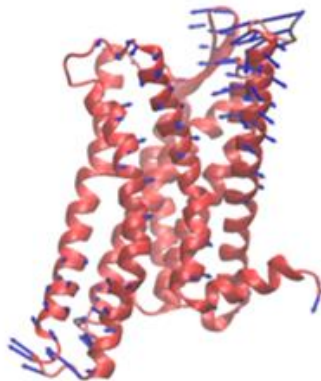
*Top 10 Low Vibrational Modes From the NMA Based on the Agonist ADL5859 Complex System in the First Trajectory (A) and Sixth Trajectory (B)*





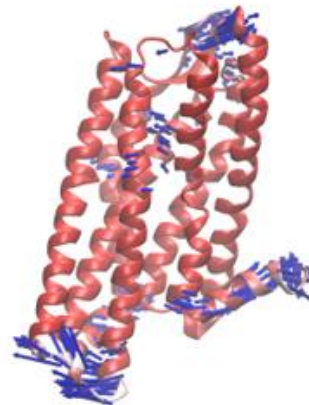
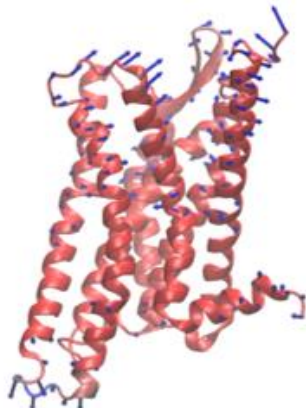
---

**Mode 5**



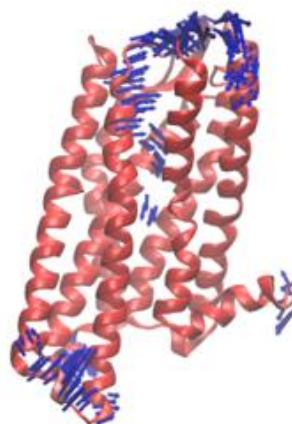
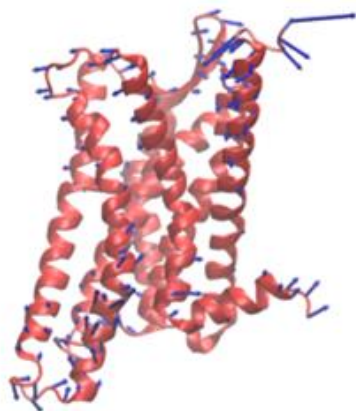
---

**Mode 6**



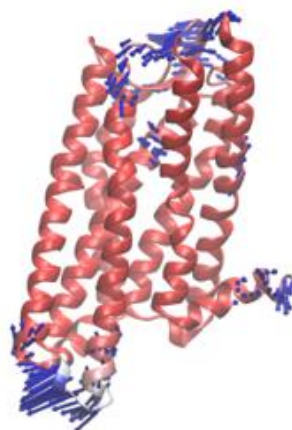
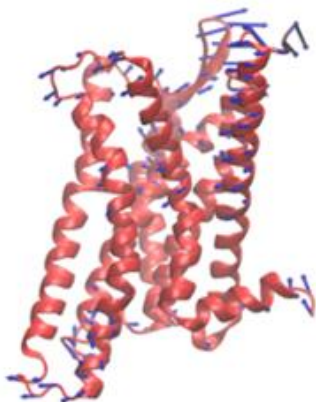
---

**Mode 7**



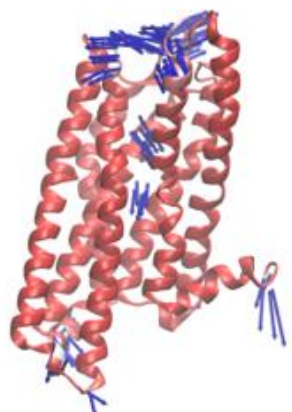
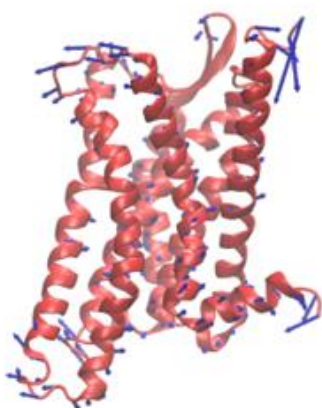
---

**Mode 8**



---

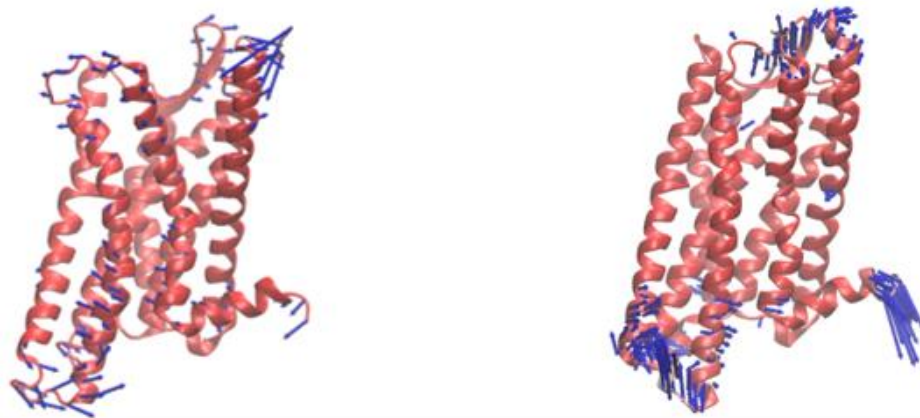
**Mode 9**



---

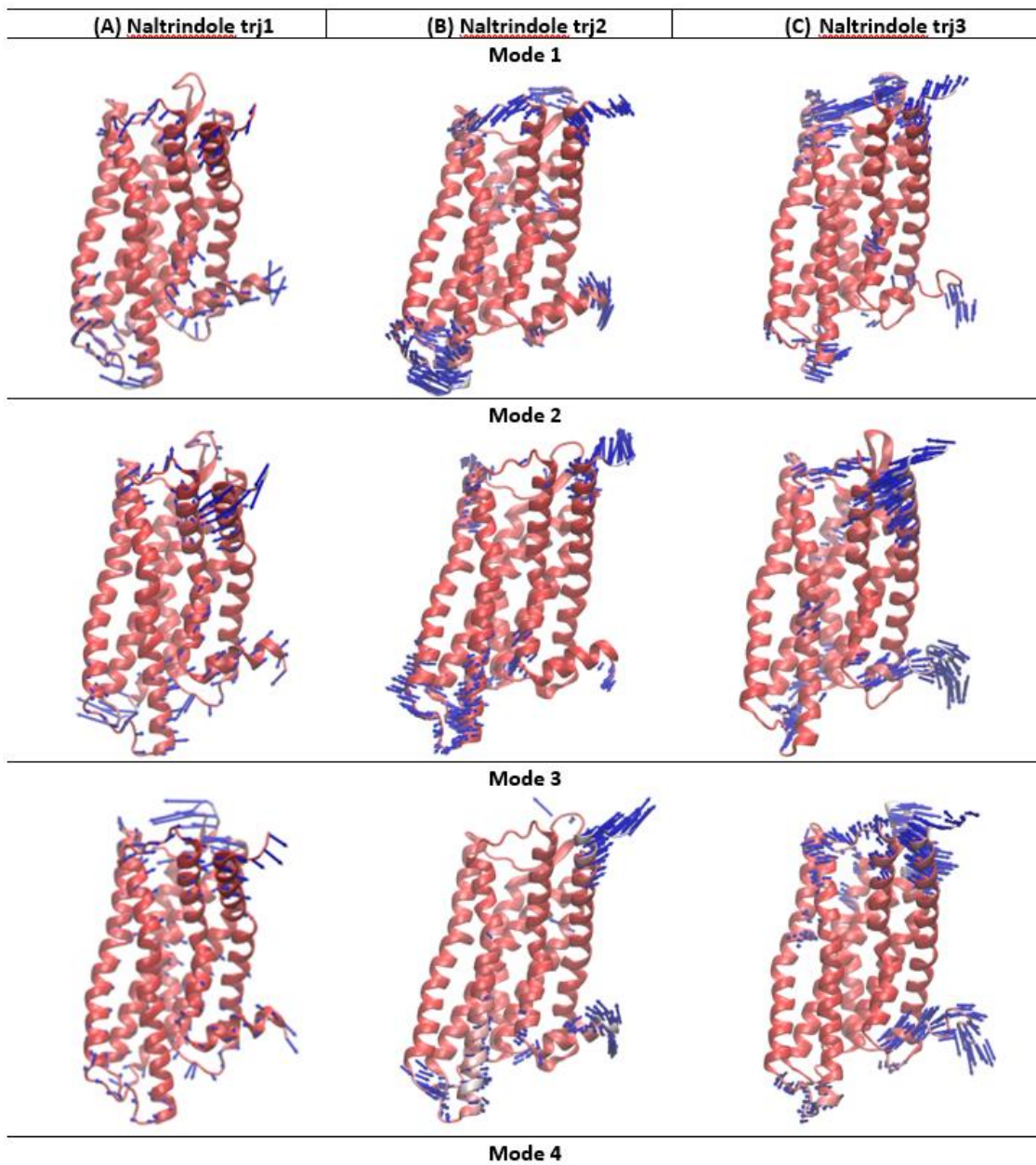
**Mode 10**

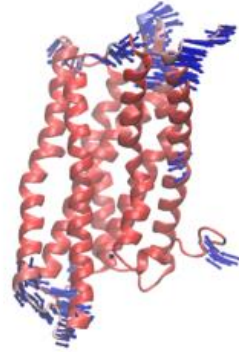
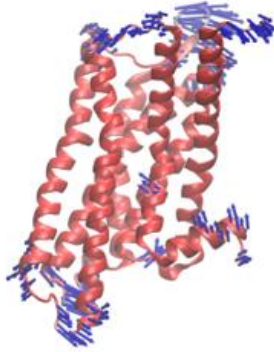
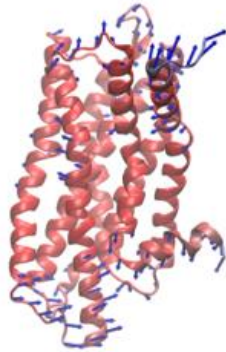




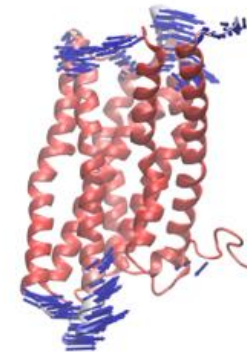
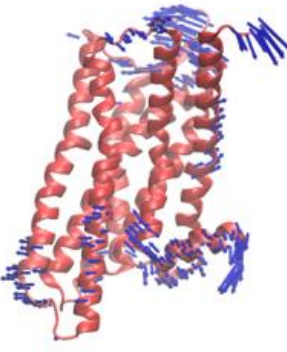
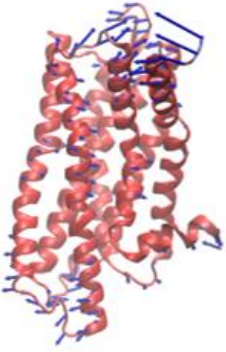
**Figure A28**

*Top 10 Low Vibrational Modes From the NMA Based on the Antagonist Naltrindole Complex System in the First (A), Second (B), and Third Trajectory (C)*

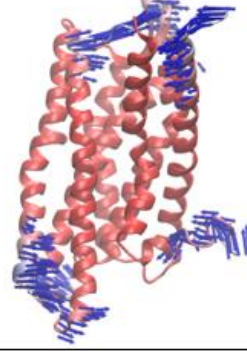
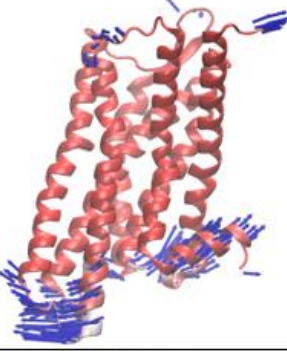




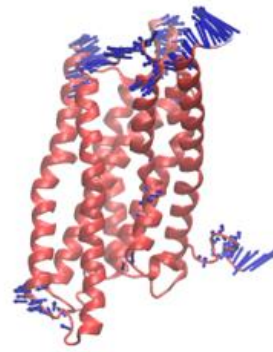
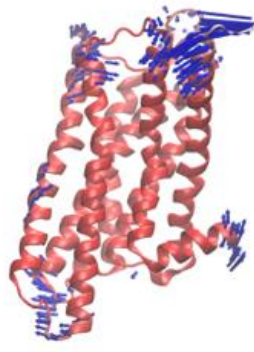
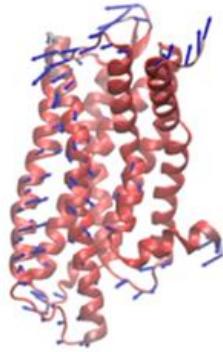
**Mode 5**



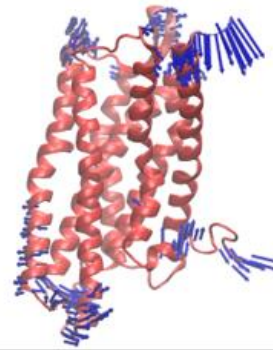
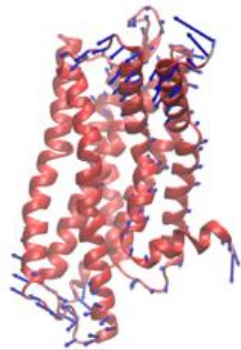
**Mode 6**



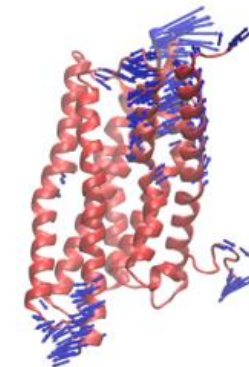
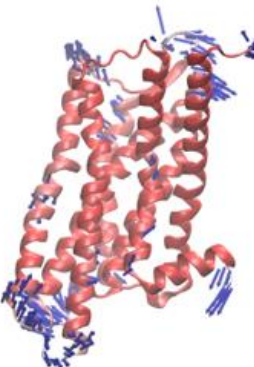
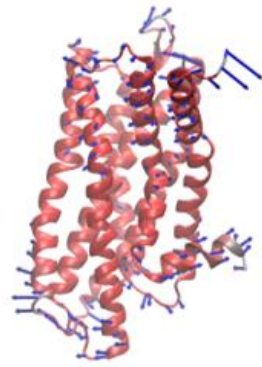
**Mode 7**



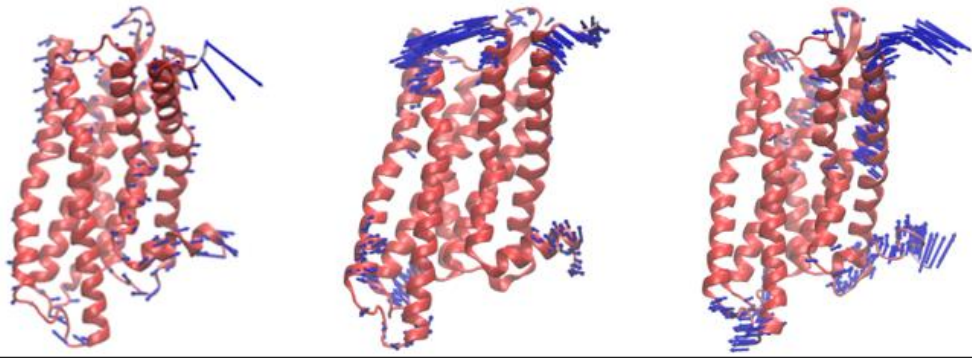
**Mode 8**



**Mode 9**



**Mode 10**



## **Appendix B**

# **To Probe Activation Mechanism of Agonist DPI-287 to Delta Opioid Receptor and Novel Agonists to Using Ensemble-Based Virtual Screening with Molecular Dynamics Simulations**



**Table B1**

*Detailed Information Regarding Various Properties From the Glide XP Docking and MD Simulations of the Compounds*

Structure	#	ZINC ID	Docking Score (kcal/mol)	VDW (kcal/mol)	ELE (kcal/mol)	Hydrophobic (kcal/mol)	MM-GBSA (kcal/mol)	Receptor RMSD <sup>1</sup> (Å)	Ligand RMSD <sup>1</sup> (Å)
	Ref.	<i>PDB ID: 6PT3</i>	-8.6	-57.0±2.8	18.5±3.7	-51.7±3.5	-90.2±6.3	2.9±0.1	2.5±0.1
CC	1	ZINC000020559278	-9.9	-44.7±2.8	-31.3±3.7	-40.8±2.3	-116.9±5.0	2.2±0.1	2.5±0.3
CC	2	ZINC000014242201	-9.9	-53.3±3.6	-25.5±7.6	-32.9±3.1	-111.7±9.6	3.9±0.2	6.8±0.5
CC	3	ZINC000562639987	-9.6	-40.3±4.1	-7.9±10.8	-31.9±3.3	-80.2±9.9	3.4±0.1	6.9±0.4
CC	4	ZINC000071763967	-9.5	-47.6±3.1	-16.3±5.3	-40.6±3.5	-104.5±7.6	2.5±0.1	2.2±0.2
CC	5	ZINC000067947687	-9.5	-42.0±3.7	-21.9±11.4	-37.1±2.6	-88.4±3.6	2.9±0.2	3.2±0.1
CC	6	ZINC000634950507	-9.4	-42.7±2.9	-11.4±7.3	-38.1±2.9	-92.2±7.6	2.2±0.1	2.6±0.2
CC	7	ZINC000072227493	-9.4	-38.6±3.9	-19.6±6.8	-43.2±4.6	-101.4±13.6	2.4±0.1	1.2±0.4
CC	8	ZINC000257262766	-9.4	-44.1±9.2	-23.1±21.4	-41.8±5.8	-108.9±29.6	2.4±0.2	12.2±0.7
CC	9	ZINC000006645700	-9.3	-41.4±2.8	-19.7±4.5	-41.2±1.9	-102.3±5.0	3.0±0.2	3.6±0.2
CC	10	ZINC000082157638	-9.3	-42.1±2.9	-15.3±6.2	-36.3±2.5	-93.7±7.6	2.4±0.1	3.2±0.2
CC	11	ZINC000091782363	-9.3	-42.4±3.6	-24.5±3.9	-32.0±2.2	-98.9±6.0	2.9±0.1	1.5±0.2
CC	12	ZINC000091595762	-9.3	-49.9±3.7	-17.9±3.9	-48.0±4.1	-115.9±7.3	2.5±0.2	1.9±0.2
CC	13	ZINC000067558896	-9.1	-39.7±2.7	-19.9±6.8	-38.6±3.2	-98.3±6.7	3.3±0.1	3.6±0.2
CC	14	ZINC000757213857	-9.0	-22.1±4.6	-60.3±8.7	-29.3±2.6	-111.8±9.2	3.0±0.1	3.7±0.3
CC	15	ZINC000218867772	-9.0	-29.2±2.8	-23.6±5.9	-38.7±3.3	-91.5±7.8	2.6±0.1	3.7±0.4
CC	16	ZINC000013637398	-8.9	-47.6±4.7	-25.0±7.4	-24.3±2.2	-97.0±7.9	2.2±0.1	1.7±0.2
CC	17	ZINC000078515864	-8.9	-36.2±3.8	-25.9±5.3	-50.9±2.9	-113.1±6.1	2.6±0.1	2.7±0.2
CC	18	ZINC000014538415	-8.9	-65.5±5.0	-25.4±6.3	-62.6±6.3	-153.6±11.6	3.2±0.1	5.4±0.2
CC	19	ZINC000218873420	-8.9	-23.1±3.6	-53.8±6.0	-29.1±2.4	-106.1±7.1	2.5±0.1	2.4±0.2
CC	20	ZINC000001743629	-8.9	-43.7±3.1	-17.7±7.1	-50.8±3.8	-112.3±9.7	2.4±0.1	3.9±0.8
CC	21	ZINC000028295259	-8.9	-47.0±5.9	-19.3±6.2	-45.1±4.8	-111.4±8.9	2.6±0.1	3.3±0.2
CC	22	ZINC000014536536	-8.9	-51.3±3.9	-23.5±3.3	-52.6±4.7	-127.5±7.5	2.8±0.1	3.0±0.2
CC	23	ZINC000147095213	-8.8	-31.4±3.6	-34.4±5.7	-39.1±3.8	-104.9±8.7	3.8±0.1	2.9±0.2
CC	24	ZINC000095698957	-8.8	-40.5±4.4	-22.0±8.8	-38.4±2.9	-100.9±8.4	3.1±0.1	3.2±0.2
CC	25	ZINC000014888594	-8.8	-46.9±4.2	-30.8±5.5	-44.7±3.1	-122.5±7.8	3.4±0.2	3.0±0.4
CC	26	ZINC000015080658	-8.8	-50.0±3.7	-17.0±5.3	-36.5±4.7	-103.5±11.3	3.5±0.2	2.4±0.3
CC	27	ZINC000096027748	-8.8	-24.6±3.3	-27.0±15.4	-26.2±2.5	-77.8±16.4	2.5±0.1	2.4±0.3
CC	28	ZINC000067675691	-8.8	-47.5±4.9	-22.0±6.2	-45.2±6.1	-114.7±12.4	3.2±0.1	5.4±0.3
CC	29	ZINC000011691661	-8.7	-40.4±7.1	-37.2±19.1	-42.2±3.3	-119.8±16.1	4.0±0.2	8.1±0.3
CC	30	ZINC000096312018	-8.7	-43.6±3.3	-16.5±7.5	-36.7±2.7	-96.8±8.2	2.8±0.1	3.6±0.4
CC	31	ZINC000248261142	-8.7	-42.3±4.5	-22.7±7.4	-44.2±3.9	-109.2±9.3	3.3±0.1	3.0±0.5
CC	32	ZINC000036160706	-8.7	-53.2±5.0	-23.1±5.0	-43.7±3.1	-120.0±10.0	2.6±0.1	4.3±0.6
C1	1	ZINC000025329384	-10.2	-57.2±3.6	-19.9±9.4	-57.7±4.1	-134.9±11.3	2.4±0.1	2.9±0.4
C1	2	ZINC000037556415	-9.4	-58.5±2.4	-9.6±2.3	-43.8±2.6	-111.9±5.1	3.4±0.2	6.0±0.1
C1	3	ZINC000095456365	-9.2	-53.6±3.8	-24.6±5.8	-36.2±1.9	-114.5±6.2	2.1±0.1	3.1±0.2
C1	4	ZINC000225318193	-9.2	-33.6±6.7	-12.4±5.3	-26.6±5.5	-72.6±14.8	2.1±0.2	9.7±0.6
C1	5	ZINC000299770618	-9.2	-48.0±4.2	-8.7±5.6	-35.7±3.7	-92.5±7.3	2.9±0.1	2.5±0.3

<b>C1</b>	<b>6</b>	<b>ZINC000827360794</b>	<b>-9.1</b>	<b>-43.7±3.5</b>	<b>-18.8±8.4</b>	<b>-41.6±2.8</b>	<b>-104.2±11.1</b>	<b>2.4±0.1</b>	<b>2.9±0.1</b>
C1	7	ZINC000035373220	-9.1	-56.6±4.2	-17.3±9.4	-54.8±3.1	-128.8±9.1	2.3±0.1	1.0±0.1
<b>C1</b>	<b>8</b>	<b>ZINC000072430969</b>	<b>-9.0</b>	<b>-46.3±3.0</b>	<b>-5.2±3.3</b>	<b>-44.1±3.1</b>	<b>-95.7±5.8</b>	<b>2.2±0.1</b>	<b>1.9±0.2</b>
<b>C1</b>	<b>9</b>	<b>ZINC000078648574</b>	<b>-9.0</b>	<b>-50.4±5.2</b>	<b>-4.1±3.5</b>	<b>-54.1±6.5</b>	<b>-108.7±13.1</b>	<b>2.8±0.1</b>	<b>6.3±0.5</b>
C1	10	ZINC000005344596	-9.0	-53.9±3.8	-7.5±5.5	-39.5±4.8	-100.9±11.6	3.5±0.3	2.2±0.4
C1	11	ZINC000069348668	-8.9	-57.2±2.4	-13.9±3.4	-44.5±2.3	-115.7±5.8	2.2±0.1	3.9±0.1
<b>C2</b>	<b>1</b>	<b>ZINC000057999653</b>	<b>-10.1</b>	<b>-47.1±4.1</b>	<b>-8.6±13.5</b>	<b>-38.9±2.4</b>	<b>-94.6±10.9</b>	<b>2.3±0.1</b>	<b>2.7±0.2</b>
C2	2	ZINC000002877267	-9.9	-48.2±5.3	-3.8±6.1	-40.2±4.1	-92.3±9.2	2.5±0.1	6.7±0.6
C2	3	ZINC000408693879	-9.8	-61.9±4.6	-31.9±13.1	-54.7±3.1	-148.5±14.0	3.8±0.1	3.2±0.2
C2	4	ZINC000000880008	-9.8	-61.5±3.8	-12.0±4.3	-49.0±3.2	-122.6±6.3	3.1±0.1	2.8±0.3
<b>C2</b>	<b>5</b>	<b>ZINC000006664413</b>	<b>-9.8</b>	<b>-46.4±2.8</b>	<b>-20.1±7.0</b>	<b>-43.4±3.2</b>	<b>-109.9±8.9</b>	<b>2.6±0.1</b>	<b>3.6±0.3</b>
C2	6	ZINC000001408226	-9.7	-35.0±4.1	-17.3±7.9	-23.5±3.0	-75.8±11.4	3.3±0.1	3.3±0.3
C2	7	ZINC000001045477	-9.7	-45.9±5.1	-11.7±5.7	-28.3±2.4	-86.0±11.7	2.9±0.1	3.6±0.2
C2	8	ZINC000005493735	-9.7	-46.3±3.0	-5.2±3.3	-44.1±3.1	-95.7±5.8	2.2±0.1	1.9±0.2
C2	9	ZINC000001641702	-9.6	-36.2±3.4	-2.6±5.0	-30.3±2.2	-69.1±6.0	2.8±0.2	5.7±0.3
C2	10	ZINC000000302628	-9.5	-39.3±2.7	-12.9±3.3	-36.7±1.9	-89.1±3.8	2.6±0.1	1.8±0.3
C2	11	ZINC000095418373	-9.3	-48.3±3.1	-9.0±5.4	-36.1±2.9	-93.5±7.6	2.6±0.1	4.0±0.2
<b>C2</b>	<b>12</b>	<b>ZINC000006750553</b>	<b>-9.3</b>	<b>-44.6±3.5</b>	<b>-21.4±8.8</b>	<b>-42.9±3.1</b>	<b>-109.1±10.8</b>	<b>2.9±0.1</b>	<b>2.8±0.3</b>
C2	13	ZINC000097002851	-9.3	-34.0±5.7	-29.8±9.4	-27.3±3.7	-91.2±10.2	2.9±0.1	6.6±0.6
C2	14	ZINC000005776998	-9.3	-43.2±3.3	-25.4±6.5	-44.0±3.3	-112.6±9.2	3.3±0.1	2.7±0.8
C2	15	ZINC000004663101	-9.3	-45.0±2.7	-6.9±3.5	-47.9±2.5	-99.9±5.3	2.9±0.1	2.8±0.3
C2	16	ZINC000005604766	-9.2	-35.7±3.3	-18.2±14.1	-32.7±2.8	-86.6±14.7	3.0±0.1	3.5±0.2
C2	17	ZINC000225173433	-9.1	-51.5±3.7	-5.2±2.1	-47.2±2.7	-103.9±5.9	2.0±0.1	3.0±0.1
C2	18	ZINC000034720963	-9.1	-49.2±5.6	-50.2±13.8	-44.9±3.4	-144.3±10.4	2.8±0.1	5.4±0.3
C2	19	ZINC000409066936	-9.1	-40.1±2.6	-4.0±5.9	-34.2±3.3	-78.4±9.5	2.9±0.1	5.2±0.4
C2	20	ZINC000014750115	-9.0	-50.6±3.4	-12.2±2.9	-43.3±3.5	-106.1±6.7	3.0±0.1	3.4±0.2
C2	21	ZINC000059677349	-8.9	-52.4±2.5	-3.6±2.7	-50.7±3.3	-106.7±4.6	3.3±0.2	4.5±0.2
C2	22	ZINC000002690402	-8.9	-67.4±6.3	-14.6±3.9	-47.7±4.7	-129.8±11.1	2.9±0.1	3.7±0.2
C2	23	ZINC000020572602	-8.9	-53.5±3.2	-9.5±3.3	-53.5±3.6	-116.6±6.2	2.5±0.1	2.2±0.3
C2	24	ZINC000408729576	-8.9	-33.7±3.4	-24.7±11.3	-29.9±2.2	-88.4±11.9	2.8±0.1	1.5±0.3
C2	25	ZINC000009660785	-8.9	-58.5±4.6	-21.7±4.5	-49.4±3.0	-129.7±8.5	2.8±0.1	2.0±0.3
C2	26	ZINC000334160398	-8.8	-58.9±3.5	-21.5±4.1	-42.0±1.9	-122.5±5.7	2.7±0.1	2.4±0.3



**Table B2**

*The Predicted ADME Properties for Top Compounds*

Structure	Compound	GI absorption	BBB permeant	CYP1A2	CYP2C19	CYP2C9	CYP2D6	CYP3A4	Lipinski rule	PAINS	Brenk
	Crystal Structure (PDB ID:6PT3)	High	Yes	No	No	No	Yes	Yes	Yes; 0 violation	0 alert	0 alert
CC	ZINC000020559278	High	Yes	Yes	No	No	Yes	Yes	Yes; 0 violation	0 alert	0 alert
CC	ZINC00014242201	Low	No	No	No	No	No	Yes	Yes; 0 violation	0 alert	0 alert
CC	ZINC000562639987	High	No	No	No	No	No	No	Yes; 0 violation	0 alert	0 alert
CC	ZINC000071763967	High	Yes	No	No	No	No	No	Yes; 0 violation	1 alert: catechol_A	1 alert: catechol
CC	ZINC000067947687	High	Yes	Yes	No	No	Yes	No	Yes; 0 violation	1 alert: catechol_A	1 alert: catechol
CC	ZINC000634950507	High	Yes	No	No	No	No	No	Yes; 0 violation	0 alert	0 alert
CC	ZINC000072227493	High	Yes	Yes	Yes	Yes	No	No	Yes; 0 violation	0 alert	0 alert
CC	ZINC000257262766	High	No	No	No	No	Yes	Yes	Yes; 0 violation	0 alert	0 alert
CC	ZINC000006645700	High	Yes	Yes	Yes	No	Yes	No	Yes; 0 violation	0 alert	0 alert
CC	ZINC000082157638	High	No	No	No	No	No	No	Yes; 0 violation	0 alert	0 alert
CC	ZINC000091782363	Low	No	No	No	No	No	No	Yes; 0 violation	0 alert	1 alert: hydantoin
CC	ZINC000091595762	High	Yes	No	No	No	No	No	Yes; 0 violation	0 alert	0 alert
CC	ZINC000067558896	High	No	No	No	No	No	No	Yes; 0 violation	0 alert	0 alert
CC	ZINC000757213857	High	No	No	No	No	No	No	Yes; 0 violation	0 alert	0 alert
CC	ZINC000218867772	High	Yes	No	No	No	No	No	Yes; 0 violation	0 alert	0 alert
CC	ZINC00013637398	High	No	Yes	Yes	No	No	Yes	Yes; 0 violation	0 alert	1 alert: thiocarbonyl_group
CC	ZINC000078515864	High	Yes	No	No	No	Yes	No	Yes; 0 violation	0 alert	0 alert
CC	ZINC00014538415	High	No	No	No	No	No	No	Yes; 0 violation	0 alert	0 alert
CC	ZINC000218873420	High	No	Yes	No	No	No	No	Yes; 0 violation	0 alert	0 alert
CC	ZINC000001743629	High	Yes	Yes	Yes	Yes	Yes	No	Yes; 0 violation	0 alert	0 alert
CC	ZINC000028295259	High	Yes	No	No	No	No	No	Yes; 0 violation	0 alert	0 alert
CC	ZINC00014536536	High	No	No	No	No	No	No	Yes; 0 violation	0 alert	0 alert
CC	ZINC000147095213	High	Yes	Yes	No	No	No	No	Yes; 0 violation	0 alert	0 alert
CC	ZINC000095698957	Low	No	No	Yes	No	No	No	Yes; 0 violation	0 alert	0 alert
CC	ZINC00014888594	High	Yes	No	No	No	No	No	Yes; 0 violation	0 alert	0 alert
CC	ZINC00015080658	High	No	No	No	No	No	No	Yes; 0 violation	0 alert	1 alert: phthalimide
CC	ZINC000096027748	High	No	No	No	No	No	No	Yes; 0 violation	0 alert	2 alerts: imine_1, imine_2
CC	ZINC000067675691	High	No	No	No	No	No	No	Yes; 0 violation	0 alert	0 alert
CC	ZINC00011691661	High	No	Yes	Yes	Yes	No	Yes	Yes; 0 violation	0 alert	1 alert: isolated_alkene
CC	ZINC000096312018	High	Yes	Yes	Yes	Yes	Yes	Yes	Yes; 0 violation	0 alert	0 alert
CC	ZINC000248261142	High	Yes	Yes	No	No	Yes	No	Yes; 0 violation	0 alert	0 alert
CC	ZINC000036160706	High	No	No	No	Yes	No	Yes	Yes; 0 violation	0 alert	1 alert: nitro_group

C1	ZINC000025329384	High	Yes	No	No	No	Yes	Yes	Yes; 0 violation	0 alert	0 alert
C1	ZINC000037556415	High	Yes	No	Yes	Yes	Yes	Yes	Yes; 0 violation	0 alert	0 alert
C1	ZINC000095456365	High	No	No	Yes	Yes	Yes	Yes	Yes; 0 violation	0 alert	0 alert
C1	ZINC000225318193	High	Yes	Yes	Yes	No	No	No	Yes; 0 violation	0 alert	0 alert
C1	ZINC000299770618	High	No	Yes	No	No	Yes	No	Yes; 0 violation	0 alert	0 alert
C1	ZINC000827360794	High	Yes	No	No	No	Yes	Yes	Yes; 0 violation	0 alert	0 alert
C1	ZINC000035373220	High	No	No	No	Yes	No	No	Yes; 0 violation	1 alert: catechol_A	1 alert: catechol
C1	ZINC000072430969	High	Yes	Yes	Yes	Yes	Yes	Yes	Yes; 0 violation	0 alert	0 alert
C1	ZINC000078648574	High	Yes	No	Yes	Yes	Yes	No	Yes; 0 violation	0 alert	0 alert
C1	ZINC000005344596	High	Yes	No	No	Yes	No	No	Yes; 0 violation	0 alert	0 alert
C1	ZINC000069348668	High	Yes	Yes	Yes	Yes	Yes	Yes	Yes; 0 violation	0 alert	1 alert: triple_bond
C2	ZINC000057999653	High	Yes	Yes	Yes	Yes	Yes	Yes	Yes; 0 violation	0 alert	0 alert
C2	ZINC000002877267	High	No	Yes	Yes	Yes	Yes	Yes	Yes; 0 violation	0 alert	0 alert
C2	ZINC000408693879	High	No	No	No	Yes	No	Yes	Yes; 0 violation	1 alert: ene_six_het_A	2 alerts: michael_acceptor_1, michael_acceptor_4
C2	ZINC000000880008	High	No	No	Yes	Yes	Yes	Yes	Yes; 0 violation	0 alert	1 alert: thiocarbonyl_group
C2	ZINC000006664413	High	Yes	Yes	Yes	Yes	Yes	Yes	Yes; 0 violation	0 alert	0 alert
C2	ZINC000001408226	High	Yes	Yes	No	No	No	No	Yes; 0 violation	0 alert	1 alert: imine_1
C2	ZINC000001045477	Low	No	Yes	Yes	Yes	Yes	No	Yes; 1 violation: MLOGP>=4.15	0 alert	1 alert: thiocarbonyl_group
C2	ZINC000005493735	High	No	No	Yes	Yes	No	Yes	Yes; 0 violation	0 alert	0 alert
C2	ZINC000001641702	High	Yes	Yes	Yes	Yes	Yes	No	Yes; 0 violation	0 alert	0 alert
C2	ZINC000000302628	High	Yes	Yes	Yes	No	No	No	Yes; 0 violation	0 alert	0 alert
C2	ZINC000095418373	High	No	Yes	Yes	Yes	Yes	Yes	Yes; 0 violation	0 alert	0 alert
C2	ZINC000006750553	High	Yes	Yes	Yes	No	Yes	No	Yes; 0 violation	0 alert	0 alert
C2	ZINC000097002851	High	No	Yes	No	No	Yes	No	Yes; 0 violation	0 alert	0 alert
C2	ZINC000005776998	High	No	No	No	No	Yes	No	Yes; 0 violation	1 alert: indo_3yl_alk	0 alert
C2	ZINC000004663101	High	Yes	Yes	Yes	No	Yes	No	Yes; 0 violation	1 alert: anil_alk_ene	1 alert: isolated_alkene
C2	ZINC000005604766	High	No	Yes	Yes	No	No	No	Yes; 0 violation	0 alert	2 alerts: imine_1, imine_2
C2	ZINC000225173433	High	No	Yes	Yes	Yes	No	Yes	Yes; 0 violation	0 alert	1 alert: thiocarbonyl_group
C2	ZINC000034720963	High	No	Yes	Yes	Yes	No	No	Yes; 1 violation: MLOGP>=4.15	1 alert: ene_five_het_B	1 alert: michael_acceptor_1
C2	ZINC000409066936	High	Yes	Yes	Yes	Yes	Yes	Yes	Yes; 0 violation	0 alert	1 alert: michael_acceptor_1

C2	ZINC000014750115	High	No	No	No	No	No	No	Yes; 0 violation	0 alert	0 alert
C2	ZINC000059677349	High	Yes	Yes	Yes	No	Yes	Yes	Yes; 0 violation	1 alert: indol_3yl_alk	0 alert
C2	ZINC000002690402	Low	No	No	No	Yes	No	Yes	Yes; 0 violation	0 alert	1 alert: thiocarbonyl_group
C2	ZINC000020572602	High	No	No	No	Yes	No	Yes	Yes; 0 violation	1 alert: hzone_phenol_B	1 alert: imine_1
C2	ZINC000408729576	High	No	No	No	No	No	No	Yes; 0 violation	0 alert	1 alert: imine_1
C2	ZINC000009660785	High	No	No	No	Yes	Yes	Yes	Yes; 0 violation	0 alert	1 alert: hydantoin
C2	ZINC000334160398	High	No	No	No	Yes	Yes	Yes	Yes; 0 violation	0 alert	0 alert

**Table B3**

*Critical Nodes Identified From the Network Analysis or the DPI-287/DOR System and the Top 8 Compound Systems*

Critical Nodes								
crystal	CC1	CC17	C1 01	C1 02	C1 06	C1 09	C2 01	C2 05
V59	L48	V59	A43	L48	Y56	L48	62	L55
G63	N67	I88	L48	S57	G63	A61	88	V59
K81	L69	D95	L55	C60	L91	L65	D95	N67
Y87	I74	A98	V59	I86	D95	I86	T99	V70
L91	L91	T99	A92	Y87	T99	I88	A107	M80
A94	D95	T101	D95	I88	T101	N90	M111	T84
D95	A98	L102	L97	L91	L102	L91	T113	I86
A98	T101	F104	T113	T113	Q105	L93	F116	L91
Y129	L102	Q105	A123	M132	Y109	D95	Y130	L97
N131	F104	Y109	I127	F133	T113	L97	F133	A98
M132	T113	T113	D128	T134	A123	T99	T134	K108
S135	V124	L120	Y129	F137	I127	L102	I136	Y109
I136	I127	I127	M132	T138	Y130	T113	T138	L110
F137	D128	D128	L139	T140	T134	I127	L139	M111
L139	M132	N131	S143	L157	I136	D128	T140	E112
T140	T138	F133	A165	T161	F137	M132	R146	I127
M142	T140	S135	N169	I172	T138	I136	G178	Y130
Y147	M142	I136	V196	A176	T140	L139	P182	N131
A149	M186	F137	Q201	G180	M142	V150	M186	F133
R160	V196	T138	P203	M186	S143	L157	F202	T134
P162	F202	L139	V217	V196	D145	T161	K214	T138
M186	K214	T140	F218	F202	L157	I172	I215	L157
V188	F218	M141	V224	F218	T161	A176	F218	R160
K214	L219	S143	L227	L219	V196	V196	L219	T161
C216	A221	M186	I229	V224	L200	Q201	F220	P162
V217	F222	V196	R244	P225	F202	P203	F222	K166
L219	V224	F202	D253	R244	V223	K214	M236	I172
A269	P225	L219	V266	D253	L227	C216	R239	W173
F270	V265	F220	G268	R258	M262	F218	M262	M186
W274	A269	F222	F270	M262	V265	L219	C273	F202
I277	H278	V224	W274	V267	A269	F220	I277	W209
H278	V281	P225	H278	F270	A275	F222	V281	V212
	A298	I229	R292	W274	I279	R239	C303	P225
	Y308	Y233	P294	H278	V297	R261	N310	I228
	N310	M262	A305	V297	A298	V265	P315	V281
	Y318	V266	L306	L306	H301	A269	V316	V287
		F270	G307	Y308	A305	F270	Y318	I289
		V271	Y308	A309	G307	H278		
		W274	N310	N310	Y308	V297		
		V297	S312	L313	N310	N310		
		A309	Y318		S311	S312		
		S311	L321		L313	N314		
		L313			N314			
		Y318			Y318			
		L321			L321			
		N324						
		K326						
<b>32 total</b>	<b>36 total</b>	<b>47 total</b>	<b>42 total</b>	<b>40 total</b>	<b>45 total</b>	<b>42 total</b>	<b>37 total</b>	<b>37 total</b>
	<b>11 same</b>	<b>13 same</b>	<b>9 same</b>	<b>10 same</b>	<b>8 same</b>	<b>11 same</b>	<b>8 same</b>	<b>7 same</b>

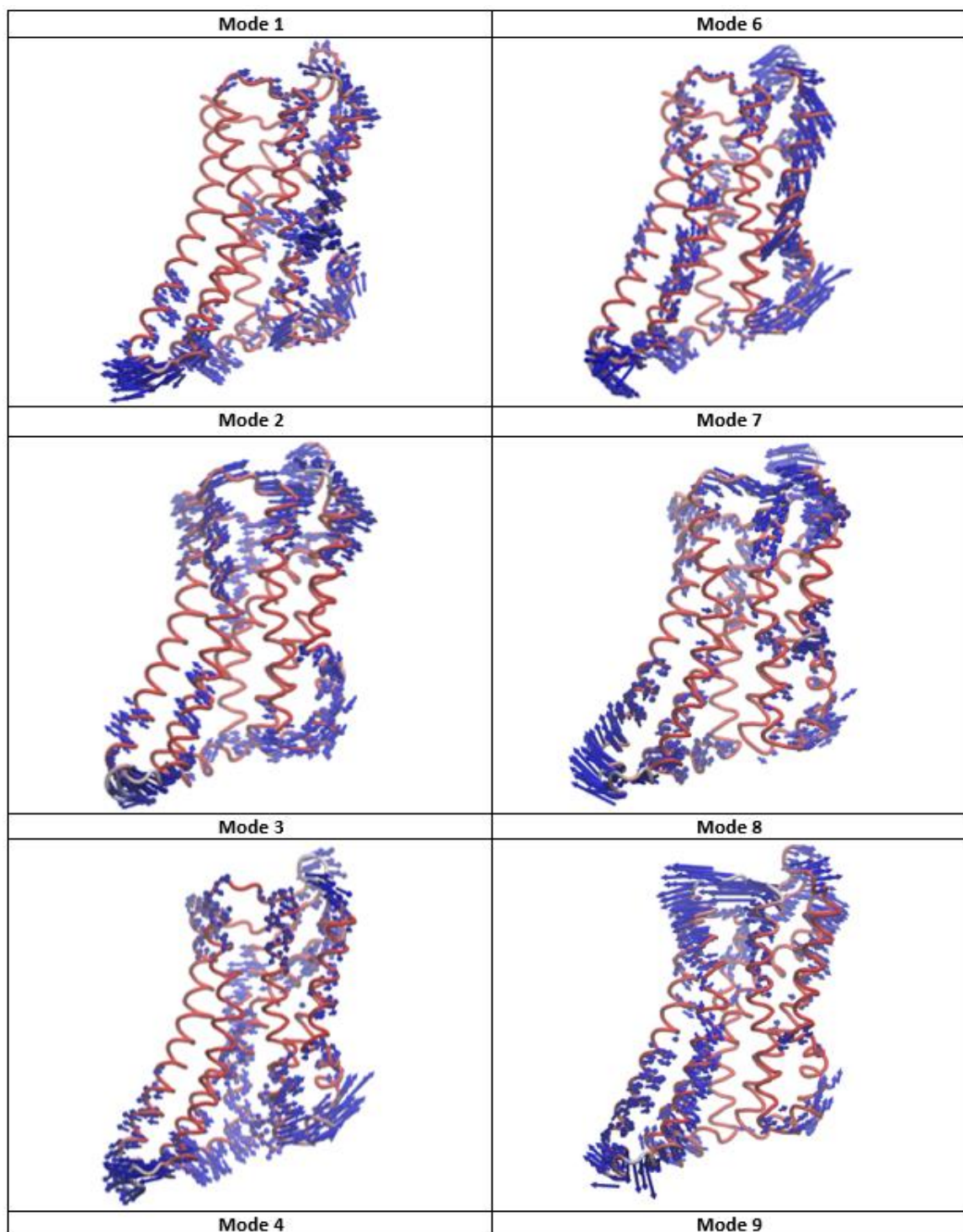
**Table B4**

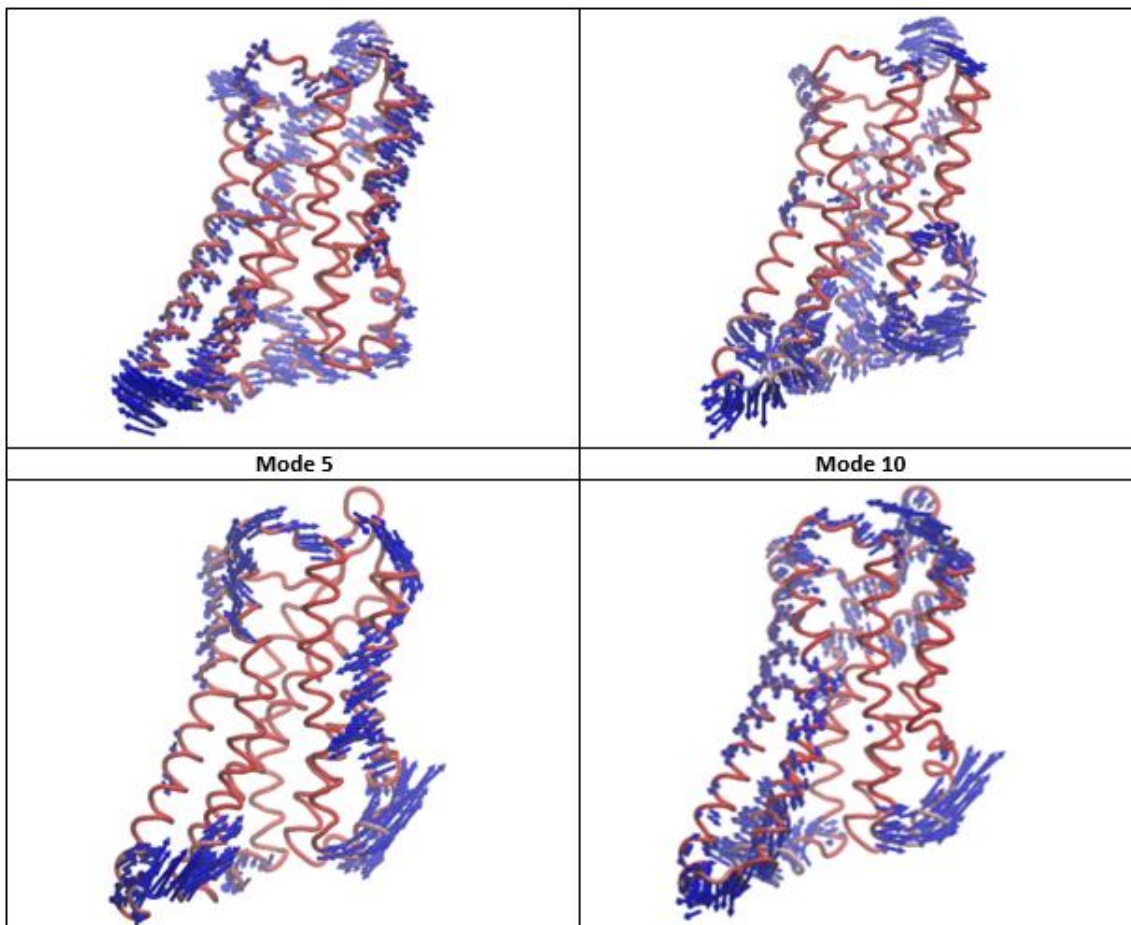
*The Optimal Path of the Transmission and Tyrosine Toggle Switch Generated From the Network Analysis for the Crystal Complex and the Top 8 Compounds*

Molecular Switch Optimal Path								
crystal	CC1	CC17	C1 01	C1 02	C1 06	C1 09	C2 01	C2 05
<b>Transmission Switch</b>								
Ligand	Ligand	Ligand	Ligand	Ligand	Ligand	Ligand	Ligand	Ligand
W274	W274	W274	W274	W274	I304	V281	Y308	N131
F270	F270	F270	F270	F270	L306	I279	S312	F133
G268	V266	V266	G268	V267	C273	A275	N314	F137
L264	M262	M262	L264	V265	A269	V271	Y318	T140
R261	R258	R258	R261	M262	V265	G268	M262	V144
R258	S255	S255	R258	R258	M262	V265	R258	R146
S255			S255	S255	R258	R261	S255	I259
					S255	R258		S255
						S255		
<b>7 total</b>	<b>6 total</b>	<b>6 total</b>	<b>7 total</b>	<b>7 total</b>	<b>8 total</b>	<b>9 total</b>	<b>7 total</b>	<b>8 total</b>
	4 same	4 same	7 same	4 same	2 same	4 same	2 same	1 same
<b>Tyrosine Toggle Switch</b>								
crystal	CC1	CC17	C1 01	C1 02	C1 06	C1 09	C2 01	C2 05
Ligand	Ligand	Ligand	Ligand	Ligand	Ligand	Ligand	Ligand	Ligand
G307	Y308	Y308	S311	S311	Y308	S311	Y308	S311
N310	S311	N310	N314	P315	N310	N314	S312	N314
N314	N314	N314	Y318	Y318	N314	Y318	N314	Y318
Y318	Y318	Y318			Y318		Y318	
<b>4 total</b>	<b>4 total</b>	<b>4 total</b>	<b>3 total</b>	<b>3 total</b>	<b>4 total</b>	<b>3 total</b>	<b>4 total</b>	<b>3 total</b>
	2 same	3 same	2 same	1 same	3 same	2 same	2 same	2 same

## Figure B1

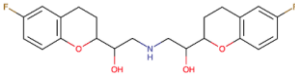
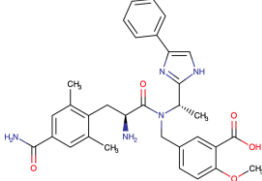
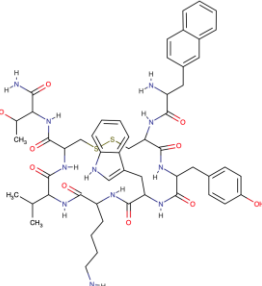
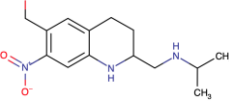
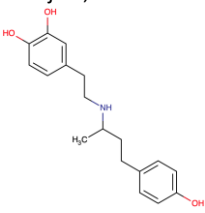
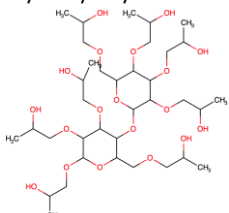
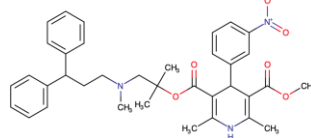
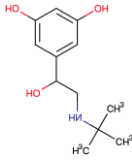
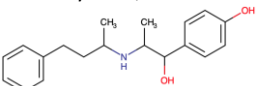
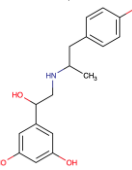
*Top 10 Low Vibrational Modes From the NMA Based on the Active Conformation DOR Agonist DPI-287 System*





**Figure B2**

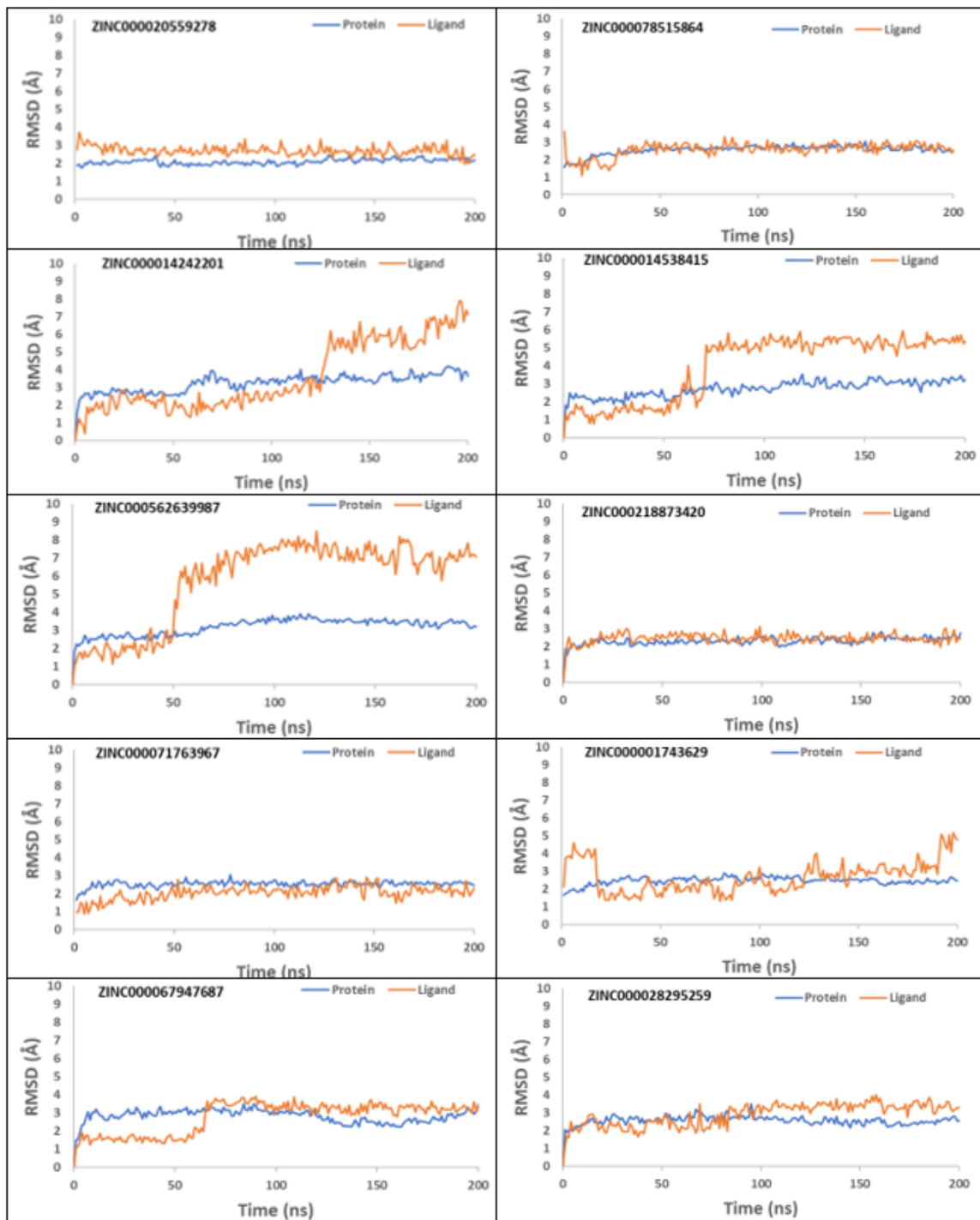
*Top 10 From the FDA Approved Drug Compounds for the Crystal Conformation*

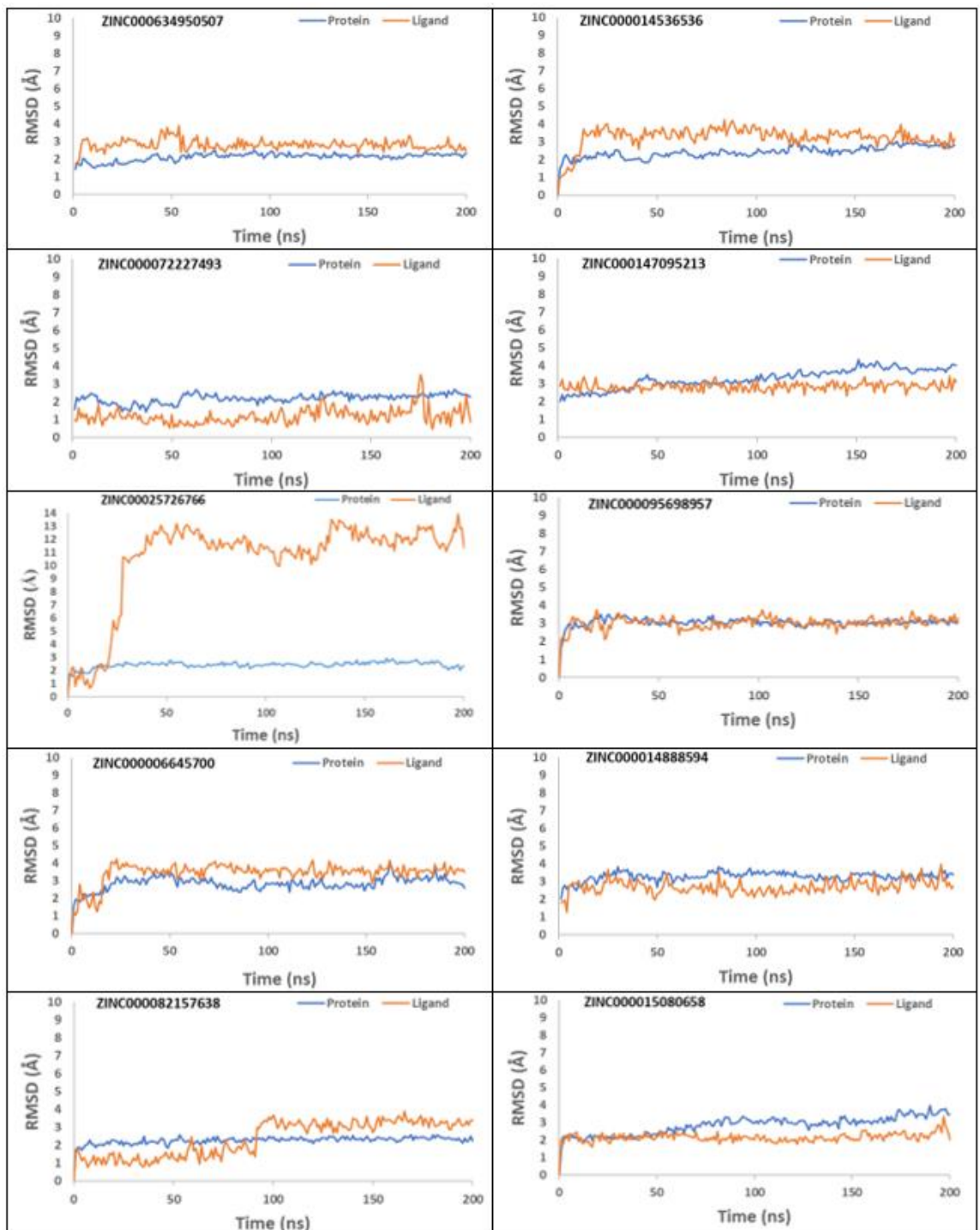
No	FDA approved drugs/ Structure/ Docking score	No	FDA approved drugs/ Structure/ Docking score
1	Lobivon; Nebivolol  Docking Score: -8.467 kcal/mol	6	Eluxadoline  Docking Score: -7.297 kcal/mol
2	Lanreotide  Docking Score: -8.037 kcal/mol	7	Oxamniquine; Mansil  Docking Score: -7.202 kcal/mol
3	Dobuject; Dobutamine  Docking Score: -7.638 kcal/mol	8	Hydroxyethyl cellulose  Docking Score: -7.132 kcal/mol
4	Lercanidipine  Docking Score: -7.504 kcal/mol	9	Terbutaline; Brethaire  Docking Score: -7.054 kcal/mol
5	Nylidrin; Arbid  Docking Score: -7.482 kcal/mol	10	Fenoterol; Alveofen  Docking Score: -6.965 kcal/mol

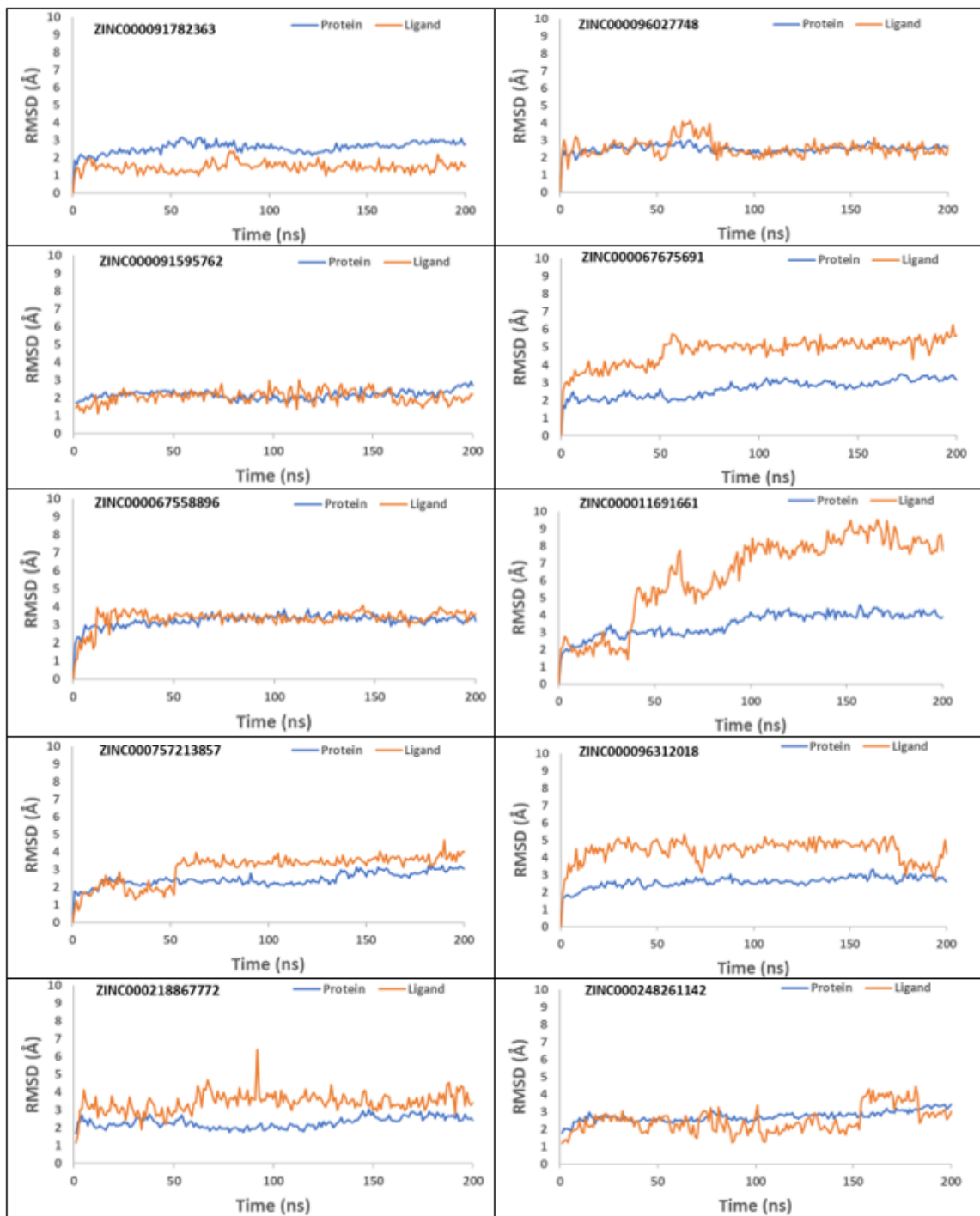


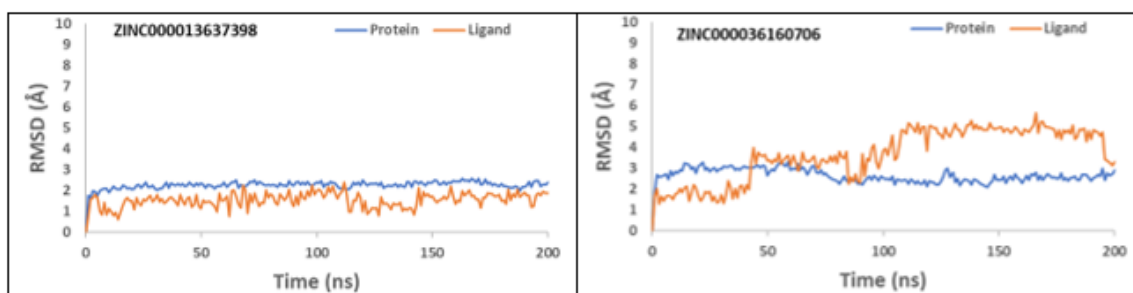
**Figure B3**

*Ca RMSD of the Top Zinc Compounds During 200ns MD Simulation in Reference to the Crystal Active Conformation*



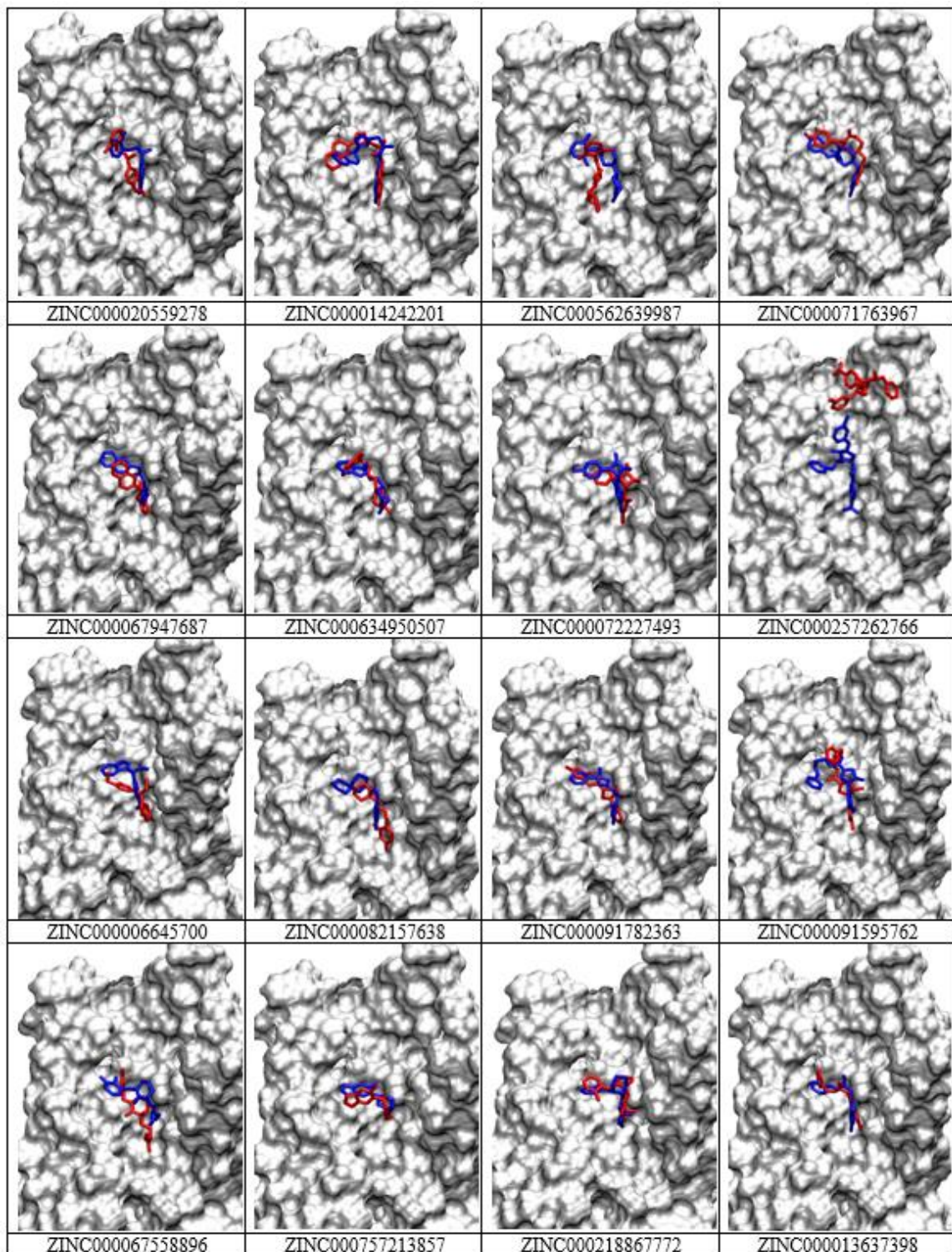




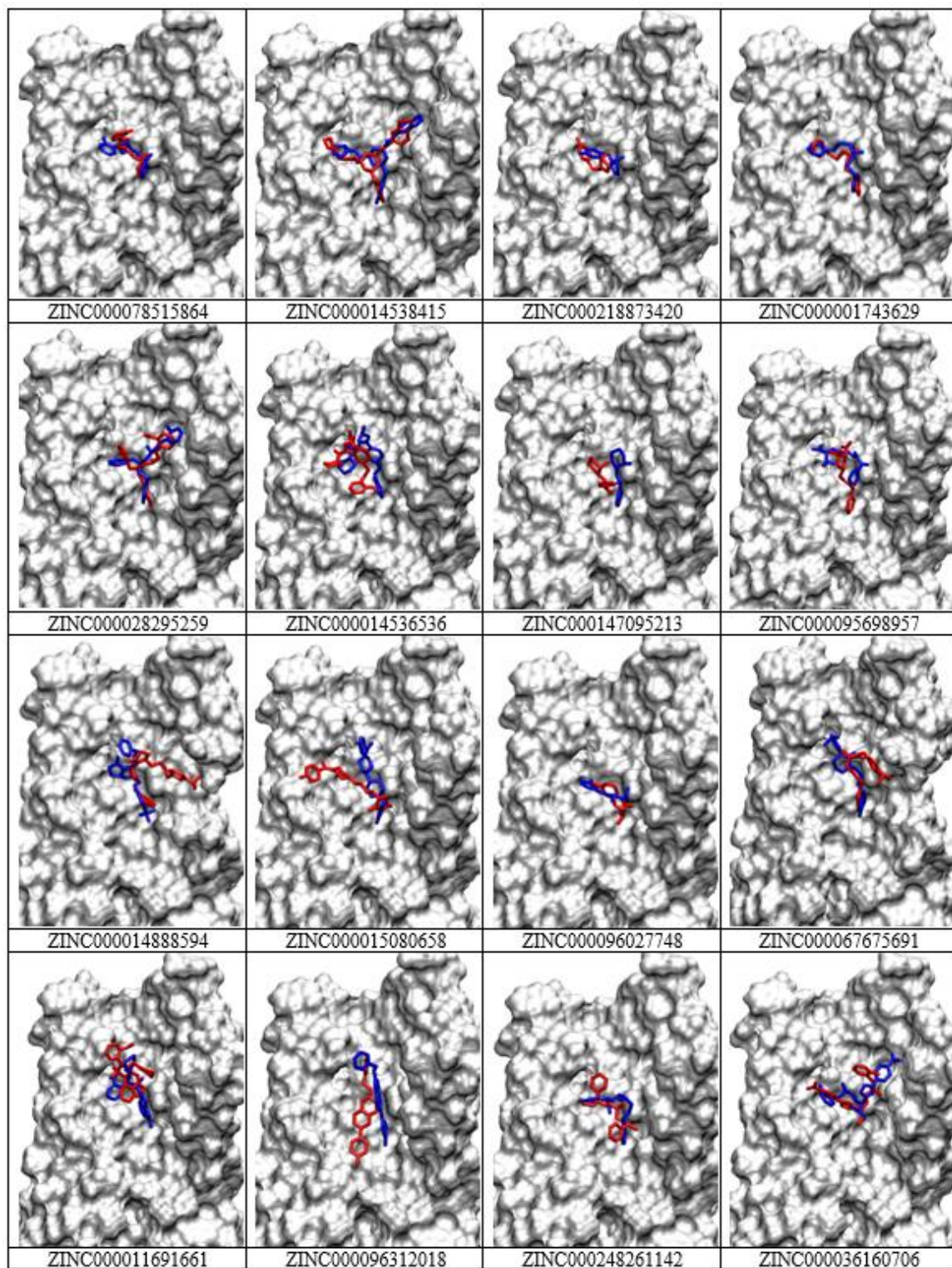


### Figure B4

Comparison of 32 Zinc Compounds for the Crystal Conformation in the Docked Pose (Blue) and the MD Simulation Pose (Red)

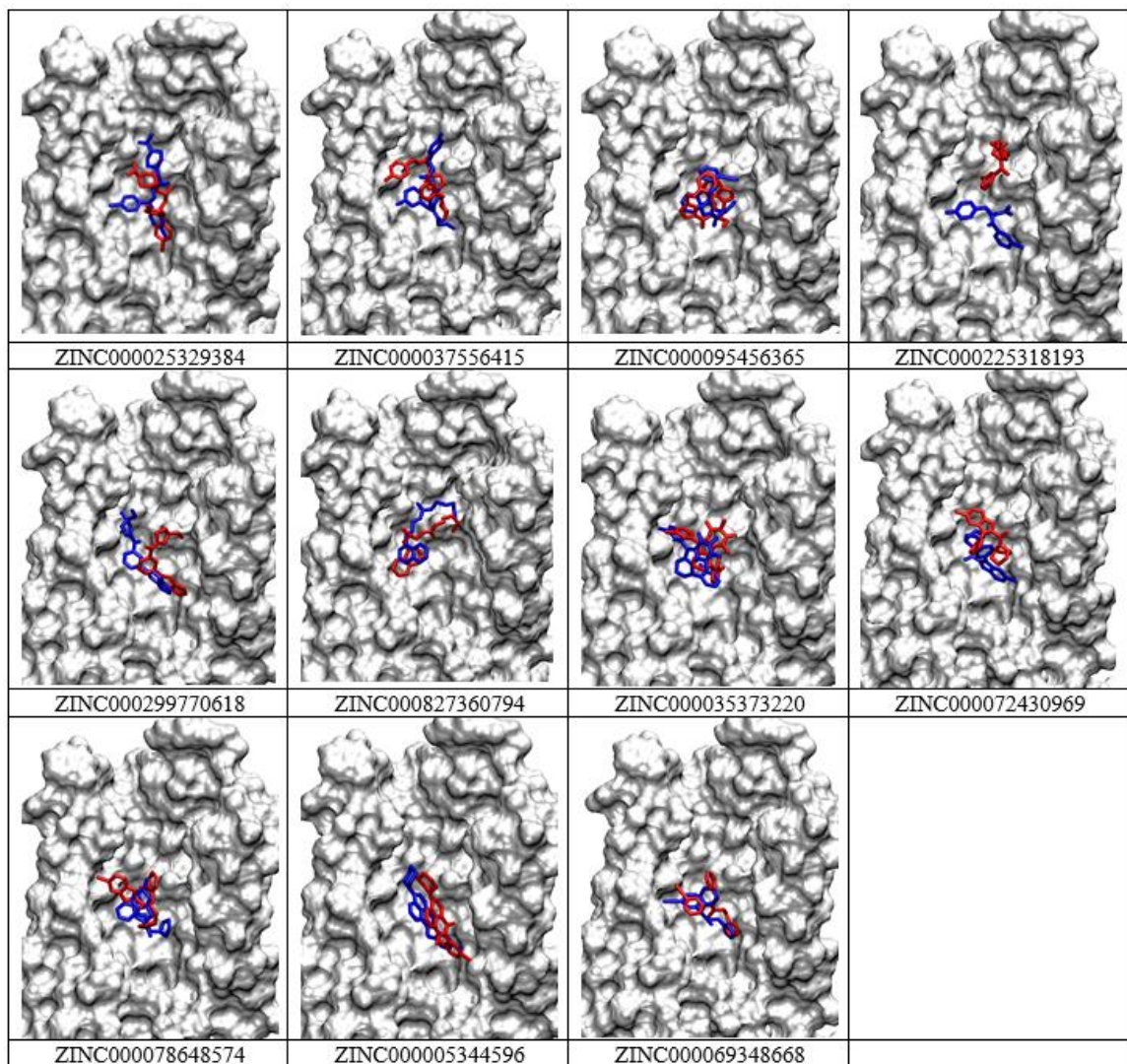






### Figure B5

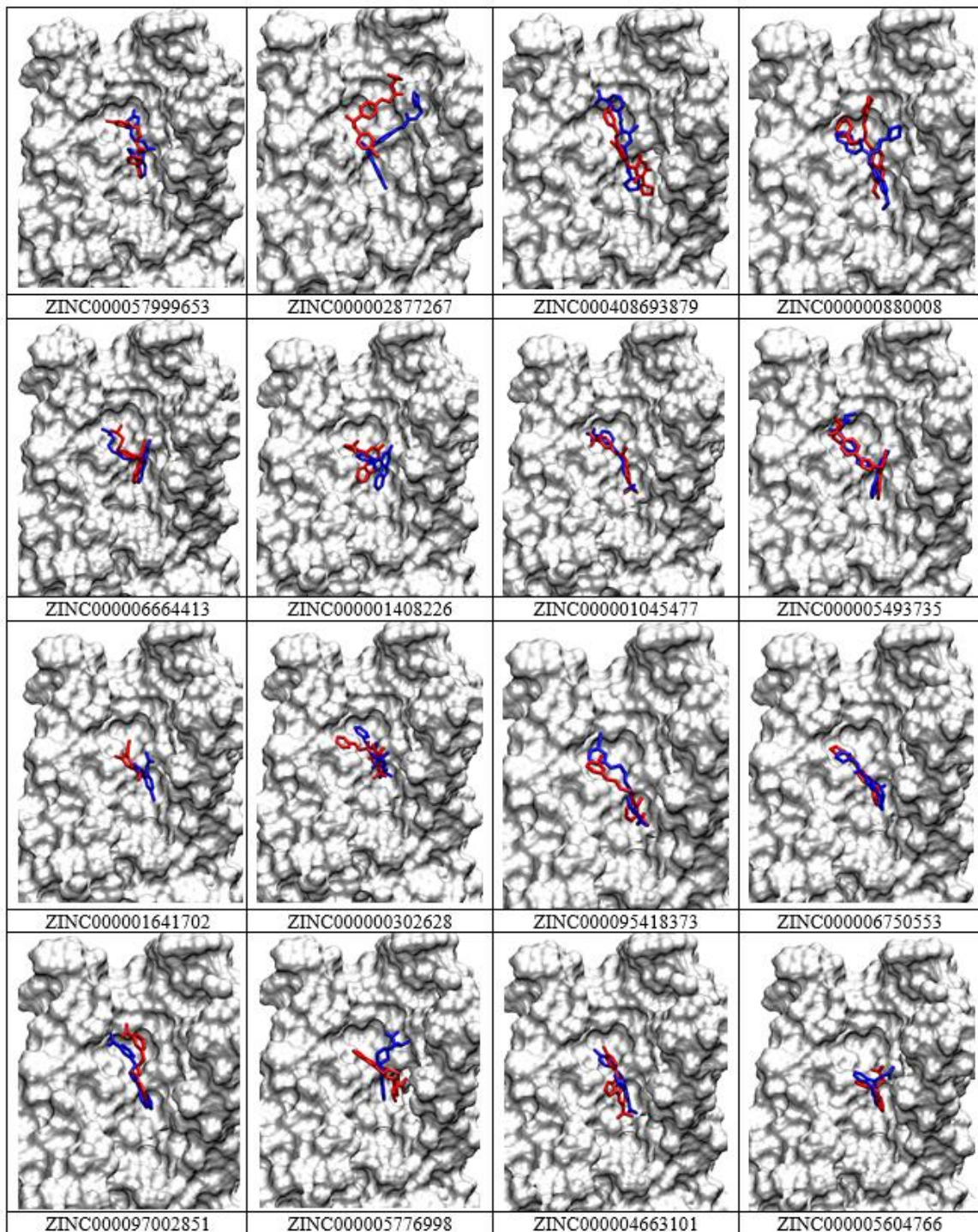
Comparison of 11 Zinc Compounds for the First Representative Structure From the MD Crystal Conformation in the Docked Pose (Blue) and the MD Simulation Pose (Red)



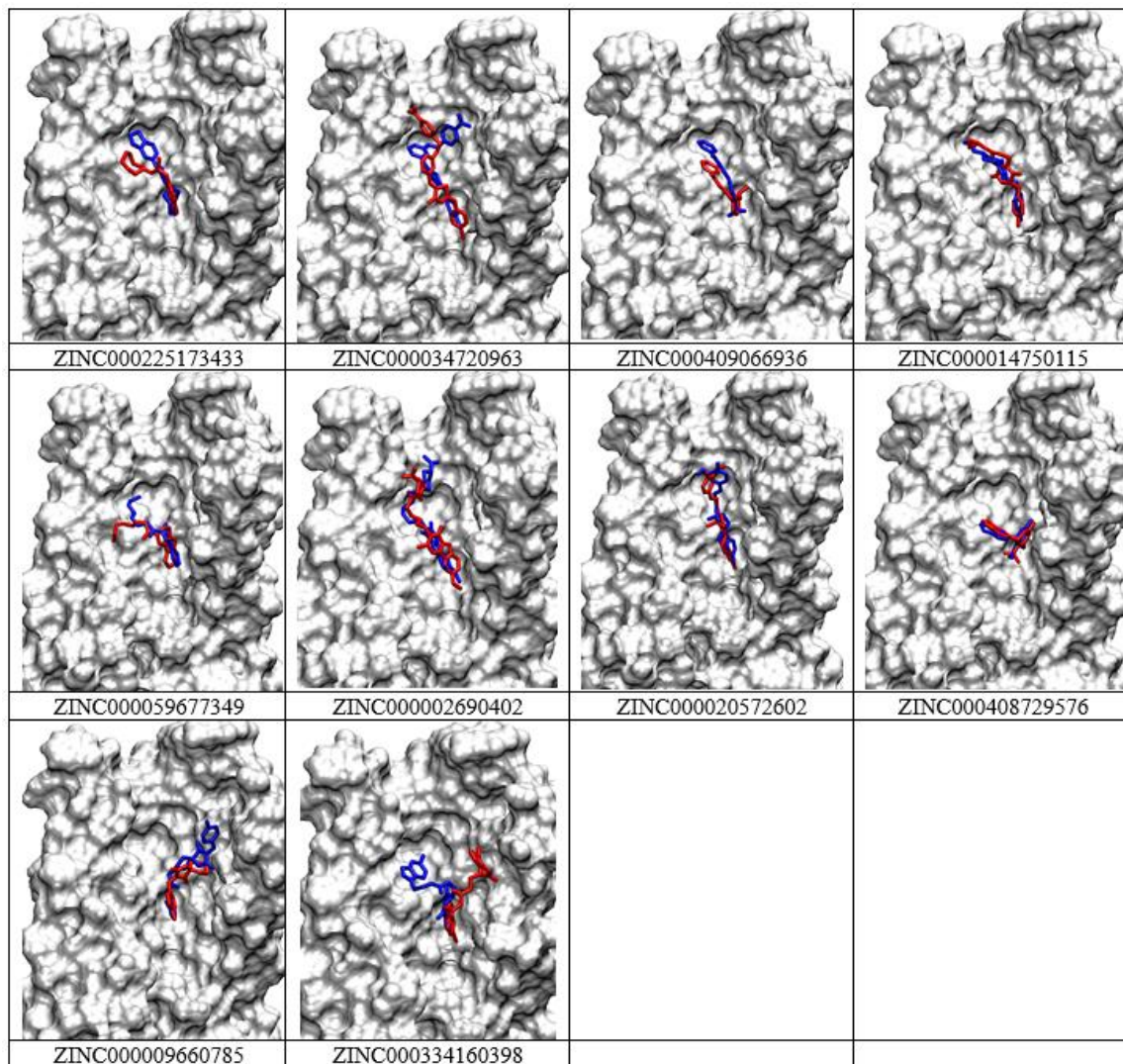


## Figure B6

Comparison of 26 Zinc Compounds for the Second Representative Structure From the MD Crystal Conformation in the Docked Pose (Blue) and the MD Simulation Pose (Red)

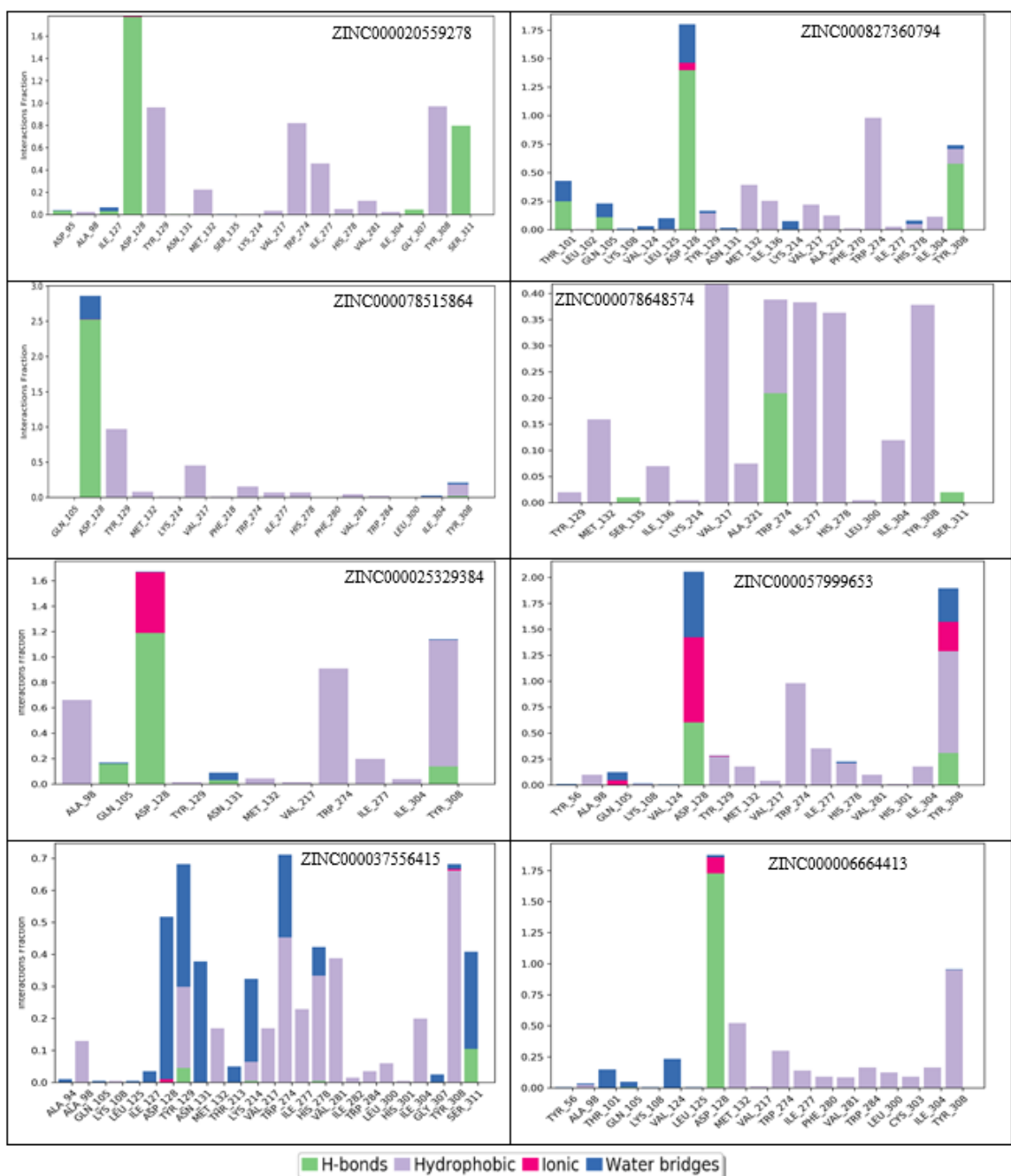






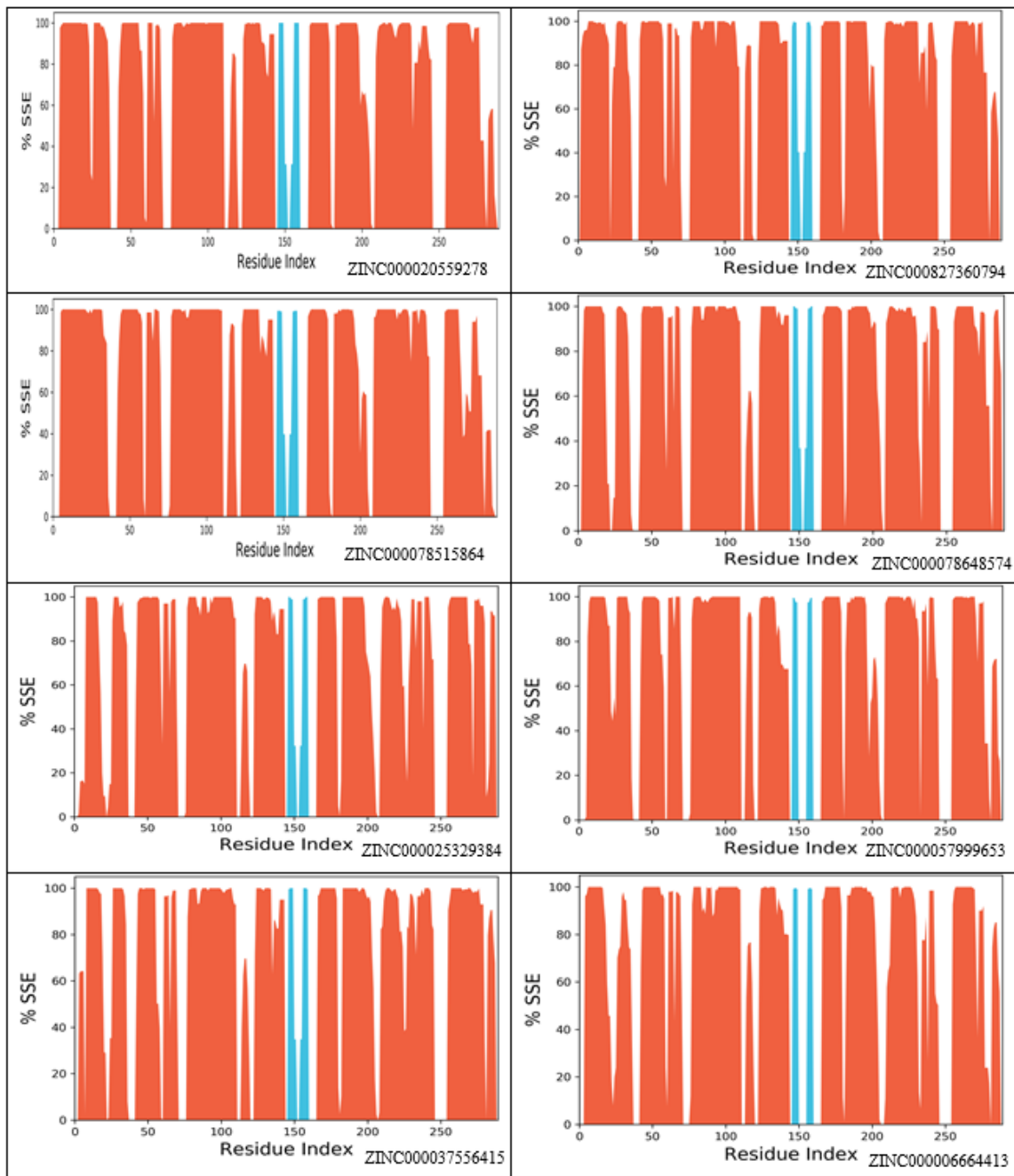
**Figure B7**

*Protein-Ligand Contacts During MD Simulations for the Top 8 Compounds*



**Figure B8**

*Protein Secondary Structure Elements (SSE) of the Receptor in Complex With the Top 8 Compounds*



## Figure B9

*The  $\alpha$  Root Mean Square Fluctuation (RMSF) of the Receptor in Complex With the Top 8 Ligands*

